



Università degli Studi di Firenze

Scuola di Ingegneria

DIEF - Department of Industrial Engineering of Florence

PhD School: *Energetica e Tecnologie Industriali ed Ambientali Innovative*

Scientific Area: *ING-IND/08 - Macchine a Fluido*

HIGH-FIDELITY NUMERICAL INVESTIGATIONS OF A HYDROGEN ROTATING DETONATION COMBUSTOR

PhD Candidate: ING. PIER CARLO NASSINI

Tutor: PROF. ING. ANTONIO ANDREINI

Academic supervisor: PROF. ING. BRUNO FACCHINI

PhD School Coordinator: PROF. ING. GIOVANNI FERRARA

XXXIV PhD School Cycle - 2018-2021

©Università degli Studi di Firenze – Faculty of Engineering
Via di Santa Marta, 3, 50139 Firenze, Italy.

Tutti i diritti riservati. Nessuna parte del testo può essere riprodotta o trasmessa in qualsiasi forma o con qualsiasi mezzo, elettronico o meccanico, incluso le fotocopie, la trasmissione fac simile, la registrazione, il riadattamento o l' uso di qualsiasi sistema di immagazzinamento e recupero di informazioni, senza il permesso scritto dell' editore.

All rights reserved. No part of the publication may be reproduced in any form by print, photoprint, microfilm, electronic or any other means without written permission from the publisher.

*Scientists study the world as it is;
engineers create the world that has never been.
- Theodore von Kármán*

Acknowledgements

Here I am, finally at the end of the PhD. It has been an incredible and painful journey full of stimulating experiences, travels, frustrations, hard work, discouragements, hopes, afflictions and, finally, rewards. But this is the research right?

When I started working on detonation, the final goal appeared simply impossible. Probably, the most important thing I have learned during this experience is that every problem, no matter how hard it is, can be solved step by step with hard work and perseverance. However, it was also an incredible human experience being member of the HTC Group. It has been harder without your daily company and jokes during these two years of pandemic. My profound gratitude for all of you cannot certainly be expressed within these few lines.

First of all, I would like to thank Prof. Bruno Facchini for giving me this incredible opportunity to grow professionally and personally. The large research group that he built reached and is still achieving incredible objectives. In this regard, I also want to sincerely acknowledge Prof. Antonio Andreini for his invaluable guidance, the always challenging activities and the constant faith in my work. A really heartfelt thanks goes to Daniele Pampaloni, for his constant help and mentorship, you have been not only my best co-author but also an always cheerful colleague which taught much more than running simulations and writing papers. I owe a special gratitude also to Simone Castellani, for his virtual support and company during the years of the pandemic, you made me really proud of being your tutor.

I wish to thank all the guys passed through my office, friends over colleagues: Tommy D., Simo P., Matte P., Mazze, Sabri, Lore W., Giulio; the ones in the others: Langa, Palo, Albe, Matte A., Carlo, Davide, Pietro, Lapo; the lab guys Lore C., Asif, and all the THT guys. It was really a pleasure sharing this journey with all of you.

I want to thank sincerely Prof. Myles Bohon and Dr. Eric Bach for the precious suggestions the intriguing discussions on the data processing. Your advices really drove me where I wouldn't have ever thought!

I would like to express my gratitude also to the CERFACS guys for the support in using their tough code, and in particular Dr. Thierry Poinsot, Dr. Laurent Gicquel, Dr. Omar Dounia and Dr. Nicolas Odier. I still remember your hospitality during the training in Toulouse!

Finally, I would like to thank my whole family and the most precious gift, my wonderful girlfriend, for supporting me in the hardest situations and making the any other moment special.

Abstract

In the next decades, the continuous growth of the energy demand and the increasing share of renewable sources will challenge the engineers to provide flexible, highly efficient solutions to supply energy. The storage of surplus energy and the use of alternative fuels as hydrogen are certainly two key technologies that will shape the future energy scenario. In this framework, the gas turbines have the potential to hold a position in the decarbonisation, thanks to their unique flexibility in operability, size and fuels. A further increment of the efficiency of these machines could be potentially achieved by adopting other combustion modes which involve a pressure gain during the heat addition, such as the detonation, unlocking a new generation of highly efficient gas turbines.

Among all the pressure-gain devices, the Rotating Detonation Combustors (RDC) are particularly suitable for the adoption in gas turbines, as the high-frequency rotating detonation mitigates the reduction of turbine efficiency for the flow unsteadiness. On the other hand, the extraordinary complexity of these devices imposes the adoption of advanced analysis tools to limit the costs and the safety issues linked to experiments. The modern high-fidelity numerical analyses can be successfully adopted to overcome these limitations and obtain an incomparable level of spatial and temporal resolution, complementing the measurements in the description of the underlying physics behind the rotating detonation. The systematic study of this technology with modern tools will provide the knowledge required for mastering the detonation regime and the operation of the RDCs in practical applications.

The present work provides a contribution to the understanding of the rotating detonation and proposes simulation strategies, numerical methods and post-processing techniques for the study of the RDCs, that involve extremely fast transients and peculiar phenomena.

In the first part, the numerical modelling of the hydrogen-air detonation is tackled, exploring different solutions to describe the explosion process without compromising the computational demand of a CFD analysis. The validation of the available detailed chemical schemes in the conditions relevant for a detonation provides a reference structure of the detonation front and thermodynamic states as well as the detonation speed. Building upon these descriptions, reduced chemistry models are proposed and verified in simplified cases of increasing complexity, ensuring the accuracy of the results and providing essential indications for the application of the model to realistic configurations, where the mesh requirements cannot overlook the computational costs.

In the second part of the work, the non-premixed Rotating Detonation Combustor (RDC) installed at Technische Universität (TU) Berlin is studied by means of fully compressible, multispecies, reactive Navier Stokes equations. A stoichiometric, single wave test point is considered for the analysis and investigated both in cold and reactive conditions through Large Eddy Simulations with the AVBP code. For a cost-efficient modelling of the detonation process, the global single-step scheme with real species developed in the first part and calibrated for the conditions of interest is adopted. After an overall description of the wave stabilization process and global parameters, the analysis of the results focuses on the characterization of key features of the RDC flow field, such as the shocks structures, the gas state in refill region and the transient injectors operation subject to the periodic detonation passage. Finally, an advanced analysis technique for tracking the three-dimensional evolution of the detonation front and evaluating its propagation speed is developed, allowing a stochastic characterization of both the front speed and the refill region and highlighting their correlation.

The present study demonstrates the importance of the complete res-

olution of the injection system to capture the interaction between the waves and the reactants injection, an essential aspect for the optimization of the RDC performances . In this context, this work represents a first step to characterize the main aspects related to the RDC operation and provides valuable insights for the future development of such devices.

Contents

Abstract	v
Contents	xiii
Nomenclature	xv
Introduction	xix
1 Background	1
1.1 Motivation	1
1.2 Pressure Gain Combustion	3
1.3 Rotating Detonation Combustors	8
1.3.1 Characteristic flow field of annular RDCs	8
1.3.2 Operating frequency	11
1.3.3 Technology development	12
1.3.4 Technical challenges	15
1.3.5 Numerical simulation	17
I Numerical Modelling of Hydrogen Detonation	21
2 Reaction mechanism for H_2 detonation	23
2.1 Introduction	24
2.2 Detailed kinetic mechanism	25
2.2.1 Survey of published H_2 -air schemes	27

2.2.2	Assessment of mechanisms predictions	28
2.2.2.1	Ignition delay time calculation	30
2.2.2.2	Ignition delay times comparison with ex- periments	33
2.2.3	Induction time in detonation conditions	38
2.2.4	ZND detonation structure	42
2.2.5	Sensitivity of detonation properties to initial condi- tions	45
2.3	Development of reduced mechanisms	50
2.3.1	2S1R single-step, fictive species mechanism	51
2.3.1.1	Mechanism formulation	55
2.3.1.2	Applications and off-design performances	61
2.3.2	4S1R global mechanism	66
2.3.2.1	Mechanism formulation	66
2.3.2.2	Applications and off-design performances	76
2.3.3	ZND detonation structure	82
2.3.4	Laminar flame speed	84
2.4	Concluding remarks	86
3	Analysis of 2D detonation cellular structure	89
3.1	Introduction	89
3.2	Numerical setup and methods	91
3.2.1	Frame of reference	91
3.2.2	Computational domain and boundary conditions	93
3.2.3	Models and numerical treatments	95
3.2.4	Detonation initiation procedure	96
3.2.5	Numerical smoked foil extraction method	97
3.3	Results	99
3.3.1	Development of transverse instabilities	100
3.3.2	Effect of the spatial discretization	102
3.3.2.1	Detonation front structure	103
3.3.2.2	Cellular structure	103
3.3.2.3	Post-shock states	105

3.3.2.4	Detonation front dynamics	110
3.3.3	Kinetic schemes validation	114
3.3.3.1	Detonation cells	117
3.3.3.2	Discussion of results	120
3.4	Concluding remarks	120
II	Rotating Detonation Combustor Analysis	123
4	TU Berlin RDC numerical model	125
4.1	Description of the test rig	126
4.1.1	Instrumentation	129
4.1.2	Operating modes	130
4.1.3	Investigated test point	131
4.2	Numerical model	133
4.2.1	Computational domain	133
4.2.1.1	Coordinate systems and main sections of interest	134
4.2.2	Simulation strategy	136
4.2.3	Spatial discretization	136
4.2.4	Boundary conditions	137
4.2.5	Numerical models	138
4.2.6	Detonation initiation	139
4.2.7	Computational demand	142
5	Non-reactive case analysis	145
5.1	Introduction	145
5.2	Flow-field structure	147
5.2.1	Near-injection region	150
5.2.2	Lower half of the chamber	153
5.3	Overall mixing performances	156
5.4	Mesh quality assessment	158
5.5	Concluding remarks	160

6	Reactive case investigation	161
6.1	Stabilization and operating conditions	162
6.2	Model validation	166
6.2.1	Wave rotation frequency	166
6.2.2	Pressure gain	169
6.2.2.1	Equivalent Available Pressure	172
6.3	Global flow field features	176
6.3.1	Shock structures in the combustor	177
6.3.2	Instantaneous fields	182
6.3.3	Time-averaged fields	188
6.4	Refill region description	191
6.5	Analysis of the injectors operation	200
6.5.1	Temporal trends within the injectors	200
6.5.2	Mach number and mass flow rate distributions	203
6.5.3	Reactants jets flow field in unperturbed and blocked conditions	209
6.6	Mesh quality assessment	219
6.7	Concluding remarks	222
7	Analysis of the detonation front topology and propagation	225
7.1	Data extraction procedure	226
7.1.1	Detonation speed calculation	228
7.2	Fresh mixture characterization	231
7.2.1	Periodic variation due to the discrete injectors	234
7.2.2	Local Chapman-Jouguet speed	238
7.3	Detonation front topology	242
7.4	Detonation front speed	246
7.4.1	Assessment of the tangential variation	251
7.5	Concluding remarks	255
	Conclusions	257
	List of Figures	271

List of Tables	274
Bibliography	275

Nomenclature

Acronyms

<i>AFR</i>	Air-to-Fuel ratio
<i>CFD</i>	Computational Fluid Dynamics
<i>CFL</i>	Courant-Friedrichs-Lewy
<i>CJ</i>	Chapman-Jouguet
<i>CVC</i>	Constant Volume Combustion
<i>DDT</i>	Deflagration to Detonation Transition
<i>DNS</i>	Direct Numerical Simulation
<i>EAP</i>	Equivalent Available Pressure
<i>FFT</i>	Fast Fourier Transform
<i>LES</i>	Large Eddy Simulation
<i>LW</i>	Lax-Wendroff scheme
<i>NS</i>	Navier-Stokes
<i>PDE</i>	Pulse Detonation Engine
<i>PG</i>	Pressure Gain
<i>PLEA</i>	Phase-Locked Ensemble Average
<i>PS</i>	Post-Shock
<i>RMS</i>	Root Mean Square
<i>TTG4A</i>	Two step Taylor-Galerkin 4A scheme
<i>TTGC</i>	Two step Taylor-Galerkin C scheme
<i>vN</i>	von Neumann
<i>ZND</i>	Zeldovich-von Neumann-Döring

Greeks

α	Angular position between two injectors	$[-]$
Δ	Element characteristic size	$[m]$
δ	Thickness	$[m]$
$\dot{\omega}_k$	Production rate of species k	$[kg/m^3 s]$
$\dot{\sigma}$	Thermicity	$[1/s]$
γ	Heat capacities ratio	$[-]$
λ	Detonation cell width	$[m]$
μ	Laminar dynamic viscosity	$[kg/ms]$
ω	Angular velocity	$[rad/s]$
ϕ	Equivalence ratio	$[-]$
φ	Generic gas quantity	$[-]$
θ	Angle or reduced effective activation energy	$[-]$
Θ	Relative angular position between two injectors	$[-]$

Letters

A	Area	$[m^2]$
c_p	Specific heat capacity at constant pressure	$[J/(kg K)]$
D	Detonation speed	$[m/s]$
E_a	Activation energy	$[J/mol]$
H	Molar enthalpy	$[J/mol]$
h	Specific enthalpy	$[J/kg]$
HR	Heat Release rate	$[W/m^3]$
k	Arrhenius rate of progress	$[mol, m^3, s]$
M	Mach number	$[-]$
n	Reaction order	$[-]$
P	Pressure	$[Pa]$
Q_j	Rate of progress of reaction j	$[mol/(m^3 s)]$
q	Heat released by combustion	$[J/kg]$
R	Universal gas constant	$[J/(mol K)]$
S	Smoke foil intensity	$[-]$
T	Temperature	$[K]$
t	Time	$[s]$

W	Molecular weight	$[kg/mol]$
X	Species mole fraction	$[-]$
$[X]$	Species X molar concentration	$[mol/m^3]$
Y	Species mass fraction	$[-]$
Pr	Prandtl number	$[-]$
r	Radius	$[m]$
Sc_k	Schmidt number of species k	$[-]$
U	Unmixedness	$[-]$

Subscripts

0	Stagnation or unburnt property
CJ	Relative to Chapman-Jouguet condition
det	Detonation
e	Element or exit section
$half$	Half reaction
i	Ideal
k	Relative to species k
m	Molar quantity
n	Nozzle throat section
ps	Post-shock
r	Reaction

Introduction

In the next decades, the continuous growth of the energy demand and the increasing share of renewable sources will challenge the engineers to provide flexible, highly efficient solutions to supply clean energy. The countermeasures and technologies adopted in the next 10 – 15 years will be determinant to achieve a consistent reduction of greenhouse gases emission and limit the impact of the human activities on the Earth climate [1]. As the energy produced with renewable sources is almost 30% of the total mix [2], a growing amount of highly fluctuating and non-programmable power is introduced in the grid. Thus, the storage of surplus energy and the use of alternative fuels as green hydrogen are certainly two key technologies that will shape the future energy scenario. In this framework, gas turbines own the potential to hold a position in the decarbonisation, thanks to their unique flexibility in operability, size and fuels [3]. Notwithstanding the inherent complexity of the retrofitting the turbo-machinery to hydrogen combustion, a further step could be undertaken to provide a breakthrough in combustion-based machines. During the past, while many components have been thoroughly optimised, the combustion process was carefully tuned for reducing the emissions, always basing on deflagration. However, switching to other combustion modes which involve a pressure gain during the heat addition, such as detonation, would provide a major increase of cycle efficiency, unlocking a new generation of highly efficient gas turbines.

Among all the pressure-gain devices, the Rotating Detonation Combustors (RDC) are particularly suitable for the adoption in gas turbines, as

the high-frequency rotating detonation mitigates the reduction of turbine efficiency for the flow unsteadiness [4]. On the other hand, the extraordinary complexity of these devices imposes the adoption of advanced analysis tools to reduce the costs and the safety issues linked to experiments but also to overcome the inherent limits of the experimental diagnostics. The high-fidelity numerical simulations, nowadays widely used even in gas turbines [5] thanks to the increase of the computational power, can be adopted in the study of RDCs for obtaining an incomparable level of spatial and temporal resolution, complementing the measurements in the description of the underlying physics behind the wave propagation. Only the systematic study of this technology with the modern numerical tools and diagnostics will provide the knowledge to master the use of RDCs harnessing the detonation regime.

Aim of the work

The main purpose of the present research activity has been the reactive CFD analysis of the Rotating Detonation Combustor (RDC) installed at Technische Universität (TU) Berlin. Due to the extremely fast transient and peculiar phenomena characterising these devices, the key steps enabling the numerical investigation have been carefully explored, proposing numerical methods, simulation strategies and post-processing techniques to study the test rig in reactive conditions. The research activity also covered the main aspects related to the formulation of a chemical model suitable for high-fidelity simulations of RDCs, with the development of reduced kinetic schemes specifically intended for the use in CFD.

To the present day, this work represents the first reactive study of the test rig, and provides an unprecedented characterization of key features such as the refilled mixture, the interaction between the detonation and the reactants injectors and the dependence of the wave speed on the local pre-shock properties. The investigated aspects are of paramount importance for the RDC operation and their description lays the foundations for the optimization and fine control of the reactants mixture which detonates.

Thesis outline

The work presented in the thesis is organized in two parts. In the first, the numerical modelling of the hydrogen-air detonation is tackled, exploring different solutions to describe the explosion process without compromising the computational cost of a CFD analysis. Reduced chemistry models are proposed and then verified in simplified configurations of increasing complexity, ensuring sufficiently accurate results for the application to more complex studies. In the second part of the work, the numerical investigation of the Rotating Detonation Combustor (RDC) installed at Technische Universität (TU) Berlin is presented. The numerical description is based on the models and findings achieved in the first part and takes advantage of high-fidelity simulations for characterizing the unsteady flow field which establishes in the combustor. The analysis of the results focuses on the characterization of key features of the RDC flow field, such as the gas state in the refill region and the transient operation of the injectors subject to the periodic detonation passage. Finally, an advanced analysis technique to track the three-dimensional evolution of the detonation front and evaluate its propagation speed is developed and implemented, providing an highly detailed detonation data both in time and space.

The dissertation is organized in the following chapters:

- **Chapter 1:** The context of the present research is presented, firstly focusing the discussion on the pressure gain combustion (PGC) advantages with respect to other thermodynamic cycles. Then, the implementation of PGC within the Rotating Detonation Combustors is presented, describing the distinctive details of this technology and the modelling choices of the published simulations.
- **Chapter 2:** The chapter is focused on the chemical description of the detonation process of the H_2 -air system, with the final objective of developing reduced models suitable for the application in CFD simulations. After a survey in the literature, a reference detailed mechanism for the description of a detonation in a H_2 -air

mixture is identified and validated with respect to the experimental measurements. Then, the development of two different single-step mechanisms is presented and discussed. Two single-step schemes are formulated and calibrated for the conditions of interest, enabling a cost-efficient description of the detonative combustion which can be exploited in the CFD simulations.

- **Chapter 3:** In this chapter, the two-dimensional propagation of a detonation in an atmospheric H_2 -air mixture is studied in detail. The simulations are carried out with the developed reduced mechanisms and provide both a verification and validation of their prediction in a more realistic configuration, which allows the development of the detonation front instabilities. A dedicated study of the spatial discretization highlights the impact of the front resolution on the wave propagation as the mesh is coarsened, providing essential information for the application of the model to 3D complex configurations, where the mesh requirements cannot overlook the computational costs.
- **Chapter 4:** The numerical model of the Rotating Detonation Combustor installed at Technische Universität (TU) Berlin is firstly presented, focusing on the geometric configuration investigated in the work. A brief background on the test rig is reported, focusing on the influence of the main operating parameters on the wave modes. Then, each aspect of the numerical model is described in detail, discussing the simulations setup and the approach to the problem.
- **Chapter 5:** The results of the non-reactive simulation of the RDC are presented in this chapter. The rotating detonation combustor is firstly flushed with fresh gases to initialize the injectors before the detonation initiation. The analysis of this preliminary simulation allows the assessment of the injection system performances in preparing an adequate mixture for the detonation, i.e. maximizing the uniformity of the fuel-air mixture.

- **Chapter 6:** In this chapter, the results of the reactive analysis of the TU Berlin RDC are presented and discussed. After an overall description of the wave stabilization process and the resulting operating parameters, the predictions of the model are contrasted to the available measurements. Then, the results of the simulation are analysed in detail, with specific emphasis on the flow field within the combustion chamber, the characterization of the refill region and the injectors operation. At the end of the chapter, also an assessment of the flow field resolution achieved in the simulation is discussed.
- **Chapter 7:** The high-fidelity simulation allows the detailed investigation of specific aspects related to the detonation, so in this chapter a dedicated analysis of the front topology and propagation is discussed. An advanced processing algorithm is developed for tracking the detonation front and sampling the fresh mixture state right before the wave passage, removing the stochastic turbulent components. The combined analysis enables the study of the correlation of the front topology and speed with the local gas properties.

In the last chapter, an overview of the main achievements of this research is given together with conclusions and recommendations for the future works.

Chapter 1

Background

Contents

1.1	Motivation	1
1.2	Pressure Gain Combustion	3
1.3	Rotating Detonation Combustors	8
1.3.1	Characteristic flow field of annular RDCs	8
1.3.2	Operating frequency	11
1.3.3	Technology development	12
1.3.4	Technical challenges	15
1.3.5	Numerical simulation	17

The research context of the work is presented in this chapter ...

1.1 Motivation

Human activities have a huge impact on the global environment as the widespread use of fossil fuels inherently produces pollutant emissions and greenhouse gases. According to the International Energy Agency (IEA), a total of 31.5 Gt of energy-related CO_2 were released in the atmosphere during 2020 [2]. Although the pandemic induced a reduction in the oil and coal demand, the emission lowered by only 2 Gt CO_2 with respect to

2019, leading to the highest ever average concentration in the atmosphere, about 1.5 times the value at the beginning of the industrial revolution.

The increase of greenhouse gases such as CO_2 in the atmosphere is particularly critical for the Earth energy balance as the increase of their concentration alters the equilibrium of the planetary radiative fluxes. As a result, the temperature rises not only on the Earth surface but also in the troposphere [6]. Considering as reference the average surface temperature of the planet during the period 1951-1980, NASA/GISS measurements register a current increase of $0.85^\circ C$ [7], with an alarming trend of $+0.5^\circ C$ every 20 years (Figure 1.1).

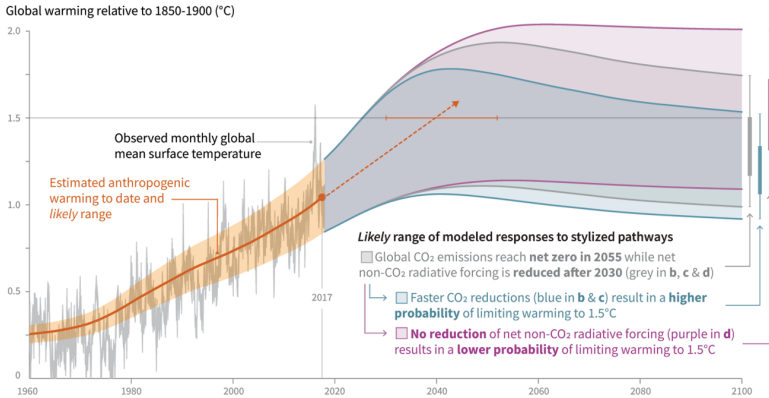


Figure 1.1: Global temperature increase relative to the average during 1850-1900° C. Adapted from [8].

In 2015, the United Nations established the goal to limit global warming to well below $2^\circ C$, preferably to $1.5^\circ C$, with respect to the pre-industrial levels, and many countries committed to pursue such objective in the Paris agreement [9]. However, the emissions cut for avoiding this temperature increase is consistent and requires a huge worldwide effort, requiring a shift toward renewable sources and the development of high-efficiency solutions. The task set by the Paris agreement appears even harder considering that the global energy demand, notwithstanding the

contraction during the first year of pandemic, restarted to rise rapidly, driven by the developing countries [1] and reaching in 2021 +0.5% of the value during 2019.

Despite the economic difficulties induced by the pandemic, also the renewables continue their rapid growth led by solar photo-voltaic and wind, with a +8% electricity generation in 2021, pushing their share in the total mix to the unprecedented value of 30% [1]. This encouraging trend will help the mitigation of the greenhouse emission reduction, however, it will also introduce in the grid an increasing percentage of highly fluctuating and non-programmable power. Thus, the storage of surplus energy and load-balancing techniques will be essential for compensating the future energy volatility and align the demand with the production [10]. In this framework, alternative fuels such as hydrogen or ammonia represent two promising energy vectors for storing the renewable energy surplus. The gas turbine, building upon decades of components optimization, could be adapted to the combustion of such fuels and provide a flexible, controlled source of clean energy for compensating the grid fluctuations. For promoting the transition toward the carbon-free gas turbines, in 2019 several manufacturers set the goal of developing a 100% hydrogen turbine by 2030 [11], thus pushing the development of the clean combustion technologies. This renovated interest stimulates the research of high-efficiency solutions based on the retrofit of existing combustion chambers on the short and mid term, but also paves the way for the adoption of innovative solutions and thermodynamic cycles, such as the pressure gain combustion.

1.2 Pressure Gain Combustion

During the past, while many components have been thoroughly optimised, the combustion process was carefully tuned for reducing the emissions, always basing on deflagration. However, switching to other combustion modes which involve a pressure gain during the heat addition, such as the detonation, would provide a major increase of cycle efficiency,

unlocking a new generation of highly efficient gas turbines [3].

The Pressure Gain Combustion (PGC) is a generic term indicating all the physical processes and configurations which provide an increase in total pressure during the combustion process within a fixed volume combustor [12]. Thus, according to this definition, the devices relying on the Otto, Diesel or similar cycles are not considered in this family since the combustion chamber varies its volume during the operation.

A lot of implementations of the PGC have been proposed and studied in the years and can be divided on the base of the confinement which is realised for obtaining the pressure gain. Except the Constant Volume Combustion [13], where a valved combustion chamber is periodically filled with reactants, ignited and then the hot gases discharged downstream, the majority of the implementations exploits gas-dynamics effects for the confinement. Common examples are the Pulsejet, the Pulse Detonation Engine (PDE) [14], the Wave Rotor (WR) combustion [15] and the Rotating Detonation Combustors (RDC) [16]. Nevertheless, the most important aspect which distinguishes these devices is the achieved combustion regime, i.e. the deflagration (CVC, WR, Pulsejet) or the detonation (PDE, RDC). The PG combustors adopting the former regime, which is associated to a negligible pressure loss across the flame front, obtain the pressure gain only after the combustion process thanks to the higher specific volume of the products [13]. On the other hand, the detonation process itself involves the presence of a leading shock compressing ($15 - 40P_0$) and heating the mixture, which explodes thereafter and expands, according to the Zeldovich-von Neumann-Döring (ZND) theory. It is worth to note that the detonation-based devices essentially operate thanks to the unsteadiness induced by the propagation of the detonation wave, which determines a total pressure rise that cannot be achieved in stationary waves [17], as standing shocks are associated to a consistent reduction of total pressure.

The differences between these two combustion modes reflect in the respective reference thermodynamic cycles, which are the Humphrey cycle for the constant volume combustion and the Fickett-Jacob for the

detonation-based combustion also called Zeldovich-von Neumann-Döring (ZND) cycle according to their theory. The two cycles are represented in comparison to the Joule-Brayton cycle in Figure 1.2, both in the temperature-entropy diagram and in terms of ideal thermodynamic efficiency.

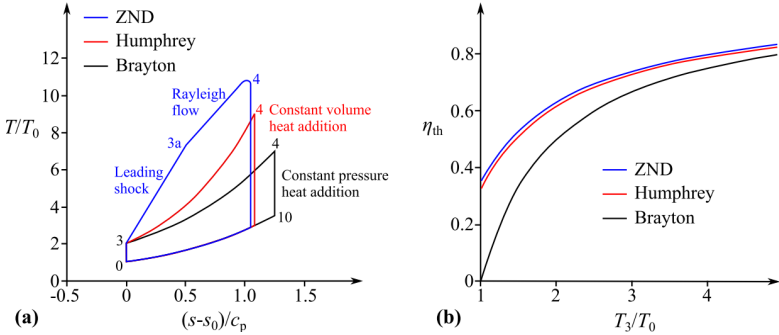


Figure 1.2: Ideal thermodynamic cycles in temperature-entropy diagram (a) and ideal efficiency (b). The ZND and Humphrey cycles are relative to a normalized heat addition of $q/c_p T_0 = 5$. Adapted from [14, 18].

Constant volume combustion: the Humphrey cycle differs from the classical gas turbines cycle from the combustion phase which is described along an isochoric transformation. Considering the same conditions at the exit of the compression, the conversion of the chemical in internal energy increases the temperature well above the corresponding isobaric heat addition. During the process, the constrained volume induces a pressure rise and the enthalpy jump across the expansion is higher than in the Brayton cycle. Considering that the maximum temperature is limited by the materials resistance and the cooling effectiveness, the same level can be achieved in the Humphrey cycle with less fuel mass than in the Brayton cycle, thus resulting superior in terms of efficiency for the lower entropy rise during the combustion [19].

Detonative combustion: the Zeldovich-von Neumann-Döring (ZND) theory describes the detonation as a non-reactive leading shock which compresses and heats the reactants mixture. At such conditions, chain-branching reactions produce radicals which lead the explosion of the gas (see Section 2.1) in a very short time interval, realising the coupling of the reaction with the leading shock. In this configuration the heat addition can be described as a Rayleigh flow, i.e. a constant area non adiabatic flow without friction. The gas is accelerated by the heat generated during the explosion, typically reaching the sonic Mach number in the reference frame fixed with the detonation. This event occurs for a particular combination of heat released and detonation speed and is called Chapman-Jouguet (CJ) condition [20]. For a fixed detonation speed, this condition can be reached if the heat released during the combustion is enough to accelerate the gases away from the front up to the sonic speed, eventually called CJ plane or state. Instead, considering a fixed energy which can be released by the mixture explosion, the sonic condition is reached only if the detonation propagates at a certain speed, defined as CJ speed (Figure 1.3). This

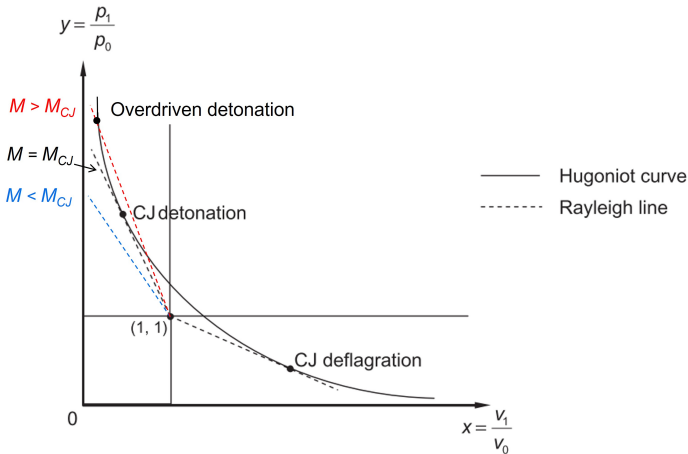


Figure 1.3: Representation of the detonation in the pressure-volume diagram. Adapted from [21].

speed represents the minimum speed at which a detonation can propagate steadily and is an equilibrium condition where the over-driven detonations ($M > M_{CJ}$) tend to stabilize, as the CJ detonation speed determines a subsonic region behind the front which is isolated from the perturbations by the sonic plane and the leading shock [20, 22]. For a given reactant mixture, the heat which can be released is fixed, so a unique detonation speed allowing the realization of the CJ condition exists. The experiments confirm that the detonations propagate in straight channels within few percentage points of the CJ speed [23–25], so the point (4) in the ZND cycle of Figure 1.2 is meaningfully represented by the CJ state. The detonative cycle achieves temperatures and pressures even higher than the constant volume combustion cycle, with a lower entropy rise, thus enabling a slightly increase of ideal efficiency with respect to the Humphrey cycle.

The comparison of the ideal efficiencies of the three cycles demonstrates that the pressure gain cycles provide a consistent improvement over the ideal Brayton-Joule cycle. However, this advantage progressively decreases with increasing T_3/T_0 or decreasing $q/c_p T_0$, which is around 10 for most fuels including hydrogen [14]. It is interesting to note that the PG cycles are able to guarantee a non-zero ideal efficiency even without pre-compression, as the pressure increase during the combustion is sufficient to generate a net work output. The considerable higher efficiency for low T_3/T_0 makes the PGC particularly attractive for the small and medium power generation classes, reducing the fuel consumption and the eventual CO_2 released in the atmosphere. In this regard, the adoption of PGC is even more promising if fed by carbon-free fuels synthesized from the excess of renewable energy, such as hydrogen produced from water electrolysis [10]. Notwithstanding the brief summary reported here takes into account only the ideal cycles, the convenience of using PGC for low compressor pressure ratios has been demonstrated considering the non-isentropic effects and the detonation unsteadiness in an entire gas turbine [3, 4].

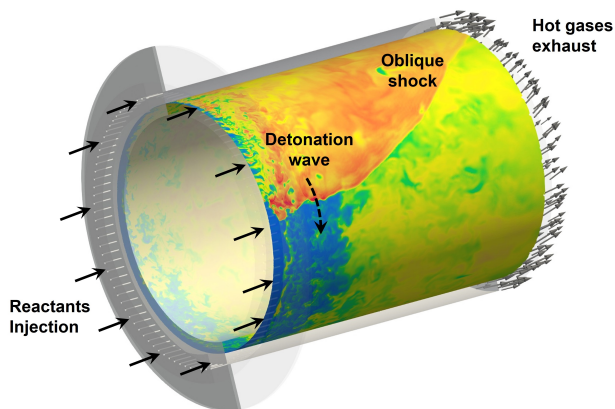
1.3 Rotating Detonation Combustors

Among the devices mentioned in the previous section, indeed the Rotating Detonation Combustors represent the most attractive solution for implementing the PGC in practical applications [3]. The operating principle of the RDCs relies on one or more detonation waves which propagate continuously in the tangential direction of the combustion chamber. The most common design of the combustion chamber has an annular shape with straight cylindrical walls but also other geometries have been proposed such as hollow cylinders [26] or disks [27], where the reactants can be either injected radially-inward or outward. The latter configuration proves to be particularly suitable for the visual diagnostics since the walls confining the chamber are straight and the optical access is facilitated with respect to cylindrical walls [17]. Although each design of the combustion chamber induces differences in the combustor operation, the base principle remains the same and each RDC features (1) an injection system, (2) a refill region where the fresh reactants mix or the pre-mixture enters the chamber, (3) the detonation which compresses and heats the gases and (4) the products which expand moving away from the detonation front, accelerating the flow toward the combustor outlet. All these flow field structures are moving tangentially with the detonation wave and can repeat themselves if distinct fronts are coexisting in the combustor simultaneously, but are generally steady in the reference frame rotating with the detonation.

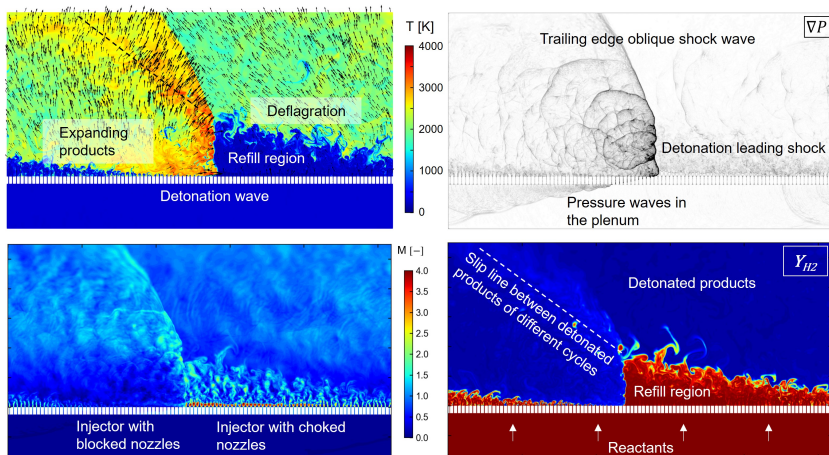
In the next parts, the description will be focused on the annular RDCs, as the most common configuration investigated at present time.

1.3.1 Characteristic flow field of annular RDCs

A schematic illustrating the operating principle of an RDC with annular combustion chamber is represented in Figure 1.4. Since the annulus width is typically small in comparison to the length of the chamber, a common approximation neglects the variation of the fields in the radial direction with respect to the others. With this assumption, the



(a)



(b)

Figure 1.4: Schematic illustrating the Rotating Detonation Combustion and the typical flow field.

idealized operation of an annular RDC can be reasonably described in the axial and tangential directions, i.e. a constant span section of the combustor.

The combustion chamber is fed with fresh reactants through injectors positioned at the base of the chamber. Due to the high pressure generated immediately behind the detonation, the injectors are temporarily blocked by the passage of the wave and progressively recover. As a consequence, the fresh reactants accumulate at the base of the chamber for an axial height increasing with the distance from the front, determining the formation of the refill region. At the top of the refilled gas, the flammable mixture is in contact with the detonation products, so an unsteady deflagration front is typically developing at the boundaries of the refill region. Since the flame speed is usually lower than the axial flow speed, the deflagration front is transported downstream by the reactants flow. This deflagration burns a little mass of reactants which does not undergo the detonation, so it is sometimes called parasitic combustion as it represents an undesired phenomenon in a detonation device, lowering its efficiency.

Nevertheless, the majority of the fresh gases is invested by the leading shock of the detonation and explodes reaching very high temperatures and pressures up to 4000 K and 40 times the initial pressure. These extreme conditions are concentrated right behind the detonation front and quickly decay with the distance, so that the pressure in the region ahead of the front, included the refill region, is not very different from the value at the chamber outlet. The hot products which expand following the detonation wave progressively accelerate in the tangential direction, however, the cyclic operation of the combustor induces the formation of a slip line between the products of a cycle and the previous one. This slip line is due to the presence of an oblique non-reactive shock at the trailing edge of the detonation wave, that compresses and accelerates the gas in the direction of the wave (in the laboratory frame), determining a different flow speed and direction than the products right behind the detonation expanding mostly axially. As a result, the overall flow direction at the outlet section of the combustor varies periodically with the passage of the

oblique shock and is typically transonic ahead of the wave and directed in the opposite direction, while it is supersonic immediately behind the shock and in the same direction of the detonation.

The presence of the detonation propagating supersonically in the combustion chamber determines the formation of trailing shock waves anchored at each boundary of the detonation front which is not confined by solid walls. The typical example is the oblique shock at the top of the wave but other trailing shocks can propagate upstream in the injector channels. For instance, in the two-dimensional example in Figure 1.4 strong pressure waves are crossing the injectors and reaching the reactants plenum, although attenuated. The shocks in the reactants feeding ducts do not only temporarily arrest the fluid, but can also induce dangerous pressure fluctuations in the plenum, so a requirement of the injectors is usually a high pressure loss to decouple the chamber dynamics from the plenum.

1.3.2 Operating frequency

The speed of the detonation in the tangential direction depends primarily on the fresh gas composition and conditions, but considering the typical small size of the RDC the rotation frequency of the wave is very high (1 – 10 kHz). This high frequency operation is one of the most significant advantages over other PG solutions such as CVC and PDC, characterised by frequencies around 100 Hz [13, 28], since the oscillations at the exhaust are simpler to be managed being faster and less intense. With respect to the Pulse Detonation combustion, the RDCs have several fundamental aspects which yields practical advantages. Since the PDCs adopts a detonation wave running through the whole length of the combustor, the detonation has to be initiated every cycle of the engine. The direct detonation initiation requires large quantities of energy so instead the Deflagration-to-Detonation-Transition (DDT) is usually adopted. This initiation involves a first ignition of a reactant mixture followed by the acceleration of the resulting deflagration front up to supersonic speeds (detonation initiation), however, it requires specific devices to promote

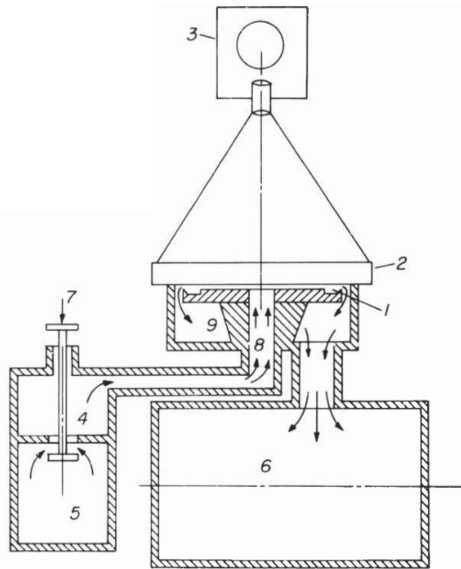
the DDT and reduce the length necessary for the transition [28]. As a result, each cycle the PDC requires the ignition of the mixture and the consequent DDT for starting the detonation process. Notwithstanding the use of DDT promoters, the axial size of a PDC is larger than a RDC. Combined with the lower operating frequency, the higher volume determines a lower power density of the combustor and thrust-to-weight ratio, making PD engines less attractive for aerospace propulsion system than the compact RD design [28]. Other important advantages of the RDCs are the absence of moving parts or valve systems, essentials for PDC, as well as the purge phase before the refill with fresh reactants.

1.3.3 Technology development

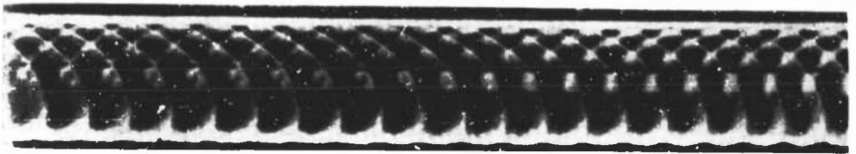
The first experiment laying the foundations for the development of the rotating detonation is usually considered the work carried out in 1960s by Voitsekhovskii [29] at the Institute of Hydrodynamics of the Siberian Division of the Soviet Academy of Sciences in Novosibirsk. The researchers succeeded in stabilizing a spinning detonation in a cylindrical combustion chamber, avoiding its typical axial propagation which induced the detonation front in a spiral path within the tubes [17]. Although their intent was only simplifying the study of spinning detonations, the test rig that they developed (Figure 1.5) actually represents the first step toward the rotating detonation.

Some years later, the first theoretical and experimental efforts on the application of the rotating detonation to the design of rocket engines were conducted in USA by Adamson and Olsson [31] and Nicholls and Cullen [30], stimulated by the possibility to increase the efficiency. The engine which they built was based on a non-premixed injection of fuel and oxidizer at the base of the combustion chamber in an impinging jets configuration (Figure 1.6). However, no success in stabilizing the detonation for more than one rotation was achieved, attributing the failure to an inefficient mixing of the reactants.

The research slowly continued in the next years in Russia and USA, until the interest in the application of pressure gain combustion for power



(a) Cross-section of the apparatus: 1 – detonation chamber, 2 – Transparent window, 3 – drum camera, 4 – mixture supply line, 5 – reservoir with fresh mixture, 6 – low pressure dump chamber, 7 – valve, 9 – Exhaust.



(b) Drum camera record of a maintained spinning detonation.

Figure 1.5: Schematic of the spinning detonation apparatus. Adapted from [30].

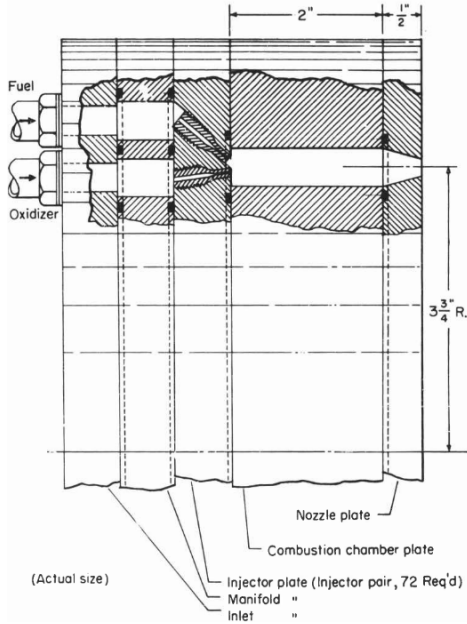


Figure 1.6: Cross-section of the RDE rig developed by Nicholls and Cullen [30].

and propulsion was renovated by the studies on Pulse Detonation Combustion [32–34]. These systematic investigations led to a huge progress and maturation of these PG devices, culminating in the first flight in a plane with multi-tubed PDC in 2008 [35] and the demonstration of their higher efficiency when adopted as combustors in gas turbines [36].

In the wake of these studies, the rotating detonation sparked again interest thanks to their simple structure, the absence of moving valves and high-frequency operation which required only one initiation of the detonation [16]. Several research programs started in the following years [18, 37] over all the world, at first in Russia [38, 39], Poland [37], France [40] and later also in USA [41–44], Japan [45], China [46] and Germany [47–49]. As a result, the theoretical performances improvement was

finally confirmed thanks to the development of experimental test rigs and investigations [17]. For instance, integrating the RDC with an un-optimized helicopter engine, Wolański [50] estimated a reduction of the specific fuel consumption of -5% thanks to the combustor. Frolov et al. [51] registered an efficiency increase up to 13% with respect to the deflagrative combustion in a rocket engine adopting RDC. The integration of a RDC in an open-loop gas turbine T63 carried out at the Air Force Research Laboratory (AFRL) by Naples et al. [43] showed a promising response of the turbine to the unsteady RDC exhaust, with no visible damage after 20 minutes of operation, demonstrating the ability of a RDC to drive an axial turbine. Further studies conducted by Fotia et al. [52] and Paxson and Naples [53] observed that an overall pressure gain can be achieved by optimising RDC inlet and length. These recent advancements demonstrate that concrete benefits can be achieved using RDCs in gas turbines and could really represent a breakthrough for a major increase in cycle efficiency.

1.3.4 Technical challenges

Although the RDC technology is actively investigated by many research groups, its readiness level is low and several technical issues still need to be properly addressed and solved.

Different researches proved that an increase in thermal efficiency can be achieved with RDC, however, a positive pressure gain has still to be demonstrated [17]. This task is even more complex considering the lack of a shared, well-defined and appropriate method to evaluate the pressure gain, which is directly related to the unsteady propagation of the detonation wave in the combustor. As a result, the total pressure representative of the high-speed, fluctuating exhaust flow is still not universally calculated. Different approaches such as using a time-averaged stagnation pressure or more complex indexes as the Equivalent Available Pressure (EAP) [54] have been proposed [18]. Irrespective of the method, a lot of work has to be devoted to discover and optimise the parameters which drive the pressure gain, as demonstrated by Bach et al. [55] considering the impact

of outlet area restrictions and varying the air injector pressure losses.

The latter parameter is one of the most important for the pressure gain, as usually high pressure loss injectors are needed for quickly refilling the combustor and reduce as much as possible the pressure feedback from the combustion chamber to the reactants manifolds. This shows as the design of the injection system in a RDC is a key element for the performances optimisation as it must conciliate conflicting targets and has a direct impact on the pressure gain and on the reactants mixing. Moreover, the characteristics of the detonable mixture as well as the flow field in the refill region are expected to influence the strength of the detonation wave and its consequent gas compression [56]. However, the high frequency and harsh environment can hardly be investigated experimentally as the current diagnostics still appears to be insufficient to study the flow with such detail. In this regard, numerical analyses can overcome the limits of the measurements with high-resolution data and represent a valuable tool for studying the flow within the RDCs.

Another critical point is the integration of the RDC with a turbine. As shown in Figure 1.4, the flow field exiting the combustor fluctuates with a kHz frequency inducing the oscillations in pressure, Mach number and flow direction [57]. Although the high frequency partially decouples the flow unsteadiness from the response time of the downstream turbine, the conventional nozzles need to be optimised for this particular application [58], avoiding the reduction of turbine efficiency compromising the gain due to the PGC. Nevertheless, the tests conducted by Naples et al. [43] demonstrated that a turbo-shaft turbine can be successfully driven by a RDC even without implementing any modification, showing unprecedented promising results.

Finally, also the cooling of the combustor represents a challenge due to the very high temperatures of the gas and the pressure wave propagating in the chamber, which dramatically increase the thermal stress of the walls. Passive solutions such as high-temperature resistant materials do not appear to be a viable solution since they could induce the autoignition of the fresh mixture before the detonation passage [28], so a dedicated

active cooling is needed. Considering air as coolant for the application in gas turbines, the high pressure and speed of the wave potentially prevent or complicate the use classical solutions such as film cooling to protect the walls from the hot gases. The experiment led by Naples et al. [43] showed how very large quantities of cooling air are needed if only the cold side of the chamber walls are cooled, but proved the feasibility of a stable, air-cooled operation for about 20 minutes.

1.3.5 Numerical simulation

Although the computational science and power were not sufficiently advanced to provide a practical support to the early development of the first detonation-based combustors, nowadays the modern CFD codes can rely on unprecedented computational resources. The advanced numerical tools developed in the years represent today an extraordinary research instrument which can play an important role in boosting the design and the analysis of the RDCs, limiting the costs of the experimental tests as well as their safety issues.

The flow within an RDC is governed by the compressible, multi-species, reactive Navier-Stokes (NS) equations coupled with an appropriate reaction mechanism for describing the detonation, inclusive of elementary reactions and minor species. Although the complete analysis of such problem is today technically possible if turbulence is modelled, for instance with the Unsteady-Reynolds Averaged or Large Eddy Simulation approach, in the years many simplified approaches have been adopted, leading to a wide range of fidelity [59]. For instance, the RDC can be reduced to an axisymmetric or two-dimensional domain [60–62] including the axial and tangential directions, allowing the description of the basic features of the flow field (Figure 1.4). The domain reduction allows limiting the computational cost of the analyses consistently, at the expense of the real 3D effects which are present in a combustion chamber, such as the presence of the chamber walls and the curvature of the annulus. Nevertheless, the growing computational power and interest in RDCs have progressively enabled the fully three-dimensional computational study, which have been

published essentially in the last 15 years. A summary of the numerical studies published on 3D RDCs is reported in Table 1.1.

Other common simplifications involve the reaction mechanism for the detonation, whose complexity depends on the fuel and oxidizer composition. Considering the simplest and widely studied case of hydrogen-air, the state-of-the-art chemical kinetics adopts about 10 species and 20 elementary steps (see Table 2.1), which is still usually prohibitive in terms of computational demand in unsteady CFD studies. The problem is usually circumvented by adopting reduced, skeletal or single-step reaction schemes calibrated for matching specific detonation properties such as the CJ detonation speed or the burnt gas temperature. Furthermore, even considering the most recent detailed schemes available in literature, in a detonation the time-scales associated to the chemical reaction are comparable to the molecular relaxation time behind a shock wave, violating the hypothesis of vibrational equilibrium which is the basis of classical kinetic mechanisms [87, 88].

Finally, another important feature which has been usually simplified is the injection of the reactants in the chamber, that is of primary interest for non-premixed systems. Several studies investigated a generic RDC with perfectly premixed injection, considering that the mixture enters the chamber through micro-nozzles, i.e. with a distributed inlet governed by the injector throat area and the counter pressure in the combustion chamber. This simplified modelling of the injector allows the flow of a single pre-mixture, but was developed for capturing the local variations due to the detonation blockage and providing an efficient description of the choked, blocked and subsonic nozzles. Although this model is still widely adopted for premixed systems, it completely neglects the pressure feedback in the injector passages and determines a perfectly uniform, premixed flow in the refill region. On the other hand, the application of such model to non-premixed systems is not of great interest today, since the separate injection of the reactants in the combustion chamber can be included in the CFD model without compromising the overall computational demand, as proven by the most recent studies in Table 1.1.

Table 1.1: Summary of recent published 3D annular RDC simulations. Legend: LIH=Laurentyev Institute of Hydrodynamics (RU), WUT=Warsaw University of Technology (PL), AFRL=Air Force Research Laboratory (US), ONERA=Office National d'Etudes et de Recherches Aéropatiales (FR); P=premixed, NP=non-premixed; S=species, R=reactions.

Reference	Year	Test rig	Reactants	Eq.	Reaction mechanism	Injector
Yi et al. [63]	2009	Generic	H ₂ -air	Euler	Ma et al. [64] (2S, 1R, Arrh. rate)	Micro-nozzles
Schwer et al. [61, 65]	2011	Generic	H ₂ -air	Euler	2S, Induction time equation	Resolved
Kindracki et al. [66]	2011	WUT	H ₂ -air	Euler	Global (4S, 1R, Arrh. rate)	Resolved
Eude et al. [67]	2011	ONERA	H ₂ -O ₂	Euler	Reduced 6S, 7R [68]	Micro-nozzles
Frolov et al. [69]	2013	LIH	H ₂ -air	URANS	Global (4S, 1R, Arrh. rate, P depend.)	Resolved
Zhou and Wang [70]	2013	Generic	H ₂ -air	Euler	Ma et al. [64] (2S, 1R, Arrh. rate)	Micro-nozzles
Schwer et al. [71, 72]	2014	Generic	H ₂ -air	Euler	2S, Induction time equation	Micro-nozzles
Escobar [73]	2014	Generic	H ₂ -air	Euler	Ma et al. [64] (2S, 1R, Arrh. rate)	Resolved
Wu et al. [74]	2014	Generic	H ₂ -air	Euler	Ma et al. [64] (2S, 1R, Arrh. rate)	Micro-nozzles
Tsuboi et al. [75]	2015	Generic	H ₂ -O ₂	Euler	Detailed 9S, 21R	Micro-nozzles
Dubrovskii et al. [76]	2015	LIH	H ₂ -air	URANS	Global (4S, 1R, Arrh. rate, P depend.)	Resolved
Cocks et al. [77]	2016	AFRL	H ₂ -O ₂	LES hyb	Abridged Jachimowski [78] (8S, 7R)	Resolved
Tsuboi et al. [79]	2017	Generic	H ₂ -O ₂	Euler	Detailed 8S, 21R	Micro-nozzles
Sun et al. [80]	2017	Generic	H ₂ -air	Euler	Reduced 7S, 8R	Resolved
Gaillard et al. [81]	2017	ONERA	H ₂ -O ₂	LES	Reduced 6S, 7R [68]	Resolved
Sato and Raman [82]	2019	AFRL	C ₂ H ₄ -air	Euler	Varatharajan 21S, 38R [83]	Resolved
Prakash et al. [56]	2021	AFRL	CH ₄ - O ₂	LES	FFCMY-12 [84] (12S, 38R)	Resolved
Sato et al. [85]	2021	AFRL	H ₂ -air	NS	Mueller [86] (9S, 19R)	Resolved

The premixed RDC investigations with simplified injection present also the advantage of neglecting the mixing of the reactants and the turbulence generated by the reactants jets. Since the effects transport phenomena is typically secondary with respect to the convection, the transport properties such as the viscosity, thermal conduction and species diffusion are neglected in many calculations and the problem is described with the reactive Euler equations [37]. This simplification is acceptable only if the near-wall effects due to the boundary layer, the reactants mixing and the heat losses are not significant for the calculation. On the other hand, when considering a non-premixed system which requires the modelling of the real injectors, the turbulent mixing of the reactant, the diffusion of species with low Lewis number as H_2 and the effective area reduction for the presence of the boundary layer are expected to be important for the operation of the RDC and thus should not be neglected.

Instead, high-fidelity approaches such as LES, rather than URANS or hybrid simulations, should be the reference tool for the characterization of these devices. However, although the LES proved to be superior to other modelling regarding the turbulence description [5], it is still a general consensus that the sub-grid effects studies and modelling for detonations have delayed with respect to the efforts spent for the turbulent deflagration models [89], and the need for such models has already been observed for highly unstable detonations [90]. In addition, the specific turbulence effects on the detonation front have never been well investigated and the stability of the wave in a turbulent flow field, as expected in the refill region of the RDCs, should be studied to gain insight in the phenomena involved in these pressure gain devices.

Part I

Numerical Modelling of Hydrogen Detonation

Chapter 2

Reaction mechanism for H_2 detonation

Contents

2.1	Introduction	24
2.2	Detailed kinetic mechanism	25
2.2.1	Survey of published H_2 -air schemes	27
2.2.2	Assessment of mechanisms predictions	28
2.2.3	Induction time in detonation conditions	38
2.2.4	ZND detonation structure	42
2.2.5	Sensitivity of detonation properties to initial conditions	45
2.3	Development of reduced mechanisms	50
2.3.1	2S1R single-step, fictive species mechanism	51
2.3.2	4S1R global mechanism	66
2.3.3	ZND detonation structure	82
2.3.4	Laminar flame speed	84
2.4	Concluding remarks	86

2.1 Introduction

Several thermo-fluid dynamic aspects differentiate the detonation combustion from the deflagration, but the most important for the chemical kinetics is the radically different ignition of the fresh mixture. Indeed, if the combustion wave in a deflagration propagates toward the fresh mixture due to the diffusion of heat and species, the supersonic nature of the flow in a detonation usually renders the diffusion almost negligible. Rather, the reactants explode after an induction or ignition delay time after the compression and adiabatic heating provided by the leading shock [20]. For this reason reaction schemes which present good performances for deflagrations can fail when the focus is the prediction of the post-shock explosion of the mixture, which influences the internal structure of the detonation front according to the Zeldovich-von Neumann-Döring (ZND) theory. Furthermore, the reduced kinetic schemes must be specifically developed for the phenomenon of interest to optimize their accuracy, since their lower computational request typically imposes simple schemes whose few calibration parameters do not always lead to a good description of both deflagration and detonation regimes.

The present chapter starts with a brief description of the explosive behaviour of the H_2-O_2 system. Then, a survey on the available hydrogen-air oxidation mechanisms is presented. Several reaction schemes are selected and tested in the conditions of interest for a detonation in terms of ignition delay time and contrasted to the experimental measurements. The study allows identifying a reference detailed mechanism for the description of a detonation in a H_2 -air mixture near the atmospheric condition.

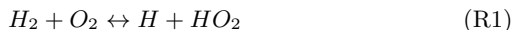
Then, the development of two different single-step mechanisms is presented and discussed. The reduction procedure is built up using as input parameters the thermodynamic states and reaction zone features predicted by the reference mechanism. Two single-step schemes are formulated and calibrated for the conditions of interest, enabling a cost-

efficient description of the detonative combustion which can be exploited in the CFD simulations.

2.2 Detailed kinetic mechanism

The hydrogen-oxygen system has been studied for many years by means of direct kinetic measurements or eventually quantum chemistry [87, 91], and the reaction rates are frequently updated with the most recent available data, which can be heavily influenced by the inherent inaccuracies of the experimental boundary conditions.

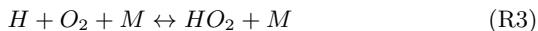
The oxidation process is started mainly by the initiation step R1:



by producing the H and HO_2 radicals which then initiate the chain-branching reaction R2:



and the pressure-dependent chain-propagation reaction R3:



The reactivity of the system is basically driven by the competition between the chain-branching reaction R2 and the chain propagation reaction R3. The complex equilibrium among those reactions determines a very different behaviour of the system when the initial conditions of pressure and temperature are varied, and can be clearly observed from the explosion limits reported in Figure 2.1.

For very low pressures, i.e. below first limit, the mixture is not explosive and is controlled by the rate at which the H radicals diffuse through the walls of the vessel. Increasing the pressure up to the second limit, the chain-branching reaction R2 presents a fast rate of progress, determining a marked explosive behaviour. Above the second limit, the reaction R3 competes with the R2 and practically inhibits the mixture

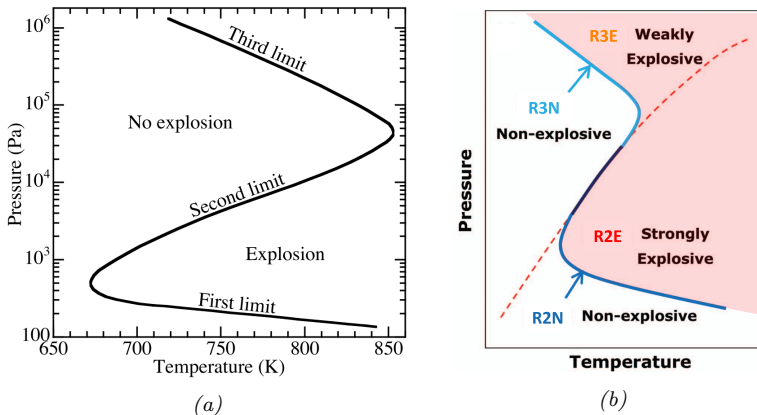
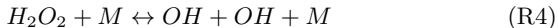


Figure 2.1: Explosion limits for hydrogen-oxygen system in a spherical vessel, showing the neutral competition between R2 and R3 as a red dashed line. Picture (a) adapted from (a) [92] and (b) [93].

from exploding. For even higher pressures, the fast rate of a different chain-branching reaction R4:



replaces the reaction R2, which was effective only at lower pressures, leading to the third explosion limit.

The post-shock conditions achieved in a detonation are typically beyond the limits of pressure and temperature shown in Figure 2.1, ranging between about 10-70 bar and 800-2500 K for hydrogen, so the limits shown are not fundamental for the description of the detonation. Nevertheless, the aforementioned post-shock conditions are intersecting the broader extended second limit that is obtained by extending the red-dashed line in Figure 2.1 (b). This limit can be clearly traced, for instance, from the ignition delay time or effective energy maps of the mechanism, which will be shown in the next sections. It is worth to note that the extended second limit can be used for comparing different kinetic schemes, but it does not represent a limiting behaviour for the phenomenon, as

Table 2.1: Summary of reaction mechanisms for $H_2 - O_2$ combustion.

Mechanism	Year	Kinetics	Spec.	Reac.	C_{max}	Ref.
GRI3.0 (H_2 only)	1999	Detailed	10	29	-	[95]
Li	2004	Detailed	11	19	-	[96]
O’Conaire	2004	Detailed	11	19	-	[97]
Naik	2009	Detailed	9	19	-	[98]
Hong	2011	Detailed	10	21	-	[99]
Boivin	2011	Skeletal	9	12	-	[100]
Burke	2012	Detailed	11	19	1	[101]
Kéromnès	2013	Detailed	15	45	1	[102]
ELTE	2014	Detailed	12	28	-	[103]
Hashemi	2015	Detailed	13	24	1	[104]
SanDiego	2016	Detailed	11	20	-	[87]
Mevel	2017	Detailed	14	40	-	[105]
Konnov0.6	2018	Detailed	15	65	-	[106]

the detonations are observed to propagate in the conditions on both its sides [94].

2.2.1 Survey of published H_2 –air schemes

Several $H_2 - O_2$ reaction mechanisms were found in the literature and collected to test them in the conditions of interest for a detonation. As highlighted in the previous paragraph, the chemistry of this system has been widely studied since the reaction steps which describe the oxidation of hydrogen are the basis for a detailed scheme of any hydrocarbon. The result of the survey is summarised in Table 2.1. The selected schemes were proposed in the last twenty years, even if the majority of the selection refer to relatively recent schemes published in between 2011 and 2020. It is important to remark that the GRI3.0 [95] mechanism was specifically optimized for CH_4 combustion and its H_2 sub-mechanism was included in the results for its widely-known accuracy for CH_4 and its tendency to avoid stiffness problems during solution which can affect other schemes. All the mechanisms are detailed mechanisms except the skeletal mechanism

proposed by Boivin et al. [100] simplifying the SanDiego [87] scheme without a significant loss of accuracy. Some schemes in Table 2.1 were described as an update to previous mechanisms in the literature. For instance, the Li et al. [96] mechanism was updated by Burke et al. [101], expanding the dataset for the calibration with high pressure data. The latter scheme was then complemented with measurements above the third explosion limit by Hashemi et al. [104], up to 100 bar. The ELTE [103] mechanism was instead the result of an optimization of K eromn es et al. [102] scheme with a very large amount of experimental data from the literature including ignition delay time, flame velocity, and jet-stirred reactor measurements. Finally, since a lot of research on hydrogen involved also syngas, three of the schemes in Table 2.1 present a maximum carbon number $C_{max} = 1$ with the inclusion of species such as CO , CO_2 and HCO , not of interest for the present study.

2.2.2 Assessment of mechanisms predictions

All the reaction mechanisms for hydrogen combustion reported in Table 2.1 were tested for evaluating their predictions mainly in terms of ignition delay time, which drives the reaction progress after the shock compression. It is then evident that the conditions of interest for a detonation are provided by the post-shock states in a reactants mixture, which for the present work is a stoichiometric H_2 -air mixture in ambient conditions ($T_0 = 298$ K, $p_0 = 101325$ Pa). As the post-shock conditions do not depend on kinetics but rather on the thermodynamic states of the mixture, the equivalence ratio does not influence significantly the post-shock state, also because of the very low mass content of hydrogen in the mixture, mainly composed by N_2 .

Experimentally, different methods can be used to measure the ignition delay time of a mixture, though the shock tube is preferable not only for the similarity of configuration with a detonation but also for the conditions range which can be achieved behind the shock and constitutes the initial state of the mixture. Despite this, the actual data available in the range of interest for a detonation in a H_2 -air mixture initially at

atmospheric conditions are not very abundant, as highlighted by Schultz and Shepherd [107, 108].

For the purposes of the present study several datasets published in the literature were analysed to assess the most appropriate ones for the investigation of the reaction mechanisms, i.e. the dataset which are distributed near the post-shock conditions in a H_2 -air detonation. Since the speed D and consequently the Mach number of the leading shock M_0 can oscillate in a detonation, the post-shock conditions were evaluated varying the detonation speed between the 40 – 140% of the CJ speed, i.e. the speed of a self-propagating detonation, and reported in Figure 2.2.

Table 2.2: Available shock-tube measurements near the conditions of interest for a H_2 -air detonation.

p_{ps} [bar]	ϕ	Dilutant	Reference
13, 34	0.3, 0.5, 1.0	Ar (98%v)	Kéromnès et al. [102]
33	1.0	Ar (97%v)	Petersen et al. [109]
33, 57	1.0	Ar (99.25%v)	Petersen et al. [109]
16	1.0	N_2 (91%v)	Herzler and Naumann [110]

For an H_2 -air stoichiometric mixture in ambient conditions the CJ speed is about $D_{CJ} = 1976$ m/s (Mach number relative to the fresh mixture $M_0 = 4.9$), leading to a speed range between $D = 800 - 2500$ m/s and $M_0 = 2 - 6.8$. Again, it is important to note that the stoichiometry and kinetic scheme have a little influence on the thermodynamic post-shock state but also on the CJ speed, so the values in Figure 2.2 can be assumed as general and independent from the mechanism, as long as the thermodynamic data is detailed.

The more relevant dataset of ignition delay time are summarised in Table 2.2 and located with respect to the post-shock points in Figure 2.2, showing that only two series of measurements actually intersect the conditions of interest, i.e. the post-shock states (points in Figure 2.2). Nevertheless, all the selected data are close to the post-shock conditions of interest and can be exploited to validate the mechanisms in Table 2.1. All

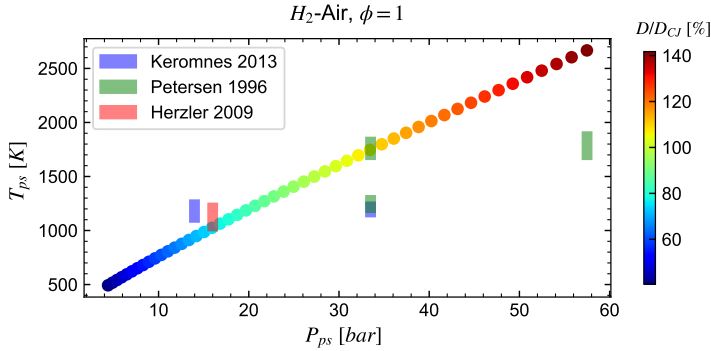


Figure 2.2: Representation of the measurements in Table 2.2 with respect to the post-shock states in an atmospheric, stoichiometric H_2 -air detonation.

the measurements in Table 2.2 were carried out in highly diluted Argon or Nitrogen baths and in shock-tubes.

2.2.2.1 Ignition delay time calculation

To assess the accuracy of the detailed mechanisms, the ignition delay time has to be evaluated numerically. The shock-tube configuration used to measure the induction time presents non-ideal effects which have to be minimized to provide significant results which can be easily compared with numerical results [107]. For instance, the heat release tends to alter the unreacted temperature of the mixture with a spurious effect and the non-uniform flow field resulting from the boundary layer interaction with either the incident or reflected shock. Although these unwanted peculiarities of the experiments are complex to be characterised in low-order models, another fundamental aspect is that the thermodynamic path of the exploding fluid is neither a constant pressure nor volume transformation, but rather approaches a Rayleigh line in steady conditions, with variations of the post-shock gas properties. Thus, the most accurate model for the shock tube would describe not only the temporal but also

the spatial extent of the test rig, requiring a higher computational cost.

Nevertheless, when the mixture is highly diluted, the reaction is basically decoupled from the fluid dynamic evolution and a fluid parcel can be described as isolated with sufficient accuracy. In other words, the resulting temperature and pressure variations are very limited and have a negligible effect on the induction time if the mixture is mainly composed of an inert bath. Moreover, the explosion is usually driven by the radicals kinetics which occurs very close to the post-shock point in a p - V plane, i.e. before the occurrence of the aforementioned variations of temperature and pressure, limiting the differences between models with either constrained temperature or pressure [107].

Therefore, in this study the ignition delay time is calculated by solving the thermodynamic state of an adiabatic 0D constant volume reactor filled with a mixture of ideal gases at the post-shock state reported by the experiments. This approach reproduces the test supposing that the shock induces an impulsive increase in p , T initiating the reaction in a fluid element at constant volume which is not influenced by the surroundings. In this model the system time evolution is only driven by the chemical reactions.

The numerical simulations of the 0D constant volume reactor are carried out using the libraries of Cantera 2.4.0 [111] for Python3, setting as initial conditions the post-shock state reported by the measurements in Table 2.2 and repeating the calculation for each mechanism of Table 2.1.

The ignition delay time is evaluated as the time between the initial condition and the instant where the maximum temperature rise occurs:

$$\tau_{ign} = t_1 - t_0 \quad \text{with} \quad t_1 : \left. \frac{dT}{dt} \right|_{t_1} = \max \left(\frac{dT}{dt} \right) \quad (2.1)$$

where the temperature rate of change is evaluated with central differences. Among alternative criteria such as the maximum of OH, pressure or thermicity, the adopted criterion is more robust since the temperature gradient always presents a well-defined maximum and is equivalent to the other approaches for high dilutions [107], even at constant pressure. A

preliminary study on the criterion definition was performed, confirming the independence of the induction time from the choice of the conventional ignition instant. For instance, the typical distributions in the reactor of temperature, thermicity and species mole fractions are reported in Figure 2.3 for a stoichiometric H_2 -air mixture. The thermicity $\dot{\sigma}$ defines

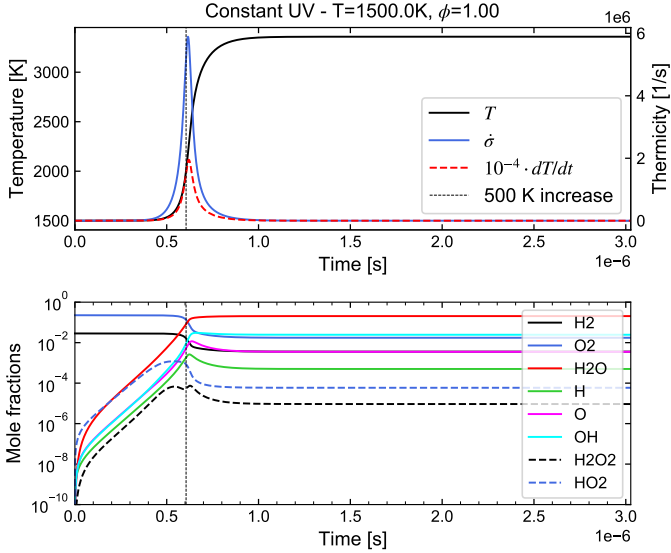


Figure 2.3: Time evolution of temperature and major species in a 0D constant volume reactor initially filled with a stoichiometric H_2 -air mixture at $T_0 = 1500$ K, $p_0 = 28$ bar (vN point), obtained with the ELTE mechanism [103].

the rate at which the chemical energy is converted in thermal energy and can be calculated for an ideal gas as [112, 113]:

$$\dot{\sigma} = \sum_{k=1}^{N_k} \sigma_i \frac{dY_k}{dt} = \sum_{k=1}^{N_k} \left(\frac{\bar{W}}{W_k} - \frac{h_k}{c_p T} \right) \frac{dY_k}{dt} \quad [1/s] \quad (2.2)$$

In the Figure 2.3, different criteria for identifying the ignition delay

time are reported, showing their coherence in the prediction.

2.2.2.2 Ignition delay times comparison with experiments

A large number of 0D constant volume reactors is simulated for each experimental condition in Table 2.2 and varying the initial temperature around the values reported in the dataset. This process is repeated for every mechanism in Table 2.1 and the results are reported in Figures 2.4, 2.5, 2.6 and 2.7.

To ease the comparison with the measurements, only the most recent mechanisms and the GRI3.0 are reported in the graphs. Among all the mechanisms of Table 2.1 the only scheme which ran into stiffness problems was the Li et al. [96] mechanism, which was thus discarded.

Globally, most of the reaction mechanisms provide an acceptable accuracy for the ignition delay time in the conditions tested. The identification of a single scheme which outperforms all the others is not easy since the accuracy varies changing experimental dataset used for reference, but overall the ELTE [103] appears to describe the explosion time slightly better than the others. For instance the scheme performs well for the high pressure conditions in Figure 2.4 (33 bar) for different values of equivalence ratio, but also for intermediate pressures Figure 2.5 (a) (13 bar) at the stoichiometric condition.

As far as concerns the dataset of Petersen et al. [109], the reaction mechanisms are all well aligned with the measurements both for 33 and 57 bar, as can be observed in the plots of Figure 2.6 (b), (c) for the higher Ar dilution. When the dilution is reduced, non-ideal effects can be introduced in the measure and be important for the low temperatures of Figure 2.6 (a). In these conditions the schemes present more scattering of the results, with the K eromn es et al. [102] and ELTE [103] reproducing the measurements with a better accuracy than the others below 1250 K.

A specific discussion has to be done for the M evel et al. [105] scheme, which presents good results for only some of the intermediate pressure conditions tested (13 – 16 bar). For instance, the reaction mechanism describes the experimental trend in Figure 2.7 with higher accuracy than

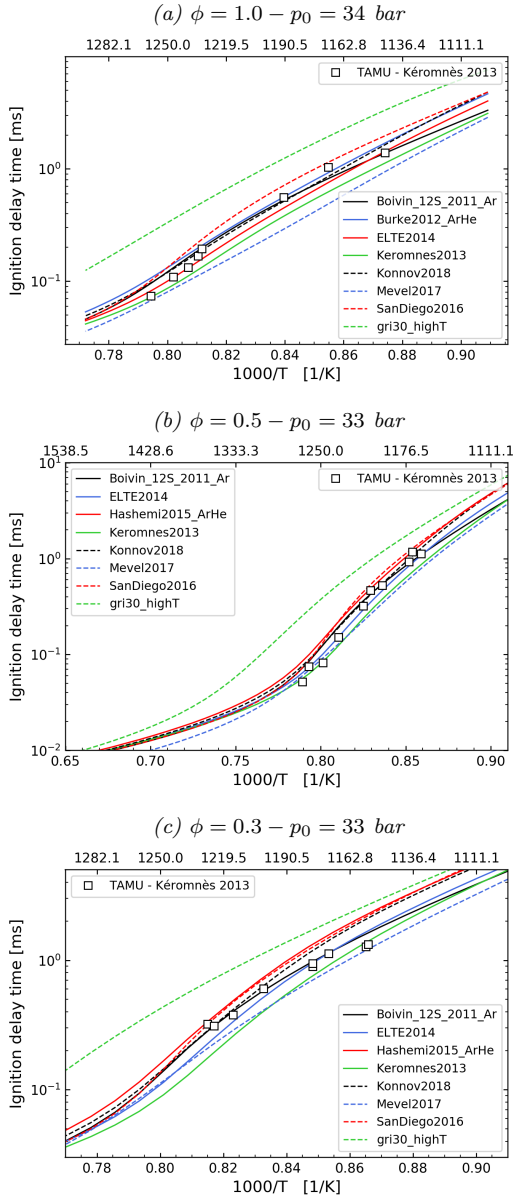


Figure 2.4: Predicted ignition delay times in comparison to the measurements by Kéromnès et al. [102] (98%v Ar dilution).

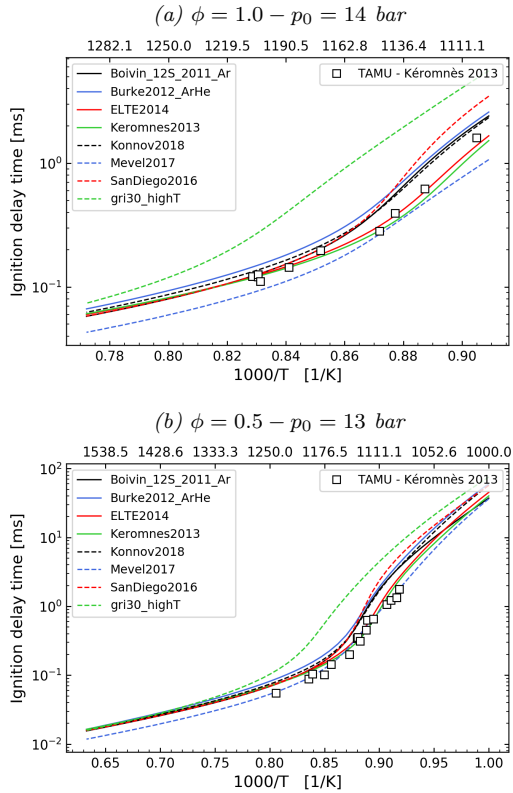


Figure 2.5: Predicted ignition delay times in comparison to the measurements by Kéromnès et al. [102] (98%v Ar dilution).

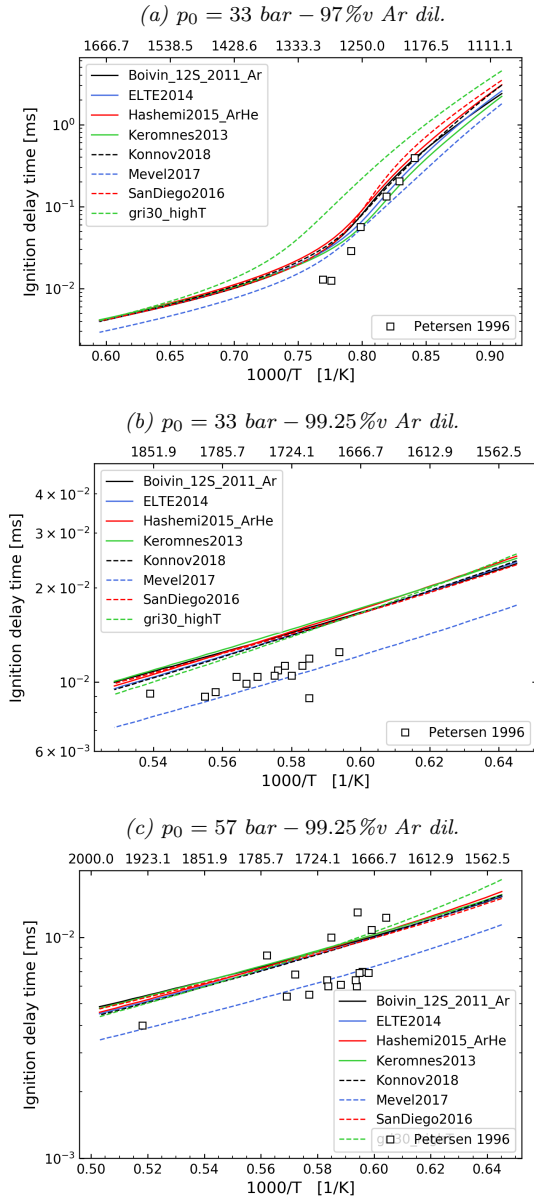


Figure 2.6: Ignition delay times predicted by different mechanisms in comparison to the measurements by Petersen et al. [109] ($\phi = 1$).

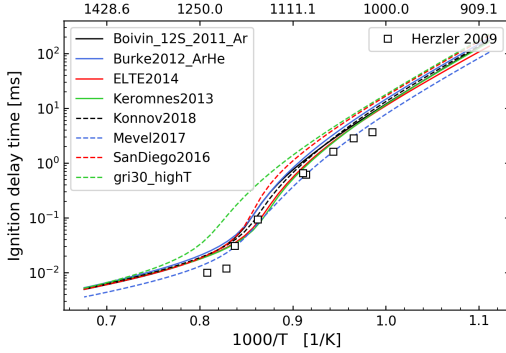


Figure 2.7: Ignition delay times predicted by different mechanisms in comparison to the measurements by Herzler and Naumann [110] ($\phi = 1, p_0 = 16$ bar, 91%v N_2 dilution).

the others. The same occurs for the values in Figure 2.5 (b) (13 bar) for $\phi = 0.5$, even if the improvement with respect to the K eromn es et al. [102] or ELTE [103] is limited. Nevertheless, the M evel et al. [105] scheme does not perform noticeably better than other mechanisms for other conditions. This probably indicates that a further evaluation of the scheme capabilities are needed to fully characterize its performances and the ranges of conditions where its adoption can be recommended.

Finally, it can be also concluded that the GRI3.0 [95] scheme cannot be recommended for problems involving the auto-ignition of a H_2 -air mixture such as a detonation. In fact, these problems lay outside the specific targets that were used for the optimization of the mechanism for the CH_4 oxidation and that made the reaction scheme very popular for such fuel. Better schemes are available and continuously updated specifically for H_2 oxidation, and the present study suggests that the optimized mechanism ELTE [103] can provide accurate results in terms of ignition delay time for a wide range of conditions significant for an atmospheric H_2 -air detonation.

2.2.3 Induction time in detonation conditions

As pointed out in the previous section, the experimental data for the ignition delay time are not available for the exact conditions of interest for a CJ detonation in a H_2 -air mixture, i.e. the post-shock $T_0 = 1538\text{ K}$, $p_0 = 28\text{ bar}$, so the comparison with the measurements was carried out following the availability of the data near such conditions.

Nevertheless, it is interesting to compare the numerical results in the exact post-shock conditions to assess the discrepancy of the reaction mechanisms in the prediction of the ignition delay time. This analysis is useful to indicate whether the scheme choice is really important or not at the conditions of interest. The same numerical approach described in Section 2.2.2.1 is adopted to obtain the induction time by solving a 0D constant volume reactor initially filled with a stoichiometric H_2 -air mixture at $T_0 = 1538\text{ K}$, $p_0 = 28\text{ bar}$, i.e. at the vN state in a CJ detonation. The simulations are repeated for the mechanisms in Table 2.1 and the results are presented in Figure 2.8. The majority of the reaction

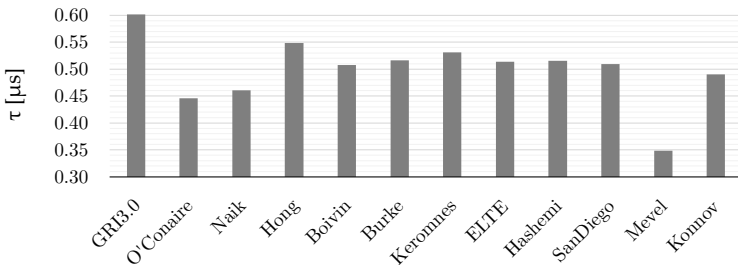


Figure 2.8: Ignition delay times of a H_2 -air stoichiometric mixture at the vN state ($T_0 = 1538\text{ K}$, $p_0 = 28\text{ bar}$) of a CJ detonation.

mechanisms predicts an explosion time between $\tau_{ign} = 0.49 - 0.53\ \mu\text{s}$. The results are coherent with the results of the previous section where some schemes as the GRI3.0 [95] always overestimated the measurements while the Mevel [105] usually provided the shortest ignition delay time. The coherence of many reaction mechanisms with the ELTE scheme

suggests their reasonable prediction, as the ELTE performed well in the conditions near the vN state. However, the lack of experimental data in these conditions prevents from determining their absolute accuracy.

Since in a freely-propagating detonation the pre-shock condition as well as the leading shock Mach number usually fluctuates around the CJ condition, the comparison of the schemes is extended to a range of post-shock pressures and temperatures around the CJ point, i.e. $1000 < T_0 < 1800$ K and $10 < p_0 < 40$ bar. For any combination of pressure and temperature a 0D constant volume reactor is solved to measure the ignition delay time of the mixture and the resulting values are mapped in Figure 2.9 for different mechanisms. The white line represents the locus

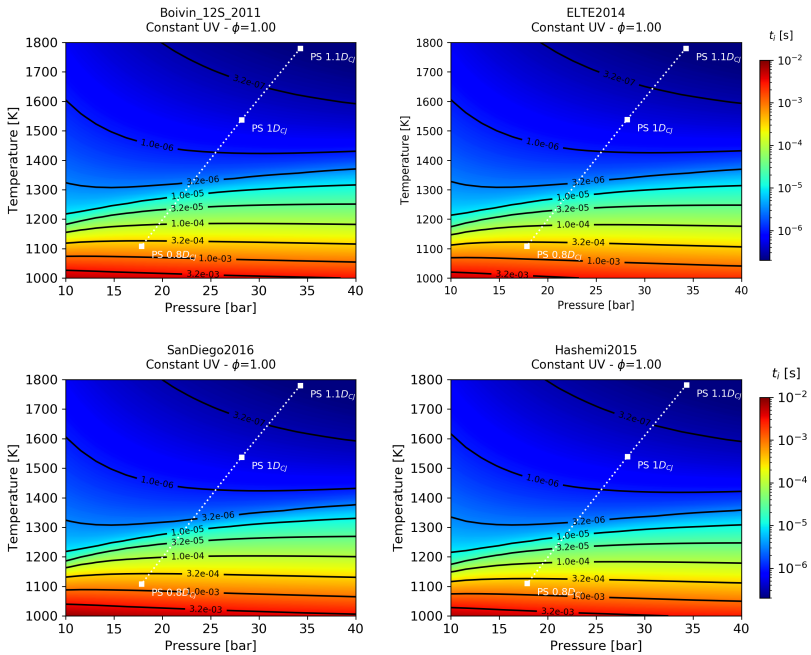


Figure 2.9: Ignition delay time maps as a function of initial pressure and temperature obtained with different reaction schemes. The white points indicates the post-shock conditions for different fractions of CJ speed.

of post-shock conditions for a detonation in a stoichiometric, atmospheric H_2 -air mixture when the detonation velocity varies between 80% D_{CJ} and 110% D_{CJ} , i.e. $D = 1580 - 2170$ m/s. The four mechanisms are selected for the comparison to assess the variation of the explosion time beyond the vN condition reported in Figure 2.8, when the mechanisms provide similar results in that condition.

Again, the schemes prove to be very coherent both qualitatively and quantitatively. It is interesting to note that the range of pressures and temperatures considered in Figure 2.9 intersects the extended second explosion limit (see Figure 2.1) which distinguishes the regimes of weak and strong explosion of the mixture. For the investigated ranges the limit depends primarily on the temperature, with the high τ_{ign} value at lower temperatures marking the weak explosion regime and the low τ_{ign} the strong explosion regime, where the induction time drops by three orders of magnitude from milliseconds to microseconds.

To compare the crossover between the two regimes a very useful quantity can be derived from the explosion time variation on the initial temperature for a fixed pressure, i.e. the reduced effective activation energy θ defined as [94, 114]:

$$\theta(p_0, T_0) \equiv \frac{E_a}{RT_0} = \frac{1}{T_0} \frac{\partial \ln \tau_{ign}(p_0, T_0)}{\partial (1/T_0)} \quad (2.3)$$

where the condition (0) refers to the initial reactor state, i.e. the post-shock (vN) state in this case. The reduced effective activation energy quantifies the sensibility of the induction time with respect to the initial temperature and can be correlated to the regularity of the cellular structure [114, 115]. In fact, a post-shock temperature variation alters induction time and the internal front structure of a detonation in proportion to θ . Eq. 2.3 is applied to the explosion time maps of Figure 2.9 evaluating the partial derivative through central differences, obtaining the θ distributions shown in Figure 2.10. Due to the crossover between the weak and strong explosion regions, the reduced activation energy maps present a ridge defining the crossover temperature for each pressure. It is worth to

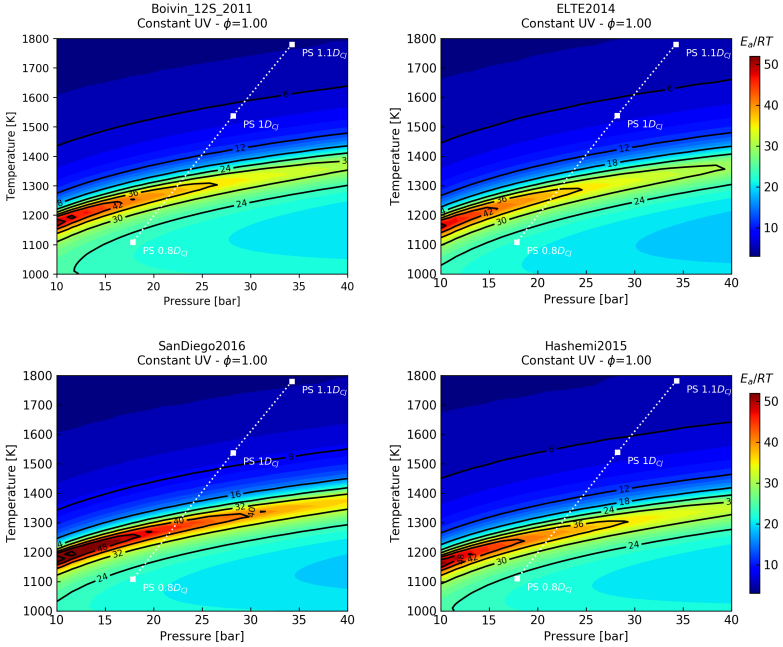


Figure 2.10: Reduced effective activation energy maps as a function of initial pressure and temperature obtained with different reaction schemes. The white points indicate the post-shock conditions for different fractions of CJ speed.

highlight that detonations are observed experimentally both above and below this temperature [114], so the post-shock conditions for $D < 0.9D_{CJ}$ can be achieved in a detonation. Despite the SanDiego [87] mechanism predicts a higher maximum value of θ and a slightly narrower ridge, the distributions do not present significant discrepancies between the reaction schemes, confirming the visual similarity of the ignition delay maps in Figure 2.9. It is also interesting to note how the skeletal Boivin et al. [100] scheme does not suffer the reduction of radicals and reactions in terms of induction time, resulting very similar to the ELTE [103] results. Nevertheless, for a reduced mechanism to capture the crossover

region, at least 5 steps are required and carefully calibrated [94, 114]. In simpler schemes, these features are inevitably lost as a cost of the reduced computational effort.

2.2.4 ZND detonation structure

The ignition delay time was considered in the previous section as the fundamental parameter for comparing the reaction schemes since the explosion of the mixture after the shock compression is basically driven by that timescale. However, as discussed in Section 2.2.2.1 the constant volume hypothesis used for the explosion simulations is only an approximation of the fluid thermodynamic path, rather following a Rayleigh line. Although such approximation can be accepted in 0D reactors, it does not actually describe the flow behind a detonation, so the ZND model of a 1D steady detonation should be preferred to test the detailed schemes and provide a reference for the reduced schemes. Therefore, in this section the detailed reaction mechanisms are compared in terms of 1D ZND steady detonation profiles. The ZND model for the detonation is solved using Cantera 2.4.0 [111] and the Shock Detonation Toolbox (SDT) developed by Shepherd [113] considering a CJ detonation in a stoichiometric H_2 -air mixture at atmospheric conditions ($T_0 = 298$ K, $p_0 = 1$ atm). The resulting profiles are reported in Figure 2.11 in the frame of reference fixed with the leading shock moving with $D = D_{CJ} \approx 1975$ m/s.

As expected, the similarity of the ignition delay time predicted by the reaction mechanisms is reflected in the internal structure of the detonation front, with the mechanisms as the Mével et al. [105] distinguishing from the others for its lower explosion time. The profiles show clearly the thermal-neutral region right after the shock where the radicals concentration rises rapidly leading to the autoignition of the mixture. This region is identified as the induction zone and extend from the shock to the maximum thermicity $\dot{\sigma}$, i.e. the peak of the heat release rate [89], and its thickness is referred to as the induction width. A similar measure of the location of the maximum heat released by the reaction is provided by

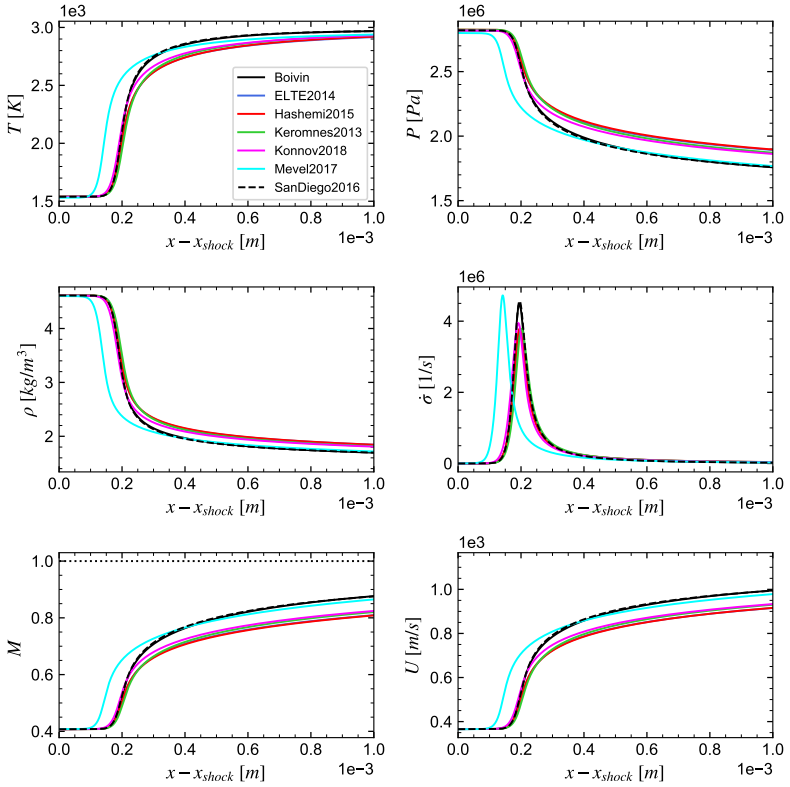


Figure 2.11: 1D CJ detonation profiles predicted through the ZND model in the wave frame of reference.

the half-reaction thickness δ_{half} , i.e. the distance from the shock where the reactant concentrations halves Ng [116]. Finally, the extent of the region where the heat release occurs can be approximated by the reaction thickness δ_r [117]. The three characteristic lengths can be then expressed mathematically as:

$$\delta_{half} = x - x_{shock} : Y_{H_2}(x) = 0.5Y_{H_2}^0 \quad (2.4)$$

$$\delta_i = x|_{\dot{\sigma}_{max}} - x_{shock} \quad (2.5)$$

$$\delta_r = \dot{\sigma}_{max}/U_{CJ} \quad (2.6)$$

where x is the position and $U_{CJ} = \rho_0 D_{CJ}/\rho_{CJ}$ is the gas velocity at the CJ point in shock-fixed coordinates.

As the reactants are converted in products the density and the pressure rapidly drop from the post-shock (vN) value, leading to the acceleration of the flow up to the sonic condition at the CJ plane, not represented in Figure 2.11. The reaction schemes except the Mével et al. [105] are very similar in their predictions, with the SanDiego and the Boivin mechanisms that model a slightly higher thermicity peak than the others. This more concentrated heat release induces a faster heating but also an anticipated expansion, with the density and pressure decreasing faster to the same CJ plane values. This difference can be also quantified by evaluating the reaction thickness δ_r in Eq. 2.6, reported in Table 2.3 for the various mechanisms beside the other characteristic thicknesses of the detonation front. As can be observed, the more pronounced differences among the schemes is linked to the reaction length, while the half-reaction thickness and the induction zone are coherently distributed between 191-202 μm , with very limited differences for a fixed scheme despite their different expression.

The characteristic lengths in Table 2.3 can be combined with the reduced effective activation energy $\theta = E_a/RT_{vN}$ of the scheme to have an estimation of the detonation cell size. According to the empirical correlation proposed by Ng et al. [117], the cell width is a function of the

Table 2.3: Characteristic reaction zone widths and estimated cell size (λ) according to Ng et al. [117] correlation.

Mechanism	δ_{half} [μm]	δ_i [μm]	δ_r [μm]	θ [-]	λ [mm]
Boivin et al. [100]	195	195	245	6.78	9.0
ELTE [103]	198	198	291	7.01	9.6
Hashemi et al. [104]	196	195	290	6.75	9.6
Kéromnès et al. [102]	202	202	290	6.77	9.8
Konnov [106]	191	194	278	6.51	9.4
Mével et al. [105]	142	141	231	6.51	7.3
SanDiego [87]	195	195	240	6.76	9.0

stability parameter χ :

$$\chi = \frac{E_a}{RT_{vN}} \frac{\delta_i}{\delta_r} \quad (2.7)$$

The correlation is applied also for the present conditions, leading the values reported in Table 2.3, in good accordance with the experimental reference of $\lambda = 9 - 10$ mm [118]. As a consequence of the limited variation the schemes are again homogeneous in their prediction and provide values within the narrow range 9 – 9.8 mm, with the exception of the Mevel mechanism.

2.2.5 Sensitivity of detonation properties to initial conditions

The comparison of the recent reaction schemes for H_2 oxidation provides confidence in their prediction and thus enables their use for predicting useful quantities about the detonation properties and their dependencies. Specifically, they can be exploited to determine the sensibility of the detonation states and velocity on the initial pressure and temperature conditions. This dependence is of interest for a real configuration since the fresh mixture typically presents both spatial and temporal dis-homogeneities, even considering a fixed equivalence ratio, for the real injection system whose choking determines highly under-expanded jets [37]. Therefore, a single initial state for the fresh mixture cannot be

considered, but rather a range of initial conditions should be identified. This aspect is very important for the development of reduced schemes, which require a reference to be calibrated and compared to.

With this objective, the detonation speed in Chapman-Jouguet (CJ) conditions, the post-shock (v_N) and CJ states are evaluated numerically considering the full thermodynamic properties of the Boivin et al. [100]. Although the scheme is skeletal, no specific inaccuracies are introduced with respect to other complete schemes, as observed in the previous sections, so its predictions can be assumed equivalent to a detailed scheme.

The CJ speed (D_{CJ}) is calculated using the Shock Detonation Toolbox Shepherd [113] extension of the Cantera 2.4.0 [111] libraries for a stoichiometric mixture of H_2 -air. Here the v_N post-shock condition refers to a shocked mixture along the unreacted Hugoniot curve, considering a frontal shock speed equal to the CJ speed. The CJ state is then found on the same Rayleigh line as the intersection with the equilibrium Hugoniot line. The computations are carried out for initial conditions which are distributed around the atmospheric condition, leading to the distributions reported in Figure 2.12 and 2.13.

The maps are basically driven by the dependence of the CJ speed on the initial pressure and temperature (Figure 2.12), which features general increase for lower temperatures and higher pressures. The pressure and temperature dependence tend to decouple for low values of each quantity, i.e. for low temperatures ($T \approx 200$ K) the pressure impact is moderate and for low pressures ($p < 1$ bar) the temperature has a very low influence on D_{CJ} . Further insight on this behaviour can be obtained considering that in the high detonation mach number ($M_{CJ} = D_{CJ}/a_0 \gg 1$) approximation of the discontinuity equations for a $2 - \gamma$ mixture, the detonation speed at the CJ condition can be expressed as [22]:

$$D_{CJ} \approx \sqrt{2(\gamma_{CJ} - 1)q} \quad (2.8)$$

where q represents the heat released by the combustion per unit mass.

According to the above equation, both the heat capacity ratio at the CJ point and the heat released by the oxidation process increase the

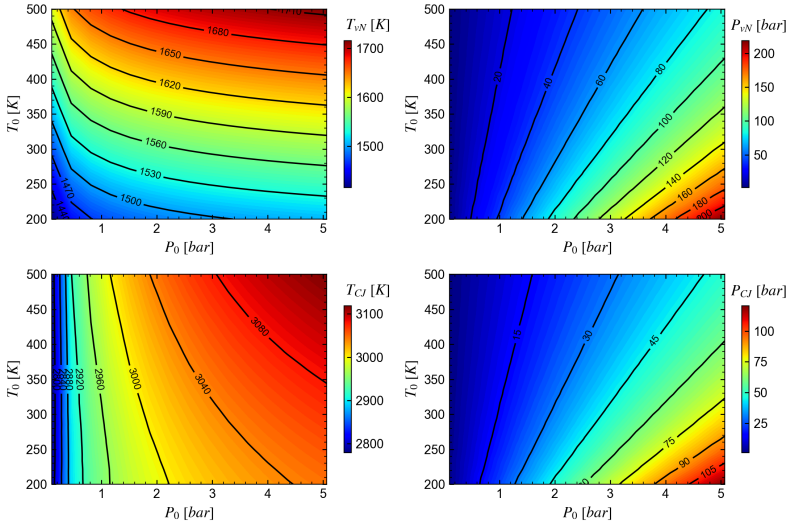


Figure 2.12: Post-shock (vN) and Chapman-Jouquet (CJ) states predicted by the Boivin et al. [100] mechanism in a CJ detonation for different combinations of initial pressure and temperature (H_2 -air, $\phi = 1$).

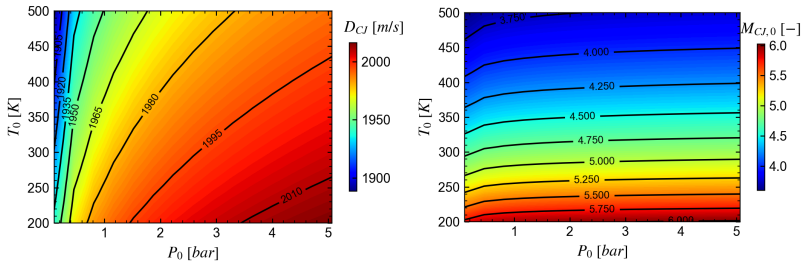


Figure 2.13: Chapman-Jouquet detonation speed (left) and Mach number (right) with respect to fresh gas predicted by the Boivin et al. [100] mechanism in a CJ detonation for different combinations of initial pressure and temperature (H_2 -air, $\phi = 1$).

detonation velocity. Although the initial composition of the mixture is fixed in the present analysis, the two quantities are still complex functions of the products composition and state at the CJ plane, since the γ_{CJ} depends on the temperature and the species mass fraction at the CJ state. The two quantities influence also the thermodynamic equilibrium of the mixture and the H_2O dissociation, leading to variations of the heat released by the reaction. Indeed the dissociation reaction is favoured by the very high temperatures reached at the CJ plane and by low pressures since the dissociation involves a reduction of moles. Although this effect was not accounted for in Jouguet's original theory [22], its importance in determining the detonation speed became clear as soon as more detailed thermodynamic and chemical models were employed [119]. To quantify the extent of the dissociation, the H_2O mass fraction is evaluated at the CJ plane and reported in Figure 2.14 with the γ_{CJ} as a function of the initial pressure and temperature conditions. As expected the water dissociation

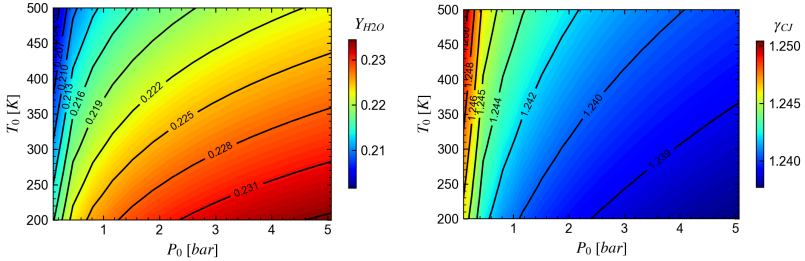


Figure 2.14: H_2O mass fraction (left) and heat capacity ratio (right) at the Chapman-Jouguet state predicted by the Boivin et al. [100] mechanism for different combinations of initial pressure and temperature.

reduces its equilibrium mass fraction especially for low pressures and high initial temperatures, and respects the trends considering the maps in Figure 2.12. Also γ_{CJ} reflects the combined distributions of $Y_{H_2O}^{CJ}$ and T_{CJ} , leading to a variation opposite to the water dissociation, i.e. high values for low pressures and high temperatures. Therefore, the two contributions in Eq. 2.8 partially compensate each other for the resulting

D_{CJ} , with the dissociation effect overcoming the one produced by the heat capacity ratio. As a result, the detonation speed in CJ conditions is dominated by the heat released during the explosion, determining in turn the frontal shock strength and the post-shock condition. The evolution of the whole coupled system is thus defined by the maps in Figures 2.12 and 2.13, useful for providing reference values for the detonation states in a range of initial conditions which can be encountered in a real configuration.

2.3 Development of reduced mechanisms

In Section 2.2 several detailed reaction mechanisms for H_2 oxidation were compared in proximity of the conditions of interest for a detonation, highlighting that the majority of the recent schemes provides coherent predictions with the experimental measurements of explosion time. Although the oxidation process of hydrogen does not involve many steps or species such as hydrocarbons, the reaction mechanisms considered in Section 2.2 describe the whole chemical process and elementary reaction steps. The resulting system then evolves exhibiting potentially complex behaviours depending on the thermodynamic conditions (see Section 2.1 and Figure 2.10). Only a sufficiently detailed chemical model is able to capture the complex variations of ignition delay time and reaction zone thickness in a detonation, mainly due to the radicals kinetics. It was also demonstrated that using a more detailed chemical kinetic model could reproduce many aspects of the direct detonation initiation and the processes that cause the detonation failure, which cannot be described by simplified reaction models [120]. A full chemical model embeds all the chain-branching and thermal explosion pathways which drive the combustion, however, such model is not practical for realistic multidimensional simulations, inducing many efforts into ad-hoc models which reproduce the main aspects of the chemical process [21, 89]. In fact, the direct transport of species, which allows an accurate physical description of the combustion process, requires more computational resources and can also run into stiffness problems as the number of species and reaction increases.

For these reasons the chemical models which can be adopted in CFD simulations are usually reduced schemes, that have to be calibrated for reproducing at least some key features of the phenomenon in the conditions of interest [121]. As a consequence, the models are usually optimized for describing either the deflagration or the detonation, since the two combustion regimes are profoundly different and their simultaneous optimization can be achieved only at the expense of the accuracy in a

single regime. In that case the targets choice has to be motivated by specific applications such as DDT [122–124].

Although the increasing computational power is enabling the adoption of detailed schemes [75, 79, 125, 126], the majority of the studies in the literature exploited specific reduced reaction mechanisms for modeling the detonation process. Moreover, only few of them adopt multi-step schemes such as the 7 species, 7 reactions mechanism developed by ONERA [60, 67, 68, 81, 127] and the 8 species, 7 reactions abridged Jachimowski [77, 78].

Instead, a lot of works were carried out using simple tuned single-step models with fictive species and constant thermodynamic properties ($1 - \gamma$), evolving through an Arrhenius rate [64, 122–124]. Specific models for the detonation were also developed adopting either $1 - \gamma$ parameters and ad-hoc finite rate models [62, 128] or $2 - \gamma$ thermodynamics coupled with an induction time model [61, 65, 71, 129, 130]. Finally, global single-step mechanism with real species and Arrhenius pressure independent rate [66] or pressure dependent rate [69, 76] have been tested for detonation simulations.

In this chapter, two different single-step schemes are derived and calibrated for the conditions of interest, i.e. the detonation of a H_2 -air mixture in ambient conditions. Two different strategies are explored, i.e. the use of a single-step, $1 - \gamma$ scheme and a global mechanism involving real species. Both the development and the calibration procedures are presented in detail highlighting the inputs and the targets of the models, so that the described procedure could be reproduced for any specific condition. The two mechanisms present a different range of validity, which determines the configurations where they can be applied, thus the off-design capabilities and performances are also discussed.

2.3.1 2S1R single-step, fictive species mechanism

The first mechanism considered in this work is based on the simplification of the Rankine-Hugoniot relations proposed by Williams [131], which allow the formulation of analytical jump relations across a detona-

tion wave. Given the initial thermodynamic conditions of a mixture, the simplification is based on the following hypotheses [131]:

1. Ideal gas mixture:

$$p = \rho RT \sum_{k=1}^N (Y_k/W_k) \quad (2.9)$$

2. Constant equilibrium composition of the burnt gas along the Hugoniot line;
3. Conservation of average molecular weight between the initial (0) and final (∞) state:

$$\left(\sum_{k=1}^N Y_{k,\infty}/W_k \right)^{-1} = \left(\sum_{k=1}^N Y_{k,0}/W_k \right)^{-1} \equiv \bar{W} \quad (2.10)$$

4. Conservation of the specific heat at constant pressure c_p :

$$\sum_{k=1}^N Y_{k,\infty} c_{p,k} = \sum_{k=1}^N Y_{k,0} c_{p,k} \equiv c_p \quad (2.11)$$

The hypotheses immediately imply that the heat capacity ratio γ is constant between the initial (0) and final (∞) state, so the model can be called single- γ or $1 - \gamma$ [22].

Assuming the hypotheses 1 – 4 and defining the heat of reaction q per unit mass as:

$$q \equiv \sum_{k=1}^N \left[(Y_{k,\infty} - Y_{k,0}) \left(\Delta h_{f,k}^0 + \int_{T^{ref}}^{T_0} c_{p,k} dT \right) \right] \quad (2.12)$$

the simplified Hugoniot relation can be then expressed as:

$$\frac{\gamma}{\gamma - 1} \left(\frac{p_\infty}{\rho_\infty} - \frac{p_0}{\rho_0} \right) - \frac{1}{2} \left(\frac{1}{\rho_\infty} - \frac{1}{\rho_0} \right) (p_\infty - p_0) = q \quad (2.13)$$

A further manipulation of Eq. 2.13 allows writing an even simpler equation

and can be obtained by substituting the dimensionless quantities:

$$p^* = p_\infty/p_0 \quad (2.14)$$

$$v^* = 1/\rho^* = v_\infty/v_0 \quad (2.15)$$

$$q^* = qW/(RT_0) = q\rho_0/p_0 \quad (2.16)$$

leading to the dimensionless Hugoniot equation:

$$p^* = \frac{\left(2q^* + \frac{\gamma+1}{\gamma-1}\right) - v^*}{\frac{\gamma+1}{\gamma-1}v^* - 1} \quad (2.17)$$

The final Eq. 2.17 is a very compact expression which describes the variation of pressure and specific volume relative to the initial condition and is a function of the heat capacity ratio γ and of the normalized heat of reaction. More details about the derivation and the implications of Eq. 2.17 can be found in [131] and are not reported here for sake of conciseness.

Eq. 2.17 can be applied at the CJ condition so that the quantities at the CJ point are calculated knowing the gas properties and the initial condition [131]:

$$p_{CJ}^* = 1 + q^*(\gamma - 1) \left(1 + \left[1 + \frac{2\gamma}{q^*(\gamma^2 - 1)} \right]^{1/2} \right) \quad (2.18)$$

$$v_{CJ}^* = 1 + q^* \frac{(\gamma - 1)}{\gamma} \left(1 - \left[1 + \frac{2\gamma}{q^*(\gamma^2 - 1)} \right]^{1/2} \right) \quad (2.19)$$

$$M_{0,CJ} = \left[1 + \frac{q^*(\gamma^2 - 1)}{2\gamma} \right]^{1/2} + \left[\frac{q^*(\gamma^2 - 1)}{2\gamma} \right]^{1/2} \quad (2.20)$$

where M_0 indicates the Mach number of the detonation wave relative to the fresh gas, i.e. $M_{0,CJ} = D_{CJ}/a_0$.

Despite the hypotheses and assumptions of the simplification, Eqs. 2.18 - 2.20 are very useful for estimating the CJ state of a detonation *a priori*, without the solution of differential equations. Functionally, they are equivalent to the normal shock or jump relations which describe the

variation of the thermodynamic state across a shock in an ideal gas mixture.

A simple form of the shock jump relations can be derived for a perfect gas, i.e. an ideal gas with $c_p = \text{const.}$, and assuming a fixed composition between the initial (0) and post-shock (1) state. It is worth to note that these conditions are included in the hypotheses of Williams [131] simplification of Hugoniot equation (Eq. 2.17), so the "frozen" Hugoniot relation can be derived from Eq. 2.17 by imposing $q = 0$:

$$\frac{p_1}{p_0} = \frac{\frac{\gamma+1}{\gamma-1} - \frac{v_1}{v_0}}{\frac{\gamma+1}{\gamma-1} \frac{v_1}{v_0} - 1} \quad (2.21)$$

Considering that for a perfect gas the sound speed can be expressed as $a = \sqrt{\gamma p/\rho}$, the following relations can be formulated [22]:

$$\frac{p_1}{p_0} = 1 + \frac{2\gamma}{\gamma+1} (M_0^2 - 1) \quad (2.22)$$

$$\frac{\rho_1}{\rho_0} = \frac{\gamma+1}{\gamma-1 + 2/M_0^2} \quad (2.23)$$

$$M_1^2 = \frac{M_0^2 + \frac{2}{\gamma-1}}{\frac{2\gamma}{\gamma-1} M_0^2 - 1} \quad (2.24)$$

In a detonation these equations allow the determination of the post-shock (von Neumann, vN) state while Eqs. 2.18 - 2.20 provide the state at the Chapman-Jouguet point, if the detonation speed matches the CJ speed. Of course the relations consider a single, constant γ which is not reflecting the reality for the majority of the cases, even for the non reacting Hugoniot equations at high Mach number, when the shock heating can alter significantly the gas specific heat c_p . Although the prediction of both vN and CJ state would benefit from the use of detailed thermodynamic data varying with temperature and composition, the relations of this section can be used as a first approximation of the two states for a detonation in a perfect gas.

2.3.1.1 Mechanism formulation

Since the present study is focused on the detonation in a H_2 -air mixture, the reduced thermodynamic and kinetic model is designed for these specific conditions of interest and denominated 2S1R, since it is constituted by two species and one reaction.

This scheme is the simplest model which can be formulated satisfying hypotheses 1 – 4 in the theory of Williams [131] explained in Section 2.3.1 and is based on a perfect gas mixture composed by species with the same molecular weight, i.e.:

$$W_k = \bar{W} = W \quad \forall k \quad (2.25)$$

$$c_{p,k} = c_p = \text{const.} \quad \forall k \quad (2.26)$$

$$\gamma_k = \gamma = \text{const.} \quad \forall k \quad (2.27)$$

Assuming these relations, the equation of state and the sensible enthalpy of the mixture read:

$$p = \rho \frac{R}{W} T \quad (2.28)$$

$$h_s = c_p(T - T_{\text{ref}}) \quad (2.29)$$

For describing the combustion, at least two species must be defined to represent the premixed reactants R and products P . Since they are both modeled as perfect gases with constant thermodynamic properties, the heat capacity ratios are equal $\gamma = \gamma_R = \gamma_P$ as well as the molecular weights $W = W_R = W_P$.

The reaction is then described as a single irreversible reaction:



whose rate of progress \mathcal{Q} is defined by an Arrhenius formulation:

$$\mathcal{Q} = \frac{\rho Y_R}{W} A \exp\left(-\frac{E_a}{RT}\right) \quad [\text{mol}/\text{m}^3 \text{s}] \quad (2.31)$$

where Y_R is the mass fraction of reactants, A the pre-exponential con-

stant and E_a the activation energy. Since the species present the same c_p , the enthalpies differ only due to the different formation enthalpies $\Delta h_{f,R}^0$, $\Delta h_{f,P}^0$ which determine the heat released in the reaction. This mechanism is named 2S1R as only 2 species and 1 reaction describe the thermodynamics and kinetics.

If the unburnt, pre-shock thermodynamic conditions of the mixture p_0 , T_0 are fixed, the model is completely described by only five parameters:

- **Thermodynamic parameters (3)**, which determine the detonation speed at Chapman-Jouguet (CJ) condition and the von-Neumann (vN) and the CJ states. Once imposed γ , W the heat of reaction is chosen to target the desired CJ speed according to the analytical relations 2.22 and 2.18 - 2.20 respectively.
- **Kinetic parameters (2)**, that influence the half-reaction thickness through the pre-exponential constant A and the detonation cells instability through E_a .

Thus, the 2S1R scheme is formulated and calibrated according to the following algorithm:

1. Impose the unburnt pre-shock conditions p_0 , T_0 and the CJ speed D_{CJ} and the half reaction thickness δ_{half} ;
2. Fix the heat capacity ratio γ and the molecular weight W ;
3. Determine the molar heat of reaction $q_m = -(\Delta H_{f,P}^0 - \Delta H_{f,R}^0)$ from Eq. 2.20 to match the detonation Mach number;
4. Evaluate and check the von Neumann (vN) and Chapman-Jouguet (CJ) states according to Eqs. 2.22 and 2.18 - 2.20. Eventually iterate to point (1) if the states are not satisfying;
5. Impose the activation energy E_a ;
6. Evaluate the pre-exponential constant A to match the imposed half reaction thickness δ_{half} .

Table 2.4: Thermodynamic and detonation properties predicted with different mechanisms thermodynamic data. The quantities are expressed in $[g/mol]$, $[kg/m^3]$, $[m/s]$, $[K]$, $[bar]$, respectively. The bold numbers highlight the values within a relative difference of $\pm 8\%$ with respect to the Boivin [100] mechanism.

Mech	Initial state			Deton.		vN state			CJ state			Err.
	γ_0	W	ρ_0	D_{CJ}	M_0	T	P	γ	T	P	γ	
Boivin [100]	1.40	20.90	0.855	1976	4.85	1538	28.20	1.32	2960	15.84	1.24	0%
ELTE [103]	1.40	20.90	0.855	1975	4.85	1538	28.20	1.32	2960	15.84	1.24	0%
Hashemi [104]	1.40	20.90	0.855	1977	4.85	1540	28.25	1.32	2964	15.87	1.24	0%
Kéromnès [102]	1.40	20.90	0.855	1977	4.85	1539	28.25	1.32	2964	15.87	1.24	0%
Konnov [132]	1.40	20.90	0.855	1975	4.85	1538	28.19	1.32	2959	15.84	1.24	0%
Mevel [133]	1.40	20.90	0.855	1968	4.83	1530	27.99	1.32	2941	15.76	1.24	0%
SanDiego [87]	1.40	20.90	0.855	1976	4.85	1538	28.20	1.32	2960	15.84	1.24	0%
Ma [64]	1.29	22.54	0.922	1973	5.24	1454	31.19	1.29	2743	16.10	1.29	8%
2S1R-t0	1.40	20.90	0.855	1976	4.85	1644	27.64	1.40	2533	14.33	1.40	6%
2S1R-tm	1.32	22.41	0.916	1976	5.17	1539	30.68	1.32	2728	15.85	1.32	6%
2S1R- T_{Cj}	1.40	24.66	1.008	1976	5.27	1887	32.62	1.40	2960	16.82	1.40	9%
	1.40	24.13	0.987	1976	5.21	1853	31.92	1.40	2900	16.47	1.40	8%
2S1R- E_{tot}	1.50	23.55	0.9631	1976	4.97	2041	29.87	1.50	2798	15.44	1.50	11%
	1.27	22.04	0.901	1976	5.24	1358	30.94	1.27	2700	15.98	1.27	9%

The above algorithm can be applied to describe a CJ detonation on a fuel-air mixture given its initial conditions and is similar to the approaches described by [64] for a Pulse Detonation Engine and by [122–124] for the transition from deflagration to detonation. In the present study the algorithm is applied to derive the parameters for a detonation in a H_2 -air stoichiometric mixture initially at atmospheric conditions. In the following paragraphs the choice of the fundamental values of γ , W and of the activation energy E_a and pre-exponential constant A is discussed in detail.

Thermodynamic parameters: Several combinations of γ , W are tested at point (2) to optimize simultaneously the accuracy of the unburnt pre-shock, the vN and the CJ states and are reported in Table 2.4. The comparison shows that the thermodynamic data of the most recent detailed mechanism is almost equivalent, leading to very similar initial, vN and CJ

states, so the thermodynamic parameters of the Boivin [100] mechanism is considered as reference for the choice of γ , W . In addition to the detailed mechanisms, in Table 2.4 the states predicted with the single-step, 3 fictive species mechanism by Ma et al. [64] are also reported. It is worth to remark that the CJ speed is an input for the 2S1R mechanism for any combination of γ , W , fixing the formation enthalpy of the species, which still need the sensible enthalpy to be defined through γ , W .

The different approaches which are adopted to determine γ , W are: (1) assuming the constant pre-shock values $\gamma_P = \gamma_R = \gamma_0$, i.e. 2S1R-t0, (2) assuming the the average values between the pre-shock and CJ states described by detailed thermodynamic data, $\gamma_P = \gamma_R = (\gamma_0 + \gamma_{CJ})/2$, i.e. 2S1R-tm and (3) optimizing specific quantities as the CJ temperature (2S1R- T_{cj}) or a global error over all the states (2S1R- E_{tot}). A score of each strategy is obtained by evaluating the total relative error in the prediction of all the states and the CJ velocity:

$$Err = \frac{1}{N} \sum_i^N |\varphi_i - \varphi_{i,ref}| \quad (2.32)$$

where φ_i indicates a generic thermodynamic quantity in Table 2.4.

Among all the approaches the most accurate for these conditions is the 2S1R-tm with the average thermodynamic data between the initial an CJ state, providing a global error of 6%. The global value is achieved also by the 2S1R-t0 but the CJ state in this case is described with lower accuracy, so it is discarded. The resulting maximum relative errors for the 2S1R-tm are within $\pm 8\%$ for the fresh and CJ state and slightly higher for the vN pressure and density, resulting in a balanced choice with respect to other approaches. A possible alternative for a balanced prediction of the states is represented by the mechanism proposed by Ma et al. [64], which however is less accurate than the 2S1R-tm. The average thermodynamic properties between the initial an CJ state are then used for the 2S1R model, implying the suffix “-tm” in the next.

Kinetic parameters: The activation energy is estimated according to the explosion theory by calculating ignition delay times at constant pressure. Considering an ideal gas reacting with a single-step reaction $F + O \rightarrow P$ and that in a constant pressure explosion the enthalpy is conserved, the following expression for the activation energy can be formulated [134]:

$$E_a = RT_0 \left(-\frac{T_0}{\tau_{ign}} \left(\frac{\partial \tau_{ign}}{\partial T_0} \right)_{p_0} + (n+1) \right) \quad (2.33)$$

This relation correlates the activation energy to the explosion or ignition delay time and the reaction order n . Eq. 2.33 can be discretized considering a small initial temperature rise $T'_0 = T_0 + T'$ with $T' \ll T_0$ and holding the initial pressure constant:

$$E_a \approx RT_0 \left(-\frac{T_0}{\tau_{ign}} \left(\frac{\tau'_{ign} - \tau_{ign}}{T'} \right)_{p_0} + (n+1) \right) \quad (2.34)$$

Practically, the activation energy can be calculated from a constant pressure explosion by quantifying the variation of ignition delay time when the initial temperature of the mixture is perturbed by the small amount T' . With this objective, the explosion of different H_2 -air mixtures in constant pressure 0D reactor is solved numerically with the Cantera 2.4.0 libraries [111] (see Section 2.2.2.1), evaluating the τ_{ign} as the time to the maximum temperature gradient and using the ELTE [103] detailed mechanism. The reactors were initially filled with the mixture at $p_0 = p_{vN} = 28.2$ bar and $T_0 = 0.9T_{CJ} = 2664$ K for calculating τ_{ign} e then τ'_{ign} by applying an isobaric initial temperature perturbation of $T' = 40$ K. The values used are similar to the criterion adopted by Bane et al. [134] who considered $T_0 = 0.9T_b$ and the initial pressure for a deflagration. The reaction order in Eq. 2.34 is set to $n = 1$ according to the reaction of the scheme (R2.30). The results of the activation energy is reported in Figure 2.15 as a function of the equivalence ratio.

Since the mixture of interest has the stoichiometric composition, the value of $E_a/RT_0 = 25$ is used for the reaction mechanism. Finally, the

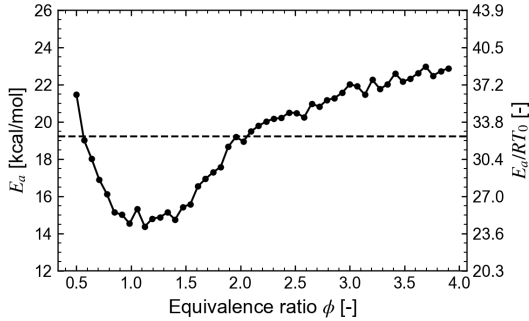


Figure 2.15: Activation energy evaluated with the explosion theory for different equivalence ratios and unity reaction order. E_a/RT_0 refers to the pre-shock temperature $T_0 = 298$ K.

pre-exponential constant A can be determined to achieve the target half reaction thickness obtained by the Boivin et al. [100] mechanism, i.e. the distance from the leading shock and the point where $Y_R = 0.5Y_R^0$.

It is worth to mention that if the activation energy would not have been a free parameter, not determined through the thermal explosion theory, for any value of the pre-exponential constant a value could be found for the activation energy to target the half-reaction thickness. In that case it is possible to impose also the target of the laminar flame speed to be satisfied. For instance this was done in [122–124] for single-step mechanisms for DDT. However, here the focus is the detonation and its stability characteristics rather than the deflagration, so the activation energy evaluated with the thermal explosion theory was preferred to provide a physics-based value which impacts the stability of the front [135, 136], rather than a value optimizing other parameters of minor interest.

The thermodynamic and kinetic parameters of the 2S1R model are finally completely defined and reported in Table 2.5.

Table 2.5: Summary of the main parameters for the 2S1R mechanism for a detonation in a stoichiometric, atmospheric H_2 -air mixture.

Design parameters		
p_0	101325	[Pa]
T_0	298	[K]
ϕ	1.0	[-]
D_{CJ}	1975.5	[m/s]
δ_{half}	195	[μm]
Model parameters		
γ	1.321	[-]
W	22.409	[g/mol]
ρ_0	0.916	[kg/m ³]
A	8.16e+07	[1/s]
E_a/RT_0	25	[-]
q/RT_0	21.95	[-]
E_a/RT_{vN}	4.84	[-]
$c_{p,m}$	34.21	[J/mol K]

2.3.1.2 Applications and off-design performances

The 2S1R mechanism described in the previous sections assumes several hypotheses which have to be considered when the scheme is applied. In addition to the inherent limitation of a perfect gas, single- γ model in the prediction of the thermodynamic states (see Table 2.4) and the use of a single step to model the reaction, the 2S1R scheme always describes the detonation in a single pre-shock fresh mixture state, i.e. for fixed p_0 , T_0 , and $Y_{k,0}$. For those conditions, unique values for the CJ speed and half reaction thickness are specified for the calibration of the kinetics and thermodynamic parameters (Table 2.5). Depending on the conditions of interest the parameters can be optimized but its accuracy decreases if the initial states departs from the one used for the formulation. Furthermore, the mechanism cannot describe any type of reactants mixing or mixtures with stratified composition, which could be limiting for real applications where the fuel and air can be injected

separately in the combustion chamber or have a spatially non-uniform composition.

In light of these limitations, two points are specifically important to be addressed for the application in a real device. Considering a perfectly premixed RDC, it is very important to (1) characterize the thermodynamic behaviour of the scheme, i.e. the state and the CJ speed, when the initial pressure and temperature vary from the values used for the calibration and (2) analyse the response of the half-reaction thickness when the detonation velocity departs from the CJ speed, i.e. what happens when the detonation front speed fluctuates around the CJ condition. Indeed both of the points arise in a RDC since the injection of the mixture has to be realised through choked injectors, which determine highly under-expanded jets of fresh reactants right before the passage of the detonation wave. Thus, the static temperature and pressure of the reactants is non-uniform both in time and space and the definition of single values for T_0 , p_0 represents an approximation. This feature of the fresh mixture, in conjunction to the turbulent fluctuations and the inherent instability of the detonation front to transverse oscillations, leads to continuous front velocity fluctuations around the CJ speed.

Detonation states dependence on initial conditions: The post-shock and CJ states in a CJ detonation propagating for a stoichiometric H_2 -air mixture are evaluated with the 2S1R model through Eqs. 2.22 and Eqs. 2.18 - 2.19 and reported in Figure 2.16 for initial temperature and pressures around the design point. The CJ speed and Mach number with respect to the fresh gas are also calculated with Eq. 2.20 and shown in Figure 2.17. The results are focused on pressure and temperature ranges which are representative of the refill region in a RDC with an atmospheric chamber outlet.

It is worth to repeat that the 2S1R mechanism is calibrated in a single point in the maps (see Table 2.5), providing the values reported in Table 2.4. The maps have to be contrasted to the ones described by the reference detailed mechanism of Boivin et al. [100] shown in Figures

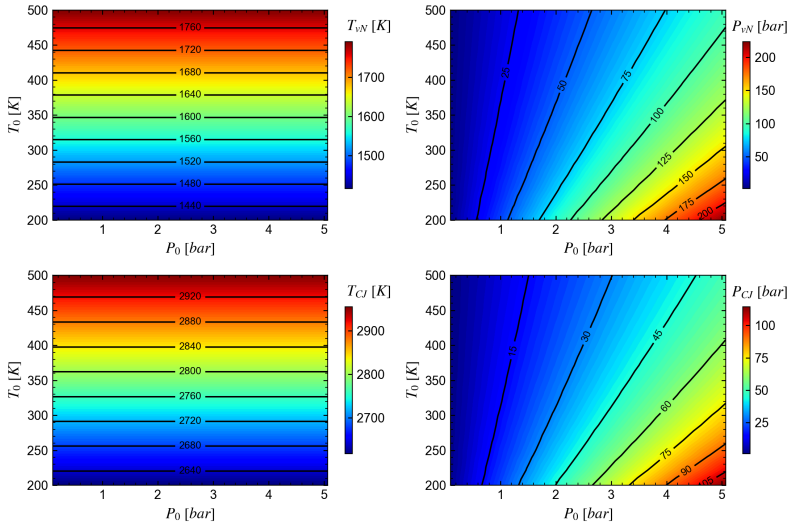


Figure 2.16: Post-shock (vN) and Chapman-Jouquet (CJ) states predicted by the 2S1R mechanism in a CJ detonation for different combinations of initial pressure and temperature.

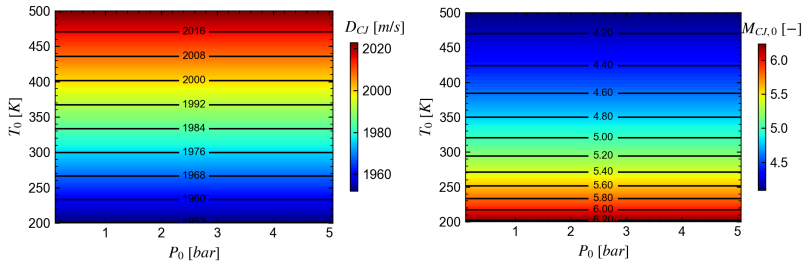


Figure 2.17: Chapman-Jouquet detonation speed (left) and Mach number (right) with respect to fresh gas predicted by the 2S1R mechanism in a CJ detonation for different combinations of initial pressure and temperature.

2.12 and 2.13. From the comparison it can be observed that both the post-shock and the CJ pressure levels are achieved with good accuracy by the simple 2S1R model, capturing well the trends and the values for the investigated range of conditions. Nevertheless, the reduced scheme presents consistent discrepancies in terms of post-shock temperature when the initial conditions depart from the normal atmospheric state, even considering the trend only. For instance, the model misses completely the pressure dependence of v_N and CJ temperatures and the behaviour of the region for low pressures. Since the results are relative to a CJ detonation, the states essentially reflect the variation of the CJ speed (Figure 2.17), which determines the Mach number of the leading shock and thus the v_N state as well as the CJ state. Despite the relatively low variations of D_{CJ} , these states are heavily impacted and the 2S1R scheme does not demonstrate a satisfying accuracy for significant deviations of the initial state from the one used for the calibration. Moreover, in a detailed model (Figure 2.13) the CJ speed is influenced by the dissociation of H_2O at equilibrium, favoured at low pressures and higher temperatures, which is not represented by the 2S1R model. These results are basically determined by the thermodynamics of the system and not by the chemical kinetics, so it can be expected that a model with more detailed thermodynamic description could improve the prediction.

Half-reaction thickness: The 2S1R scheme is used to evaluate the half-reaction thickness in a 1D steady detonation (ZND model) propagating in a stoichiometric H_2 -air initially at atmospheric pressure and temperature, i.e. the calibration conditions of the model. The detonation velocity is varied around the CJ speed to assess the resulting dependence of the half-reaction thickness. In fact, the variation of the CJ speed influences the leading shock compression and heating, inducing different times for the consumption of the reactants. In a detailed model able to describe the radicals growth, the explosion of the mixture is delayed with lower post-shock temperatures, while in a single-step model, where the radicals are not included, the reaction rate depends on the temperature through

the straight mathematical formulation of Arrhenius (Eq. 2.31). Thus for both the models a faster leading shock determines a shorter half reaction thickness.

The ZND model for the detonation is solved using Cantera 2.4.0 [111] and the Shock Detonation Toolbox (SDT) developed by Shepherd [113]. The profiles of the quantities within the detonation front are then processed to extract the half-reaction thickness δ_{half} as the distance between the leading shock and the position where $Y_R = 0.5 \cdot Y_{R,0}$. The same procedure is carried out for the Boivin et al. [100] mechanism to obtain a reference dependence of δ_{half} using H_2 as reactant species for the calculation. The results are reported in Figure 2.18 and demonstrate that the 2S1R

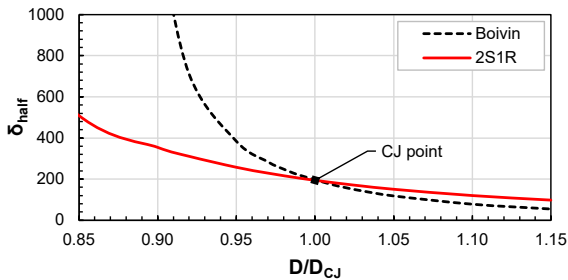


Figure 2.18: Half-reaction thickness as a function of CJ speed obtained through a 1D steady detonation (ZND) model with the 2S1R scheme.

scheme describes quite accurately the half-reaction thickness for overdriven conditions ($D \geq D_{CJ}$). On the other hand, for velocities lower than the CJ speed, the model progressively underestimates the δ_{half} with respect to a detailed mechanism. This behaviour could potentially lead to overestimate the extent of the detonation front fluctuation toward low speeds, where a more complex model would not predict a detonation for the very high half-reaction thickness that it would require.

2.3.2 4S1R global mechanism

As discussed in the previous section, the main limitation to the use of the 2S1R scheme is due to the use of fictive species for the premixed reactants, making the model applicable only to perfectly premixed cases. Moreover, the off-design performances of the model, primarily the CJ speed prediction, could reduce significantly the accuracy of the simulation in cases where the fresh mixture exhibits non-uniform conditions. These aspects can be both improved introducing a model with more detailed thermodynamic properties, thus avoiding the use of perfect, fictive species in favour of the main species involved in the hydrogen combustion. In fact, the CJ speed depends on the variation of thermodynamic properties between fresh and equilibrium and adopting an ideal gas mixture of real species allows an excellent, straightforward simplification of the detailed system. The separate introduction of reactants is also needed for modelling any non-premixed device, as the majority of the RDCs.

2.3.2.1 Mechanism formulation

Since one of the main requirements of the model, namely 4S1R, is the capacity to model the reactants mixing in a hydrogen-air system, the four species $k = H_2, O_2, H_2O, N_2$ are considered and modelled as ideal gases. With those species, the air molar composition can be approximated to $O_2 + 3.76N_2$. Then the equation of state reads:

$$p = \rho RT \sum_{k=1}^4 (Y_k/W_k) \quad (2.35)$$

The oxidation process is described by a global reversible reaction:



The net rate of progress of the global reaction is modelled with an Arrhenius formulation:

$$\mathcal{Q} = k_f[H_2]^{n_{H_2}}[O_2]^{n_{O_2}} - k_r[H_2O] \quad (2.37)$$

where $[\cdot]$ represents a molar concentration and n_k is the reaction order of the reactant species. The forward rate of progress k_f is calculated as:

$$k_f = A \exp\left(-\frac{E_a}{RT}\right) \quad (2.38)$$

while the backward rate of progress is evaluated through the equilibrium constant from the forward rate:

$$k_r = \frac{k_f}{\left(\frac{p^0}{RT}\right)^{n_{H_2} + n_{O_2} - 1} \exp\left(\frac{\Delta S^0}{R} - \frac{\Delta H^0}{RT}\right)} \quad (2.39)$$

where ΔH^0 and ΔS^0 represent the net variations in total molar enthalpy and entropy across the forward reaction and $p^0 = 1$ bar is the standard pressure. The reversibility of R2.36 is specifically intended to allow for the eventual dissociation of H_2O for high temperatures and relatively low pressures which can influence the CJ speed, so it becomes important when the initial pressure and temperature deviate from the value used for the calibration. In fact, an irreversible global reaction evolving with an Arrhenius rate can be calibrated for matching the CJ speed only on a narrow range around p_0 , T_0 , so this aspect will be discussed in detail within Section 2.3.2.2.

The reaction mechanism requires the appropriate choice of the kinetic parameters (Eq. 2.37, 2.38), the thermodynamic data and the transport coefficients to be completely defined, so each aspect will be discussed in detail in the next.

Thermodynamic data: Since the mixture is treated as an ideal gas mixture, the specific enthalpy and entropy of each species can be expressed by:

$$h_k(T) = \int_{T^0}^T c_{p,k}(T) dT + \Delta h_{f,k}^0 \quad (2.40)$$

$$s_k(T) = \int_{T^0}^T \frac{c_{p,k}(T)}{T} dT + s_k(T^0) \quad (2.41)$$

These dependencies are calculated analytically by assuming a NASA9 [137]

parametrization for the $\overline{c_p}(T)$ function:

$$\frac{c_p(T)}{R} = a_0 T^{-2} + a_1 T^{-1} + a_2 + a_3 T + a_4 T^2 + a_5 T^3 + a_6 T^4 \quad (2.42)$$

which can be integrated according to Eqs. 2.40, 2.41 to obtain the expressions for the enthalpy and entropy:

$$\begin{aligned} \frac{h(T)}{RT} = & -a_0 T^{-2} + a_1 \frac{\ln T}{T} + a_2 + \frac{a_3}{2} T + \frac{a_4}{3} T^2 + \frac{a_5}{4} T^3 \\ & + \frac{a_6}{5} T^4 + \frac{a_7}{T} \end{aligned} \quad (2.43)$$

$$\begin{aligned} \frac{s(T)}{R} = & -\frac{a_0}{2} T^{-2} - a_1 T^{-1} + a_2 \ln T + a_3 T + \frac{a_4}{2} T^2 + \frac{a_5}{3} T^3 \\ & + \frac{a_6}{4} T^4 + a_8 \end{aligned} \quad (2.44)$$

The constant coefficient a_7 deriving from the enthalpy integration is calculated to obtain the formation enthalpy at the standard state:

$$\Delta h_{f,k}^0 = h_k(T^0) \quad (2.45)$$

The same procedure is applied to the entropy for finding the coefficient a_8 which satisfies the standard state entropy. The nine parameters $a_0 - a_8$ can be retrieved from a variety of sources as the NIST-JANAF tables [138] and the NASA Glenn tables [137]. The NASA parametrization is also widely used in kinetic solvers so the reaction mechanisms provides the coefficients for the species which they include.

For the purposes of the 4S1R mechanism, the $a_0 - a_8$ species coefficients for H_2 , O_2 , H_2O , N_2 are assumed equal to the coefficients provided by the Boivin et al. [100] mechanism. Those values are completely equivalent to the ones included in the SanDiego [87] scheme thermodynamic data.

Despite the global reaction represents the main species involved in the process, the heat released by the global reaction is not exactly equivalent to a detailed mechanism, essentially due to the altered dissociation of H_2O . This inaccuracy is reflected not only in the equilibrium temperature but also on the CJ speed, so it is very important to account for the missing dissociation. A very simple correction which can improve significantly the

results is the increment of H_2O formation enthalpy, so that the heat of reaction is reduced [69, 76]. Since the formation enthalpy of water in the NASA9 parametrization is controlled by the coefficient a_7 , the value is optimized to minimize the CJ speed discrepancy with the Boivin et al. [100] mechanism for an atmospheric H_2 -air mixture. The variation of a_7 is applied for both the low and high temperature ranges, leading to a correction of:

$$\Delta a_7 = 1343 [K] \quad (2.46)$$

$$\Delta a_7 \cdot R = 11.16 [kJ/mol] \quad (2.47)$$

The resulting variations of H_2O formation enthalpy is reported in Table 2.6 considering as reference temperature for the enthalpy either 298 K or 0 K. With the implementation of the formation enthalpy correction, the

Table 2.6: Correction of the H_2O formation enthalpy for the 4S1R scheme.

	ΔH_f^{298K}	ΔH_f^{0K}	
Boivin et al. [100]	-241.82	-238.92	[kJ/mol]
4S1R	-230.66	-227.76	[kJ/mol]

detailed thermodynamic data of the 4S1R scheme determines an excellent accuracy for all the post-shock (vN), CJ states and CJ speed over the whole range of equivalence ratio considered. In Figure 2.19 these quantities are compared to the ones obtained using the reference mechanism of Boivin, showing that the simplifications of the thermodynamic data determined by pruning the species is not affecting significantly the prediction of the gas properties. This aspect is very important as for a successful simulation the thermodynamic states of the mixture have to be accurately described for any mixture composition between the pure fuel and the pure oxidizer, even beyond the flammability limits.

It is important to remark that the extent of the water dissociation depends on the temperature and pressure near the equilibrium, which in

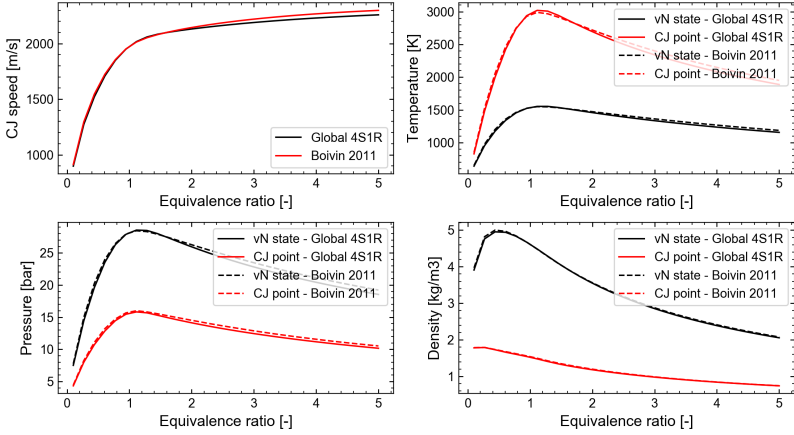


Figure 2.19: Post-shock (vN) and Chapman-Jouguet states predicted by the 4S1R mechanism for different equivalent ratios and compared with the Boivin et al. [100] mechanism.

turn are related to the initial gas conditions. The single correction of the formation enthalpy described above provides excellent results over all the compositions range but implies that a constant shift of the heat released by the reaction is sufficient to describe the dissociation accurately for all the initial conditions of interest. This aspect has to be verified and will be specifically faced in Section 2.3.2.2.

Kinetic parameters: For the definition of the model from according to Eq. 2.37, 2.38 the reaction orders n_{H_2} , n_{O_2} , the activation energy E_a and the pre-exponential constant A . The first two quantities are evaluated using the explosion theory, already exploited in Section 2.3.1.1 to determine the activation energy for the 2S1R mechanism. However, here the total reaction order is not fixed and has to be evaluated according to the thermal explosion theory. Assuming an ideal gas evolving with a single-step reaction $F + O \rightarrow P$ and that in a constant pressure explosion the enthalpy is conserved, the following expression for the effective or

total reaction order can be expressed as [134]:

$$n = -\frac{\rho}{\tau_{ign}} \left(\frac{\partial \tau_{ign}}{\partial \rho_0} \right)_{T_0} + 1 \quad (2.48)$$

This equation can be computed numerically by considering the sensibility of the ignition delay time to a small initial density rise $\rho'_0 = \rho_0 + \rho'$ with $\rho' \ll \rho_0$ while holding the initial temperature of the mixture constant:

$$n \approx -\frac{\rho}{\tau_{ign}} \left(\frac{\tau'_{ign} - \tau_{ign}}{\rho'} \right)_{T_0} + 1 \quad (2.49)$$

The Cantera 2.4.0 libraries [111] (see Section 2.2.2.1) are used to model and resolve the explosion of different H_2 -air mixtures in a constant pressure 0D reactor, evaluating the τ_{ign} as the time to the maximum temperature gradient. The reactors are initially filled with the mixture at $p_0 = p_{vN} = 28.2$ bar and $T_0 = 0.9T_{CJ} = 2664$ K to compute τ_{ign} and then τ'_{ign} by applying an isothermal initial density perturbation of $\rho' = 0.1\rho_0$. The initial parameters used are aligned to the ones imposed by Bane et al. [134] who considered $T_0 = 0.9T_b$ and the initial pressure for a deflagration. Similarly, the activation energy is evaluated using Eq. 2.34 with the same procedure described in Section 2.3.1.1, except for the reaction order value which is here set to $n = 2$. The results of the reaction order and activation energy computation are reported in Figure 2.20 for several equivalence ratio values.

The thermal explosion theory prescribes average values of $n = n_{H_2} + n_{O_2} = 1.95$ and $E_a = 23$ kcal/mol over the whole detonability range, with a very little variation of the reaction order. The activation energy shows more pronounced deviations from the average value, suggesting that the value has to be chosen according to the equivalence ratio range of interest. Specifically in a narrow range around the stoichiometric condition the activation energy presents a plateau of $E_a = 19$ kcal/mol, while progressively raises up to $E_a = 26$ kcal/mol for $\phi = 4$.

Since the final objective of the present work is the study of a non-premixed RDC, all the equivalence ratio range is considered of interest and

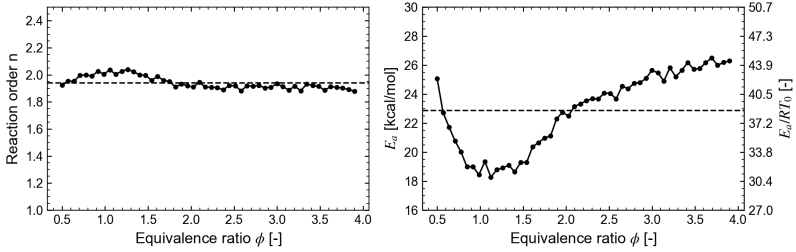


Figure 2.20: Reaction order and activation energy evaluated with the explosion theory for different equivalence ratios. E_a/RT_0 refers to the pre-shock temperature $T_0 = 298$ K.

the value for the activation energy is then taken as the arithmetic average of $E_a = 23$ kcal/mol ($E_a/RT_0 = 38.8$), accepting a slight overestimation at the stoichiometric point. As far as the reaction order is concerned, a total value of $n = 2$ is used. For deflagrations, the reaction orders impact the laminar flame speed distribution on the equivalence ratio [139, 140], and their values are usually optimized avoiding values far from the unity. In this work, a sensitivity to the single values of n_{H_2} and n_{O_2} is carried out to assess the dependency of a 1D detonation profile, observing a negligible impact of the single reaction orders on the quantities when their sum remains constant. Thus, the reaction orders for both hydrogen and oxygen are assumed to $n_{H_2} = n_{O_2} = 1$ without reducing the applicability of the 4S1R scheme.

The last kinetic parameter to be defined is the pre-exponential constant A in Eq. 2.38. The value of such constant is of paramount importance since it is proportional to the forward rate of progress of the reaction and determines the rate of the reaction in conjunction to the activation energy already determined. In a detonation, the rate of the reaction influences the internal front structure, i.e. the profiles between the post-shock state and the CJ point, since a faster reaction reduces the half reaction thickness as well as the whole reaction width. It is worth to remark that with the activation energy as a free parameter, not calculated through the thermal

explosion theory, for any constant value of A , a value for the activation energy would target the desired half-reaction thickness. In such case it would be possible imposing also another target as the laminar flame speed, as done in [122–124] for deflagration to detonation transition modeling. Here the focus is mainly on the detonation and its stability characteristics rather than the deflagration, so the activation energy evaluated with the thermal explosion theory was preferred to provide a physics-based value which determines the stability of the front [135, 136], rather than a value optimizing other parameters of secondary interest.

Therefore, the pre-exponential constant A for the 4S1R model is evaluated in order to target half-reaction thickness $\delta_{half} = 195 \mu\text{m}$ calculated with the reference Boivin et al. [100] mechanism in a 1D detonation. Thus, the ZND model for the detonation is solved using Cantera 2.4.0 [111] and the Shock Detonation Toolbox (SDT) [113] obtaining the distribution of the quantities within the detonation front for a stoichiometric H_2 -air mixture at atmospheric conditions. The profiles are then processed to extract the half-reaction thickness δ_{half} as the distance between the leading shock and the position where the reactants are half consumed, i.e. $Y_{H_2} = 0.5 \cdot Y_{H_2}^0$. The calibration at the stoichiometric point leads to a value of $A = 3.1\text{e}+13 \text{ [cm}^3/(\text{mol s})]$, which is used for the mechanism. As the calibration is carried out on the stoichiometric point, the accuracy of the resulting half-reaction width for several H_2 -air mixture compositions is assessed using Cantera and the results are reported in Figure 2.21. The δ_{half} is compared to the values predicted by both the Boivin et al. [100] and ELTE [103] mechanisms for the same conditions. The half reaction thickness is exactly matched by the 4S1R mechanism around the calibration point, while for very rich or very lean compositions the value is always underestimated with respect to the references. An iteration to the design of the 4S1R is also carried out to assess the impact of the single reaction orders n_{H_2} , n_{O_2} on the $\delta_{half}(\phi)$ dependence. The study showed that the departure is not affected by the single distribution of the reaction orders so it can be attributed to the limits of a single-step scheme, which for instance cannot capture the difference between the weak and strong

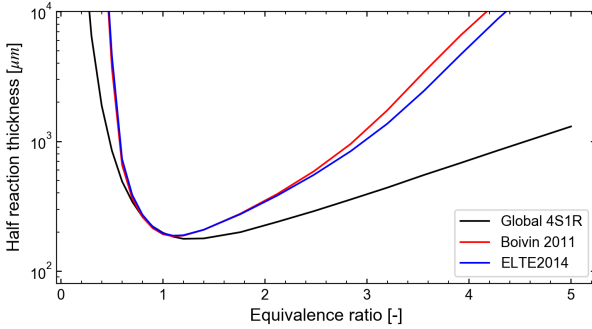


Figure 2.21: Reaction order and activation energy evaluated with the explosion theory for different H_2 -air equivalence ratios at atmospheric conditions.

explosion behaviour crossing the extended second limit (see Figure 2.1). Specifically as reported by Ng et al. [117] the weak region can be reached for the post-shock conditions in a CJ detonation above $\phi = 3.5$ and below $\phi = 0.5$ if the initial pressure is atmospheric. These aspects are beyond the capabilities of the single-step model, so the 4S1R scheme should be recalibrated if the equivalence ratio of interest deviates significantly from the stoichiometric condition. In the present work, focused on the analysis of a non-premixed RDC, although the thermodynamic properties are important to be described for any mixture composition, the detonation is expected to mainly involve mixture compositions near the stoichiometric value. Moreover, the half reaction thickness is usually of the same order of magnitude of the mesh element size, so the errors on the $\delta_{half}(\phi)$ dependence are below the spatial resolution of the typical simulation in real configurations.

The parameters characterizing the thermodynamic and kinetic behaviour of the 4S1R reaction scheme are summarised in Table 2.7 beside the predictions of the 1D detonation properties of CJ speed and half-reaction width.

Table 2.7: Summary of the main parameters for the 4S1R mechanism for a detonation in a H_2 -air mixture ($T_0 = 298$ K).

Model parameters		
n	2	
n_{H_2}	1	
n_{O_2}	1	
E_a/RT_0	38.8	[-]
E_a/RT_{vN}	7.53	[-]
A	$3.1e+13$	$[cm^3/(mol\ s)]$
$\Delta H_f^{298K}(H_2O)$	-230.66	$[kJ/mol]$
Detonation parameters		
$D_{CJ}(\phi = 1)$	1975.5	$[m/s]$
$\delta_{half}(\phi = 1)$	197	$[\mu m]$

Transport properties: One of the features of the 4S1R mechanism is the ability to model the mixing of the species. Although in a detonation the diffusion of the species has a very little impact due to the supersonic speeds involved, the reactants mixing is still very important since it determines the composition of the unburnt gas that will detonate. This aspect is thus fundamental in a CFD calculation and will be discussed here. Since the diffusion of species is already a complex problem to be solved, the CFD codes often adopt strategies to simplify the phenomenon [140]. However, when dealing with hydrogen combustion, the peculiar diffusion characteristics of this molecule has to be specifically addressed to avoid the over-simplification of the problem, i.e. the high diffusion of H_2 must be distinguished from the other species. For taking into account this aspect without losing computational efficiency, the CFD simulations of the present work adopt distinct and constant Schmidt numbers for each species:

$$Sc_k = \frac{\mu}{\rho D_k} \quad (2.50)$$

where the laminar viscosity μ is specified as a temperature function only, inducing the same dependence on each diffusion coefficient D_k .

The assumption of the laminar viscosity independence on the mixture composition is a common assumption [140], since the variation is limited and the value usually departs only slightly from pure air. To ensure that this simplification holds even in for the present case, the laminar viscosity is evaluated using Cantera 2.4.0 [111] through the kinetic gas theory using a full binary multi-component diffusion [92] for three different H_2 -air mixtures. The results are shown in Figure 2.22 between $300 < T < 3000$ K (points) and are fitted either with a Sutherland or a Power law [140]. The Power law fit describes the temperature trends of the viscosity better than the Sutherland law for every mixture composition. As expected the viscosity is a weak function of the composition so this dependence is neglected and the Power law fit of the stoichiometric composition is used to model the laminar viscosity for the whole composition spectrum:

$$\mu(T) = 1.73e-5 \cdot \left(\frac{T}{299.94} \right)^{0.704} \quad [kg/(m \ s)] \quad (2.51)$$

The species Schmidt numbers are then specified for each species as the value at the adiabatic equilibrium of an H_2 -air stoichiometric mixture initially at atmospheric conditions. For the same conditions the Prandtl number of the mixture is also evaluated and set as constant:

$$Pr = \frac{\mu c_p}{k} \quad (2.52)$$

so that the thermal conductivity k can be deduced from the viscosity (Eq. 2.51) and the c_p (Eq. 2.40). The transport properties of the 4S1R mechanism are summarised in Table 2.8.

2.3.2.2 Applications and off-design performances

Unlike the 2S1R mechanism, the global scheme 4S1R does not suffer for the simplification of the species and the related thermodynamic properties. First of all, the distinct species allow the description of the reactants mixing as well as the dilution with N_2 , and thus enable the simulation of realistic configurations of RDC, which usually involve a separate injection

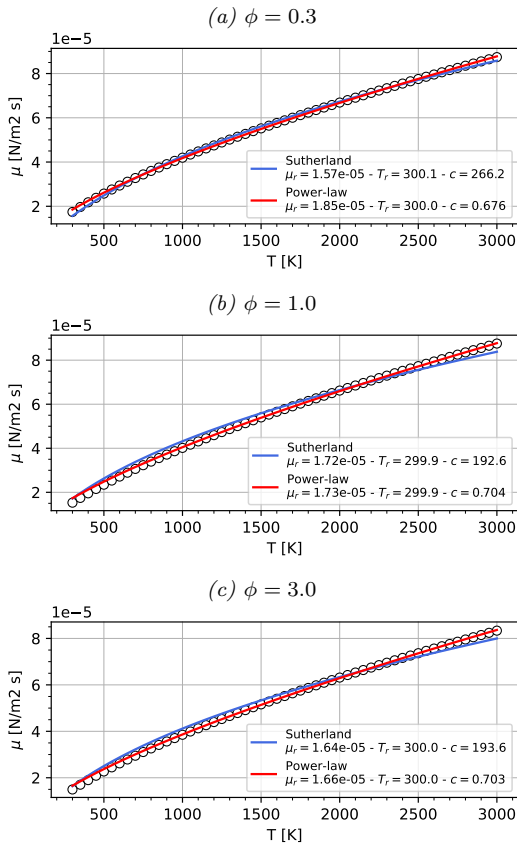


Figure 2.22: Laminar viscosity dependence on temperature of the 4S1R mechanism with either a Sutherland or Power law fit of the full multi-component description calculated with Cantera (points).

Table 2.8: Transport properties at the adiabatic equilibrium of an H_2 -air stoichiometric mixture initially at atmospheric conditions.

	Sc_k	Le_k	Pr
H_2	0.224	0.340	
O_2	0.789	1.197	0.659
H_2O	0.575	0.873	
N_2	0.893	1.355	

of the reactants in the combustion chamber for safety issues. As a result, the composition of the fresh gas can vary between pure fuel and oxidizer and the mixing process can be modeled by the 4S1R without simplifications.

Indeed, the use of real species as ideal gases does not alter noticeably the mixture state with respect to a detailed description, since the major species involved in the process are included and the contribution to the other species to the thermodynamic properties is negligible. Nevertheless, the slight variation of the heat released during the combustion required the calibration of the water vapour formation enthalpy by imposing a constant shift. This correction allows an excellent reproduction of the detailed CJ speed for all the range of compositions at atmospheric conditions (2.19). It is, however, very important to assess whether the constant shift can describe the heat of reaction defect for all the fresh mixture conditions which can be present in the refill region of a RDC due to the choked injectors. The other aspect which has to be verified is the response of the half reaction thickness to the fluctuations of the detonation speed around the CJ value. Both the aspects are discussed in the following.

Detonation states dependence on initial conditions: The post-shock and CJ states in a CJ detonation propagating for a stoichiometric H_2 -air mixture are then evaluated with the 4S1R model using Cantera 2.4.0 [111] with the Shock Detonation Toolbox (SDT) [113] and reported in Figure 2.23 for initial temperature and pressures around the atmospheric condition. The CJ speed and Mach number with respect to the fresh

gas are also calculated with the same tools and shown in Figure 2.24. The maps have to be contrasted to the ones described by the reference detailed mechanism of Boivin et al. [100] shown in Figures 2.12 and 2.13 and the ones obtained with the 2S1R scheme (Figures 2.16, 2.17). Differently from the 2S1R mechanism, the global scheme 4S1R reproduces with an excellent agreement all the post-shock and CJ states as well as the CJ speed for all the range of initial conditions considered, thanks to its accurate thermodynamic description. Even the equilibrium H_2O dissociation, which is favoured at low pressures and higher temperatures, is correctly captured by the scheme, showing that the adoption of a reversible reaction (Eq. 2.36) is important for replicating the behaviour of a detailed model (Figure 2.13). The agreement proves also that the constant shift of the heat released by the reaction constitutes a good correction for describing the dissociation for all the initial conditions of interest. This comparison demonstrates the excellent thermodynamic description of the 4S1R scheme, i.e. the good prediction of the CJ speed, the post-shock and CJ states even when the conditions depart from the atmospheric temperature and pressure, for all the flammable compositions.

Half-reaction thickness: The half-reaction thickness in a 1D steady detonation (ZND model) propagating in an atmospheric H_2 -air mixture at stoichiometric composition, i.e. the calibration point for the pre-exponential constant A of the Arrhenius rate. The detonation velocity is varied around the CJ speed to assess the resulting dependence of the half-reaction thickness. The ZND model for the detonation is solved using Cantera 2.4.0 [111] and the Shock Detonation Toolbox (SDT) [113]. The profiles of the quantities within the detonation front are then processed to extract the half-reaction thickness δ_{half} as the distance between the leading shock and the position where $Y_R = 0.5 \cdot Y_{R,0}$. The results are reported in Figure 2.25 in comparison to the detailed and the 2S1R mechanisms.

The 4S1R scheme outperforms the 2S1R for all the detonation speeds, reproducing the detailed results closely for overdriven conditions ($D \geq$

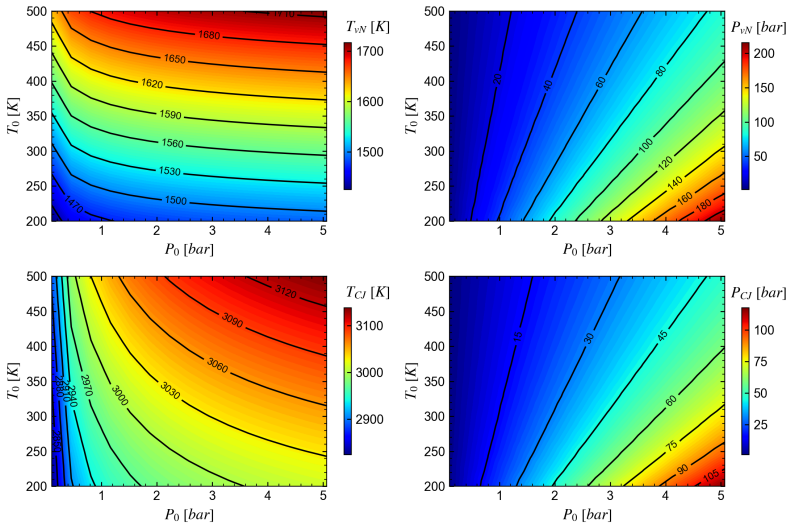


Figure 2.23: Post-shock (vN) and Chapman-Jouguet (CJ) states predicted by the $4S1R$ mechanism for different combinations of initial pressure and temperature.

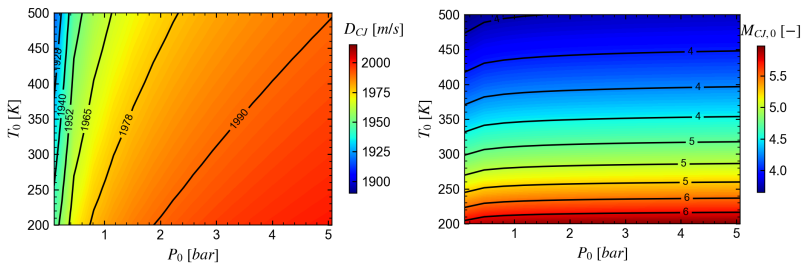


Figure 2.24: Chapman-Jouguet detonation speed (left) and Mach number (right) with respect to fresh gas predicted by the $4S1R$ mechanism for different combinations of initial pressure and temperature.

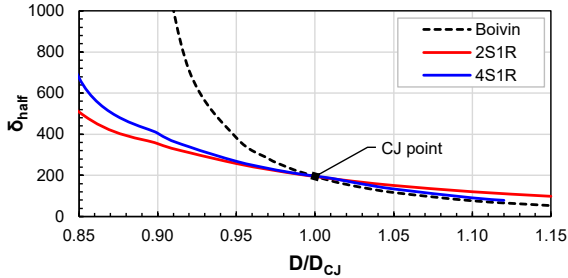


Figure 2.25: Half-reaction thickness as a function of CJ speed obtained through a 1D steady detonation (ZND) model with the 4S1R scheme.

D_{CJ}) where $\delta_{half} < 200 \mu m$. However, for velocities lower than the CJ speed both the single-step mechanisms underestimate the half reaction thickness, showing that it could be an inherent limitation due to the use of a very simple kinetic scheme. This discrepancy with the detailed mechanism could overpredict the stability of the detonation for low speed, since the model would present a shorter reaction zone behind the leading shock. Considering that the half-reaction thickness is also progressively underestimated when the equivalence ratio departs from unity (Figure 2.21), the model has to be used carefully when the δ_{half} is a parameter of interest. Specifically, its accuracy could not be sufficient for very lean or very rich mixtures or when the detonation speed frequently decreases below the CJ speed. It is also worth mentioning that these errors are typically lower than the error due to the spatial discretization in a CFD simulation, since the internal resolution of the detonation front would require 10 – 20 mesh elements ($\Delta_e \approx 20 - 10 \mu m$). Typical LES sizings are around $100 \mu m$, so the approximation of the half-reaction thickness is a second-order error since it represents a sub-grid quantity which would require a dedicated model.

In conclusion, when modelling a hydrogen detonation the 4S1R presents superior performances and a wider applicability range with respect to the 2S1R scheme. Indeed, the use of the 4S1R scheme in CFD simulation requires solving 4 additional transport equations for the species, which

added to the 5 Navier-Stokes equations increase the computational cost of the CFD model by +29% with respect to the 2S1R.

2.3.3 ZND detonation structure

In the previous sections, two single step chemical models for the hydrogen-air detonation were developed. Although they are calibrated to reproduce the initial, post-shock (vN) and CJ states as well as the half-reaction thickness, their prediction in terms of detonation front profiles has to be verified. The detonation structure in this section is determined according to the Zeldovich-von Neumann-Döring (ZND) theory [20, 112] which describes a 1D steady detonation as a non-reactive leading shock compressing and heating the reactants mixture, that explodes thereafter thanks to the radicals released by chain-branching reactions. The ZND detonation structure is calculated using Cantera 2.4.0 [111] and the Shock Detonation Toolbox (SDT) [113] and is reported in Figure 2.26 for the different reaction schemes. The Boivin et al. [100] mechanism is considered as the reference as it is equivalent to other detailed schemes, while the Ma et al. [64] single-step mechanism with two perfect gas species is reported as representative of 2S1R-like (single- γ) schemes adopted in the literature [63, 70, 73, 74].

The main discrepancy with the detailed scheme is due to the impossibility of the single-step schemes to model a proper induction region behind the shock. This is clear from the thermicity $\dot{\sigma}$ profiles which show an immediate reactivity at post-shock conditions, where the detailed model describes the radical formation leading to the explosion. The heat release reflects in a temperature rise starting at the vN state and followed by a drop in density and pressure. The single-step mechanisms evolve similarly since they are both described by an Arrhenius rate and the combustion progresses accordingly. The extent of the reaction zone and the speed of the reaction depends on the pre-exponential constant and activation energy, both higher in the Ma mechanism which thus exhibits a very short reaction zone. All the models then progress toward the CJ plane with the reaction completion and the acceleration of the flow up to the sound

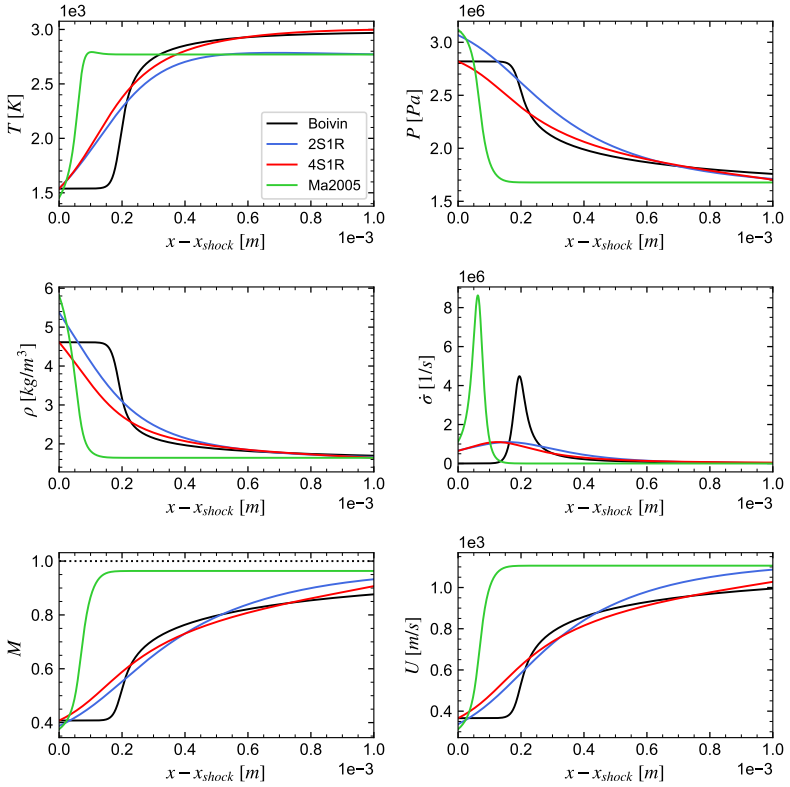


Figure 2.26: 1D detonation profiles (ZND model) for an atmospheric, stoichiometric H_2 -air mixture moving at CJ speed (1975 m/s).

speed. At this point the kinetics plays a secondary role and the state of the mixture is driven by the thermodynamic parameters of each model. The 4S1R detailed description of the species clearly outperforms the other two-species, perfect gas models which underestimate the CJ temperature by roughly 200 K (see Table 2.4).

In conclusion, accepting the intrinsic limitations of a single-step scheme in predicting the induction region, the 4S1R scheme describes with sufficient accuracy the detonation front and thus can be adopted in more complex CFD simulations. Moreover, as pointed out in the previous section, the mesh sizing used for practical Large Eddy Simulations is typically of the same order of the half-reaction thickness, so the discrepancies in Figure 2.26 do not manifest. Rather, the more relaxed gradients of the quantities within the detonation described by the 4S1R induce also fewer numerical problems with respect to the detailed mechanisms on the same mesh grid, and can be discretized with better accuracy by coarse elements. For such reasons and the possibility to describe the reactants mixing, the 4S1R mechanism can be adopted for the simulation of the detonation process in non-premixed RDCs with nearly atmospheric combustion chamber.

2.3.4 Laminar flame speed

Despite the scope of this part is the modeling of the detonation process, it is worth to discuss also the performances of the developed schemes regarding the deflagration regime. The two models presented in Sections 2.3.1.1 and 2.3.2.1 are not calibrated considering the laminar flame speed as a target, so their prediction is purely incidental. Indeed, the optimization of the mechanisms adding the deflagration among the targets would represent a further development of the models, but could also decrease their accuracy in describing the detonation, so its effective improvement will have to be assessed. In the present work, the interest in the deflagration is secondary but yet it cannot be neglected completely, since the rotating detonation involves a contact region between the fresh gas and the products, where a flame is likely to develop. The impact of

the deflagration in realistic configurations involving the 3D, turbulent reactants mixing and high speed jets has still to be determined precisely, but an alteration of the refill region is expected [56], of course depending on the specific configuration.

The reduced mechanisms are then used to solve 1D laminar unstretched flames with Cantera 2.4.0 [111] to evaluate the displacement speed S_d , i.e. the propagation speed of the flame toward the fresh reactants. The results are reported in Figure 2.27 also for the detailed scheme Boivin et al. [100] and the single-step Ma et al. [64].

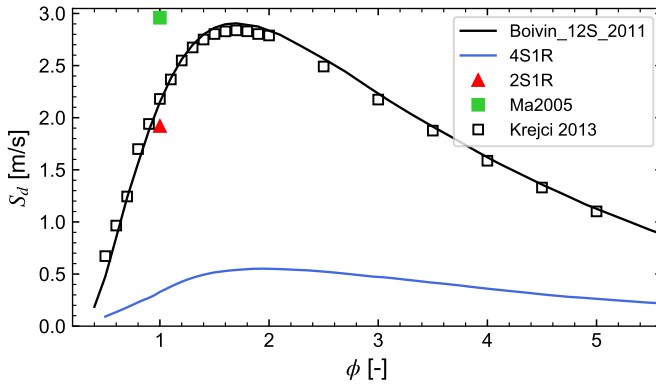


Figure 2.27: Laminar flame speed in an atmospheric H_2 -air mixture for different mechanisms. The white squares are values measured by Krejci et al. [141].

While the detailed scheme captures with good accuracy the values measured by Krejci et al. [141], the other mechanisms present a low accuracy, except the 2S1R which is close to the experiments for the only composition which can describe. The 4S1R mechanism features a peak of laminar flame speed for the correct composition, but underestimates the value by roughly 5 times. Nevertheless, the deflagration speed is not negligible, so the model is still able to reproduce a flame, even with a lower speed than it should have. In a RDC simulation this feature would

reduce the extent of the deflagration with respect to the detonation, so the results should be interpreted considering this aspect and its effects should be assessed.

2.4 Concluding remarks

In this chapter, different chemical models for modeling the detonation process in a H_2 -air mixture were analysed. Several detailed reaction schemes available in the recent literature were selected and tested in the detonation conditions in terms of ignition delay time and contrasted to the experimental measurements. Most of the schemes present coherent and accurate predictions, while others such as the GRI3.0 [95] should be avoided for this type of problems. The best overall agreement with the measurements is achieved by the ELTE [103] optimized mechanism, however, its prediction of the ZND detonation structure and half-reaction thickness presents negligible differences with respect to other mechanisms. Therefore, for the purposes of the present study, the Boivin et al. [100] mechanism is chosen as reference for describing a H_2 -air detonation, due to its accuracy and lighter computational cost. The thermodynamic description of the model is exploited to characterize the dependence of the detonation states, i.e. post-shock and CJ, from the pre-shock conditions, highlighting the impact of the water dissociation on the detonation speed. Building upon the thermodynamic states and reaction zone features predicted by the reference mechanism, two single-step mechanisms are then developed for the conditions of interest, allowing a cost-efficient description of the detonative combustion for the CFD simulations. Specifically, two different schemes are formulated for H_2 -air detonation, namely:

- 2S1R: a single-step scheme with fictive species representing the premixed reactants and products, both modeled with the perfect gas assumption, i.e. $1 - \gamma$ approach. The mechanism can be applied to stoichiometric conditions or recalibrated for other compositions, however, it is suitable for modeling only premixed cases with little variation of the design pre-shock conditions.

- 4S1R: a global scheme with real species modeled as ideal gases with temperature-dependent thermodynamic parameters. The detailed description of the thermodynamic states makes the scheme almost equivalent to a complete mechanism even when the pre-shock conditions depart from the stoichiometric, atmospheric conditions. Nevertheless, the half-reaction thickness accuracy decreases as either the detonation speed falls below the CJ speed or the equivalence ratio is very different from unity. Since the real species are considered, the model can describe the reactants mixing and diffusion without loss of accuracy.

It is worth to remark that both the mechanism are developed specifically for the detonation regime and the deflagration was not a target during the development. As a result, the laminar flame speed of the 2S1R scheme is incidentally accurate for the stoichiometric condition, while the 4S1R mechanism underestimates the values for any composition. Thus, the schemes should be used only when the detonation is the main combustion regime within the application of interest. Adopting the 2S1R scheme in a perfectly premixed RDC would allow also a reasonably good representation of the deflagration regime, provided the use of a turbulent combustion model. On the other hand, a non-premixed RDC imposes the use of 4S1R, which is able to describe the reactants mixing but it is not as accurate for the deflagration as for the detonation regime.

Chapter 3

Analysis of 2D detonation cellular structure

Contents

3.1	Introduction	89
3.2	Numerical setup and methods	91
3.2.1	Frame of reference	91
3.2.2	Computational domain and boundary conditions	93
3.2.3	Models and numerical treatments	95
3.2.4	Detonation initiation procedure	96
3.2.5	Numerical smoked foil extraction method	97
3.3	Results	99
3.3.1	Development of transverse instabilities	100
3.3.2	Effect of the spatial discretization	102
3.3.3	Kinetic schemes validation	114
3.4	Concluding remarks	120

3.1 Introduction

For a long time the researchers considered the detonation a 1D steady phenomenon both for the excellent agreement of Chapman-Jouguet's

speed with the measurements and the lack of advanced instruments able to capture the local details of the front structure [20]. However, by the end of 1950s, novel diagnostics such as smoked foils, piezo-electric transducers and high speed schlieren were introduced and allowed a consistent improvement of the detonation front knowledge, clearly demonstrating its unsteady and multi-dimensional nature. If one-dimensional detonations can exhibit instability only with longitudinal pulsations [115], multi-dimensional detonations are characterized by transverse oscillations constituted by shocks which propagate on the front, determining a very complex, unsteady structure [20, 21, 89]. Parts of the leading shock are accelerating and other decelerating at the same time in different positions of the front, inducing the continuous formation of new transverse shocks and triple points.

The advent of computational fluid dynamics progressively complemented the measurements by providing additional detailed knowledge on the phenomenon. Although the detonation cellular structure has been extensively studied in the past [88, 105, 114, 122, 142–144], the prediction of the cell width still represents a challenge. The unsteady behaviour of the front determines very high local Mach numbers ($< M_{CJ}$), inducing a marked reduction of the half-reaction thickness and the consequent mesh sizing required for a proper discretization [20]. Furthermore, the time-scales associated to the chemical reaction are comparable to the molecular relaxation time behind a shock wave, violating the hypothesis of vibrational equilibrium which is the basis of classical kinetic mechanisms [87, 88]. These modeling complexities, combined with the high uncertainty and subjectivity of the measurements [89], still limit the quantitative validations allowing the assessment of the simulations accuracy. Nevertheless, the qualitative comparison and analysis of the detonation front can be exploited to estimate the fidelity of the numerical model.

In this chapter, the fully compressible AVBP code is used to study the propagation of a 2D detonation in a stoichiometric H_2 -air mixture, initially at atmospheric conditions. The simulations are carried out with the reduced mechanisms 2S1R and 4S1R presented in Sections 2.3.1.1,

2.3.2.1 respectively and provide a validation of their prediction in a more realistic configuration, which allows the development of the detonation front instabilities, i.e. the cellular structure. A specific initiation strategy is adopted to accelerate the development of the front and the process is discussed in detail. Then, the results of the simulations are analysed in terms of post-shock state, detonation speed, half-reaction thickness and cellular structure, which is compared qualitatively with experiments. A dedicated study of the spatial discretization highlights the impact of the front resolution on the wave propagation as the mesh is coarsened, providing essential information for the application of the model to 3D complex configurations, where the mesh requirements cannot overlook the computational costs.

All the simulations performed in this chapter investigate the propagation dynamics and the structure of a detonation in a quiescent atmospheric H_2 -air mixture at stoichiometric conditions. This specific composition is selected not only for its generality, but also because it is the most demanding in terms of spatial discretization, i.e. determines the minimum half-reaction thickness.

3.2 Numerical setup and methods

3.2.1 Frame of reference

In principle, the propagation of a detonation wave can be studied either in a fixed frame of reference or in a relative frame moving at the same speed of the wave, so that the mean detonation position is stationary. For the inherent complexities linked to the hypersonic speed of the wave, most the experiments investigating the detonation structure are carried out in long channels filled with quiescent reactants [23, 136, 145, 146]. On the other hand, stationary detonation waves typically need to be stabilized through bluff bodies, oblique shocks or physical obstacles invested by a supersonic flow [147]. In this configuration, the standing shock wave constitutes a stable leading shock for the detonation, fixing its mean position. The stabilization of a detonation in a supersonic wind tunnel

without using obstacles is impractical both for the highly unsteady nature of the detonation front and its initiation, i.e. the decay from the overdriven conditions to the CJ state, which would require varying the flow speed with extreme accuracy and frequency.

Since the numerical models are not constrained by the measurements difficulties, a free detonation propagation can be replicated either in the fixed or relative frame of reference equivalently. The analysis in the fixed frame models the same dynamics observed during the experiments and requires the imposition of quite simple conditions, mainly related to the wall treatment. However, the detonation can potentially require a long distance to develop completely, inducing a consistent computational cost both in terms of cells and simulated time. The other approach implies the injection of supersonic reactants in the domain, that can be modelled without loss of accuracy, while an unsteady extrapolated outlet condition is required to match the conditions which change in function of the distance from the leading shock [105, 142]. Since the detonation is inherently unstable, both the inlet and outlet conditions have to be adjusted to stabilize the detonation position and provide a realistic rear condition for the hot gas expansion. Nevertheless, the simulation in a relative frame allows to reduce consistently the elements counts, as the domain needs only to extend around the wave. It also is worth to note that using Automatic Mesh Refinement (AMR) algorithms would fill the cost difference between the two approaches, provided that the interest is focused on the detonation wave only, rendering the study in a fixed frame preferable [88].

In the present study, the propagation of a detonation wave in a quiescent, atmospheric, stoichiometric H_2 -air mixture is analysed in the fixed frame of reference with a static mesh, as avoiding the specification of a outlet boundary condition for the hot gas was considered sufficient for compensating the increased computational cost due to the use of a static mesh grid.

3.2.2 Computational domain and boundary conditions

The computational domain for the simulations is a 2D channel of length 1 m and width 0.03 m, extending along the x and the y -direction, respectively. The origin of the coordinate system is placed in the bottom-left corner. The width is chosen to include at least 3 complete detonation cells (3λ), whose measured width is around $\lambda = 8 - 9$ mm [145]. From previous numerical studies, this precaution is needed for reducing the influence of the domain size on the development of the cellular structure [88, 142].

The mesh and the computational domain are represented in Figure 3.1. Since the length needed by the detonation front to fully develop is not

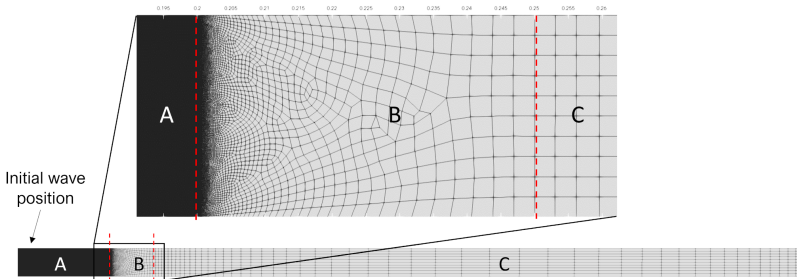


Figure 3.1: Computational grid with the different refinement criteria. A: region of interest, B: buffer region, C: far field.

known *a priori*, a very long channel is considered for the analysis, but only the limited part of interest is finely discretized. This strategy takes advantage of the supersonic nature of the wave, which cannot be perturbed by the quiescent flow ahead of the wave, but also of the peculiarity of CJ condition that, once reached, protects the wave from rear perturbations. According to these considerations, the mesh needs only to be discretized between the shock and the CJ plane position, allowing a discrete relocation of the mesh refinement if the detonation has still to develop. A similar strategy was adopted by [124] for modelling DDT in a long duct. This procedure enables the simulation of the wave up to 1 m by progressively repositioning the refinement and interpolating the solution

on the new mesh. In this study, the length of the refined part is chosen as approximately 20λ , well above the distance between the shock and the CJ plane, in order to reduce the number of the refinement relocations.

As shown in Figure 3.1, the mesh is composed by three different regions:

- A: region of interest, a uniform structured quad mesh (0.2 m long)
- B: buffer region, a mixed quad-tria mesh which allows a fast coarsening from the region A to B without compromising the element quality (0.05 m long)
- C: far field, a quad mesh with elongated elements

The wave propagates from the left to the right hand side, so the mesh represented in Figure 3.1 is suitable only for the first 0.2 m of propagation. Despite the short length, the detonation initiation used for the simulations proved to be very effective in inducing a fast stabilization, so all the results reported in the present work did not require the forward movement of the refined region A. As a consequence, the adopted mesh is exactly the configuration represented in Figure 3.1, with the regions B and C not contributing to the solution.

The region of interest A is discretized with a regular grid of squared elements with increasing lengths, i.e. 10, 30, 50 and 100 μm . The resulting element count and the average timestep are reported in Table 3.1. The element sizings are specifically selected to cover the critical range between an acceptable discretization of the detonation front (approximately $\delta_r = 600 \mu m$ thick using the single-step mechanism, Figure 2.26) and an acceptable sizing for the analysis of practical systems.

The symmetry condition is imposed in all the boundaries of the domain with the exception of the right boundary, where the atmospheric pressure is specified, allowing the detonation to eventually exit the domain. However, the latter boundary does not influence the solution since the wave is supersonic.

Table 3.1: Details of the tested grids.

Δ_e [μm]	Δ_e/δ_{half}	Δ_e/δ_r	Elements	Δt [μs]
10	19.5	60	60 M	0.0016
30	6.5	20	6.7 M	0.0050
50	4	12	2.4 M	0.0080
100	2	6	0.6 M	0.0170

3.2.3 Models and numerical treatments

The analysis is carried out with the AVBP 7.5 code [148, 149] developed by CERFACS and IFPEN by solving the fully compressible, multispecies, reactive Navier-Stokes (NS) equations. The fourth-order in time and third in space Taylor-Galerkin TTG4A scheme [150] is used as convection scheme to ensure a low dissipation error. The explicit time integration is carried out enforcing a maximum CFL number of 0.7, which determines the timesteps reported in 3.1. The dynamic Smagorinsky-Lilly formulation [151] is used for modeling the sub-grid fluctuations. The use of LES instead of DNS was specifically intended to test a numerical setup that can be applied in real devices such as RDCs, where the turbulent flow field imposes the use of LES to handle the turbulent fluctuations. The shock-capturing method proposed by Cook and Cabot [152] is used to improve the accuracy of the model across the shock by reducing over and under-shootings due to the high-order scheme.

The hydrogen-air detonation is modelled using both the 2S1R (Section 2.3.1.1) and the 4S1R (Section 2.3.2.1) single-step schemes. Specifically, for the 2S1R scheme the laminar viscosity of the mixture is specified as a function of the temperature with a power law:

$$\mu = 1.74\text{e-}5 \left(\frac{T}{299.94} \right)^{0.704} \quad (3.1)$$

The species diffusivities are set by imposing the Schmidt numbers for both the species R and P to 0.81 while the Prandtl number is set to 0.66

The transport properties for the 4S1R scheme are set according to

Section 2.3.2.1.

3.2.4 Detonation initiation procedure

The numerical initiation of the detonation is a critical choice since it should not only induce numerical problems, but also avoid the creation of strong fluctuations which can persist during the analysis, delaying the stabilization of the wave, the development of the cellular structure and consequently increasing the time to be simulated. For these reasons, a good guess of the detonation front structure can reduce consistently the initial transient of the simulation, so it should be preferred over Heaviside or hyperbolic tangent profiles.

For all the simulations, the domain is firstly filled with a uniform, stationary H_2 -air stoichiometric mixture at 298 K and 101325 Pa. A 1D detonation (ZND) profile propagating at the CJ speed is solved with Cantera [111] using the mechanism of interest and is linearly interpolated on the mesh and superimposed to the uniform mixture to initiate the detonation along the x -direction. In Figure 3.2 the profiles used for the simulations with the 2S1R mechanism are reported. No transverse velocity component is imposed. Additionally, the x velocity is relaxed to zero within the first 0.2 mm to satisfy the symmetry condition, while no correction is applied on top and bottom symmetries since the interpolated 1D profile does not feature gradients in the transverse direction.

To trigger the onset of the front instabilities and accelerate the development of the cellular structure, the shock plane is staggered by placing the 1D profile at $x = 4$ mm between $8 < y < 20$ mm and at $x = 5$ mm in the remaining part of the channel width (Figure 3.3). The symmetry plane of the receded part is intentionally placed out of the symmetry plane to determine different shock reflections on the top and bottom boundaries, so that the chaotic development of the detonation cells is faster.

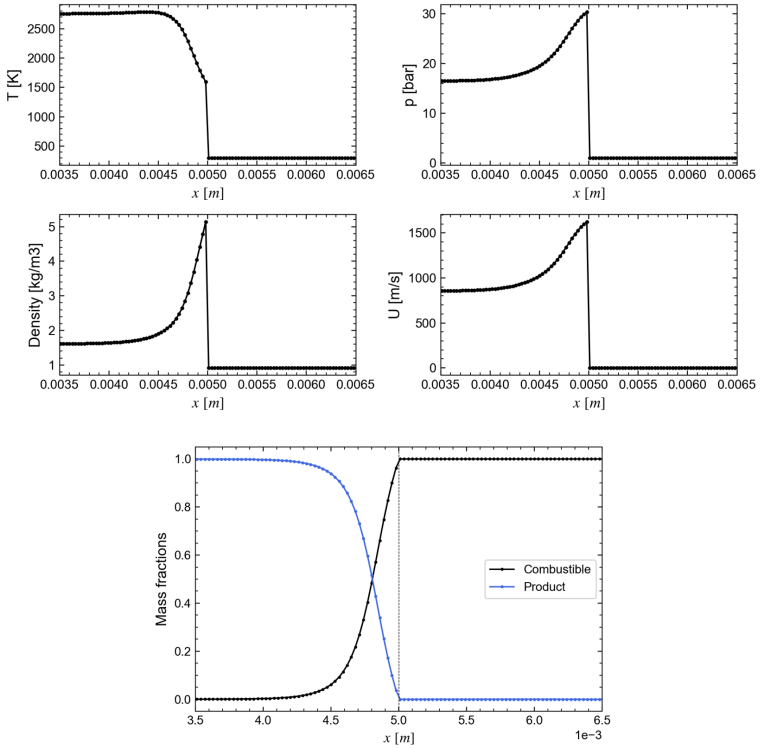


Figure 3.2: 1D detonation profile (CJ speed) used for the initialization (2S1R mechanism).

3.2.5 Numerical smoked foil extraction method

One of the simplest approaches to visualize the detonation cellular structure is the smoked foil or sooted foil records [153]. This technique involves the application of a thin layer of soot on a film which will be directly exposed to the detonation. With the passage of the wave, the soot on the surface is partially removed according to the local pressure: the very high value occurring in the triple points marks the trajectories of the transverse shocks that confine the detonation cells.

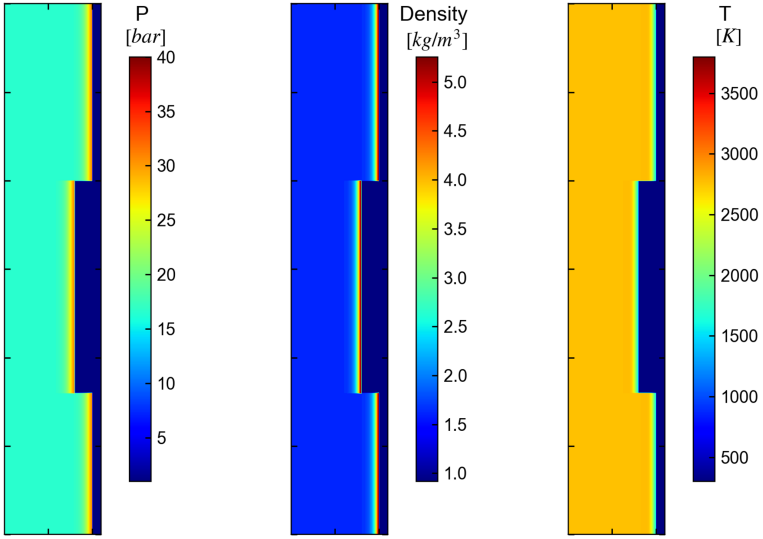


Figure 3.3: Detail of the initial solution showing the staggered 1D detonation profiles (2S1R mechanism).

An equivalent procedure has to be adopted in CFD to trace the position of the stronger pressure peaks as the detonation passes through the domain. Since the pressures reached in the triple points is consistently higher than the pressure reached behind the front shock (vN state) and than every other node, the trajectories can be obtained from the pressure fluctuations normalized with respect to the mean pressure. From the simulations the root mean square pressure P_{rms} is calculated and then normalized to find the quantity S :

$$S = \frac{P_{rms}(x, y)}{P_{rms}^{avg}(x)} \quad (3.2)$$

where:

$$P_{rms} = \sqrt{\overline{P^2} - \bar{P}^2} \quad (3.3)$$

$$P_{rms}^{avg}(x_i) = \frac{1}{N_y} \sum_j^{N_y} P_{rms}^{ij} \quad (3.4)$$

with N_x, N_y being the number of nodes in each direction and $i \in [1, N_x]$, $j \in [1, N_y]$ the progressive indexes of the nodes. The normalization by $P_{rms}^{avg}(y)$ is used to compensate for the different mean pressure which decreases along the length of the channel and is evaluated by averaging the P_{rms} for each x_i position over the equidistributed N_y nodes.

3.3 Results

The numerical setup and procedures described in the previous sections are exploited to perform several simulations of the detonation front propagating in a H_2 -air stoichiometric mixture at atmospheric conditions. The analyses are carried out to investigate two main aspects related to the numerical description of the detonation, specifically:

- The impact of the spatial discretization on global and local features of the wave, when the element sizing does not allow resolving the reaction zone behind the shock.
- The behaviour of the unstable detonation front resulting from the reduced mechanisms 2S1R and 4S1R, assessing the fidelity of the cellular structure with respect to experimental evidences;

At first, the development of the transverse instabilities of the front is reported and discussed, focusing on the first instants after the initial solution described in Section 3.2.4 and evaluating the effectiveness of the initialization in triggering the onset of the instabilities. Then, each aforementioned aspect is studied according to the test matrix in Table 3.2 and presented.

Table 3.2: Summary of the simulations.

Δ_e [μm]	Reaction mech.	Ea/RT_0 [-]	Scheme
10	2S1R	25	TTG4A
30	2S1R	25	TTG4A
50	2S1R	25	TTG4A
100	2S1R	25	TTG4A
30	4S1R	38.8	TTG4A

3.3.1 Development of transverse instabilities

Here the first instants after the initialization are reported and discussed to assess the ability of the initial solution to start the detonation propagation. The analysis is carried out with the 2S1R reaction mechanism and a mesh element size of 10 μm elements using the TTG4A convection scheme.

In Figure 3.4 the instantaneous fields of pressure and temperature are reported to describe the rise of the transverse shocks which origin directly from the initial solution, shown Figure 3.3. The irregular detonation profile that constitutes the initial solution determines the collapse of the edges delimiting the receded part, since the high pressure at the edges is not balanced towards the centre. At the same time, the detonation front moves uniformly at the CJ speed of 1975 m/s, according to the propagation imposed by the 1D profile ($t = 5\text{e-}7$ s). After roughly 2 mm ($t = 1\text{e-}6$ s), two transverse shocks develop in proximity of each edge. The shock (A) propagating toward the internal part of the domain moves on the detonation front with a transverse (vertical) speed of about 1400 m/s, determining the collision with its homologous symmetric shock after 3e-6 s. The high pressure and temperature reached in the collision event give rise to the first detonation cell ($t = 5\text{e-}6$ s, $x_{shock} = 15$ mm), with the front shock exhibiting the typical cyclical behaviour characterised by an acceleration followed by a deceleration [21]. The further collision in (C) at $t = 6\text{e-}6$ s generates another cell but also a new transverse shock (D), following the (C) in direction. At the same time a secondary shock

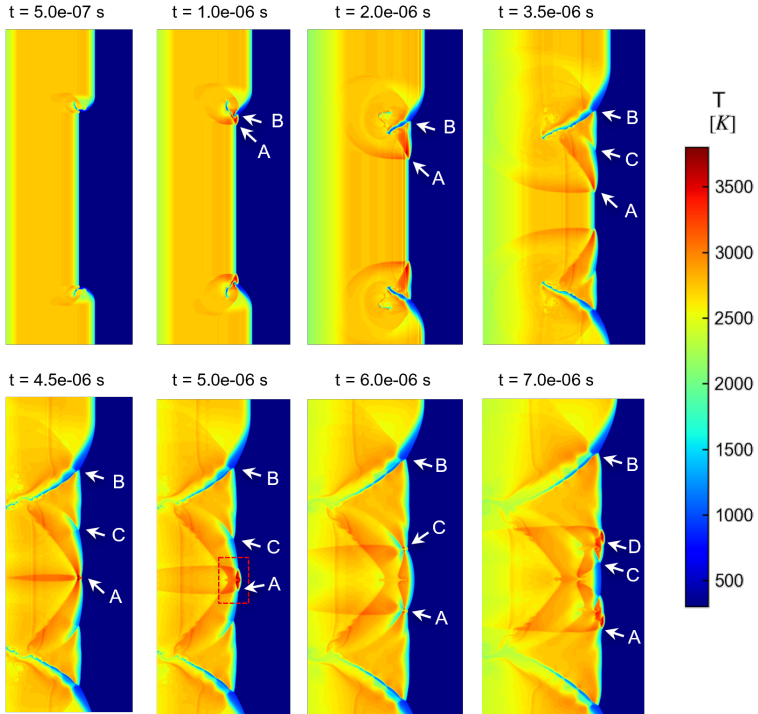


Figure 3.4: Temperature fields showing the formation of transverse instabilities. The white arrows and letters indicate the triple points which originates in the top half part of the domain.

(B) propagates toward the top boundary but its angled direction reduces consistently its vertical speed, delaying its arrival to the boundary. After that, the combination of the shocks collision and reflection establishes a progressive chaotic behaviour with the first complete detonation cells appearing within the 25 mm advance of the front, corresponding to $t = 10 \mu s$. Then, the cell formation fully develops in the next 80 – 90 mm, reaching a stable structure, which is reported in the next sections through the numerical smoked foils.

With respect to a simple ZND profile without recess, the adopted initi-

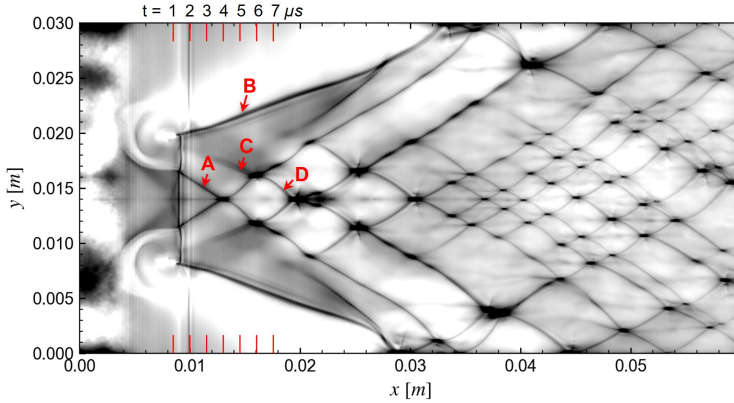


Figure 3.5: Numerical smoked foil during the development of cellular instabilities showing the pressure peaks traces.

ation proved to be very effective in inducing the instabilities in a very short time interval, leading to an overall reduction of the computational effort. The presence of the irregularities in the initial profile could be optimized to further reduce the time required for the cell development, however this is beyond the scope of the present study and all the simulations were initialized with the solution shown in Figure 3.3.

3.3.2 Effect of the spatial discretization

The simulation of the detonative combustion in practical devices imposes the adoption of grids which do not allow resolving the internal reaction zone. Although the detonation speed is not a thermo-diffusive subsonic wave like a deflagration, where the diffusion and the resolved gradients determine the propagation speed, the resolution of the leading shock is still crucial for the prediction of the von-Neumann (vN) state, affecting the induction time and the internal structure of the detonation consequently. Even a partial bypass of this state could potentially affect the propagation dynamics of the whole detonation wave.

It is then necessary to carefully address the impact of the spatial discretization on the detonation to avoid unphysical deteriorations of the model. Indeed, only a model that captures with good accuracy at least the initial and the Chapman-Jouguet (CJ) thermodynamic states, as well as the detonation speed, is suitable for the application to RDCs. With this objective, four different uniform mesh sizings (Table 3.1) are tested and the results are compared to assess the level of inaccuracy coming from a progressive coarsening of spatial resolution.

3.3.2.1 Detonation front structure

The instantaneous structure of the detonation front is reported in Figure 3.6 through the fields of static pressure and temperature for three different mesh sizings. The solutions are representative of the fully-developed cellular structure as they are about 175 mm after initial position.

The detonation front predicted by the simulations shows the typical corrugation due to the coexistence of parts accelerating and others decaying. Several triple points are produced at the intersection of transverse and front shocks, well visible in all the simulations. However, not every element size allows capturing the minor instabilities of the front which originate from the collision of the triple points. Specifically, the 10 μm and 50 μm grids present a comparable degree of front corrugation and transverse shocks, even if the size of the instabilities scales with the element size, confirming the similarity of the resulting smoked foils (Figure 3.7). A further mesh coarsening induces a heavy diffusion of the front, smoothing consistently the weakest transverse shocks and smallest instabilities. With the lack of minor instabilities, the strong transverse shocks which characterize the 100 μm grid are very regular and describe a cellular structure evidently different from the other simulations.

3.3.2.2 Cellular structure

The different behaviour emerging from the instantaneous detonation front structure can be analyzed through the traces of the pressure peaks

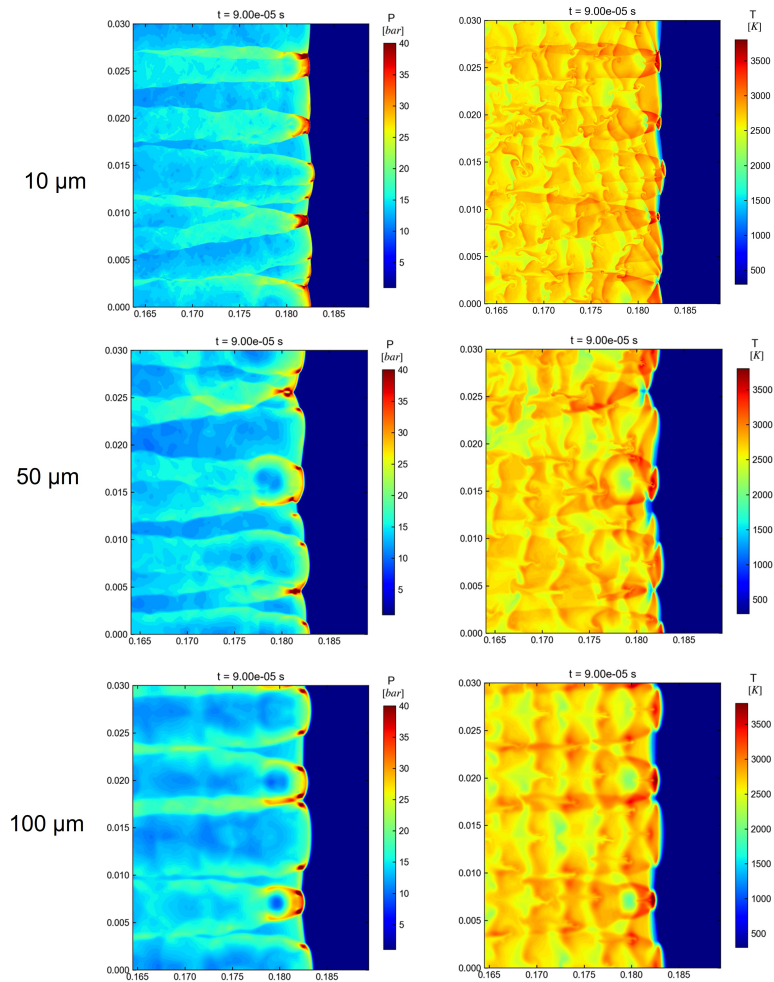


Figure 3.6: Instantaneous detonation front for three mesh sizings (2S1R mechanism).

shown in the numerical smoked foils (Figure 3.7).

Notwithstanding the differences observed in the instantaneous fronts, as the element size is increased the average cell width does not change significantly and ranges between $\lambda = 5-8$ mm. This value is slightly lower than the experimental measurements for the present operating conditions, that registered an average cell width between $\lambda = 8-9$ mm [118, 145]. It is well known that the cellular structure is strictly related to the numerical and chemical model, although, even using detailed schemes and very fine meshes, its prediction is still complex (see Section 3.1). Nevertheless, the accuracy of the prediction is satisfactory for the purposes of the present work and results are comparable to the experimental measurements, as will be shown in Section 3.3.3.

The mesh coarsening is associated with the increasing alteration of the cellular structure. Taking as reference the structure obtained with $\Delta_e = 10 \mu m$, fairly regular for the low activation energy of the mechanism, the cells maintain their structure only increasing in size using wider elements of $\Delta_e = 50 \mu m$. Then with $\Delta_e = 100 \mu m$ the average cell size remains roughly unaltered while their structure is significantly more regular and uniform in size. This is basically due to the suppression of the small transverse shocks for the element coarsening, that in turn induces a reduction of the chaotic behaviour favouring a more regular cell development where only the strongest shock reflections influence the front.

3.3.2.3 Post-shock states

Since the spatial discretization influences also the shock compression of the fresh mixture, it is very interesting to analyse this specific aspect. A clear representation of the post-shock states can be obtained by plotting the thermodynamic state of the unburnt mixture in the pressure-volume diagram, following [88]. This is done in Figure 3.8 by collecting only the nodes with fresh gas over several temporal instants. The frozen post-shock (Hugoniot) line is also represented, marking the vN states relative to a shock speed equal to 75%, 100% and 110% of the CJ speed

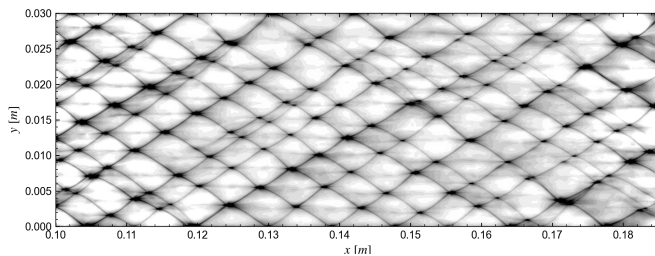
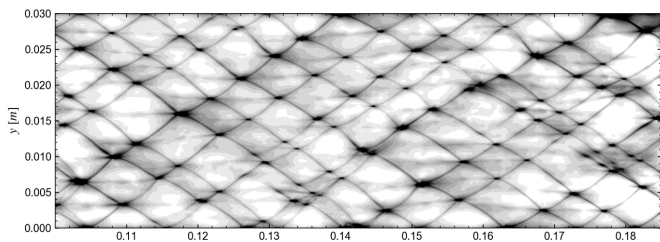
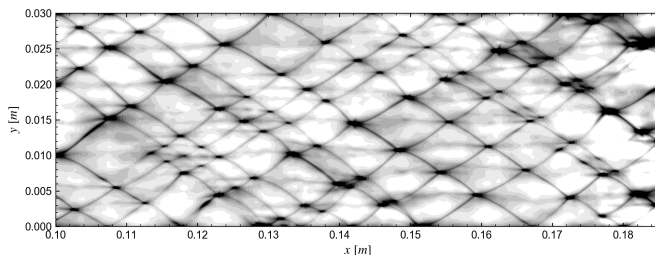
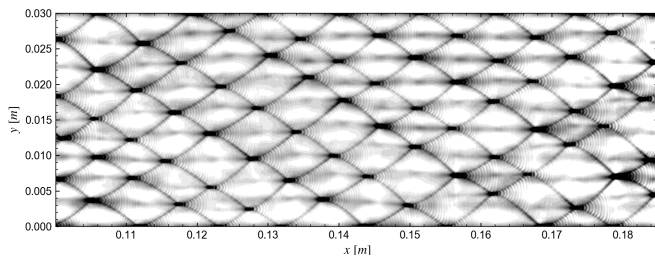
(a) $10 \mu\text{m}$ (b) $30 \mu\text{m}$ (c) $50 \mu\text{m}$ (d) $100 \mu\text{m}$

Figure 3.7: Numerical smoked foils varying the mesh element size.

D_{CJ} , considering the thermodynamic parameters modeled by the 2S1R mechanism. Additionally, the double post-shock states starting from the vN points relative to 75% and 110% D_{CJ} are drawn to mark the conditions of the unburnt mixture after a second compression by transverse shocks.

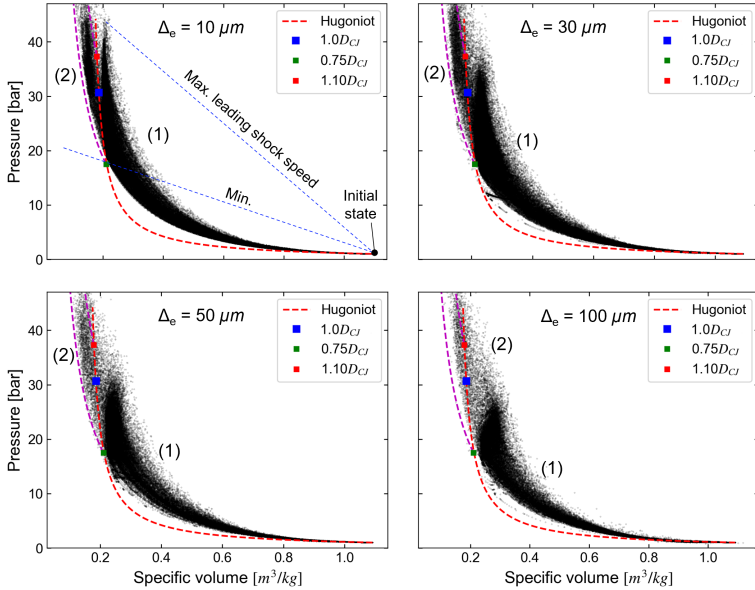


Figure 3.8: Scatter plots of the unburnt mixture state. The red dashed line describes the post-shock points varying the shock speed. The magenta dashed lines are additional post-shock states starting from the post-shock state at 75% and 110% of the CJ speed.

Two clusters of points can be observed in the diagrams of Figure 3.8. Group (1) is constituted by the nodes on the discrete frontal shock which compresses the fresh mixture and represents the CFD thermodynamic trajectory to reach the vN state on the Hugoniot line. The distribution of group (1) is basically determined by the numerical model, as a combination of the effects of the spatial discretization, the convection scheme and the shock-handling method. The maximum density of cluster (1)

represents the post-shock or vN conditions which are actually reached in the simulations and that should lay on the Hugoniot line. Considering the finest mesh, the post-shock state is well captured and is distributed around the vN point (i.e. post-shock relative to a shock moving at CJ speed), showing that the leading shock velocity oscillates around the CJ speed within roughly $\pm 25\%$. Within the detonation front the compressed mixture then reacts and follows a Rayleigh line, with the pressure reducing to the CJ point due to the gas expansion which provides the forward thrust. It is worth noting that since the scatter plot in Figure 3.8 considers only the unreacted mixture, this thermodynamic path is not visible. Despite that, the $50 \mu m$ and $100 \mu m$ grids show that group (1) does not completely reach the vN state on the Hugoniot line, except for low shock speeds ($\simeq 75\% D_{CJ}$). Evidently, the shock is smoothed by the coarsest meshes and the vN peak pressure is partially bypassed, i.e. the shock compresses the mixture to a lower density and temperature. The bypass of vN state is clearly visible from the detonation front profiles extracted for a constant y position, shown in Figure 3.9 against the ZND structure for the same combustible mixture analyzed.

The post-shock gas in group (1) is then eventually further compressed by the transverse shocks, describing the points in the group (2) in Figure 3.8. Indeed, the distribution follows well the double post-shock lines originating from the vN state and indicates a strong dependence on the spatial discretization. The mesh effect on these diagrams is evident and can be partially attributed to the different vN state reached in the simulations: as larger elements progressively smooth the vN peak, the transverse shocks compress a mixture with lower pressure, leading to an reduction of the average maximum temperature and density of the fresh mixture. It also interesting to note that the vN state reached with the $10 \mu m$ element sizing is obtained with the $100 \mu m$ sizing only after the second compression by transverse shocks.

This profound alteration of the detonation structure is expected to be critical for a chemical model which captures the post-shock autoignition of the mixture, as the conditions are heavily impacted by the discretization

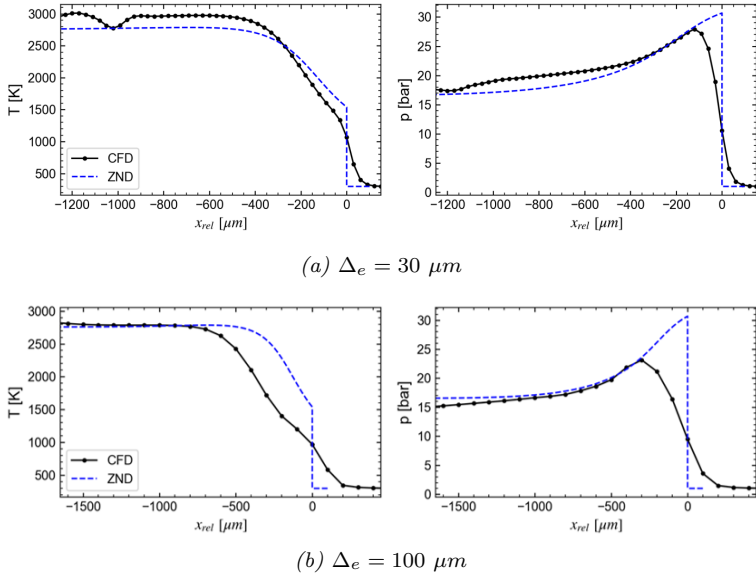


Figure 3.9: Instantaneous detonation profiles along the $y = 4 \text{ mm}$ line. The detonation speeds are 2060 m/s for (a) and 1995 m/s for (b) respectively.

of the leading shock. A coarse mesh induces in average lower values of post-shock temperature that alters significantly the induction time and thus the half reaction length, since the ignition delay time of the mixture decreases rapidly around 1300 K (see Figure 2.9).

As shown in Section 2.3.3 both the two 2S1R and 4S1R mechanisms are not able to describe the autoignition of the mixture which would require the description of the exponential growth of radicals characterising the chain-branching, thermal explosion [89]. Rather, the two reaction mechanisms rely on a single rate basically governed by an Arrhenius rate, leading to an immediate reactivity that increases with the temperature as soon as the post-shock conditions are reached. Therefore a longer half reaction thickness for the meshes with coarse elements can be expected and will be analysed in the next section.

3.3.2.4 Detonation front dynamics

In the previous section it was observed that not all the tested grids allow capturing the theoretical v_N state properly. As a matter of fact, the prediction of the v_N state is usually prohibitive for practical applications where the mesh size cannot be locally refined arbitrarily. A partial or even total bypass of the state is often accepted, but the verification of the wave propagation speed is mandatory to ensure that the global dynamics of the front is not altered.

After the development of the cellular instabilities, the leading shock x position is registered as the location of the maximum pressure gradient to evaluate its propagation speed. The calculation is carried out for multiple constant y sections and the specific results for $y = 4$ mm are reported in Figure 3.10.

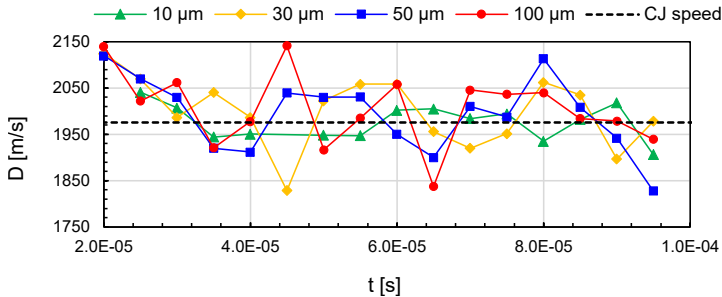


Figure 3.10: Time trends of the leading shock speed at $y = 4$ mm for the different element sizings.

Since only limited differences on the velocity trends are observed varying y position, those results can be assumed as representative of the whole front behavior. The sampling time is $2.5 \mu\text{s}$ so that the value temporal evolution is relative only to major, large and relatively slow fluctuations of the detonation front. Despite the marked differences that arise changing the element size, both considering the front (Figure 3.6) and the v_N state (Figure 3.8), in all the cases the front speed oscillates around the CJ value with an increasing amplitude as the mesh is coarsened. To

characterize the global detonation speed, the time-averaged leading shock speed is then calculated considering several y locations. The results shown in Table 3.3 for all the tested meshes provide a slightly higher value than the CJ speed (D_{CJ}), with a weak dependence on the mesh.

Table 3.3: Average detonation characteristics calculated from the simulations.

Δ_e [μm]	D [m/s]	$D/D_{CJ} - 1$	δ_{half} [μm]	δ_{half}/Δ_e
10	1982	+0.4%	214	21.4
30	1986	+0.6%	274	9.1
50	1986	+0.6%	309	6.2
100	1998	+1.1%	323	3.2

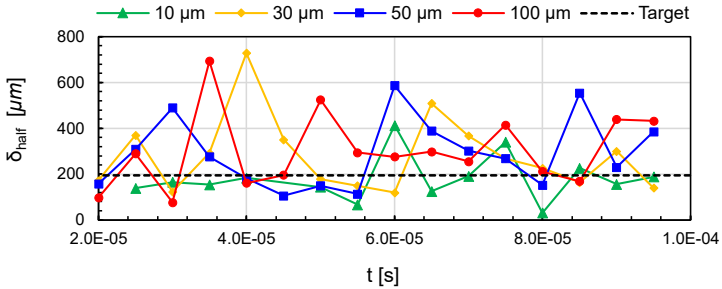


Figure 3.11: Time trends of the half reaction thickness at $y = 4$ mm for the different element sizings.

The good agreement with the CJ speed and the consistency of the results changing the element size shows how the vN state prediction is not essential at least for capturing the global detonation speed within few percentage points of the CJ speed. Nevertheless, the local, fast fluctuations are inevitably lost as the grid is progressively coarsened, and this could potentially affect the propagation in three dimensions and also for channel geometries different than the one of the present study.

The half-reaction thickness δ_{half} is also extracted from the simulations along several y locations and time instants by calculating the distance

between the shock, i.e. the position of the maximum pressure gradient, and the nearest point with $Y_R = 0.5$ on the same y coordinate. It is worth mentioning that the half reaction point is not taken as a nodal value but it is calculated through a linear interpolation to get a positioning error lower than the element size. The values obtained are shown in Table 3.3 and in Figure 3.11 for $y = 4$ mm with respect to the target value $\delta_{half} = 195 \mu\text{m}$ used for the calibration of the mechanism. As expected, the coarsening of the mesh elements induces an increase of the half reaction thickness which is due to the lower post-shock temperature resulting from the partial bypass of the vN state (Figure 3.9).

In a detailed kinetic model, the half-reaction thickness depends on the post-shock conditions which influence the radicals growth and vary according to the unsteadiness of the frontal shock propagation. On the contrary, using the 2S1R single-step model, the half-reaction thickness is rather governed by the temperature only, still determined by the shock compression, so it is interesting to analyze the dependence of δ_{half} on the shock speed. The values calculated from the different grids are represented in Figure 3.12 against the front shock speed. As a reference, the values obtained from the 1D ZND model using both the single-step mechanism (2S1R) and the reference Boivin mechanism [100] are also plotted. It is worth noting that the 2S1R single-step mechanism is calibrated at the CJ point, so its accuracy decreases as the speed deviates from that condition.

The results calculated from the 2D simulations are all distributed around the CJ point, with a higher average δ_{half} than the one predicted with the steady ZND model. This over-prediction and the deviations are again increasing with the element size (Table 3.3, with a relative error of $1 \simeq 2\Delta_e$). However, the simulations show a slight shift toward higher detonation velocities, even if it is limited to +0.8% when the mesh element is doubled. Considering all the grids, the average front features are concentrated around 1989 m/s and 283 μm , with a denser concentration for wave velocities higher than CJ speed. This distribution partially avoids the poor single-step model accuracy for low wave speeds ($\leq 93\%CJ$), leveraging the limited discrepancy with the Boivin mechanism for higher

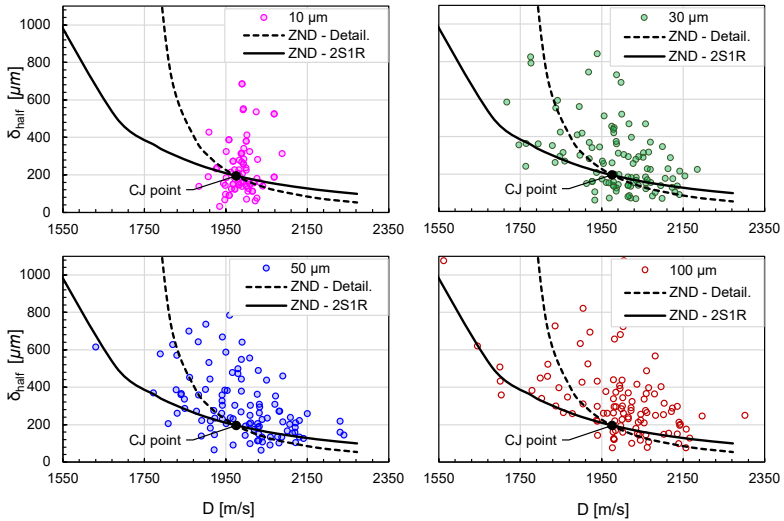


Figure 3.12: Half-reaction thickness as a function of the detonation wave speed for the 2D detonations (points) compared to the results from the 1D steady ZND model (lines) with both the Boivin [100] and the single-step reaction mechanisms.

wave speeds. However, the more intense fluctuations of the front predicted by the coarser meshes determine the occurrence of conditions where the nominal prediction of the half-reaction thickness deviates from the 1D detailed calculations.

In conclusion, the effect of the spatial discretization, as expected, impacts primarily the internal structure of the detonation front, i.e. the half reaction thickness whose prediction is inevitably subjected to the node distance. Nevertheless, the mesh sizing does not influence the average detonation speed, confirming that the wave propagation depends on the thermodynamic properties of the gas rather than the resolution of the internal reaction structure, at least in conditions far from the detonation limits. In a real application like a RDC this feature is of paramount importance since an affordable mesh sizing is typically of the same order

of magnitude as the half reaction thickness, not allowing the complete resolution of the reaction zone. This study suggests that the average detonation speed is essentially independent of the spatial discretization, thus giving confidence also in the results obtained with coarse meshes when the detonation front has a stable propagation. However, this observation cannot be considered universal, especially for mixtures far from stoichiometric or very different channel geometries, where the impact of the unresolved front fluctuations could be determinant for an accurate description. In the literature this was observed specifically for highly unstable detonations [90], which also require the correct characterization of the subgrid turbulent fluctuations and the development of specific models for closing these contributions in applications of interest [89].

3.3.3 Kinetic schemes validation

In the previous section the 2S1R reaction mechanism was exploited to perform a mesh sensitivity of the detonation characteristics, showing a limited dependence on the mesh sizing of the front speed, notwithstanding the increasing bypass of the v_N peak behind the shock. All the observations carried out by varying the mesh element size can be extended to the 4S1R reaction mechanism, without loss of generality. In fact, despite the different number of species and the consequent thermodynamic states between the mechanisms, they are both a single-step schemes which present very similar front profiles and reactivity after the shock compression (Figure 2.26). Both the mechanisms are basically driven by the Arrhenius formulation for the reaction progress, whose effect completely overwhelms the different species diffusion and determines the similar features and dynamics of the detonation front. Therefore, no reason leads to expect a different response to the element size variations with the two kinetic models, and only the mesh with $\Delta_e = 30 \mu m$ is simulated with the 4S1R mechanism to analyse the impact of the reaction mechanism for the same spatial discretization.

An immediate evidence of the similarity of the two reaction mechanisms is provided by the scatter plots of unreacted mixture, reported in Figure 3.13 and collected from the detonation obtained with the $\Delta_e = 30 \mu m$

mesh. The fresh gas reflects only the quantitative differences due to

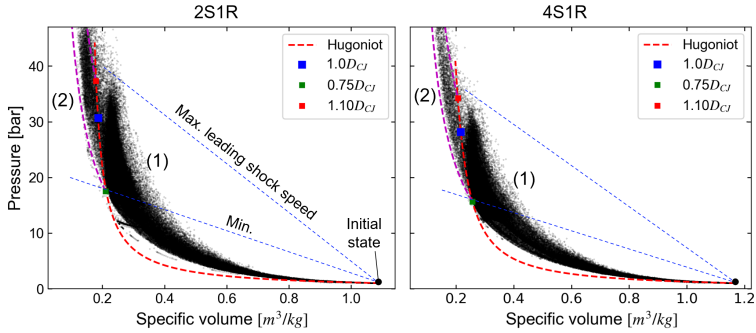


Figure 3.13: Scatter plots of the unburnt mixture state ($\Delta_e = 30 \mu\text{m}$). The red line describes the post-shock points varying the shock speed. The magenta lines are additional post-shock states starting from the post-shock state at 75% and 110% of the CJ speed.

the presence of real species in the 4S1R, which provides more accurate thermodynamic states than the 2S1R mechanism, such as the initial and vN pressure. Besides that, the graphs do not show specific qualitative discrepancies either in the frontal shock (1) or in the transverse shock compression (2), with the latter commonly delimited by the double post-shock lines. It is worth to remark that the qualitative similarity between the mechanism in terms of internal front structure and shock compression does not imply a similar development of the detonation cells, which, for instance, presents a strong dependence on the effective activation energy of the kinetic scheme [142].

In this section, the 2S1R and 4S1R predictions are compared each other but also contrasted to measurements to validate the kinetic models and establish whether the numerical model induces the development of realistic detonation cells. With this objective, the simulation results are processed to extract the cellular structure, the detonation speed and the half-reaction thickness. Specifically, the front speed and the half-reaction thickness δ_{half} are extracted from the simulations along several

y locations and time instants by tracing the position of the leading shock with the maximum pressure gradient and the point where the reactants mass concentration halves with respect to the one in the fresh gas.

The time-averaged values obtained are reported in Table 3.4 beside the experimental measurements performed by Ciccarelli et al. [118] for the same conditions. The experiments confirm the excellent accuracy

Table 3.4: Average detonation characteristics calculated from the simulations ($\Delta_e = 30 \mu\text{m}$) and experiments.

Mechanism	D [m/s]	$D/D_{CJ} - 1$	δ_{half} [μm]	δ_{half}/Δ_e	λ [mm]
2S1R	1986	+0.6%	274	9.1	6
4S1R	1997	+1.1%	268	6.2	4
Exp. [118]	2014	+1.9%			9

of the CJ speed D_{CJ} , which is widely known to capture the detonation speed within few percentage points [20, 23–25], proving again that the CJ speed is a good target for the calibration of the numerical models. Indeed, the two reaction mechanisms 2S1R and 4S1R present very similar predictions of the detonation speed, with the latter approaching the experimental value even if exceeding the $D_{CJ} = 1975$ m/s used for the calibration. On the contrary, the 2S1R respects the same target D_{CJ} with greater accuracy. Nevertheless, the accordance between the average speed extracted from the simulations and the experiments is very good and validates the ability of the numerical model to describe the propagation speed. It is also important to highlight that all the grids tested in the previous section and summarised in Table 3.3 provide a similar degree of accuracy, despite the differences in the cellular structure.

Considering the instantaneous samples of detonation speed obtained from the simulations and shown in Figure 3.14 (top) for a single transverse location, the kinetic schemes feature again similar oscillations around the average value, with the 2S1R mechanism reaching slightly lower minimum values of velocity. Both the mechanisms are also aligned in the values of the half-reaction thickness which is reported in Figure 3.14 (bottom)

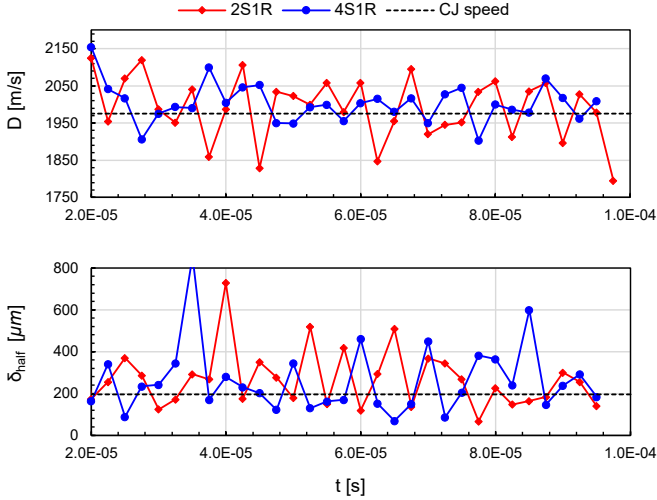


Figure 3.14: Time trends of the detonation speed (top) and half reaction thickness (bottom) at $y = 4$ mm for the different reaction mechanisms.

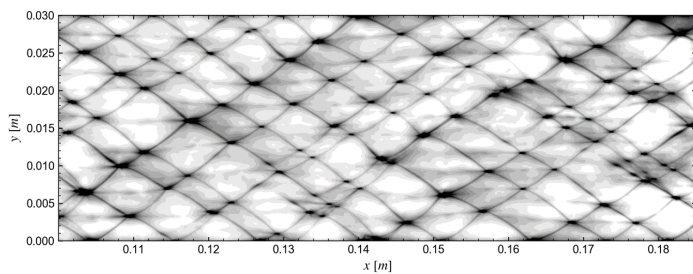
beside the target value of $\delta_{half} = 195 \mu m$ predicted by the ZND model and used for the calibration of the mechanisms. The oscillations of half-reaction thickness are concentrated above the average value of roughly $270 \mu m$, showing eventual dilatations of the reaction front always followed by a recovery, which reduces the distance between the shock and the half-reaction point. This perturbation-stabilization process appears very similar and stable for both the mechanisms.

3.3.3.1 Detonation cells

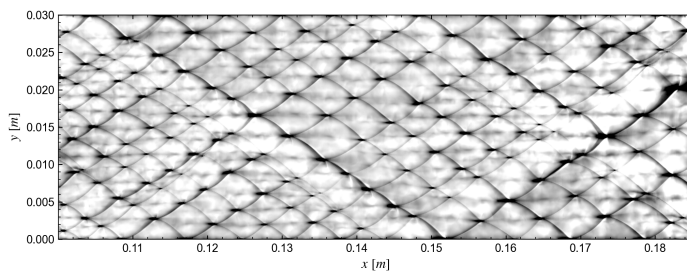
Although the 4S1R and 2S1R mechanisms proved to be equivalent in the prediction of the detonation speed and half reaction thickness, they present differences in the detonation cellular structure. The smoked foils evaluated from the simulations using the procedure described in Section 3.2.5 are reported in Figure 3.15 and compared to the experimental foil obtained by Bull et al. [23]. It is worth to note that the smoked foil

was obtained for a slightly lower pressure than the simulations ($p = 0.961$ atm) and that the researchers reported only the cell length of 15.9 ± 2 mm rather than the cell width, which can be estimated approximately between $\lambda = 10 - 12$ mm. This value is some millimeters above the more recent measurements of Ciccarelli et al. [118, 145] used in Table 3.4, probably for the different pressure and experimental setup, but unfortunately the photographs of the smoked foils were not published. For this reason the reference value of the cell width is taken as $\lambda = 9$ mm while the smoked foil in Figure 3.15 (c) is considered from a qualitative point of view.

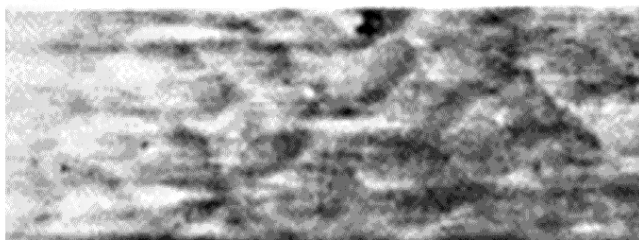
Both the mechanisms predict a moderately regular cellular structure, with an average cell width of $\lambda = 6$ mm for the 2S1R mechanism and $\lambda = 4$ mm for the 2S1R mechanism. Although both the values are lower than the experimental reference, the structure of the cells appears realistic when considering the slightly elongated diamond shape and their stacking. Despite the fact that the results confirm the good performances of the two reaction mechanisms, they also show how the numerical prediction of the cell size is still controversial, meaning that models with strong simplifications as the ones tested in this work can eventually outperform highly detailed approaches. For instance it is interesting to mention the numerical results obtained by Taylor et al. [88] by solving the Euler equations coupled with the 8 species, 27 reactions Burke et al. [101] mechanism. Although the adaptive mesh refinement allowed element sizings up to $2.4 \mu\text{m}$, the cell width predicted by the simulations was only around $\lambda = 2 - 3$ mm, with a consistent underestimation. The authors attribute the discrepancy to the hypothesis of thermochemical equilibrium underlying the reaction mechanisms, which is not achieved in the chemical time-scales involved in a detonation. Thus, it is clear that this is an open problem and further studies are needed to propose new solutions to describe the physics better but also enable a cost-efficient analysis for practical systems.



(a) 2S1R mechanism



(b) 4S1R mechanism



(c) Experimental smoked foil [23]

Figure 3.15: Numerical smoked foils (a,b) obtained with two different kinetic mechanisms ($\Delta_e = 30 \mu\text{m}$) and experimental smoked foil (c) for a stoichiometric H_2 -air mixture at $p=0.961 \text{ atm}$ [23] (the image has been cropped and resized to match the scale of the numerical results).

3.3.3.2 Discussion of results

Considering only the accuracy of predicting the average detonation speed and cell width, summarised in Table 3.4, one could argue that the 2S1R mechanism performs better than the 4S1R scheme, notwithstanding its greater simplicity. Indeed, for these specific conditions the cell width described by the 2S1R scheme is more accurate than the one with the 4S1R. However, it is of paramount importance to remember that the fictive species adopted by the 2S1R model, in conjunction with its single- γ description of the thermodynamic parameters, induce inaccuracies, for instance, in the fresh gas state and the equilibrium temperature, which can reduce significantly the relevance for engineering applications (Section 2.3.1). On the other hand, the 4S1R mechanism features very realistic thermodynamic states, whose improvement can be observed easily from the instantaneous fields of pressure and temperatures reported in Figure 3.16.

Up to this point all the discussion was carried out considering a perfectly premixed case, but it is worth to highlight again that the 4S1R scheme is also able to model the mixing of the reactants and is a forced choice with non-premixed or partially-premixed mixtures. In conclusion, both the performances of the 2S1R and 4S1R mechanisms are satisfactory for the purpose of the present study and provide the basis for their application to more complex configurations as a rotating detonation combustor. Since the scope is the analysis of a non-premixed RDC, the next investigations will be carried out using the 4S1R global scheme.

3.4 Concluding remarks

In this chapter, the fully compressible Navier-Stokes equations are solved with AVBP code for studying the propagation of a 2D detonation in a stoichiometric H_2 -air mixture initially in atmospheric conditions. The simulations are analysed in detail by calculating the detonation speed, half-reaction thickness and cellular structure. Specific investigations of the impact of both the spatial discretization and the reaction scheme are

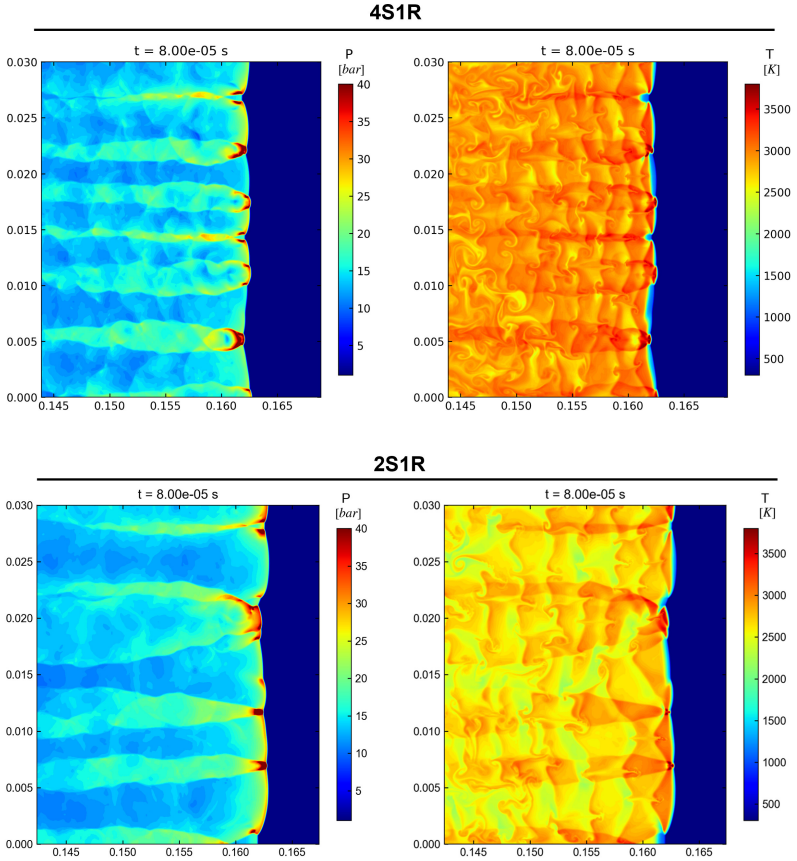


Figure 3.16: Instantaneous detonation front for the two mechanisms *4S1R* (top row) and *2S1R* (bottom row).

carried out and discussed. Despite the two-dimensions, the case configuration is sufficiently realistic to allow the comparison with experimental measurements and validate the results.

The main outcomes of the study can be summarised as follows:

- The detonation cell size does not change significantly increasing

the element size, ranging between $\lambda = 5 - 8$ mm for the 2S1R mechanism. However, the cellular structure is much more regular with coarse elements, due to the numerical diffusion of the minor transverse shocks.

- When the grid refinement is decreased, the von-Neumann state is partially bypassed with the $50 \mu\text{m}$ ($\Delta_e/\delta_{half} = 4$) and $100 \mu\text{m}$ ($\Delta_e/\delta_{half} = 2$) elements, inducing inaccuracies in the gas conditions just before reacting.
- Despite the differences in the post-shock state prediction, the average detonation speed is marginally affected by the element size, deviating of a maximum +1.1% with respect to the nominal CJ speed, both using the 4S1R and 2S1R schemes. However, the amplitude of the major fluctuations slightly increases with a lower spatial resolution.
- Both the 2S1R and 4S1R mechanisms are accurate in the description of the detonation speed, with maximum deviations of few percentage points with respect to the experimental measurements.
- The two reaction mechanisms provide equivalent values of detonation speed and half-reaction thickness, while they differentiate in the cell size, with the 4S1R scheme predicting narrower cells. With respect to the experimental measurements, the cell width is always underestimated, but the qualitative shape appears to be captured.

In conclusion, the analysis confirms that the numerical model and the reduced kinetic schemes are suitable for the simulation of multi-dimensional H_2 -air detonation, with a limited degeneration of the performances when the element size does not allow to resolve completely the reaction zone. This finding is of great interest since the element size adopted in real configurations is usually larger or similar to the half-reaction thickness, so the present study ensures that no unexpected behaviour is exhibited by the numerical model with coarse meshes.

Part II

Rotating Detonation Combustor Analysis

Chapter 4

TU Berlin RDC numerical model

Contents

4.1	Description of the test rig	126
4.1.1	Instrumentation	129
4.1.2	Operating modes	130
4.1.3	Investigated test point	131
4.2	Numerical model	133
4.2.1	Computational domain	133
4.2.2	Simulation strategy	136
4.2.3	Spatial discretization	136
4.2.4	Boundary conditions	137
4.2.5	Numerical models	138
4.2.6	Detonation initiation	139
4.2.7	Computational demand	142

In this chapter, the numerical model of the Rotating Detonation Combustor installed at Technische Universität (TU) Berlin is presented, focusing on the geometric configuration investigated in the work. At the begin of the chapter a brief background on the test rig is reported, focusing on the influence of the main operating parameters on the wave modes. Then, each aspect of the numerical model is described in detail, discussing the simulations setup and the approach to the problem. The

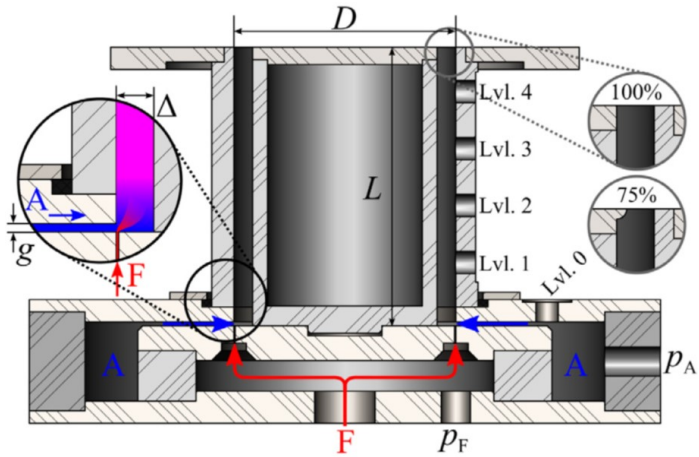
results of the numerical analyses concerning both the non-reactive flushing of the rig and the reactive operation are presented in the next chapters.

4.1 Description of the test rig

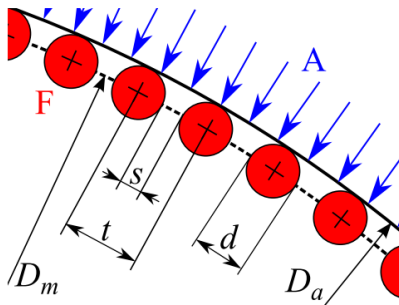
The present study is focused on the modular RDC installed at TU Berlin [49], reported in Figures 4.1, 4.2. The combustor is based on a down-scaling of the US Air Force Research Lab (AFRL) geometry [154] featuring a radially-inward air injection [18, 47]. The rig is entirely realised by machined stainless steel and is highly modular, with the possibility to change the fuel, air and restrictor plates, thus altering the respective geometric features. For instance, different outlet restrictions, air gap heights and fuel injectors configurations can be obtained [48, 55]. The combustor usually works with choked air injection, occurring at the exit of the air slot, i.e. at the connection to the chamber, since the air gap height is constant.

The specific configuration analysed in this work presents an annular combustion chamber of $L = 110$ mm with an internal radius of $r_i = 37.4$ mm and an external radius of $r_o = 45$ mm, directly discharging into the atmosphere without any outlet restriction. The chamber is fed with the separate injection of hydrogen and air through, respectively, $N = 100$ axial injectors positioned at the base of the chamber and a gap along the outer wall with height $g = 1.21$ mm, which realizes a radially-inward cross-flow for the hydrogen jets (Figure 4.1). The fuel injectors are constituted by equispaced ($\Delta\theta_{inj} = 3.6$ deg) straight channels with a diameter of $d = 0.5$ mm (machining tolerance ± 0.05 mm [18]) and are positioned tangentially to the outer radius of the chamber, as represented in Figure 4.1 (b). The chamber annulus width of 7.6 mm is not varied from the AFRL design and guarantees the stability of the detonation propagation despite it is of the same order of magnitude of the critical annulus dimension registered in previous studies [18, 155]. The parameters of the geometric configuration considered in the present work are summarised in Table 4.1.

Both the air gap and the injectors are directly connected to the



(a) Cross-section of the test rig. Adapted from [48].



(b) Injectors scheme. Adapted from [48]

Figure 4.1: Schematics of the TU Berlin RDC test rig.

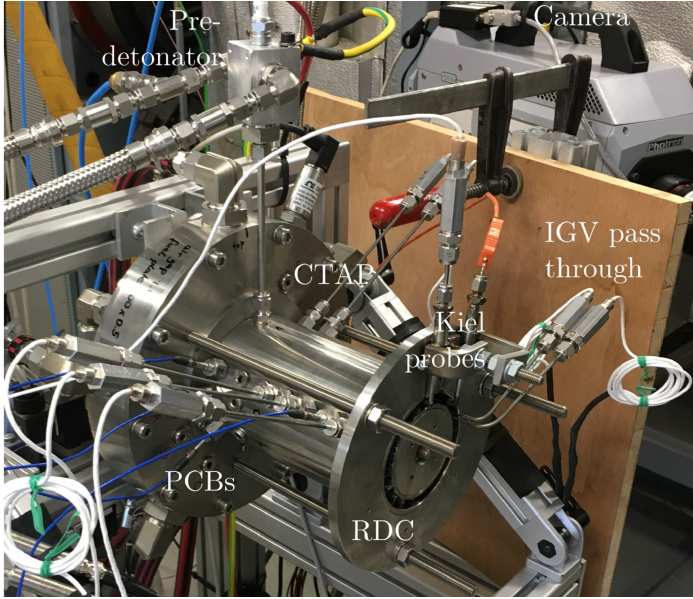


Figure 4.2: Picture of the test rig with the instrumentation [55].

respective plena and the mass flow rates are controlled by using a system of sonic nozzles and pressure sensors (semi-conductor strain gauge relative sensors), specifically developed for the combustor [18].

The detonation wave is typically initiated through the use of a predetonator (Figure 4.2) connected to base of the chamber. In the predetonator a stoichiometric mixture of hydrogen-air is ignited with a spark plug and then is subjected to DDT without the use of any promoter. The initiation using the predetonator results in a robust and reliable start of the combustor. The RDC is also equipped with a spark plug on the outer wall which allows a simpler ignition, but effective only for low mass flow rates [18].

Table 4.1: Geometric dimensions of the configuration analysed.

Inner annulus diameter (D_i)	mm	90
Outer annulus diameter (D)	mm	74.8
Annulus width (Δ)	mm	7.6
Mean perimeter (P_m)	mm	258.9
Fuel injectors diameter (d)	mm	0.5
Fuel injectors axis diameter (D_m)	mm	89.5
Fuel injectors number (N)	–	100
Air gap height (g)	mm	1.214
Chamber length (L)	mm	110
Annulus area (A_{cc})	mm ²	1967.39
Fuel injectors area (A_f)	mm ²	19.63
Air gap throat area (A_a)	mm ²	343.25
Air gap to annulus area ratio (A_a/A_{cc})	–	0.174

4.1.1 Instrumentation

Several sensor ports are present in the rig (Figure 4.1) and are distributed in the plena (p_A , p_F), in the air top plate (Lvl. 0, $D = 164$ mm) and in the chamber outer wall at different axial locations (Lvl. 1 – 4). In these locations, relative or absolute dynamic piezo-electric pressure sensors with a resonance frequency of 200 kHz are used with different adapters to reduce the damage due to the hot gas environment [18]. The static pressure can be measured in the chamber by connecting the absolute pressure sensors specific adapters according to the Capillary Tube Attenuated Pressure (CTAP) method. In addition to those sensors, a L-shaped Kiel probe positioned 2 mm upstream the outlet section of the combustion chamber is also used to measure the time-averaged value of total pressure and evaluate the pressure gain of the device [49, 156].

Finally, a high-speed camera (87500 frames per second) captures the visible luminosity emitted by the hot gas and exiting the chamber outlet and reflected through a mirror. The camera recordings allow a direct visualization of the wave propagation and are particularly useful for the analysis complex wave configurations, although the exposure of $8.75 \mu s$

combined with the line-of-sight integration consistently reduce the details which can be observed [47].

4.1.2 Operating modes

The RDC described in the previous section has been widely investigated through experiments during the last few years. One of the most interesting aspects which was encountered is the variety of operating modes exhibited by the device depending on the mass flux, the injector loss (A_a/A_{cc}) and the outlet section restriction (A_e/A_{cc}). Specifically, the main combustion modes which were observed increasing the mass flow rate were the following [48, 49] (Figure 4.3):

- Two counter-rotating waves at equal speed (2CR): occurring at the lowest mass fluxes and characterised by a low speed of propagation, so that they could represent choked deflagration fronts and not detonations;
- Single wave with counter-rotating secondary components (SWCC): represents the progression of 2CR when the mass flow rate is increased, with one of the two waves being stronger than the other one;
- Dominant single wave (SW): usually the prosecution of SWCC with a further increase of mass flux, when a single wave without secondary components is present in the chamber, propagating faster than the previous modes;
- Two pairs of counter-rotating waves (4CR): this mode could represent a transition between SW and two single co-rotating waves, which would require a mass flow rate beyond the capabilities of the rig;
- Axially pulsating combustion (L): characterised by a fast pulsation in axial direction, while no tangential propagation is registered. This mode is attained only for some combinations of operating conditions and geometries.

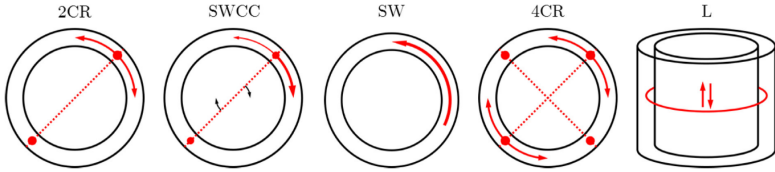


Figure 4.3: Representation of the different wave modes observed experimentally [49].

As reported by Bach et al. [49], the typical transition 2CR to SW through the SWCC mode is aligned with the choking mass flow rate of the outlet section of the chamber, connected with an increased pressure in the chamber and a stronger detonation, reaching speeds up to 80% CJ. In fact, the SW regime allows generally a faster wave propagation than what is achieved in other modes.

When an outlet restriction is added to the chamber (see Figure 4.1), the lower choking mass flow rate anticipates the transition to the SW mode. The impact of the outlet restrictions is also determinant in reducing the overall pressure loss through the device (i.e. $PG = p_{0,e}/p_{0,a} - 1$ [49]), as the higher pressure gain in the chamber tends to compensate the pressure drop due to the injectors. In general, the pressure gain of the device is promoted by either an outlet restriction or the use of injectors with lower loss (higher A_a/A_{cc}), although they can determine, if combined, the rise of longitudinal mode pulsations [49] or even acoustic fluctuations in the air plenum around 1 kHz. Notwithstanding these operational limitations, the maximum pressure gain of $PG = -8\%$ was measured at around 300 kg/s, low-loss injectors ($A_a/A_{cc} = 0.460$) and 50% outlet area restriction [156].

4.1.3 Investigated test point

The RDC configuration described in Section 4.1 is investigated numerically in a stoichiometric, dominant single-wave operating condition, reported in Table 4.2.

Table 4.2: Main operating conditions of the analysed test point.

		Cold case	Reactive case
Air manifold pressure	<i>bar(a)</i>	6.75	7.42
Fuel manifold pressure	<i>bar(a)</i>	13.19	13.12
Air temperature	<i>K</i>	291	291
Fuel temperature	<i>K</i>	289	289
Air \dot{m}_{is}	<i>g/s</i>	549.0	554.9
Fuel \dot{m}_{is}	<i>g/s</i>	16.22	16.13
Chamber mass flux	<i>kg/m²s</i>	287	290
Equivalence ratio	–	1.01	0.99
Wave mode	–	–	Single wave
Wave frequency	<i>Hz</i>	–	6287
Wave speed ωr_o	<i>m/s</i>	–	1778
Pressure gain	%	–	–58

The experimental test usually consists of a first cold flushing of the combustor lasting roughly 50 ms, when the mass flow rate is set to the desired value, followed by the subsequent reactive condition. The combustor is ignited and the detonation wave stabilizes rapidly in the chamber, so that the complete test can be carried out over few hundreds of milliseconds. During the reactive condition the mass flow rate is held constant through the mass flow controller, so that the high-pressure determined by the detonation wave is reflected in a lower effective area of the air gap, while the fuel shows a negligible sensitivity to the detonation. As a consequence, the air plenum pressure rises to compensate the detonation blockage (Table 4.2) Since the injector passages are choked, the isentropic mass flow rates are calculated as:

$$\dot{m}_{is} = \frac{Ap_0}{\sqrt{T_0}} \sqrt{\frac{\gamma}{R_{\text{gas}}}} \left(\frac{\gamma + 1}{2} \right)^{-\frac{\gamma+1}{2(\gamma-1)}} \quad (4.1)$$

Thus, the detonation blockage on the air gap can be expressed by

considering the variations between the cold and reactive conditions:

$$\frac{A^R}{A^C} = \left(\frac{\dot{m}_{is}}{p_0} \right)_R \cdot \left(\frac{p_0}{\dot{m}_{is}} \right)_C = 0.92 \quad (4.2)$$

On the other hand, a fuel blockage is not evident, probably due to the geometrical configuration and the high pressure drop across the small fuel channels.

As reported in Table 4.2, the detonation stabilizes in a single, dominant wave, i.e. the SW mode in Figure 4.3, since the mass flux is sufficiently high to choke the outlet section of the chamber. In this mode, the wave speed at half span is relatively high (1627 m/s), reaching 82% of the CJ speed, considering a stoichiometric H_2 -air mixture ($D_{CJ} = 1975$ m/s). However, the combination of no outlet restriction and high-loss air injector is particularly detrimental for the overall pressure gain $PG = p_{0,e}/p_{0,a} - 1$ of the present configuration, which achieves a value of -58% according to the measurements carried out by Bach et al. [156].

4.2 Numerical model

In this section, the details about the numerical model developed for investigating the TU Berlin RDC are presented.

4.2.1 Computational domain

The complete fluid domain of the RDC in Figure 4.1 is considered for the numerical analysis, including the full injection system constituted by the air gap, the 100 fuel channels and the respective feeding plena. Although the choice of modelling the injector consistently increases the computational cost of the whole model as well as its complexity, it enables the accurate description of the reactants mixing. A previous URANS study [157] focused on the non-reactive mixing of a single hydrogen jet in the TUB RDC revealed that the flow field near the injectors is constituted by a complex shock structure, due to the supersonic jet in cross-flow configuration. Capturing these features is fundamental for the

whole operation of the combustor, since the reactant injection determines not only the mixture which detonates, but also the turbulent flow field characteristics in the refill region, that are likely to impact the detonation front. Moreover, the inclusion of the injectors and the plena allows a detailed description of the interaction between the detonation and the feeding ducts, avoiding the adoption of simplified micro-nozzles models which can be justified only in premixed configurations [65, 79].

No considerable modifications are adopted for the fluid domain with respect to the test rig, except for the plena feeding pipes which are removed and replaced by a uniform axial inlet at the base of each plenum. The edges of the air gap and fuel channels outlets, which can influence significantly the flow field, are reproduced on the base of the nominal geometry, i.e. using sharp edges, thus neglecting the eventual smoothing due to exposure to the high temperature and pressure environment. The presence of the sensor ports is completely neglected in the model, as well as the presence of the predetonator tube connected to the outer wall of the chamber. Finally, since the configuration studied here does not feature outlet restrictions and is expected to be choked at the outlet, the model does not include a discharge plenum at the outlet for modelling the laboratory atmosphere. Previous studies on other RDCs [158] showed that the addition of an exhaust plenum determines only a minimal variation on the flow field and performances, only slightly altering the flow at the exit plane. The use of a mixed subsonic-supersonic outlet boundary condition, as done here, is then considered an excellent description of the combustor discharge and avoids the use of an exit plenum.

4.2.1.1 Coordinate systems and main sections of interest

The global cartesian coordinate system (x, y, z) is aligned with the combustor so that the axis of the combustor lies along the y coordinate and the $x - z$ plane coincides with the base of the chamber and air gap, i.e. the top of the fuel plate. For the analysis of the results, also a cylindrical

coordinate system (θ, r, y) is adopted, using the following transformations:

$$r = \sqrt{z^2 + x^2} \quad (4.3)$$

$$\theta = \arctan\left(\frac{x}{z}\right) \in [0, 2\pi] \quad (4.4)$$

The resulting cylindrical coordinate system is thus aligned with the axis y of the combustor with the zero angular position corresponding to the z, y plane and increasing in the counter-clockwise direction observing the combustor from the outlet (Figure 4.4).

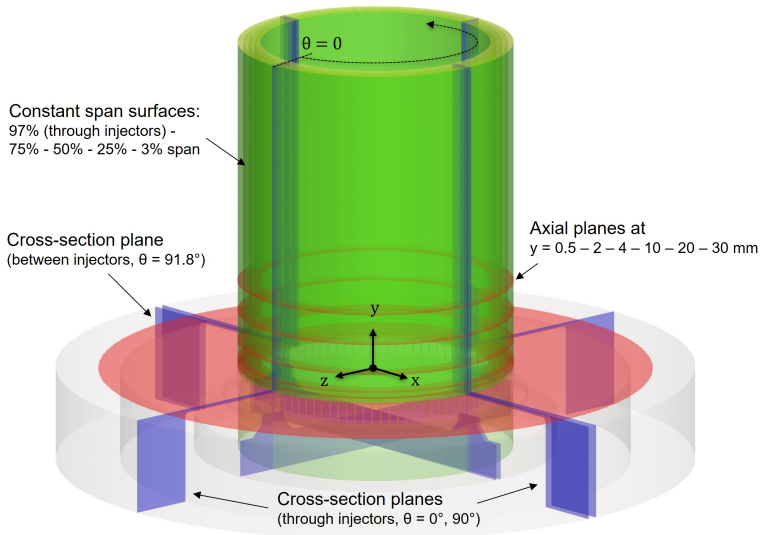


Figure 4.4: Schematic of the coordinate systems and sections of interest within the domain.

The complete 3D domain is analysed in several sections of interest, which are represented in Figure 4.4. For simplifying the analysis of the cylindrical constant-span sections, in the results they will be reported as flattened $\theta - y$ periodic surfaces.

4.2.2 Simulation strategy

Although the modeling of the injectors allows a proper description of the reactants mixing, it also introduces an additional part of the domain which has to be correctly initialized well before the mixture ignition. This is particularly critical considering the extreme speed of the wave which has to be immediately and continuously fed with fresh reactants, so the injectors must be already refilling the combustion chamber at full capacity when the detonation is present in the system, as there would be no time for their stabilization. As a consequence, the numerical simulation has to reproduce the steps of experimental test, with a preliminary cold flushing of the combustor to initialize primarily the flow field in the injectors. Only after this step the detonation wave can be initiated, so that after an initial stabilization the system reaches eventually the stationary operation.

For this reason, the reactive case in Table 4.2 of the RDC is simulated only after a preliminary non-reactive flushing. The cold flow is simulated for a physical time of 2 ms, roughly equivalent to 6 flow-through times of the chamber. Then, the detonation is initiated and the simulation is carried out for additional 2.5 ms, corresponding to about 25 revolutions of the wave. The fast stabilization of the detonation is due to the peculiar initiation procedure which emulates the basic flow field of a 2D RDC and will be presented in Section 4.2.6. Despite the focus of the present work is on the reactive case, the preliminary cold flushing is also presented and discussed in Section 5.

4.2.3 Spatial discretization

The fluid domain described in Section 4.2.1 is discretized in a pure tetrahedral mesh constituted by 178 million elements and 31 million nodes, adopting specific refinements of the sizing in the regions of surrounding the injectors as shown in Figure 4.5. In particular, the smallest refinements are set within the fuel channels ($80 \mu m$) and in the region including the hydrogen jets at the base of the combustion chamber ($100 \mu m$). Then, the mesh size progressively increases to $170 \mu m$ both inside the air-gap

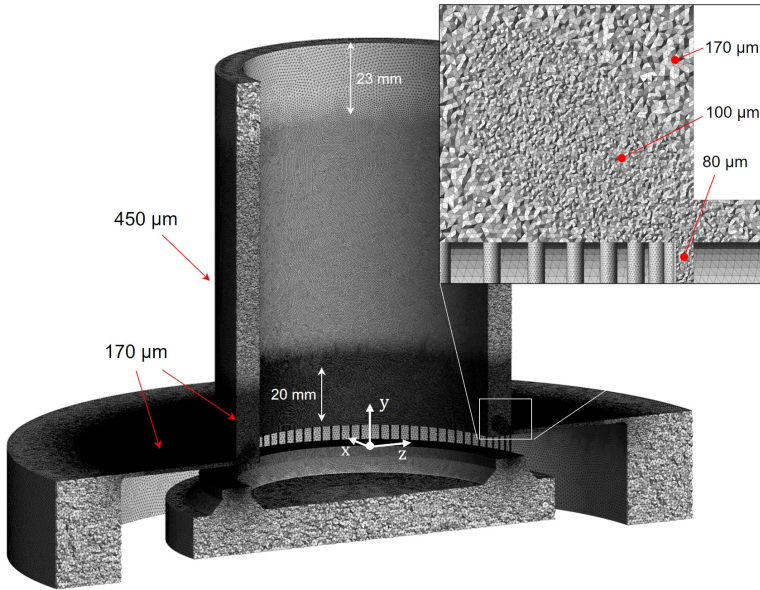


Figure 4.5: Cross-section of the mesh used for the simulations with the characteristic element size.

and in the first 20 mm of the chamber, which then is discretized with $450\ \mu\text{m}$ elements. The different sizing within the combustion chamber was justified by the need to limit the computational cost while maintaining a good discretization near the injection, which is expected to be important for the reactants mixing. At the end of the chamber, a buffer region with a larger element size is adopted for smoothing the fluctuations of the flow near the outlet boundary condition.

4.2.4 Boundary conditions

The air and hydrogen inlets are set at the base of the respective feeding plena (Figure 4.5), imposing the temperature, pressure and mass composition through the partially non-reflecting Navier-Stokes characteristic boundary (NSCBC) conditions [140]. Since the experimental test is carried

out with fixed mass flow rate (see Section 4.1.3), the detonation blockage induces a slightly higher pressure in the air plenum with respect to the cold case. The direct prescription of the mass flow rate in the simulation would reproduce this behaviour, however, due to the larger uncertainties related to the measurement of the mass flow rates, the prescription of the plenum pressure was preferred. However, the specification of two different pressures (Table 4.2) for the cold and reactive case would require a change of inlet boundary condition during the detonation initiation and the early stabilization. Due to the very short rotation time of the wave compared to the time required for pressurizing plena, this numerical procedure should be avoided, so the pressure is directly set to the one of the reactive case (7.42 bar), even during the cold flushing. All the values are then imposed according to the reactive case in Table 4.2, modeling the air mass composition as 0.233 O_2 and 0.767 N_2 . As a result, the preliminary cold flow simulated is slightly different from the cold condition reported in Table 4.2, since the higher pressure without the detonation blockage determines a higher air mass flow rate and a leaner composition. As soon as the detonation is ignited, the effective area of the air gap and the air mass flow rate reduce, matching the stoichiometric condition. This procedure has also the advantage to provide initially a large mass flow rate of reactants, thus enhancing the possibility of stabilization of the detonation.

At the outlet surface the atmospheric pressure (101325 Pa) is set through the NSCBC in the subsonic regions and switching to a supersonic outlet where needed.

The walls are modeled using turbulent adiabatic wall functions [159], except the walls adjacent to the inlet surfaces which are set as free-slip walls not to interfere with the inlet boundary conditions.

4.2.5 Numerical models

The numerical analysis is carried out with the AVBP 7.5 code [148, 149] developed by CERFACS and IFPEN by solving the fully-compressible, multispecies, reactive Navier-Stokes (NS) equations. The third-order in

time and space Taylor-Galerkin TTGC scheme [150] is used as convection scheme for the preliminary non-reactive case while the second-order Lax-Wendroff (LW) [160] scheme is adopted for the reactive simulation. The explicit time integration is carried out by enforcing a maximum CFL number of 0.7, resulting in an average timestep of $6.3e-9$ s. The NS equations are spatially-filtered to obtain the LES formulation and the sub-grid terms are closed through the WALE model [161], specifically developed for wall bounded flows. The localized artificial diffusivity (LAD) model [162] based on density and pressure is also adopted to stabilize the centered schemes and capture the discontinuities within the domain.

The hydrogen-air detonation is modelled using the 4S1R single-step scheme, specifically developed for the conditions of interest (Section 2.3.2.1). According to the 4S1R scheme, four species, i.e. H_2 , O_2 , H_2O , N_2 , are included in the model. However, for the non-reactive case the H_2O is not transported and its concentration is assumed zero to reduce the computational effort. The laminar transport properties for the species scheme are specified according to Section 2.3.2.1, imposing distinct Schmidt numbers for each species (Table 2.8). The turbulent Schmidt and Prandtl numbers are set to 0.6.

4.2.6 Detonation initiation

The ignition of the test rig requires several hundreds of milliseconds, since both the detonation and the injection system have to reach a stationary operation. Such a long transient would result in a prohibitive computational cost of the simulation and does not represent the focus of the present study, so the ignition procedure adopted in the experimental tests is not reproduced numerically.

Instead, a specific strategy for starting the detonation process and at the same time initialize a basic RDC flow field is developed and adopted in the simulation, allowing a consistent reduction of the time for stabilizing the wave and thus of the computational demand. At first the initialization procedure is developed and verified in a simplified 2D domain of the combustor and then is extended to the 3D domain by

mapping the 2D initial solution along the tangential-axial directions of the combustion chamber, without considering any variation along the radial direction. However, the realistic configuration of the injection requires a particular attention to the initialization of the flow field in the injectors (see Section 4.2.2). Since the reactive simulation is carried out after a preliminary cold flushing, the detonation is initiated by superimposing the basic RDC flow field only in the combustion chamber above $y = 6$ mm, leaving the non-reacting solution unaltered below, i.e. in the injectors and plena. This precaution allows the injectors to feed the chamber at full capacity as soon as the detonation is started.

The flow field superimposed to the non-reactive solution is represented in Figure 4.6 and is composed by the following regions:

1. 1D overdriven (110% D_{CJ}) ZND detonation profile, extending up to the CJ plane along the tangential direction, so that the resulting shock is a radial-axial surface. For the profile, an atmospheric H_2 -air stoichiometric mixture is used;
2. Expansion region, following the detonation profile in tangential direction. There the pressure and the tangential speed are relaxed quadratically to the atmospheric and zero value respectively, while the temperature is determined according to an isentropic expansion:

$$T = T_{CJ} \left(\frac{P}{P_{CJ}} \right)^{\frac{\gamma_{CJ}-1}{\gamma_{CJ}}} \quad (4.5)$$

This region is introduced to provide a slow relaxation behind the wave to the static, atmospheric condition, preventing the backward propagation of the detonation and mimicking the Taylor-Zeldovich expansion [22]. The CJ products composition is set throughout this zone uniformly;

3. Refill region, increasing in the tangential direction linearly ahead of the front, with a maximum refill height of $y = 25$ mm. Here, a constant atmospheric H_2 -air stoichiometric mixture is imposed, so

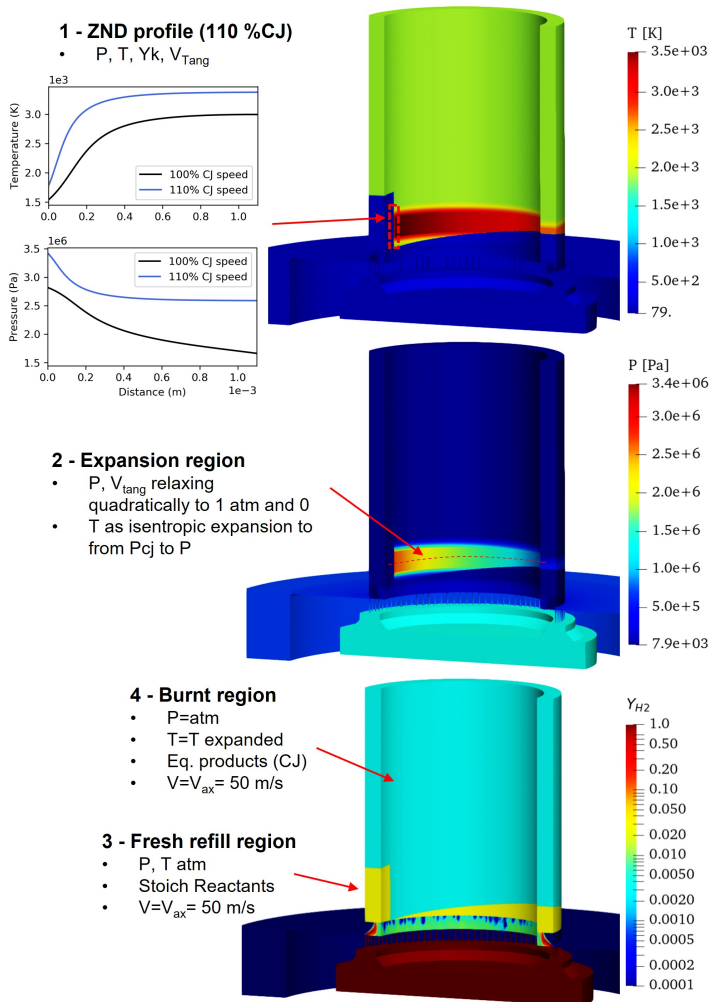


Figure 4.6: Initial solution adopted for the reactive simulation.

that a detonable, uniform mixture is provided in the early instants of the wave propagation;

4. Burnt region, constituted by the remaining part of the combustion chamber and filled with CJ products at atmospheric pressure and temperature resulting from the isentropic expansion of the region (2). Since the gas is not flammable, only shocks can propagate in this region.

In all the RDC Figure , i.e. above $y = 6$ mm an axial velocity of 50 m/s is imposed for initializing the discharge through the outlet, while no radial velocity component is set.

The use of an overdriven detonation rather than a CJ detonation profile in (1) was adopted after a first failure of the detonation initiation with a ZND profile at 100% D_{CJ} . A higher detonation speed was then necessary for reaching higher pressure and temperature and starting successfully the detonation in the simulation. The system then stabilizes within 4 – 5 revolutions of the wave, corresponding to approximately 0.6 ms of physical time.

4.2.7 Computational demand

The simulations were carried out using a 6 nodes on a HPC cluster with 40 Intel[®] Xeon[®] Gold 6248 CPUs (base and maximum frequencies of 2.50 GHz and 3.90 GHz and cache of 27.5 MB) per node. On this hardware, the return time for the overall simulation of 4.1 ms of physical time was 650 hours, i.e. 163 simulation hours per physical millisecond. The total CPU time was then about 151k CPUh. The details about the computational demand of the simulations are reported in Table 4.3.

Table 4.3: Computational requirements of the simulations.

		Cold case	Reactive case	Total
Equations		8	9	
Convection scheme		TTGC	LW	
Simulated time	<i>ms</i>	2.1	2.0	4.1
CPUh	$10^3 \times$	97	54	151
n° timesteps	$10^3 \times$	340	286	626
Timestep size	<i>ns</i>	6.17	6.37	6.26

Chapter 5

Non-reactive case analysis

Contents

5.1	Introduction	145
5.2	Flow-field structure	147
5.2.1	Near-injection region	150
5.2.2	Lower half of the chamber	153
5.3	Overall mixing performances	156
5.4	Mesh quality assessment	158
5.5	Concluding remarks	160

5.1 Introduction

The rotating detonation combustor is firstly flushed with fresh gases for initializing the injectors before the detonation initiation, as explained in Section 4.2.2. Although the focus of the work is the reactive condition, the results of the non-reactive simulation are presented in this chapter. Their analysis allows assessing the performances of the injection system in preparing an adequate mixture for the detonation, i.e. maximizing the uniformity of the fuel-air mixture.

Indeed, the design of the injection system is one of the most important aspects of a RDC and can determine the propagation and the stability of

the detonation wave [44, 81]. Previous experimental campaigns highlighted also that the combustor operation and pressure gain are strongly related to the area ratio between the air and fuel injectors [49]. Although several parametric tests have been carried out in a water-tunnel model of the rig [18, 163], the compressibility effects of the gas are expected to govern the flow field in proximity of the injectors, as observed by Weiss et al. [157]. For this reason, the results obtained here from the fully-compressible LES could provide further insight into the mechanisms involved in the mixing process within the TUB combustor.

It is worth to remark that the same pressures of the reactive case (Table 4.2) are imposed to the plenum, so the non-reactive test point has a slightly higher mass flow rate with respect to the preliminary flushing carried out experimentally. The prediction of the LES simulation in terms of mass flow rates are reported in Table 5.1 as time-averaged values during the last 1.5 ms of the simulation, when the combustor exhibits a stationary operation.

Table 5.1: Operating conditions resulting from the LES with respect to the nominal isentropic values (non-reactive case).

		Nominal (is.)	LES
Air manifold pressure	$bar(a)$	7.42	7.42
Fuel manifold pressure	$bar(a)$	13.12	13.12
Air temperature	K	291	291
Fuel temperature	K	289	289
Air \dot{m}	g/s	603	536
Fuel \dot{m}	g/s	16.13	13.87
Chamber mass flux	kg/m^2s	314	279
Equivalence ratio	–	0.91	0.88

The numerical simulation predicts mass flow rates of 89% and 86% of the isentropic values (Eq. 4.1) for the air and the fuel respectively. This reduction can be attributed to the viscous and three-dimensional effects of the real geometry and walls. As a consequence, the equivalence ratio

predicted by the LES is slightly lower than the nominal value, so the final value during the reactive operation has to be checked to avoid drifts from the desired test point.

In the next sections the structure of the flow field within the RDC during the non-reactive case is reported and discussed.

5.2 Flow-field structure

The air and hydrogen are injected in the combustion chamber through a radial slot at the base of the outer wall and 100 axial holes at the chamber head. As a result, the hydrogen jets are hit by a radial-inward flow of air, realising a jet in cross-flow configuration. Since the chamber pressure is well below the critical pressure of both the air (3.9 bar) and the fuel (6.9 bar), the passages are choked at the respective throats and then the reactants enter in the chamber as highly under-expanded jets.

For the interpretation of the results, it is also useful to report the commonly accepted flow field structures associated to the configurations present in the combustor, i.e. the highly under-expanded jet (Figure 5.1) and the interaction between a transverse jet with a supersonic cross-flow (Figure 5.2).

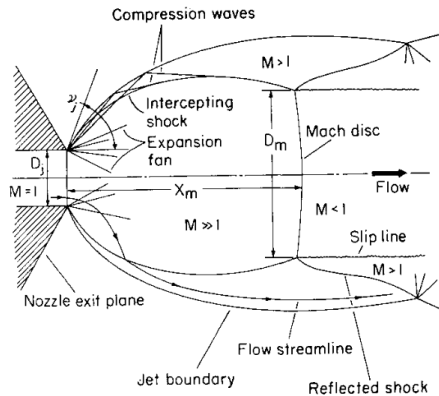


Figure 5.1: Schematic of a highly under-expanded jet [164].

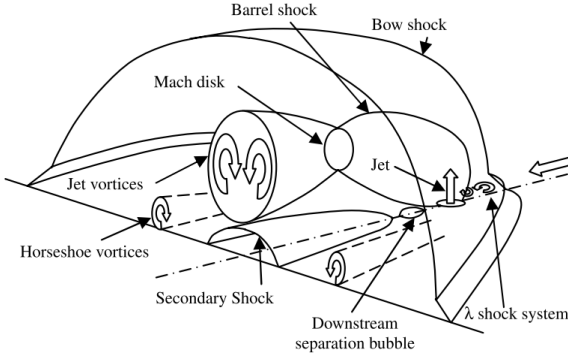
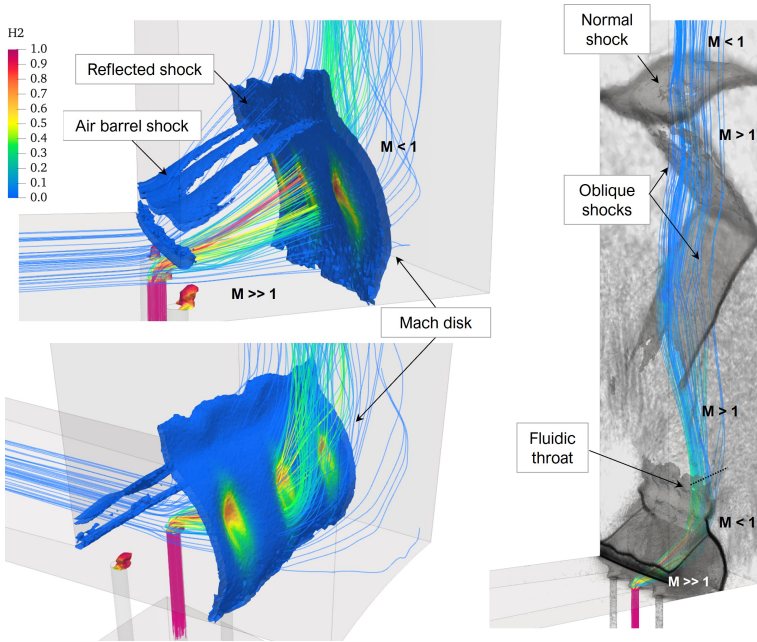


Figure 5.2: Schematic of a transverse jet in a supersonic cross flow [165].

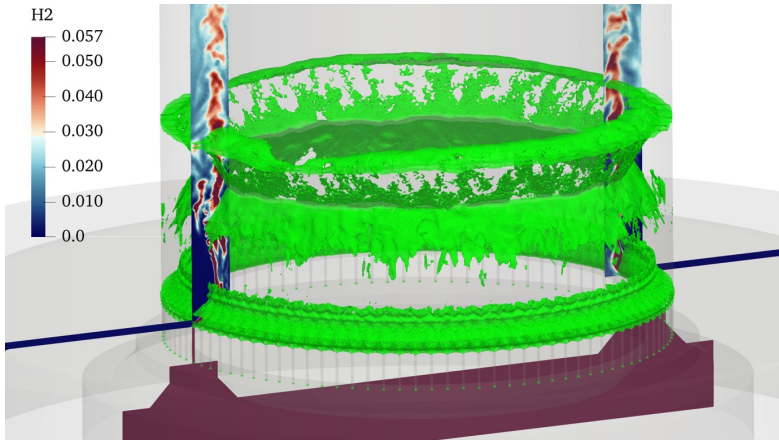
In the present case, however, the position of the fuel jet in the proximity of the air gap throat prevents the formation of a bow shock in the air flow, as the cross-flow is sonic when it impinges with the jets. The resulting shock complex in the combustion chamber is reported in Figure 5.3. The shocks are identified from the instantaneous fields predicted by the simulation as isosurfaces of the relative magnitude of the pressure gradient $\nabla P/P$. The values are chosen to highlight the strongest shocks present in the domain. From Figure 5.3 two shock complexes can be clearly identified, depending on the position within the chamber:

- Near-injection region ($y \leq 5$ mm): shocks of the under-expanded jet of air in radial inward direction, composed by a barrel shock anchored at the outer wall around $y = 2$ mm, a Mach disk and a reflected shock between the disk and the jet boundary;
- Lower half of the chamber ($13 \leq y \leq 35$ mm): a shock complex constituted by two oblique shocks which deviate twice the supersonic flow before a normal shock which reports the Mach number below unity.

The two regions are presented separately in the following. Due to the significant presence of stationary, supersonic structures which govern



(a) $\nabla P/P$ isosurface and velocity streamlines colored by Y_{H_2} .



(b) $\nabla P/P$ isosurface (green) and Y_{H_2} in the cross-section.

Figure 5.3: 3D visualization of the shocks in the combustor.

the flow field in the region of interest, the instantaneous result will be presented to highlight the discontinuities in the domain.

5.2.1 Near-injection region

The air flow coming from the air gap toward the hydrogen jets reaches the sonic conditions right after the discharge in the combustion chamber ($r > 44$ mm), so the hydrogen jet is deflected and contributes to the definition of the throat area for the air injector. The detail of the flow structure near the injection is reported in Figure 5.4 in the cross-section plane passing through an injector axis (x, y plane, $\theta = 90$ deg) and between two injectors ($\theta = 91.8$ deg). As soon as the the air enters the chamber, it rapidly expands to very low pressures accelerating up to $M = 3.5$. The presence of the jet induces a small separation bubble (see Figure 5.2) behind the jet where the flow is subsonic, which is clear from Figure 5.4 and is completely absent between the injectors. The hydrogen jet is under-expanded as well and thus exhibits a little barrel shock up to half the heigh of the air gap and a Mach disk. The first part of the jet is deflected by a sonic air flow at higher radii, while it is laterally confined by a supersonic flow, since the air is accelerated immediately after the discharge in the chamber. As a result, the fuel jet above $y = 1$ mm is completely embedded in a supersonic flow which reduces consistently its mixing with the air (Figure 5.4, bottom). The supersonic air prevents the hydrogen from reaching the recirculation region above the air gap, while it can only partially mix at the sides due to the presence of the shear layers. Below the jet, the mixing is promoted by the subsonic bubble at the base of the chamber, however, since this region is completely confined by a supersonic flow, the hydrogen is still limited in its tangential expansion, so that no fuel concentration is present between the jets (Figure 5.5).

The supersonic flow constituted by the air and the hydrogen jet is then subjected to a strong compression for the presence of a Mach disk with a reflected shock at the top, positioned near the 50% of the annulus span. The strong shock decelerates the flow to subsonic speeds and allows the curvature of the flow in the axial direction to accommodate the presence

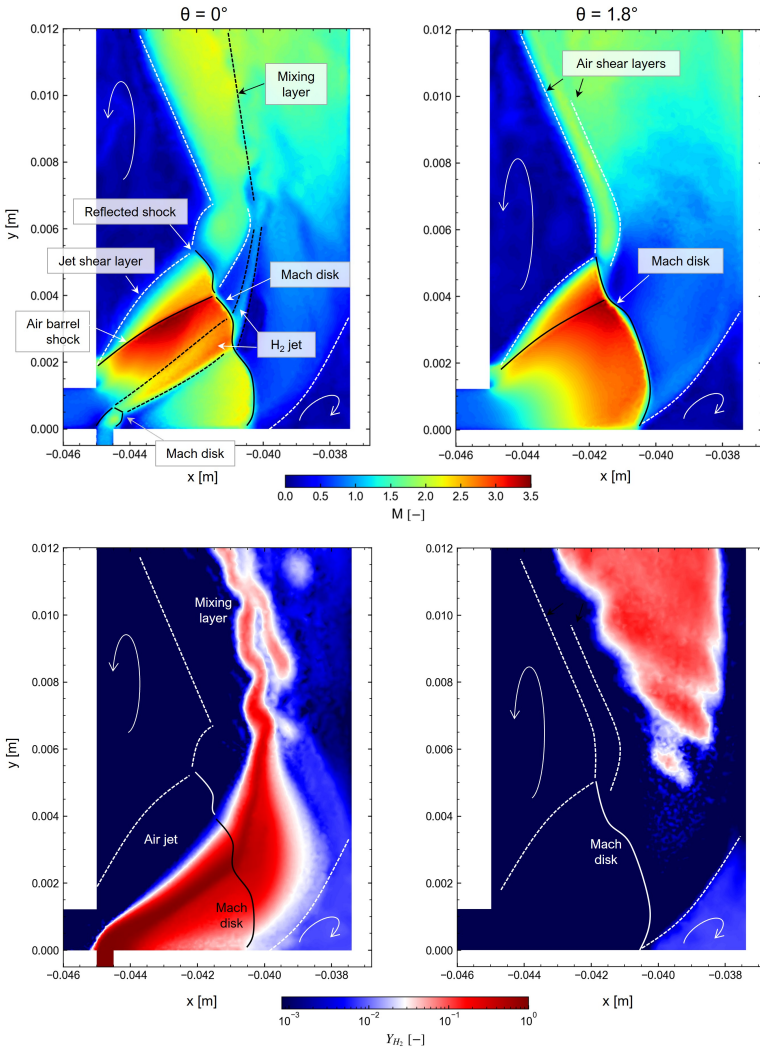


Figure 5.4: Distributions of Mach (top) and H_2 mass fraction (bottom) in the cross-sections passing through (left) and between (right) the injectors. The white color corresponds to $\phi = 1$.

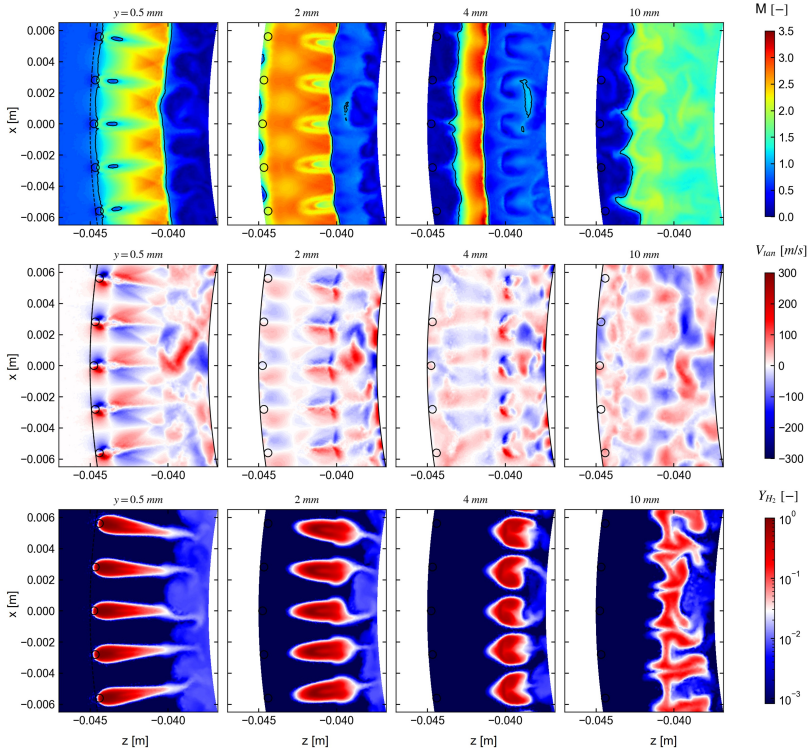


Figure 5.5: Mach number, tangential velocity and Y_{H_2} in the axial planes near the injection. The white color for the Y_{H_2} corresponds to $\phi = 1$ while positive V_{tan} is counter-clockwise.

of the inner wall. Another recirculation zone is formed at the base of the chamber along the corner with the internal wall, and is filled with a slightly lean mixture of H_2 -air which exhibits a constant tangential composition (Figure 5.5). The subsonic speed of the flow enables the formation of instabilities along the shear layer of the fuel jet, which roll up in a pair of counter-rotating vortices at $y = 4$ mm, clearly identifiable in the corresponding axial plane from both the tangential velocity and the H_2 mass fraction (Figure 5.5). These fluctuations improve the mixing significantly so that the fuel jets begin to coalesce tangentially around $y = 6 - 8$ mm.

This flow field structure depends significantly on the operating conditions of the combustor such as the blowing ratio, the equivalence ratio and the mass flow rate, as was observed in the study carried out by Weiss et al. [157], which simulated the non-reactive mixing up to 300 g/s. Nevertheless, although the present case has a higher mass flow rate, the shock complex shown in Figure 5.4 is very similar to the stoichiometric, 300 g/s case reported by Weiss et al. [157], even considering the distribution of hydrogen in the inner corner and its absence in the recirculation region above the air gap.

5.2.2 Lower half of the chamber

The Mach disk slows the flow down to subsonic speeds and this allows the gas to curve and deflect from a radial inward to the axial direction, aligning with the inner chamber wall (Figure 5.3). However, the conformation of the flow field determines the formation of a fluidic throat, i.e. a restriction of the passage area seen by the fluid located axially at $y = 6$ mm and spans lower than 50%. As a consequence, the high-pressure subsonic gas flows through a converging-diverging nozzle which accelerates again the fluid up to $M = 2 \approx 2.5$. The throat and the path of the fluid is evident from Figures 5.6 and 5.7, and well-defined between the injectors.

Specifically, the flow is confined between the inner wall of the chamber and the recirculation zone above the air gap up to about $y = 17$ mm.

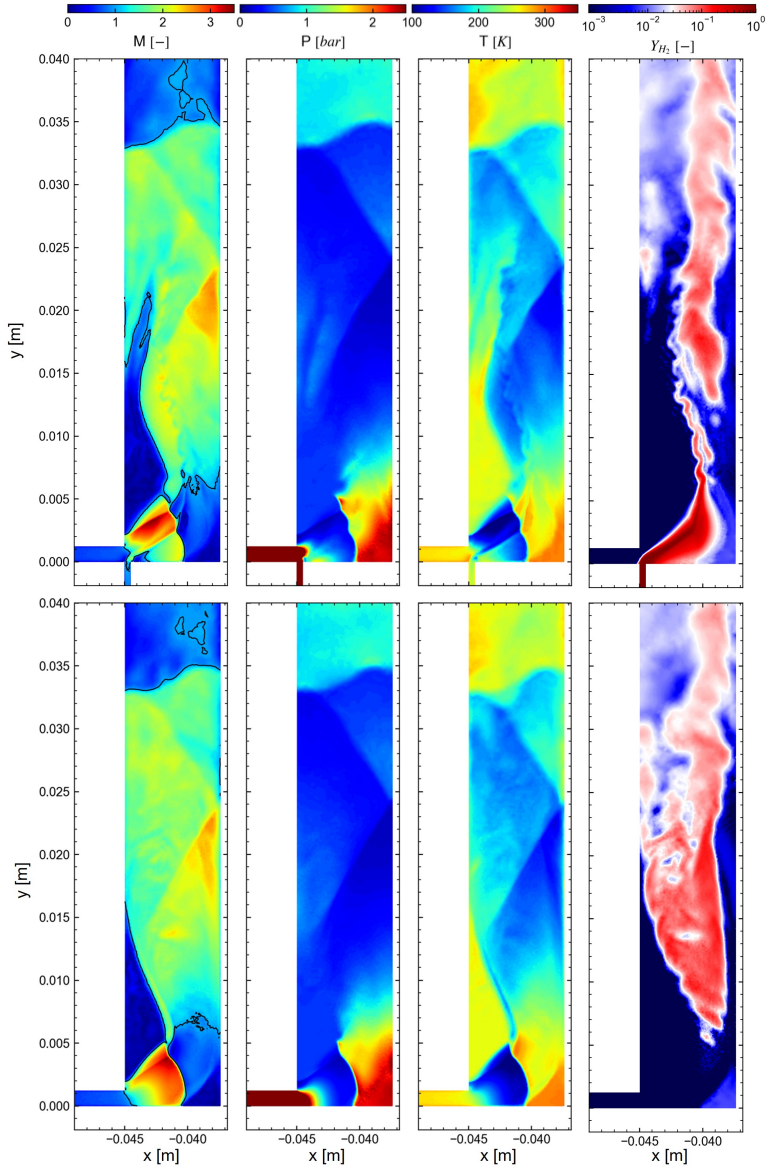


Figure 5.6: Fields in the cross-sections passing through (top) and between (bottom) the injectors. The black line represents $M = 1$.

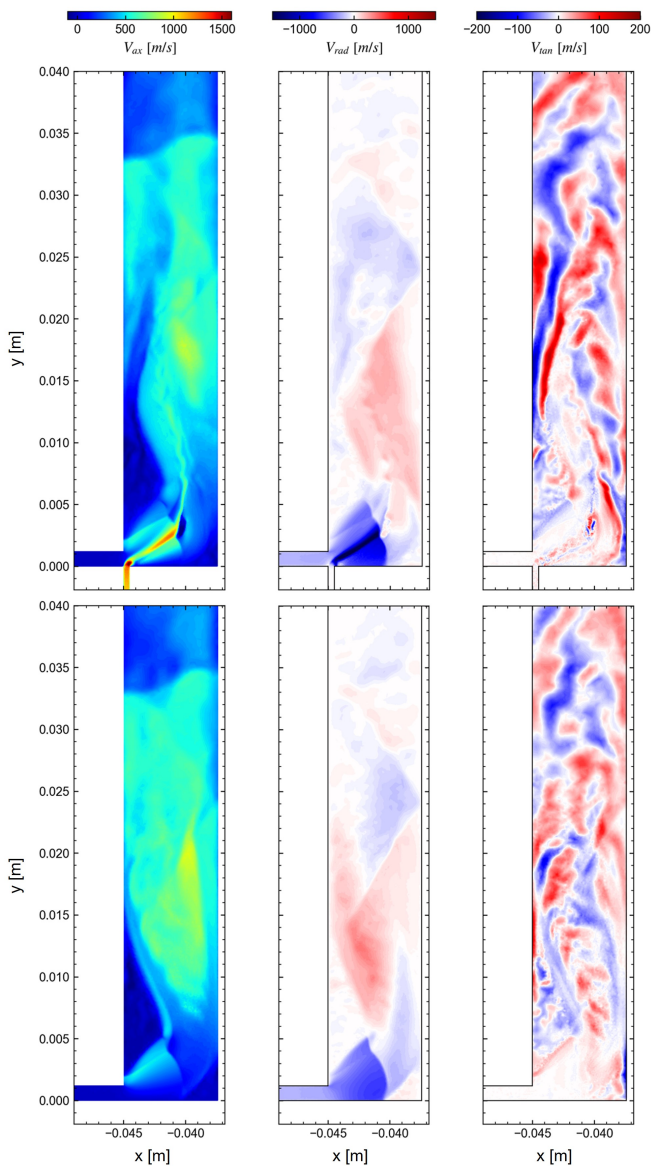


Figure 5.7: Velocity components in the cross-sections passing through (top) and between (bottom) the injectors.

Around this axial location, a first oblique shock straightens the flow, not only reducing but also inverting its radial velocity component (Figure 5.7). Then, another oblique shock generated by the reflection of the first one on the inner chamber wall deviates again the flow in radial direction. Since the speed in this zone is supersonic, the mixing of the hydrogen is poor and proceeds only thanks to the shear layers, remaining confined near the inner wall. The recirculation region above the air gap is thus completely isolated from a layer of supersonic air and no H_2 reaches this zone. The flow speed is finally reduced to subsonic values between $y = 33 - 35$ mm through a normal shock distributed over all the annulus of the chamber. Although the presence of the shock, the axial flow speed maintains a radial non-uniformity, with a faster propagation at low span which convects downstream the richer composition near the inner wall.

5.3 Overall mixing performances

The complex supersonic flow structure reported in the previous section does not promote the mixing of hydrogen and air, resulting in a poor mixing. The hydrogen mass fraction is reported in Figure 5.8 for constant-span section of the complete combustion chamber.

Although the normal shock is located around $y = 35$ mm and thus the flow is subsonic for axial positions above, streaks with high concentration of hydrogen ($\phi \approx 2$) persist up to $y = 60 - 70$ mm. Below this position, the mixture features a stratified composition with rich regions for spans $\leq 50\%$ and lean for higher spans. Only downstream $y = 70$ mm, the composition starts homogenizing in every direction, reaching also the outer wall of the chamber.

It is important to note that although the simulated condition has a higher mass flow rate than the one typically used for this RDC, the flow field is coherent with the findings of Weiss et al. [157] for lower mass flow rates. The poor performances in terms of mixing beyond a mass flow rate threshold is also typical for this geometrical configuration and has been characterised also by other research groups [166, 167]. The major

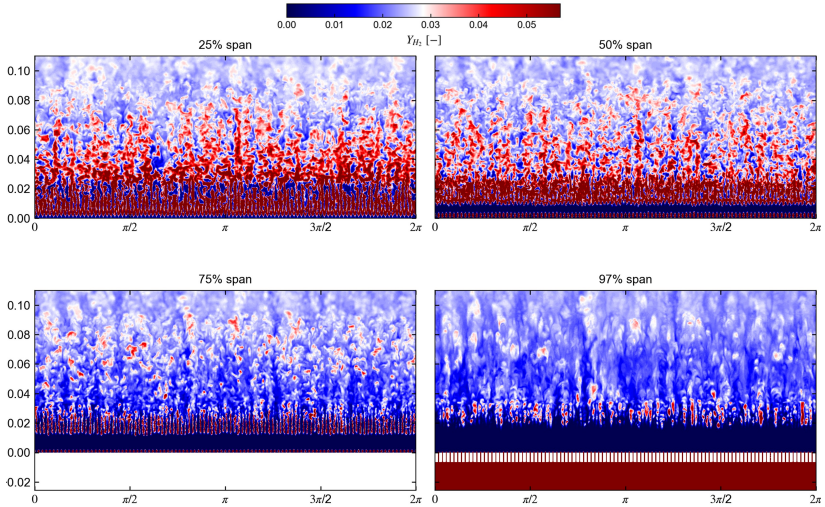


Figure 5.8: Unwrapped cylindrical sections at different spans of the combustion chamber. The white color indicates $\phi = 1$.

cause of the performance loss is the establishment of the supersonic flow field due to the highly under-expanded jet of oxidizer, which also favours the formation of a fluidic throat and a convergent-divergent flow path. As a result, the recirculation zone above the injection of the oxidizer is completely segregated from the fuel, not participating to the mixing of the reactants. Thus, the fuel jet remains coherent and is convected downstream at supersonic speed for the convergent-divergent flow path, further delaying its mixing.

The scarce mixing efficiency of the system could have a negative impact on the stability of the detonation wave or even prevent its correct stabilization. However, it is worth to remark that the presence of the detonation wave not only alters the inlet mass flow rate and thus the blowing ratio of the fuel jet, but it induces also flow field variations both in time and space. The injectors are periodically blocked by the high pressure wave and require a non-negligible time interval to recover. The maximum

injection capacity which is reached by the injectors is determined by the frequency and number of combustion waves in the chamber. It is then evident that a non-reactive solution can be useful for studying a stable injection, but consistent differences should be expected when the RDC is ignited (see Section 6.5.3).

5.4 Mesh quality assessment

In this section, an assessment of the simulation resolution is carried out to determine the adequacy of the mesh element size for describing the flow field. When a LES is considered, the good resolution implies a correct reproduction of the most energetic flow features, which are usually connected to the largest structures of the flow field. The sub-grid models should not introduce a significant error in the solution, and this is possible if the filter resolution is sufficient for capturing the main turbulent fluctuations.

The determination of the LES quality is not trivial since it is determined by a combination of numerical discretization errors and modelling errors [168]. The two most adopted indexes for evaluating the quality of a LES are the Pope's criterion [169], based on the fraction of resolved turbulent kinetic energy, and the Celik's parameter [168], relying on the simulation effective viscosity. Since the evaluation of the turbulent kinetic energy requires the determination of a time-averaged flow field, not available from this preliminary non-reactive simulation, the Celik's parameter is preferred for the quality assessment.

The Celik's quality index based on the viscosity QI_v is defined as [168]:

$$QI_v = \frac{1}{1 + \alpha_v \left(\frac{\mu_{\text{sgs}} + \mu_{\text{num}}}{\mu} \right)^n} \quad (5.1)$$

with $\alpha_v = 0.05$ and $n = 0.53$. The parameter depends on the ratio between the simulation effective viscosity $\mu_{\text{eff}} = \mu_{\text{sgs}} + \mu_{\text{num}}$ where μ_{num} represents the apparent viscosity induced by the numerical discretization. This viscosity is very complex to be determined and here is neglected

with respect to the sub-grid value determined according to the WALE model [170]. The resulting quality index is reported in Figure 5.9.

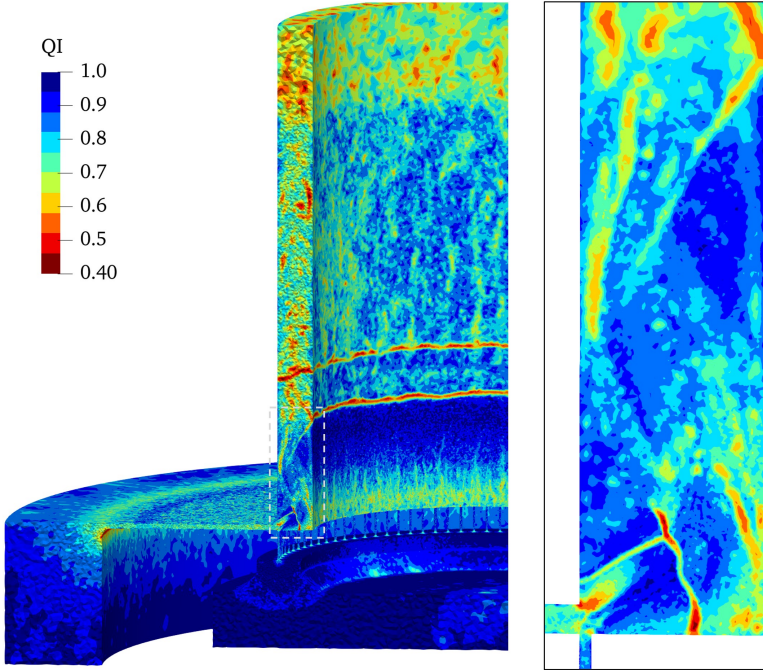


Figure 5.9: Celik's quality index for the non-reactive case LES.

As the sub-grid model depends on the grid size, the index also varies according to the refinement regions adopted (see Figure 4.5). Very high values of the index ($QI_v > 0.95$) identifies DNS-like resolutions while values above 0.8 indicate a good LES. Since the shock waves represent discontinuities in the fields, the index is not suitable for those regions and lower values cannot be avoided. Apart from the shocks, the overall quality index is satisfactory for the present analysis, with values around 0.8 – 0.9 in the refined region at the base of the chamber ($y < 25$ mm) and 0.7 above. The central part of the combustion chamber could benefit from a further reduction of the mesh sizing, since the high turbulent fluctuations

of the flow persist far downstream the injection. However, the complex shock structure near the injectors and the surrounding flow field reported in Section 5.2 are properly discretized by the mesh.

Finally, it is also worth to note that limited information can be inferred from the quality index of the cold case and extended to the reactive case. Indeed, not only the mass flow rate will be lower for the presence of the detonation, but most importantly the flow field will be completely altered, and the mesh requirements far from the injector will depend on the unsteady occurrence of the supersonic flow field. As the mesh resolution is good near the base of the chamber, where both the injector shock structures and the subsonic region are expected in the reactive refill region, the adopted mesh is expected to be appropriate for the reactive case. Nevertheless, the quality index will be evaluated also for the reactive condition and will be reported in Section 6.6.

5.5 Concluding remarks

In this chapter, the non-premixed RDC installed at TU Berlin is studied numerically by solving the spatially-filtered, fully-compressible, multispecies, reactive Navier-Stokes equations with the AVBP code. The combustor is studied in the non-reactive conditions preliminary to the ignition of the detonation wave with the objective of characterizing the flow field and the consequent reactants mixing.

The results of the simulation highlight the presence of a complex shocks structure within the combustion chamber, arising from the under-expanded reactants jets and their interaction with the chamber walls. The high flow-rate of the cold condition induces a supersonic speed for the lower half of the chamber, leading to a scarce overall mixing efficiency of the reactants which cannot take advantage of the turbulent fluctuations.

Chapter 6

Reactive case investigation

Contents

6.1	Stabilization and operating conditions . . .	162
6.2	Model validation	166
6.2.1	Wave rotation frequency	166
6.2.2	Pressure gain	169
6.3	Global flow field features	176
6.3.1	Shock structures in the combustor	177
6.3.2	Instantaneous fields	182
6.3.3	Time-averaged fields	188
6.4	Refill region description	191
6.5	Analysis of the injectors operation	200
6.5.1	Temporal trends within the injectors	200
6.5.2	Mach number and mass flow rate distributions	203
6.5.3	Reactants jets flow field in unperturbed and blocked conditions	209
6.6	Mesh quality assessment	219
6.7	Concluding remarks	222

In this chapter, the results of the reactive analysis of the TU Berlin RDC are presented and discussed. After an overall description of the wave stabilization process and the resulting operating parameters, the

predictions of the model are contrasted to the available measurements. Then, the results of the simulation are analysed in detail, with specific emphasis on the flow field within the combustion chamber, the characterization of the refill region and the injectors operation. At the end of the chapter, also an assessment of the turbulent flow field resolution achieved is presented.

6.1 Stabilization and operating conditions

After the preliminary cold flushing presented in Section 5 and the complete stabilization of the injectors, the combustor is ignited using the initiation method described in Section 4.2.6. The method is based on the super-imposition of a simplified RDC field built upon a 1D overdriven detonation profile in the combustion chamber, while leaving unaltered the non-reactive solution below $y = 6$ mm, including the injectors and the plena. This procedure was developed and adopted for both initiating the detonation and initializing the RDC flow field at the same time, reducing significantly the time required for the establishment of a stable operation.

The rapid stabilization of the wave is clear from the time histories of the inlet mass fractions and the maximum thermodynamic properties in the domain, reported in Figures 6.1 and 6.2 respectively.

In the diagrams the $t = 0$ ms corresponds to the initiation of the detonation on the non-reactive solution. The fuel and air inlets respond to the presence of the detonation with different delays due to their geometrical features. The short fuel channels and the smaller plenum determine a very fast feedback at the hydrogen inlet within the first 0.02 ms, inducing a reduction of flow rate which persists for the whole simulation. The extremely fast feedback is also favoured by the high sound speed in the hydrogen (1300 m/s) which is almost four times higher than in the air (341 m/s). This difference in the properties, combined with the length of the air gap, the 90 bend and the larger plenum, delays the arrival of the pressure waves at the air inlet to 0.2 ms. After that the initial plenum feedback, the inlet mass flow rates exhibit an adjustment period

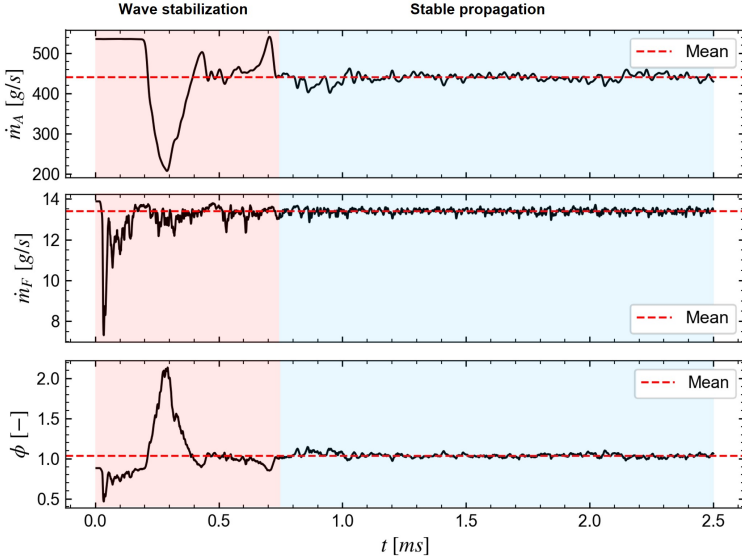


Figure 6.1: Temporal history of the inlet mass flow rates and the resulting equivalence ratio.

up to 0.75 ms, contemporary to the stabilization of the wave. In fact, as shown by the maximum pressure, temperature and heat release rate within the domain (Figure 6.2), the detonation is started immediately after the initiation (≈ 0.02 ms) but it requires about 0.65 ms to reach a steady state, equivalent to 6 revolutions of the chamber (Figure 6.3). As a result, the whole system stabilizes in a stationary operation within 0.75 ms from the initiation. From these results the importance of the preliminary initialization of the injectors is clear as the fluid domain upstream the combustion chamber requires multiple wave rotations to stabilize completely. For the purposes of the present analysis, only the stabilized condition is relevant, so all the results will be relative to the stable operation, i.e. $t \geq 0.75$ ms.

During this condition the inlet mass flow rates predicted by the simulation are time-averaged and reported in Table 6.1.

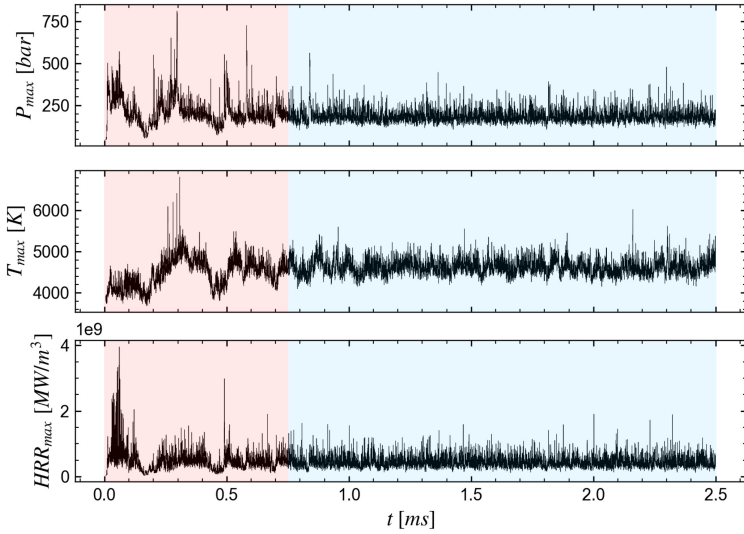


Figure 6.2: Temporal history of the maximum temperature, pressure and heat release rate in the domain (7.7 MHz sampling).

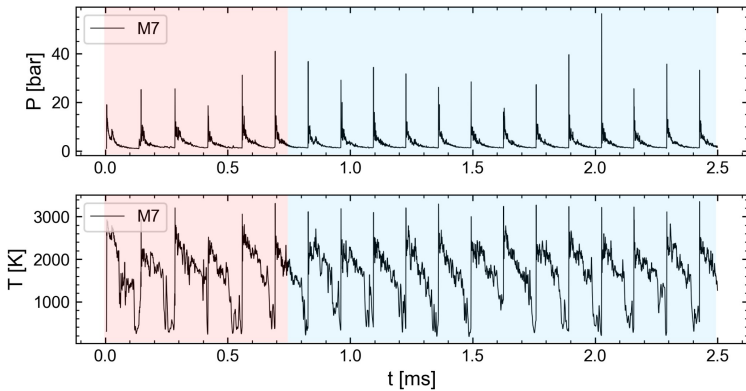


Figure 6.3: Static pressure and temperature signals sampled at 50% span and $y = 25$ mm (7.7 MHz sampling).

Table 6.1: Operating conditions resulting from the LES with respect to the nominal test point (reactive case).

Reactive case		Nominal	LES
Air manifold pressure	$bar(a)$	7.42	7.42
Fuel manifold pressure	$bar(a)$	13.12	13.12
Air temperature	K	291	291
Fuel temperature	K	289	289
Air \dot{m}	g/s	554.9 (is.)	445
Fuel \dot{m}	g/s	16.13 (is.)	13.3
Chamber mass flux	kg/m^2s	290 (is.)	233
Equivalence ratio	–	0.99	1.01

The average mass flow rate which enters in the domain is 445 g/s (74% \dot{m}_{is}) for the air and 13.3 g/s (82% \dot{m}_{is}) for the fuel, resulting in a stoichiometric equivalence ratio. As expected, the presence of the detonation wave reduces the effective area of both fuel and air passages with respect to the cold flow condition (Table 5.1). More specifically, the area blockage $1 - A^R/A^C$ evaluated according to Eq. 4.2 is 17% for the air and 4% for the fuel, both slightly higher than in the experiments, as shown in Table 6.2.

Table 6.2: Predicted and measured blockage of the detonation with respect to the non-reactive condition.

A^R/A^C	Exp.	LES
Air	0.92	0.83
Fuel	1.00	0.96

It is worth to note that the reactive simulation is carried out using the Lax-Wendroff scheme, which is known to be more dissipative than the TTGC scheme of the non-reactive simulation, so a little contribution to the blockage is likely due to the higher numerical viscosity of the simulation.

Despite these differences, the global equivalence ratio of the LES

matches the stoichiometric value of the experiment, so the results of the simulation can be reasonably compared to the experimental test.

6.2 Model validation

For the present operating condition a dominant single detonation wave stabilizes in the chamber annulus (SW mode, see Section 4.1). The simulation reproduces the same behaviour observed experimentally with the stabilization of a well-defined single wave in about 6 revolutions (0.7 ms) after the initiation (Figure 6.3). It is worth highlighting that no evidences of the dependence of the stable mode on the initiation strategy was observed neither in the simulations or the experiments [18]. Preliminary 2D RDC simulations demonstrated that other detonation modes with multiple waves can arise spontaneously for specific conditions or models, despite the use of the single-wave initial solution. This indicates that the mode does not present hysteresis but rather depends on the operating conditions and modelling choices. Therefore, the prediction of the single wave can be considered a result independent from the initial solution and a first indicator of the numerical model adequacy.

In the next sections the predicted wave rotation frequency and combustor pressure gain will be compared to the available experimental measurements to assess the accuracy of the numerical model.

6.2.1 Wave rotation frequency

Although the simulation enables more accurate and detailed procedures for determining the detonation speed and rotation frequency, in this section the same procedure adopted experimentally is exploited for allowing the comparison of homogeneous quantities. Specifically, here the rotation frequency f of the wave in the laboratory coordinate system is calculated from the pressure signals in different locations within the combustion chamber over 14 revolutions (1.8 ms). The signals are sampled with a frequency of 7.7 MHz (130 ns) at $y = 25$ mm on the inner, outer and mid radial positions, however, since they were found to be equivalent

regarding the frequency value, only the signals at 50% span are reported in Figure 6.4 and discussed.

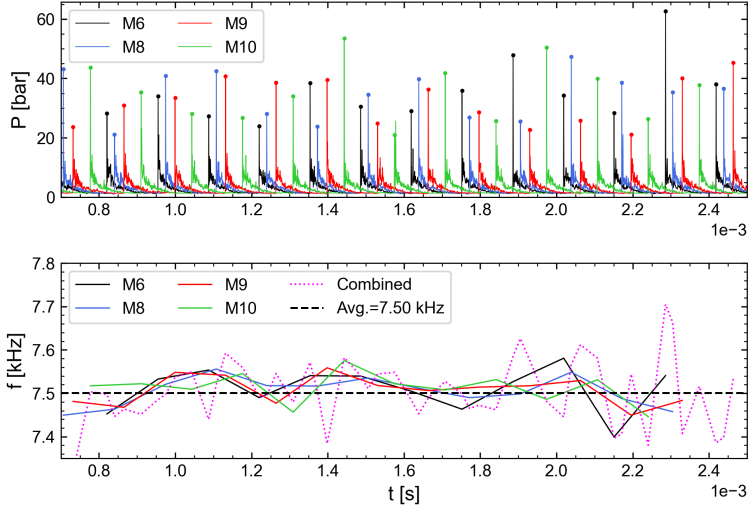


Figure 6.4: Static pressure signals sampled at 7.7 MHz in four consecutive locations within the chamber at $y = 25$ mm and 50% span (top) and the resulting rotation frequency (bottom).

The probes differ only for the angular position which is for M6, M8, M9, M10 of $\theta = 340, 33, 100, 220$ deg, respectively. The rotation frequency is calculated as the average angular velocity between two adjacent pressure peaks:

$$f = \frac{\omega}{2\pi} = \frac{1}{2\pi} \frac{\Delta\theta}{\Delta t} \quad (6.1)$$

For the calculation, the probes are considered either separately ($\Delta\theta = 2\pi$) or combined, i.e. by considering their angular position and measuring the temporal interval between the passage of the wave through any station. Experimentally, the pressure signals are sampled with a frequency of 200 kHz for a several hundreds of milliseconds and then processed with FFT leading to a measured frequency of 6287 Hz. The wave predicted by the

simulation rotates with minor frequency fluctuations of roughly ± 100 Hz around an average value of 7509 Hz. Considering a reference CJ speed of 1975 m/s for a detonation in an atmospheric H_2 -air stoichiometric mixture, to achieve this rotation frequency the tangential velocity of the detonation is distributed around the Chapman-Jouguet value, resulting in a slightly under-driven condition along the inner wall and over-driven in the outer wall. The rotation frequency predicted by the simulation is then 19% higher than the one measured during the experimental test, as reported in Table 6.3.

Table 6.3: Predicted and measured wave features.

		LES	Exp.
Wave type	[-]	Single	Single
Wave frequency	[Hz]	7509	6287
ωr_o	[m/s]	2123	1778

It is worth to note that assuming a $D_{CJ} = 1975$ m/s the predicted detonation would be over-driven along the outer wall, the opposite of what can be inferred from the experimental measurements. Nevertheless, the comparison of the rotation speed to a nominal CJ speed is not very meaningful for the present non-premixed case, since large inhomogeneities are present in the fresh mixture ahead of the detonation, leading to consistent variation of the CJ speed even in radial direction, as will be shown in Section 7.2.2. Moreover, the rotation frequency does not correspond to the actual detonation front speed except for a front with a purely tangential propagation in a static gas.

The causes of the frequency overestimation are still not clear, since previous studies with realistic non-premixed configurations observed both an overestimation [77] and an underestimation [56] with respect to the measurements. In the present analysis the overestimation could be either linked to the adiabatic treatment of the chamber walls or to the use of a global scheme which underestimates the deflagration speed and could limit the fresh gas consumption in the refill region. Both of these two modeling choices will be subject of further developments of the numerical

model.

Although the simulation predicts a detonation frequency higher than the experiments, this discrepancy is reasonable and aligned with other studies, so that the analysis of the interaction with the injector as well as the detonation front structure represents a valuable contribution for understanding the phenomenon.

6.2.2 Pressure gain

As reported in Section 4.1.3, the present configuration does not allow to achieve a positive pressure gain, but rather it represents one of the most penalizing condition for this parameter. It is worth to point out that determining the effective pressure gain of RDCs is not trivial as it is related to the flow unsteadiness induced by the supersonic wave propagation, and not only by presence of the detonation itself [17], so the methods for measuring this quantity are still under active investigation.

For the purposes of this work, adopting a quantity consistent with the experimental tests can be useful to assess the validity of the predicted flow and the accuracy of the numerical model. In the experiments carried out by Bach et al. [156], to determine the pressure gain the total pressure at the RDC discharge was measured, obtaining a value of $p_{0,e} = 3.12$ bar for the present test point. Considering the air plenum pressure of $p_{0,a} = 7.42$ bar, this leads to a pressure gain based on total pressure of $PG = p_{0,e}/p_{0,a} - 1 = -58\%$. Since the measure was obtained with a Kiel probe, characterised by a slow response, the value can be interpreted as a time-average [49].

For providing a quantity coherent with the test, during the simulations the exit total pressure is extracted by sampling the values at the combustor outlet section with a frequency of 100 kHz. Then, according to the perfect gas hypothesis the total pressure is evaluated as:

$$p_0 = p \left(1 + \frac{\gamma - 1}{2} M^2 \right)^{\frac{\gamma}{\gamma - 1}} \quad (6.2)$$

using the local values of γ (≈ 1.26) and Mach number. The pressure is

area-averaged over all the section and is compared with the experiments in Figure 6.5. Since the total pressure field presents a significant spatial

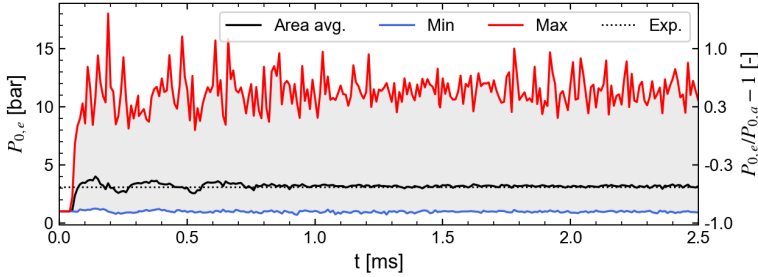


Figure 6.5: Instantaneous total pressure calculated at the outlet section. The dotted line indicates the measurements by Bach et al. [156].

variation, with its maximum and minimum located behind and ahead of the moving shock respectively, also the extreme values in the section are reported in the diagram.

After the initialization the exit total pressure stabilizes rapidly ($t = 0$ ms) and its average value matches the measurements with excellent accuracy (Table 6.4). In the whole section, the total pressure varies from the atmospheric value to post-shock peaks of 11 – 12 bars, without distinct cycle-to-cycle fluctuations.

Table 6.4: Predicted and measured exit total pressure and gain.

		LES	Exp.
Exit total pressure $p_{0,e}$	[bar]	3.177	3.120
Pressure gain PG	[-]	-0.57	-0.58

The agreement with the experiment in terms of overall pressure levels and gain, notwithstanding the wave frequency overestimation, seems to indicate that the sole detonation speed is not directly related to the pressure gain, at least considering a single wave mode without outlet restrictions. This result can be also inferred from the tests carried out by Bach et al.

[49], which led the researchers to conclude that other parameters are needed for characterising the performances of the combustor.

For analysing in more detail the total pressure variation along the axial direction of the combustor, different spanwise locations are considered. The total pressure is then averaged both in time and along the tangential direction to obtain the axial profiles in Figure 6.6.

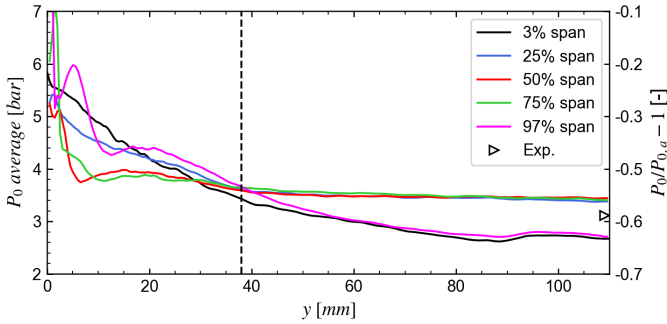


Figure 6.6: Time-averaged axial distributions of total pressure at different spans of the combustion chamber. The dashed line indicates the refill height. The experimental value is reported from Bach et al. [156].

The distributions of total pressure exhibit a considerable spanwise variation only in the first 40 mm of the chamber, while they are more coherent downstream. Above the refill height, where the total pressure is mainly driven by the moving oblique shock, the trend is almost constant, except at 3% and 97% span which are located within the boundary layers. Most of the total pressure drop occurs in the first 5 mm of the chamber, where reasonably the reactants jet decay and mix. However, this decrease is more gradual in the 25% span with respect to 50% and 75%, indicating that the flow features a considerable variation along the span. As the major total pressure drop occurs across a standing shock, the profiles in Figure 6.6 are likely driven by the shock structure near the injection, leading to a fast pressure loss only in the outer half of the chamber. These specific variations will be subject of Section 7.2. Regardless of what

happens in the refill region, the bulk of the chamber shows a total pressure of 3.6 bar, slowly decreasing to 3.4 bar at the combustor outlet. Including also the contributions of the boundary layers leads to the slightly lower value reported in Table 6.4 and Figure 6.5.

The analysis carried out in this section supports the model predictions as the pressure levels across the combustor appear to be well described. Therefore, there is no evidence that the error in the wave frequency invalidates the global flow field structure, so that the complex supersonic features present in the chamber are expected to be representative of the real RDC. The detailed description of these features is relevant for promoting further design improvements as well as the optimization of the RDC performances, so it will be discussed in the next sections.

6.2.2.1 Equivalent Available Pressure

As explained in the previous section, the estimation of the effective pressure gain of unsteady devices such as RDCs is not an easy task and a consolidated procedure has still to be developed. For instance, several methods of averaging the outlet pressure are possible and can impact significantly the pressure gain value which is associated to a combustor. To address this issue and propose a relevant parameter, Kaemming and Paxson [54] introduced the Equivalent Available Pressure (EAP), defined as the flow stagnation pressure which is representative of flow's ability to do work or provide thrust. Since the combustor has to be coupled with a downstream component, either a nozzle or a turbine, the parameter describes a total pressure of an equivalent, steady and homogeneous flow which is able to reproduce actual output of the engine (thrust or work). The EAP can be evaluated either experimentally from the power or thrust measurements or estimated from simulations of the combustor by assuming an expansion of the flow to ambient pressure, thus representing the combustor performances only [54].

The EAP calculation procedure proposed by Kaemming and Paxson [54] for a ram RDE includes a nozzle at the engine discharge and distinguishes between the nozzle throat (n) and the combustor exit (e)

sections. In the configuration studied in this work, the RDC has no outlet restrictions, so the two sections corresponding to the nozzle throat (n) and the combustor exit (e) are assumed equivalent ($n \equiv e$) and extracted from the LES solution at the outlet. Nevertheless, the generic procedure with the explicit distinction is reported for generality.

The ideal Mach number M_{ei} at the engine exit can be evaluated at each node of the LES instantaneous solution through an isentropic expansion to ambient pressure $p_{out} = 1 \text{ atm}$:

$$\frac{p_{0,n}}{p_{out}} = \left(1 + \frac{\gamma - 1}{2} M_{ei}^2\right)^{\frac{\gamma}{\gamma - 1}} \quad (6.3)$$

Then, the ideal exit velocity can be calculated as:

$$V_{ei} = M_{ei} \cdot \sqrt{\gamma R_g T_{ei}} \quad \text{with} \quad T_{ei} = T_{0,n} \left(1 + \frac{\gamma - 1}{2} M_{ei}^2\right)^{-1} \quad (6.4)$$

Assuming that only the axial component of the velocity can be effectively used by a turbine or a nozzle, while the non-axial momentum cannot be easily recovered [54], only the axial component of the ideal exit velocity is considered:

$$V_{ei,ax} = \sqrt{V_{ei}^2 - V_{n,tan}^2 - V_{n,rad}^2} \quad (6.5)$$

The effects of all the flow particles are combined by mass-flow averaging:

$$\bar{V}_{ei,ax} = \frac{\sum \rho_e A_e V_{e,ax} V_{ei,ax}}{\sum \rho_e A_e V_{e,ax}} \quad (6.6)$$

$$\bar{T}_{0,n} = \frac{\sum \rho_n A_n V_{n,ax} T_{0,n}}{\sum \rho_n A_n V_{n,ax}} \quad (6.7)$$

The static temperature of the equivalent flow preserves the total temperature, included the non-axial kinetic energy, and corresponds to an axial expansion to the exit ideal velocity:

$$\bar{T}_{ei} = \bar{T}_{0,n} - \frac{1}{2} \frac{\bar{V}_{ei,ax}^2}{c_p} \quad (6.8)$$

Finally, the EAP_i that is associated to the isentropic expansion of the

equivalent flow to p_{out} can be expressed as:

$$EAP_i = p_{out} \left(\frac{\bar{T}_{0,n}}{\bar{T}_{ei}} \right)^{\frac{\gamma}{\gamma-1}} \quad (6.9)$$

Alternatively, a different EAP_i can be evaluated in the case that also the non-axial components of the momentum could be exploited to produce output. The ideal static temperature after the expansion is now:

$$\bar{T}_{ei}^{full} = \bar{T}_{0,n} - \frac{1}{2} \frac{\bar{V}_{ei}^2}{c_p} \quad (6.10)$$

And the EAP_i relative to the full expansion of all momentum components reads:

$$EAP_i^{full} = p_{out} \left(\frac{\bar{T}_{0,n}}{\bar{T}_{ei}^{full}} \right)^{\frac{\gamma}{\gamma-1}} \quad (6.11)$$

An example of the LES instantaneous exit quantities used for the calculation are reported in Figure 6.7, relatively to a point probe located at $(\theta, r, y) = (340^\circ, 41.2 \text{ mm}, 109 \text{ mm})$. It is interesting to observe that the total pressure presents stronger fluctuations than the static value due to the high speed flow following the shock. The exit flow is essentially aligned with the axial direction and carries the axial momentum, which is a positive contribution to EAP_i . The combustor outlet can be assumed choked in average as the Mach number oscillates around unity, mainly reflecting the axial velocity with a secondary contribution of the tangential component.

These quantities at each node of the outlet section are used to compute the instantaneous EAP_i and EAP_i^{full} according to Eqs. 6.9 and 6.11, respectively. The resulting values are reported in Figure 6.8 beside the area-averaged total pressure $p_{0,e}$ predicted by CFD and measured by Bach et al. [156].

The temporal trends show that the EAP_i is coherent with the instantaneous total pressure at the outlet of the combustor, capturing not only the average value but also its fluctuations. This accordance is not surprising and was also observed in other studies which registered a limited

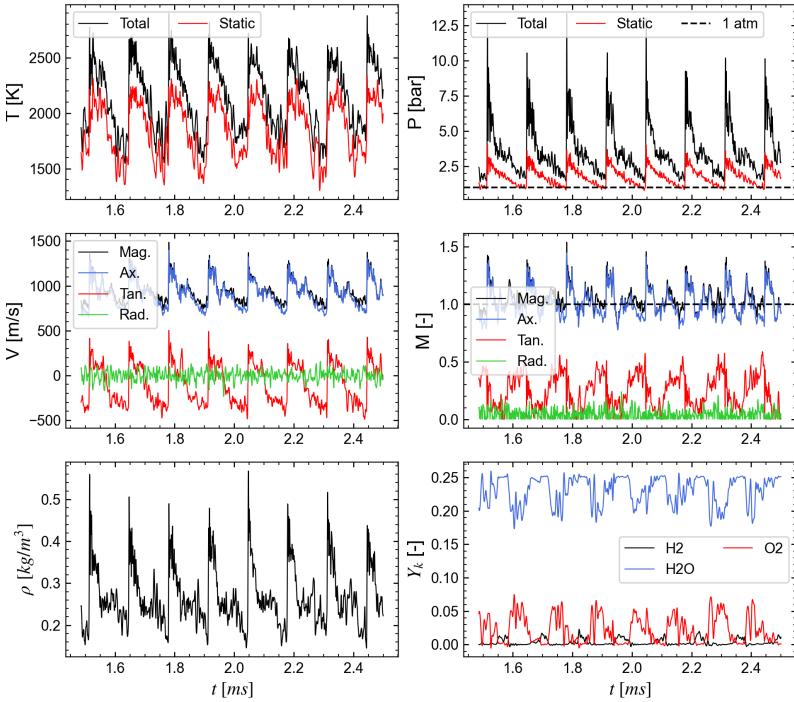


Figure 6.7: Instantaneous, punctual quantities predicted at the half span of the outlet section (e), i.e. $(\theta, r, y) = (340^\circ, 41.2 \text{ mm}, 109 \text{ mm})$.

difference between the time-averaged EAP_i and the total pressure at the combustor exit [54, 171].

The distinct approaches for evaluating the outlet total pressures in Figure 6.8 are also time-averaged during the stable propagation of the wave ($t \geq 0.75$) to calculate the respective pressure gain, reported in Table 6.5. As expected from the time trends, the pressure gain is not affected by the choice of using EAP_i or the exit total pressure $p_{0,e}$, while the more optimistic value of EAP_i^{full} , including also the non-axial momentum, leads to slightly higher value (+2% increase). The findings of this section suggest that the total pressure at the exit can be used as a meaningful

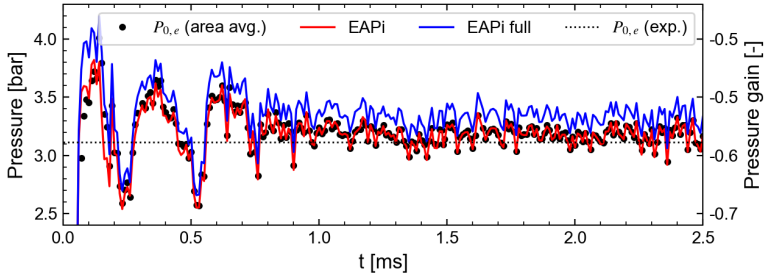


Figure 6.8: Instantaneous EAP_i and total pressure calculated at the outlet section. The dotted line indicates the total pressure measurements by Bach et al. [156].

Table 6.5: Predicted total pressure and EAP_i at the combustor exit and corresponding pressure gain.

	Exit value [bar]	Pressure gain [-]
Total pressure $p_{0,e}$	3.177	-0.57
EAP_i	3.173	-0.57
EAP_i full	3.335	-0.55

value to evaluate the pressure gain of the device, thus supporting the approach carried out in the experiments [18, 49, 172], where a Kiel probe at the outlet is adopted.

Regardless the choice of EAP_i or the exit total pressure $p_{0,e}$, the pressure gain of the device is well-captured by the simulations. In the next sections the discussion will be focused on the detailed analysis of the flow field in the RDC, which cannot be inferred from the experiments, so its description is of paramount importance for understanding the device operation.

6.3 Global flow field features

The complex flow field resulting from the presence of the detonation wave is very important to be characterized since each RDC geometry

and injection system exhibits peculiar features, depending also on the operating condition. Thus, the analysis of the flow field allows a global understanding of the main aspects related to the operation of these devices, such as the three-dimensional detonation features, the development of the refill region and the interaction between the wave and the injectors. These essential aspects will be analysed in the next sections.

6.3.1 Shock structures in the combustor

Similarly to what was observed for the non-reactive case, the primary features which develop within the combustion chamber are directly related to the presence of the shocks and the detonation front. Indeed, these structures drive the operation of the RDC since they influence the mixing of the reactants ahead of the detonation as well as the flow field of the products which expands behind the wave.

For visualizing the main discontinuities present in the combustion chamber, the pressure relative gradient $\nabla P/P$ isosurface is reported in Figure 6.9. The surface is coloured by the values of static pressure, allowing a quantification of the pre-shock and post-shock side of the surface and thus the orientation of the shocks. For a better understanding of the shocks and the induced flow field, the distributions of static pressure and radial velocity are also reported in Figures 6.10 and 6.11.

Several shock complexes are present within the flow and can be divided in the following groups:

- **Detonation front:** it is associated to the maximum compression for its high Mach number ($\approx 4 - 5$) and extends for the whole annulus up to $y = 38 - 40$ mm. The front presents a peculiar three-dimensional shape, especially below $y = 10$ mm as shown by the sections of pressure field in Figure 6.10, which could resemble a Mach reflection along the inner wall. However, the complexity of the fresh gas flow field and the front shape requires a dedicated analysis, which will be discussed in detail in Section 7. Moreover, along the inner wall a higher pressure is reached than in the outer, contrary

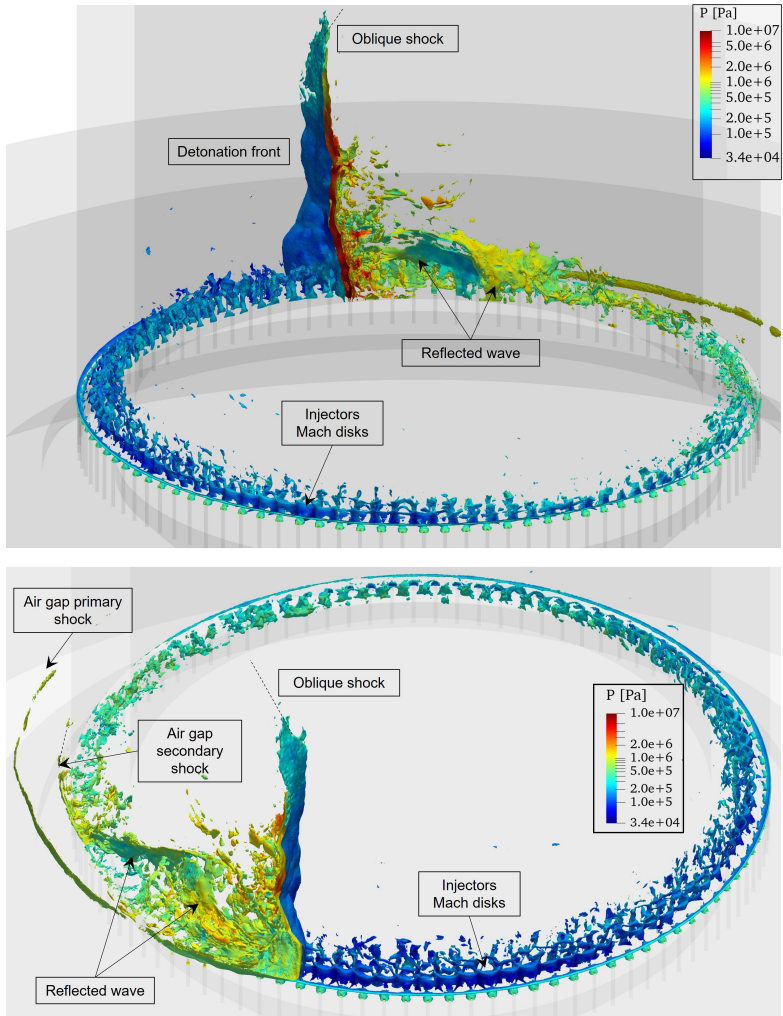


Figure 6.9: Shock structures visualised through the $\nabla P/P = 2000 \text{ m}^{-1}$ isosurface and coloured by static pressure.

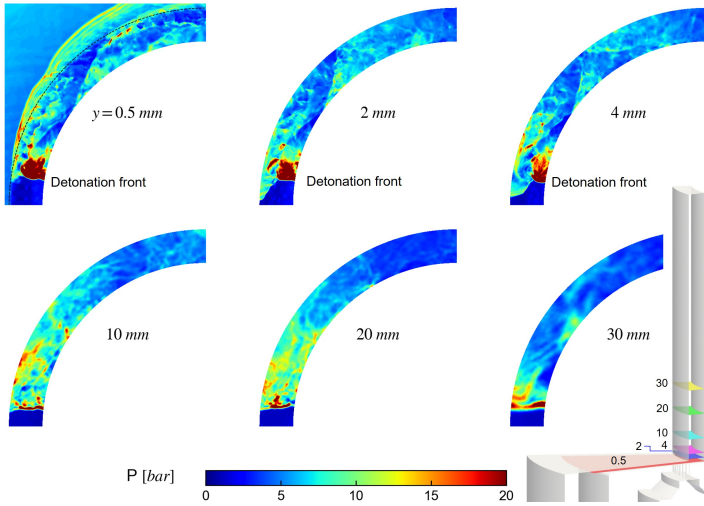


Figure 6.10: Static pressure in different axial sections near the detonation.

to what expected for the presence of expansion waves on the convex wall and compression waves on the concave wall [79, 173];

- **Oblique shock wave at the trailing edge:** it is due to the supersonic propagation of the detonation front which induces an oblique shock starting at the top of the detonation front and reaching the outlet with a spiral shape for the circular annulus.
- **Reflected waves:** a train of reflected shocks follows the detonation front. The first oblique shock starts as a reflection of the leading shock on the outer wall and propagates toward the inner wall, where it is further reflected in direction of the outer wall, describing a sawtooth path. The shocks are evident from the pressure fields in Figure 6.10, but appear only near the base of the chamber. Their main effect on the flow field is visible from the radial velocity distribution in Figure 6.11, and realizes in an inversion of the radial direction of the flow. Specifically, behind the detonation front, the

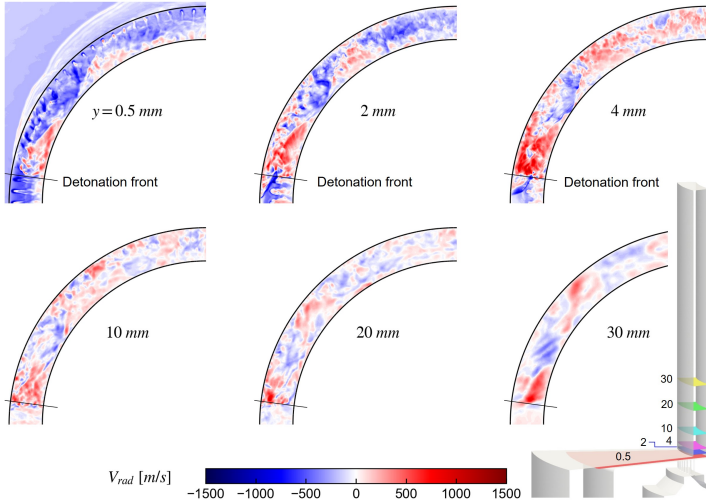


Figure 6.11: Radial velocity in different axial sections near the detonation.

flow expands in the outward radial direction, but after the oblique shock compression shows an inward direction, followed by another deflection. This oscillating motion is expected to influence the injection of the reactants, as will be discussed in Section 6.4. The other velocity components do not show consistent variations across the shock as the radial component. Similar shock waves have been observed in other premixed combustors [17, 70].

- Oblique shock waves in the air injector:** the supersonic rotation speed of the detonation front determines an oblique shock in each un-confined nearby region. The air gap is then invested by a primary spiral-shaped oblique shock which is originated at the intersection of the detonation front with the outer chamber wall. There is however a secondary oblique shock in the air gap determined by the presence of incidence of the reflected shock on the outer wall. Due to the inclination of the reflected wall, the secondary shock originates in

the air gap roughly $\Delta\theta = -55$ deg (14–16 fuel injectors) behind the detonation front (Figure 6.10). The shocks progressively coalesce while propagating upstream in the air flow, weakening their strength, as shown by the numerical schlieren in Figure 6.12.



Figure 6.12: Numerical schlieren ($\nabla P/P$) the base of the chamber ($y = 0$ mm).

- Shocks of the reactants under-expanded jets:** after the detonation blockage, the pressure at the exit of the injectors drops, falling below the critical pressures (3.9 bar for the air and 6.9 bar for the fuel) of the reactants. Since the ducts are both choked, the flows enter the chamber as highly under-expanded jets, determining the formation of the several shock waves (see Figure 5.1). The strongest shocks appear in the isosurface in Figure 6.9, i.e. the Mach disks perpendicular to the reactants flow assuming a semi-cylindrical shape intersecting each other between the injectors. This shock structure is evidently different from the one observed for the non-reactive case

(Figure 5.3). Since the structure of the flow field resulting from non-premixed injection is of particular interest for the optimization of the design and combustor operation, it will be analysed specifically in Section 6.5.

It is worth to remark that the structures described in the present case are specific not only of the geometry but also of the operating condition, so different detonation modes with secondary detonation waves are likely to induce also very different shock structures.

6.3.2 Instantaneous fields

Although several shock complexes are present within the combustor, as shown in the previous section, the flow field is basically driven by the detonation and the oblique shock at the trailing edge, while the shocks near the injectors are smaller structures which influence primarily the fresh gas refill.

For analysing the global features of the flow field in the RDC, the combustion chamber is sectioned at different spanwise locations, represented in Figure 6.13. The instantaneous fields of static temperature, pressure and species mass fraction on such cylindrical sections are reported unwrapped in Figures 6.14, 6.15, 6.16. From all the fields the detonation wave (1) is evident and positioned near $\theta = \pi$. The maps show the typical flow field associated to two-dimensional rotating detonations, especially at the the low-span sections. The oblique shock (2) starting at the trailing edge of the detonation front compresses the burnt products raising their temperature and pressure. The presence of the shock induces the formation of a slip line (3) between the detonated products of one rotation (5) and the products of the previous one. The refill region (4) is linearly increasing after the blockage of the detonation, which partially blocks the flow of fresh reactants.

Nevertheless, the flow field and the detonation front demonstrate a consistent variation with respect to the radial position. The major difference is the alteration of the gas temperature and composition in

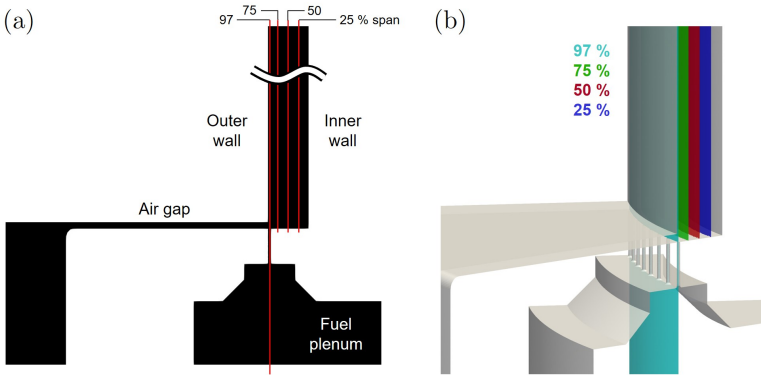


Figure 6.13: Position of the cylindrical sections at constant span in the combustion chamber. (a) xy plane cross section, (b) three-dimensional view.

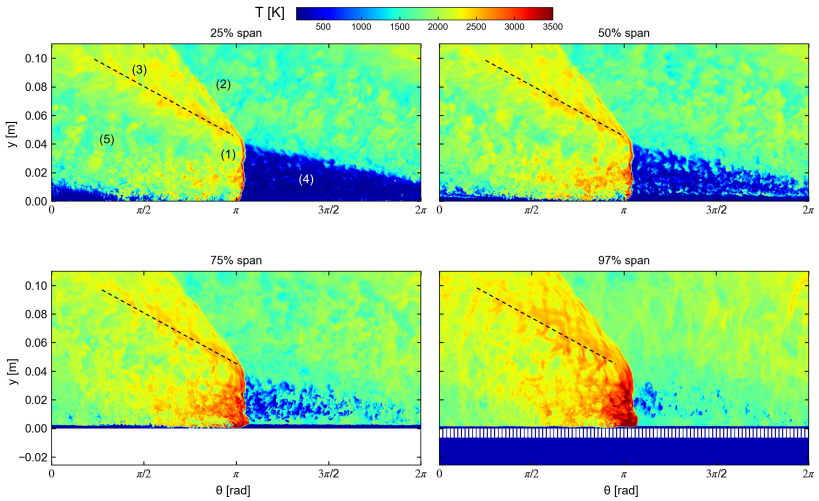


Figure 6.14: Instantaneous temperature on unwrapped cylindrical sections at different spans of the combustion chamber. The dashed line indicates the slip line. (1) detonation; (2) oblique shock; (3) slip line in products; (4) refill region; (5) detonation products.

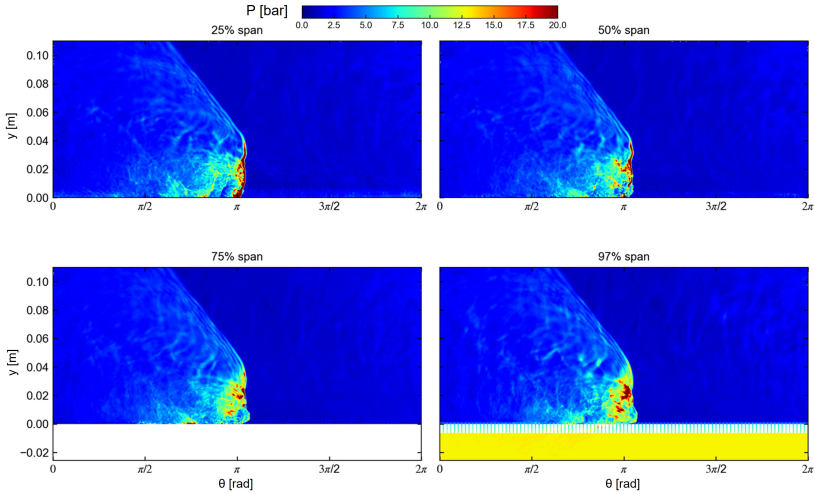
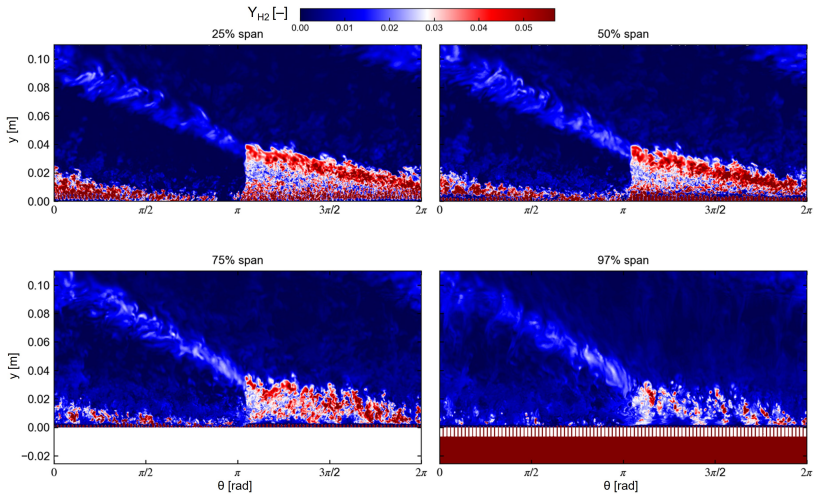


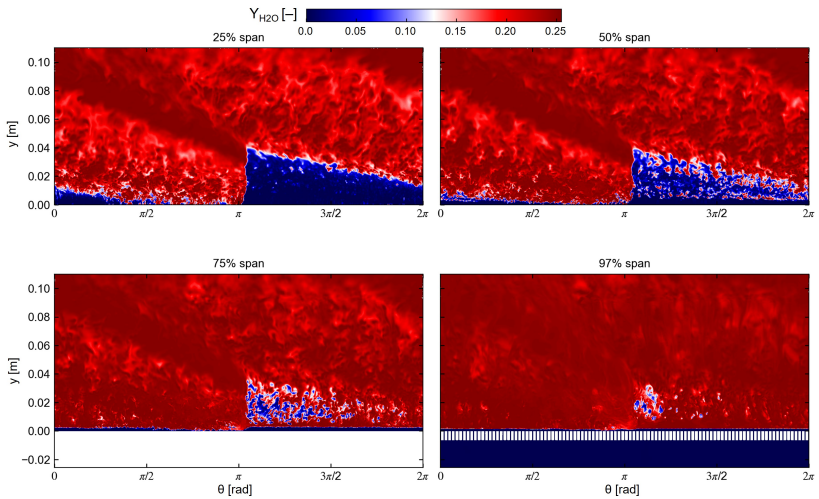
Figure 6.15: Instantaneous static pressure on unwrapped cylindrical sections at different spans of the combustion chamber.

the refill region ahead of the detonation depending on the span-wise position. In fact, the refill region is almost completely constituted by burnt gas stirred with pockets of reactants in the outer half of the chamber (Figure 6.16), while at lower radii the reactants refill is much more efficient, flushing away the products. The pressure maps show that at high span the detonation is also more corrugated and irregular in shape, likely due to the less reactive, vitiated mixture, resulting in a more distributed compression of the flow (Figure 6.15) in comparison to inner radii. Another consequence of the increasing content of products in the refill at higher span is that the detonation compresses and heats already hot gases, leading to temperatures above 3500 K at the outer wall in a relatively wide region (Figure 6.17).

Both the fields of temperature and hydrogen mass fraction (Figure 6.14, 6.16 (a)) present peculiar distributions which are primarily dependent on the reactants injected through the fuel channels and the air gap. Despite the increase in computational demand, the importance of the inclusion



(a) Y_{H_2} . The white color indicates $\phi = 1$ when mixed with air.



(b) Y_{H_2O} .

Figure 6.16: Instantaneous species mass fractions on unwrapped cylindrical sections at different spans of the combustion chamber.

of the whole injection system in the numerical model is evident. Indeed, a simplified injection would miss many fundamental aspects such as the interaction between the wave passage and the flow in the channels as well as the turbulence which is generated by in the refill region (see [70, 71, 74, 79]). In the present model, the complete coupling between the combustion chamber, the injector and the plenum is described accurately, allowing not only the prediction of the feedback above the chamber but also the turbulent mixing which produces the flammable mixture which detonates.

Although the pressure above the fuel injectors behind the detonation is approximately 10 bar (97% span, Figure 6.15) and induces several waves travelling upstream to the fuel plenum, the injectors do not experience any backflow of burnt gases. This desired behaviour is probably due to the high pressure loss of the injector, which decouples the plenum from the combustion chamber and prevents the complete blockage of the fuel flow in the chamber.

As far as the air gap is concerned, experiencing a much stronger pressure feedback than the fuel injectors for the presence of two oblique shocks (see Figure 6.12), no backflow of hot gases occurs outside the chamber wall, as can be observed from the axial section cutting through the height of the air gap ($y = 0.5$ mm) in Figure 6.17. Instead, the temperatures at the base of the chamber are significantly lower than in every other axial section of the chamber, indicating that the hot gas is immediately diluted by fresh reactants. This is a very important aspect since the fresh air keeps the temperature of the chamber head to relatively low values, indicating that this wall could be cooled without much effort.

The interaction between the detonation and the injectors and the characterization of the fresh mixture ahead of the wave are two essential aspects for understanding the operation of the RDC and the propagation of the front, and will be discussed in detail in Section 6.5 and Section 7.2 respectively.

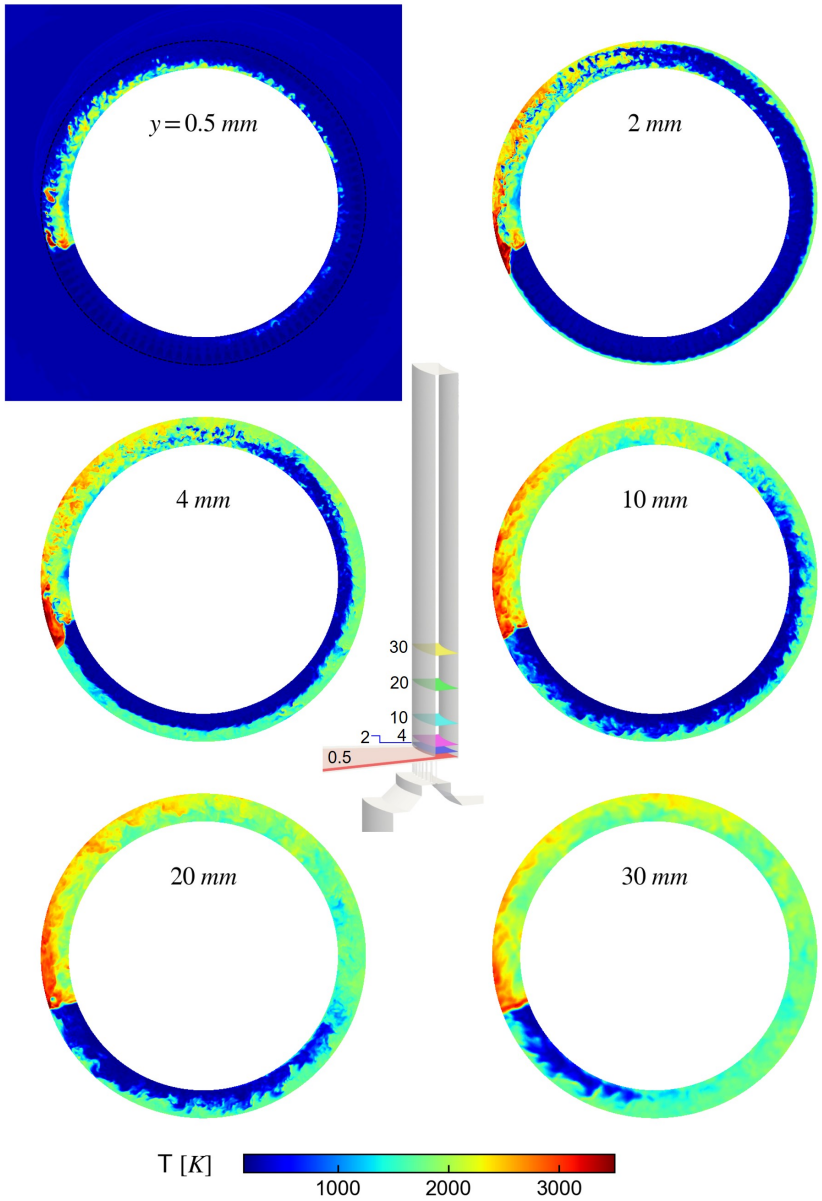


Figure 6.17: Instantaneous temperature on different axial planes of the combustion chamber.

6.3.3 Time-averaged fields

The flow field which characterizes the combustor is not only influenced by the supersonic propagation of the detonation wave but also by the unsteady turbulent fluctuations which are generated by the discrete injection and determine the reactants mixing. Since those fluctuations are stochastic and present small-scale structures, a better understanding of the flow within the combustor can be achieved by a time-average to cancel the turbulence contribution.

With this objective, the instantaneous fields at different span-wise locations are time-averaged in a reference system fixed with the detonation front, which is conventionally traced through the maximum pressure value in the $20 \leq y \leq 30$ mm axial band. The relative time-averaged quantities $\tilde{\varphi}$ are then calculated in each constant span section as:

$$\tilde{\varphi}(\theta_{\text{rel}}, y) = \frac{1}{\Delta t} \int_{t_0}^{t_1} \varphi(\theta - \theta_{\text{det}}(t), y, t) dt \quad (6.12)$$

where $\theta_{\text{det}}(t)$ is the angular position of the detonation in the section and $\Delta t = t_1 - t_0$ is the total time interval with stable propagation. The averaged fields are reported in Figures 6.18, 6.19 and 6.21, where the relative θ_{rel} is shifted by half rotation to ease the visualization.

Flow field: The streamlines of the averaged velocity are superimposed to the Mach number field in Figure 6.18. The maps reveal large differences when the radial section is varied. As observed in the previous section, for low spanwise locations the flow field is similar to a typical two-dimensional RDC field while it progressively develops alterations approaching the outer wall of the chamber. More specifically, the burnt gas flow behind the detonation wave ($0 \leq \theta_{\text{rel}} \leq \pi$) presents a tangential velocity in direction opposite to the front (left), which increases its inclination with the distance from the front. The products which propagates tangentially in the same direction of the front (right) are confined between the oblique shock and the slip line as a result of the oblique shock compression. Within this region the flow is slightly supersonic (≈ 1100 m/s). The sections at

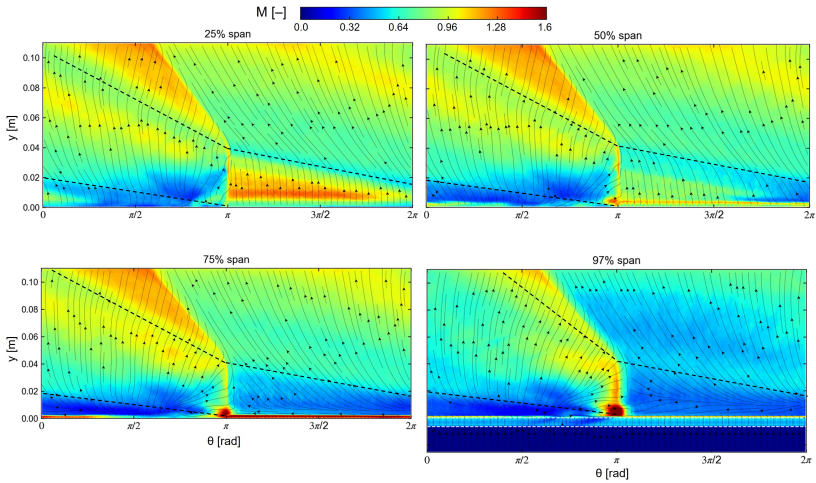


Figure 6.18: Averaged Mach number on unwrapped cylindrical sections at different spans of the combustion chamber and velocity streamlines. The dashed lines denote the refill region.

25% and 50% span exhibit these features, while the section at 75% span shows a lower tangential speed behind the detonation. Near the outer wall of the chamber, the products behind the detonation expand for a longer distance, leading to a tangential velocity mostly aligned with the detonation propagation and a downstream shift of the slip line in the products. However, most of the differences at 97% span could be due to the vicinity of the outer wall of the chamber which prevents a radial expansion.

Gas temperature: The fields of temperature within the combustor feature a consistent dependence on the radial position (Figure 6.19), especially in the refill region. As a result, the inner and the outer adiabatic wall temperatures are quite different, indicating that a cooling system could be focused on the outer wall and achieve a lower efficiency on the inner wall. The time scales associated with the heat transfer in the metal

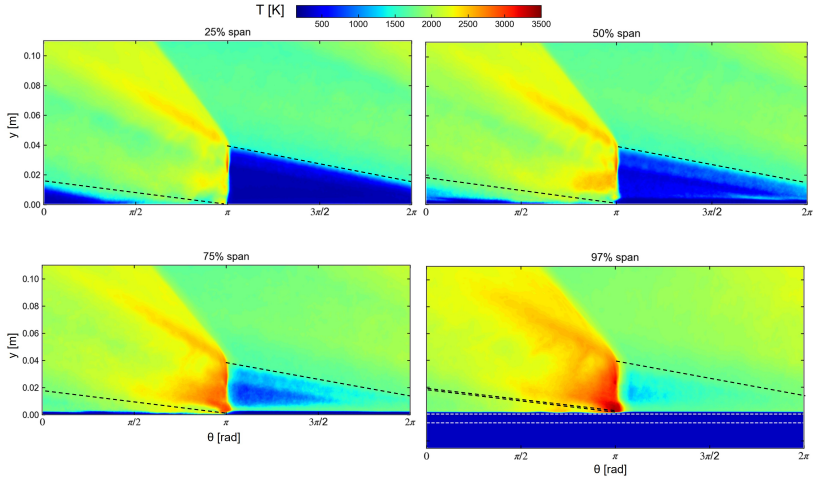


Figure 6.19: Averaged temperature on unwrapped cylindrical sections at different spans of the combustion chamber.

walls are however much shorter than the scales of the detonation passage, so the conduction is not likely to respond to the local temperatures present behind the detonation front. Rather, the relative averaged temperature fields in Figure 6.19 are significant for the heat transfer only regarding their axial and radial variation, so they are averaged in the tangential direction and reported in Figure 6.20.

The profiles show clearly that the major dependence of the temperature is concentrated in the refill region, while above $y = 38$ mm the axial and radial variations are limited (1800 – 2100 K). Within the refill zone, the temperature reflects the radial-inward injection of the air, which forces the fresh gases to the inner wall and thus reduces the temperature at the inner wall. On the other hand, increasing the spanwise position, the temperature progressively increases up to 2000 K, as the hot gases expanding from the detonation moves tangentially along the outer wall and the reactants pockets are likely to deflagrate contributing to the higher heat load.

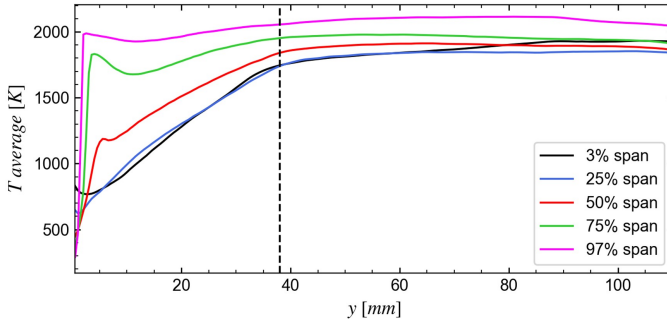


Figure 6.20: Time-averaged axial distributions of temperature at different spans of the combustion chamber. The dashed line indicates the refill height.

6.4 Refill region description

As observed in the previous section, the refill region features a strong dependence on the span-wise position. Again, the peculiarities are present in the outer half of the chamber, where the gases are not refilled as usual with axial flow, but rather through a mostly tangential flow moving away from the detonation (Figure 6.18). The effect of this tangential flow is the vitiation with hot gas of the few reactants which reach the refill region at high span, as evident from the temperature maps in Figure 6.19. As pointed out for the instantaneous distributions, the high pre-shock temperature determines very high post-detonation temperatures along the outer wall, which are not visible in the inner half of the chamber, leading to a consistently lower heat load on the inner wall.

The different flow fields settling in the refill region also influence the mixture composition in this zone, reported in Figures 6.21 and 6.22.

The colormap of hydrogen mass fraction is distributed around the stoichiometric value ($Y_{H_2} = 0.0285$), so that when mixed with air, .i.e. where H_2O is negligible, the white colour indicates a fresh mixture with $\phi = 1$. Since the time-average describes only the average hydrogen mass

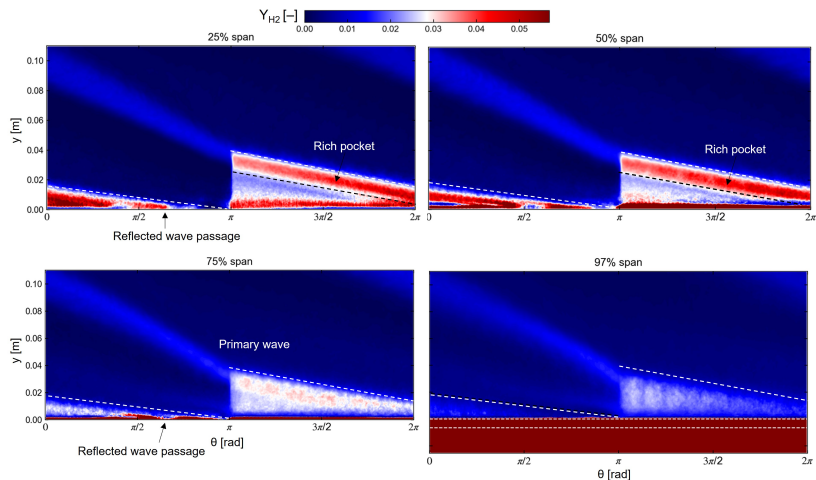


Figure 6.21: Averaged Y_{H_2} on unwrapped cylindrical sections at different spans of the combustion chamber. The white color indicates $\phi = 1$ when Y_{H_2O} is negligible.

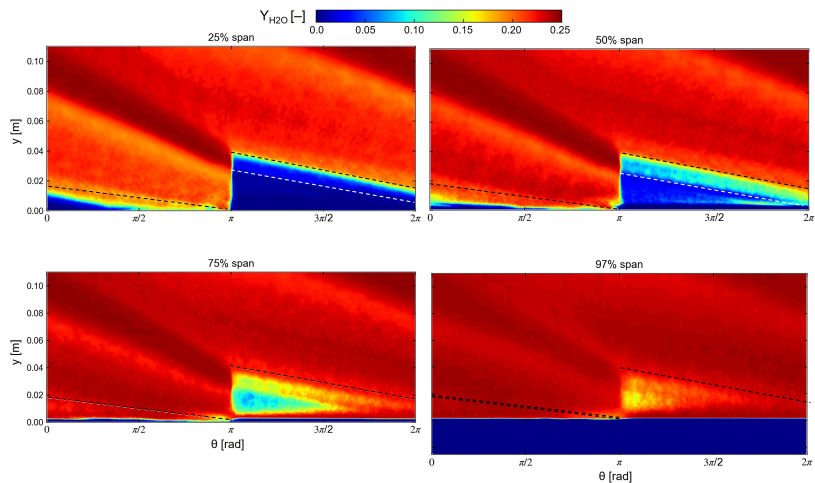


Figure 6.22: Averaged Y_{H_2O} on unwrapped cylindrical sections at different spans of the combustion chamber.

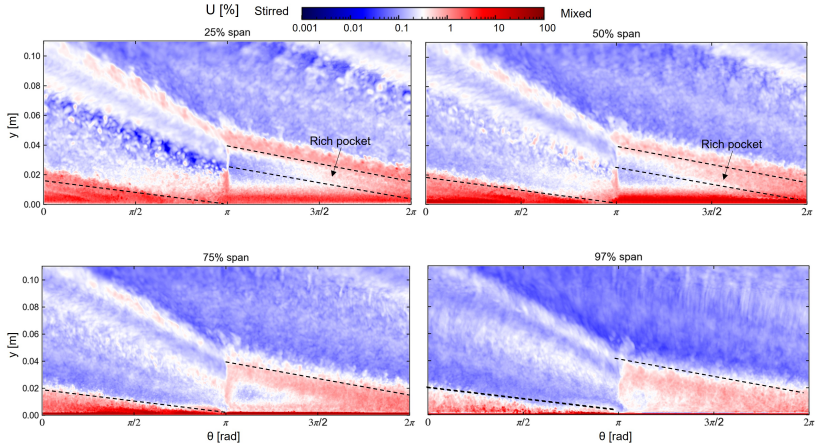


Figure 6.23: Hydrogen unmixedness on unwrapped cylindrical sections at different spans of the combustion chamber.

fraction, a single value could represent either pockets of hydrogen stirred with another gas or a gas mixture with little fluctuation of the hydrogen concentration.

To discriminate between these two opposite cases, the variance $\overline{Y_{H_2}^2}$ of the hydrogen concentration has to be considered. A useful quantity for measuring the level of the hydrogen mixing is the unmixedness U_{H_2} which can be calculated as [157, 174]:

$$U_{H_2} = \frac{\overline{Y_{H_2}^2}}{\overline{Y_{H_2}}(1 - \overline{Y_{H_2}})} \quad (6.13)$$

The unmixedness is an index of the relative variance of the hydrogen mass fraction and is reported for different constant span sections in Figure 6.23.

The features exhibited by the gas in the refill region depend on both the radial and axial position, and are described in the following, discriminating between the inner and outer half of the chamber.

Low-span regions (< 50%): the fuel entering the chamber is immediately stirred with air ($y < 8mm$) and presents a relatively high initial concentration, leading to a rich layer along the base of the chamber (Figure 6.21). However, below 25% of the span a lean, the mixture is homogeneous, probably due to the presence of a recirculation zone at the inner corner as observed for the non-reactive case (Figure 5.4). For higher axial positions, the fuel is well-mixed (low U_{H_2}) and a slightly lean mixture is generated, representing an excellent mixture for the post-shock explosion. This mixture is formed below a H_2 -enriched gas distributed in a defined band at the top of the refill region, for any angular position. The unmixedness in this pocket is unchanged with respect to the underlying lean mixture, indicating that about $90\ deg$ in front of the detonation there is also an axial stratification of the mixture, with a rich gas at the top of the refill height.

The peculiar linear shape of the rich pocket suggests that it is formed at the base of the chamber during the instants following the injectors blockage and then convected downstream almost unaltered (Figure 6.24). The generation of this pocket can be partially attributed to the presence of the reflected wave shown in Figure 6.9, which follows the detonation front and determines the emergence of a secondary shock hitting the fuel jets and later the air gap. This shock reaches the outer wall about $60\ deg$ behind the front and provokes another perturbation of the injectors in addition to main leading shock of the detonation, since it is a high pressure wave and also inverts the radial velocity component (Figure 6.11). As a result, the total blockage of the injectors is relatively long compared to the overall period of rotation, allowing the formation of a rich region at the chamber base during the blockage and early recovery of the reactants streams. The hydrogen jets blockage is clear from Figure 6.25 where the refill region is represented by the nodes with low water mass fraction ($Y_{H_2O} \leq 0.125 \approx Y_{H_2O}^{eq}/2$), i.e. high reactants concentration.

The rich region at the top of the refill region seems to indicate that the interaction of the detonation and the reflected wave with the injectors appears to determine a blockage of the air flow more than the fuel. Since

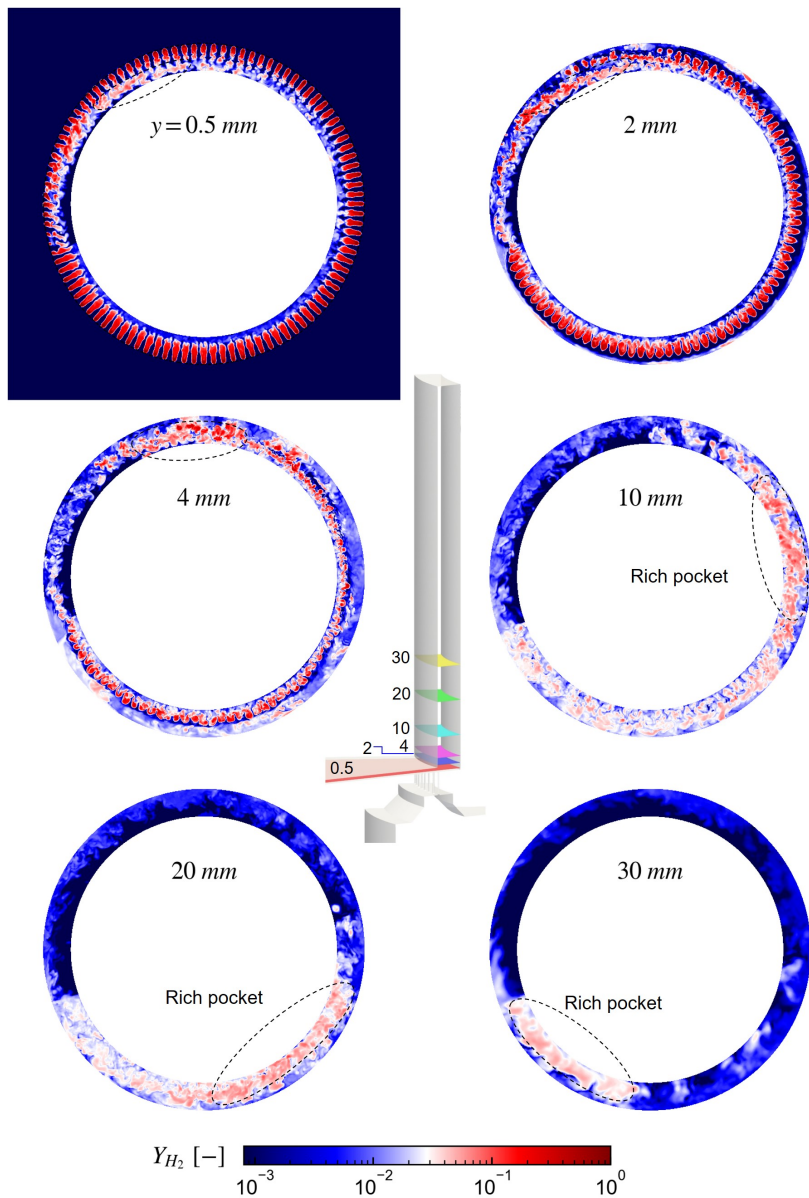


Figure 6.24: Instantaneous Y_{H_2} on different axial planes of the combustion chamber.

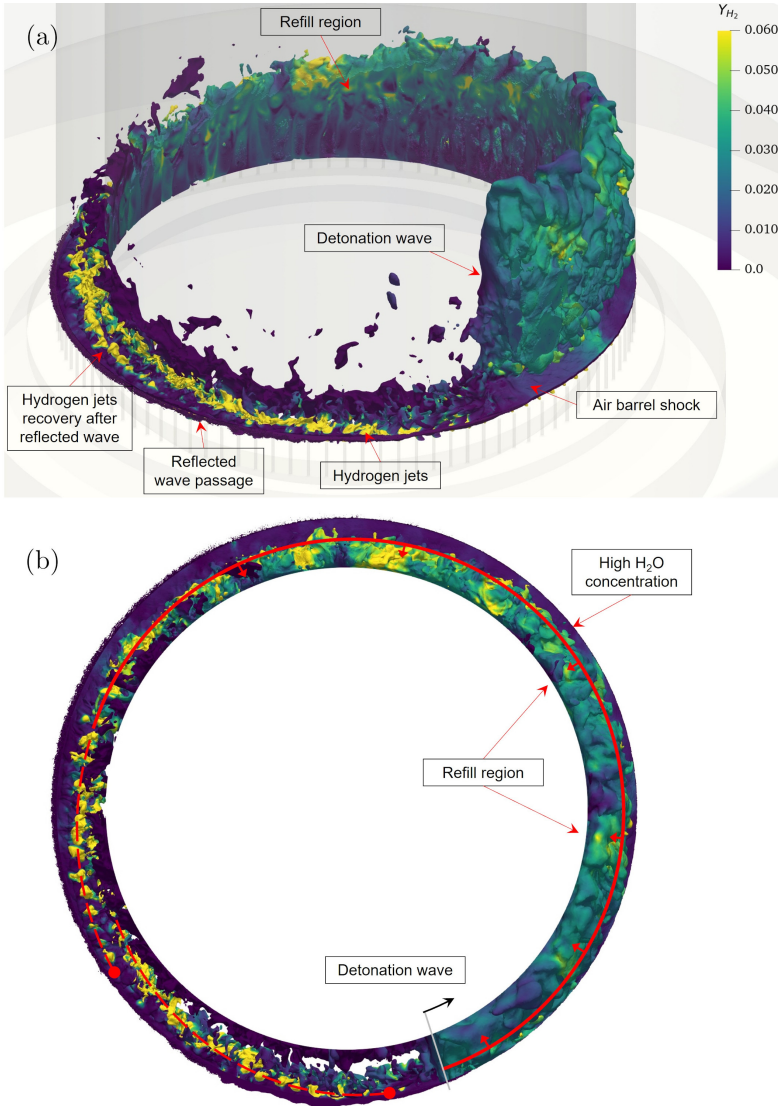


Figure 6.25: Refill region visualised by the nodes with $Y_{H_2O} \leq 0.125$ and coloured by Y_{H_2} . (a) isometric view, (b) top view.

the air flow is the major contribution to the total flow rate, this translates in a local axial velocity deficit which concentrates the fuel near the base of the chamber. Once formed at the base of the chamber, the pocket is transported downstream by the recovered flow. As a consequence, the rich band is present in any axial section of Figure 6.24, where it is highlighted by black dashed lines.

The influence of the reflected shock is thus very important for the fresh gas refill in the lower half of the chamber as it:

- contributes to the blockage of the injectors, generating a wide rich mixture pocket at the top of the refill region (Figure 6.21);
- increases the time required by the injectors for recovering, and consequently widens the region of the perturbed nozzles up to about 100 – 120 *deg* behind the detonation.

The detailed analysis of the injectors operation is thus of major interest for the quality of the mixture generated and will be discussed in Section 6.5.

Apart from the axial variations in hydrogen concentration, at low span the refill of the fresh gas is efficient and replaces the burnt gas, moving downstream the H_2O (see Figure 6.22). Increasing the span-wise position, the rich gas at the top of the refill region starts to show a non-negligible vitiation by the presence of H_2O . This is likely associated to the presence of a deflagration front which forms when the reactants are injected in the chamber filled with hot products, and is then progressively transported axially.

High-span regions (> 50%): here the refill region departs from the ideal characteristics which are exhibited at lower spans. The fresh gases are stirred with hot products starting right above the air gap ($y = 1.2\text{ mm}$), and the variation in the axial direction is less important than in the inner half of the chamber.

These differences between low and high span regions are likely related to the flow field generated by the radially-inward injection of the air, which will be discussed in greater detail in Section 6.5. The inefficient refill

of reactants at high span determines the vitiation of the fresh mixture which does not only reduces the mixture available for the detonation in this region, but also allows the formation of flames where the fuel is oxidated avoiding the detonation regime. As a consequence, the proper refill region extends radially only in the inner part of the combustion chamber ($\leq 50 - 75\%$ span, Figure 6.25), and is surrounded at each boundary, i.e. at its top and radial exterior, by hot products, which induce the formation of deflagration fronts.

Parasitic combustion: the contact between the fresh gas and the products at the boundaries of the refill region is typically associated to the development of a deflagration front which consumes part of the reactants before the detonation. This is an undesired phenomenon in a RDC, where ideally all the fresh mixture should detonate and is referred to as parasitic combustion. In the present case, the deflagration is likely to occur not only at the top of the refill region but also alongside the entire refill region at high span, where the continuous stirring between the reactants and the high temperature products suggests that the deflagrative combustion could be important also in that zone.

To assess the intensity of the deflagration in the simulation, the heat release rate is reported in Figure 6.26 for different spans. The maps confirm that the deflagrative combustion is present both at the top of the refill region and at high spans. The deflagration in the contact layer at the top of the refill region is more intense as the distance from the detonation is reduced, being almost negligible few degrees in front of the wave. The same feature is exhibited by the deflagration at high span, which is more distributed in all the height of the refill region as small flames around pockets of flammable mixture.

It is important remarking that the chemical model adopted for the analysis, namely the global 4S1R scheme, is optimized for the description of the detonation process and underestimates the laminar flame speed for all the compositions. Moreover, no sub-grid turbulent combustion model is used in the present analysis. This modelling limitations suggest that

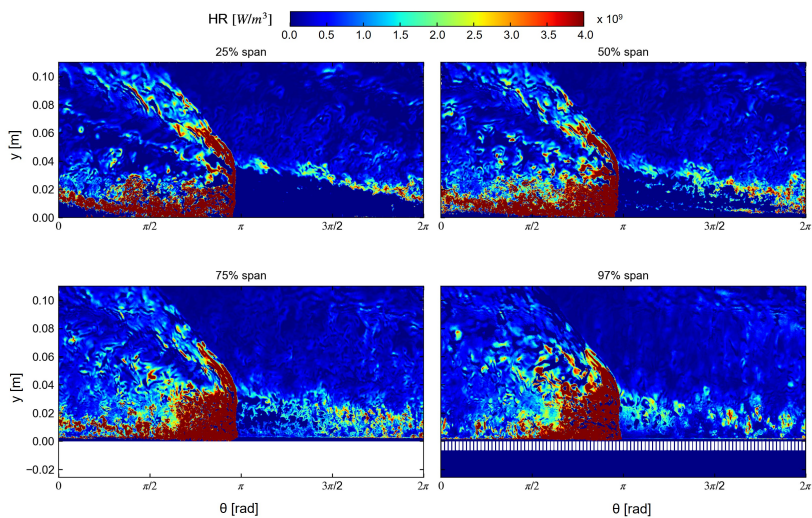


Figure 6.26: Instantaneous heat release rate on unwrapped cylindrical sections at different spans of the combustion chamber.

the deflagration contribution could be underestimated in the simulation, preventing a quantitative confidence in the model when comparing the detonation heat release rate to the one associated to the deflagration. Nevertheless, the chemical scheme does reproduce the dependence on the mixture composition (see Figure 2.27), so at least the qualitative analysis of the regions with higher and lower deflagrative heat release rate could be justified. Indeed, further investigations should take into account also the full contribution of the deflagration on the chemical description for achieving a more accurate description of all the combustion regimes present in the combustor.

6.5 Analysis of the injectors operation

The correct operation of the injectors in a RDC is very complex since a high mixing degree is required during a periodic transient due to the detonation blockage. For this reason, the injectors performances depend inherently on the interaction between the detonation and secondary shock waves in the domain, which alter significantly the flow field which would be associated to the injector in a non-reactive condition. Moreover, the pressure feedback in the injector channels can potentially modify the flow field leading to an inversion of the velocity direction or other disturbances which further delay the recovery of the injection after the detonation passage.

In Section 6.4 the refill region analysis showed distinct features connected with the passage of a secondary reflected wave behind the detonation (see Figure 6.9). It is then interesting to investigate what happens to the flow inside the air and fuel injector considering this double perturbation.

6.5.1 Temporal trends within the injectors

The static pressure signals within the combustion chambers at $y = 25$ mm are compared to the velocity before the end of the air gap ($r = 46$ mm, 1 mm before the chamber) and within a fuel injector ($y = -3$ mm before

the chamber) at the same angular position ($\theta = 90 \text{ deg}$). It is worth to note that the distance between the probes and the chamber is different, so the dynamics of the fuel and air injector are slightly delayed with respect to the pressure peaks. The velocity is reported in the direction of each channel toward the combustion chamber, such that a positive value indicates a flow entering the chamber while a negative value a backflow. The signals are reported for three detonation passages in Figure 6.27.

The pressure in the combustion chamber shows clearly the instant corresponding to the detonation arrival, exhibiting a well-define peak of 60 – 80 bar. The primary peak is then followed after about 0.01 ms by the compression of the reflected wave anchored behind the detonation front, which determines values of pressure around 8 – 12 bar. This secondary peak is evident and more intense at the inner wall of the chamber (I7), probably for the compression due to reflection of the wave in the wall, while at mid radius (M7) the passage of the shock is less clear from the instantaneous values. This difference is also confirmed by the pressure maps in Figure 6.10. Then, the pressure decreases with a negative exponential rate during the period of 0.13 ms which corresponds to the 7.5 kHz rotation frequency of the detonation wave. After the primary pressure peak, the flow in the injector responds very rapidly within 0.01 ms, showing a consistent deceleration to low speed values. More specifically, the air radial-inward speed drops from 210 m/s ($M = 0.7$) to 10 – 20 m/s ($M = 0.1$) while the fuel axial velocity decreases from 1000 m/s ($M = 0.82$) to 500 – 600 m/s ($M = 0.4 - 0.5$). The air flow is thus instantaneously arrested by the shock which propagates upstream in the air gap, while the fuel channels are more resistant to the blockage for their small diameter and high pressure loss.

As already observed in Figures 6.14 and 6.17, again it is worth to note that the static temperature inside the injectors (Figure 6.27) shows that they are interested only by shock waves passage, without any backflow of hot gases neither in the air gap or in the fuel nozzles.

The fuel and air flows respond quite differently also in the duration of the velocity perturbation, as the fuel shows an instantaneous drop

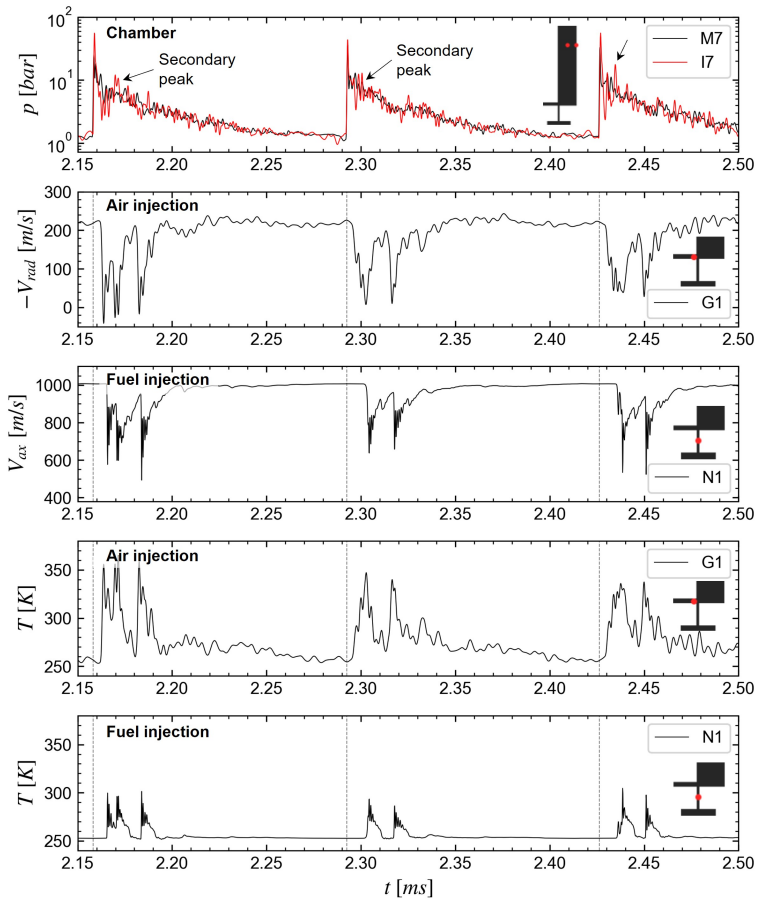


Figure 6.27: From top to bottom: static pressure at the inner (I7) and mid (M7) radius of the chamber ($y = 25$ mm); radial and axial speed and static temperature in the air gap (G1) and in a fuel injector (N1) respectively 1 and 3 mm before the exit in the chamber. The signals are sampled at 7.7 MHz.

of the speed followed by an immediate and fast recover, while the air responds slower to the perturbation and the flow requires more time to accelerate again. As a result, the air velocity drop is longer than the one of fuel. This different dynamic behaviour is likely related to the four-fold difference in the sound speed for the reactants (1300 m/s in hydrogen and 341 m/s in air) and to the geometrical differences of the ducts.

The very interesting aspect is that after the primary blockage, the injectors should start to recover up to the condition before the detonation passage, however, they are again perturbed by the passage of the reflected wave behind the detonation. As shown in Figures 6.9 and 6.10, this wave starts at the outer wall and is oriented in the direction of the inner wall, where it is further reflected toward the air gap. The sawtooth path of this shock delays its incidence on the fuel and air gap to around 60 – 80 deg after the detonation, as the shock has to hit the outer wall of the chamber. This determines a time delay between the secondary pressure peak (occurring 10 μs after the primary) and the perturbation of the injectors which is observed roughly 22 μs later, i.e. 22 μs after the detonation passage. The delay of this secondary perturbation is thus relatively long since it happens at about 20% of the total refill time and its effects on the channels are comparable to the ones due to the main detonation front passage. As a consequence, the double blockage of the injectors determines a considerable time interval for the flow to recover, extending for about 48 μs , a third of the rotation period.

The secondary peak present in the pressure signals 10 μs after the primary cannot be easily observed experimentally, since it is of the same order of magnitude of the sampling time (200 kHz). Even ignoring the delay due to the physical connection to the chamber, the peaks are likely to merge in a longer pressure impulse in the piezo-electric outputs.

6.5.2 Mach number and mass flow rate distributions

Since the combustor flow with a single wave is roughly periodic over one rotation, the transient operation of the injectors can be also visualized by considering the instantaneous flow field along the tangential direction,

i.e. one period, rather than monitoring a single point in time. Indeed, the representation of the quantities in the tangential space enables an effective visualization of the different phases experienced by the flow within the injectors due to the periodic wave passage, allowing a clear definition of the corresponding angular delays. The Mach number components of the flow inside the air and fuel injectors at a fixed instant are reported as a polar plot in Figure 6.28. Additionally, a summary of the events which are experienced by the injectors both in time and space is reported in Table 6.6. In Figure 6.28, a numerical schlieren at the base of the combustion chamber is also represented to highlight the shock structures inside the RDC.

The blockage due to the detonation front occurs at roughly 10 deg behind the wave position and is affecting both the fuel and air at the same time. The injectors then starts recovering until the reflected wave perturbs again the flow about 60 deg behind the detonation, with an intensity only slightly lower than the first blockage. The combined effects of the detonation and reflected wave results in an overall severe perturbation of the injectors up to about 130 deg behind the main front.

Despite the blockages happening at nearly the same time and position to the air and fuel injectors, their effects are considerably higher in the air gap, as can be seen from the flow Mach number components in Figure 6.28 and the flow speed in Figure 6.27. This difference can be mainly attributed to the geometry and feeding pressures of the reactant ducts, which make the air more prone to a severe blockage, not experienced by the fuel injectors.

Since the combustor nominally operates at stoichiometric condition, any local alteration to the fuel and air mass flow rates induces regions which depart from $\phi = 1$. For characterising the local imbalance, i.e. the departure from the ideal stoichiometric condition, the polar diagrams of reactants mass flux and the resulting local air to fuel mass ratio (AFR) are reported in Figure 6.29. The calculated mass fluxes are normalized with respect to their maximum value and highlight clear distinct phases of the reactants injection. In correspondence to the detonation position,

Table 6.6: Timeline of the injectors operation.

$t - t_{\text{det}}$ [μs]	$(t - t_{\text{det}})/T$ [%]	$\theta - \theta_{\text{det}}$ [deg]	Event description
0	0	0	Detonation passage
3.7	3	10	Detonation blockage onset
22	17	60	Reflected wave blockage onset
48	36	130	Recovery to unperturbed injection
133	100	360	Detonation passage

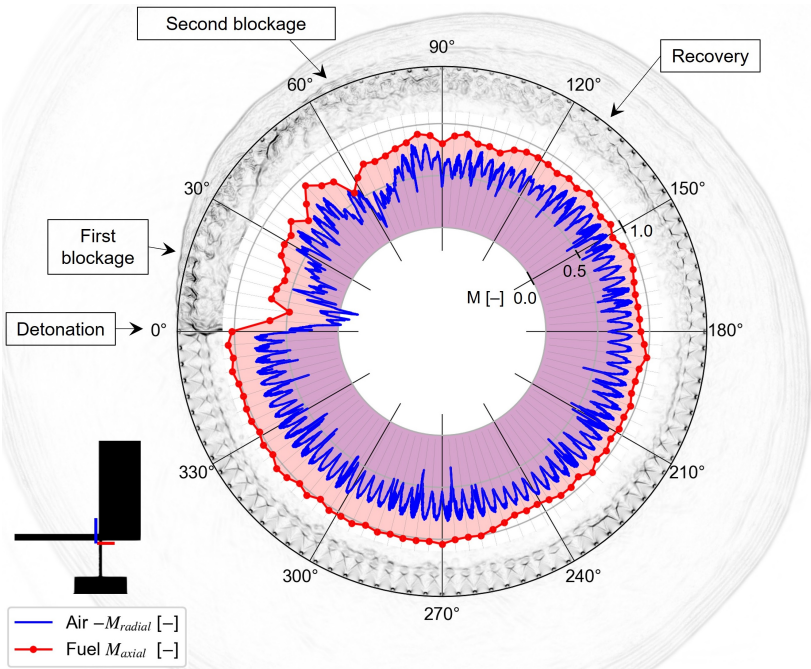


Figure 6.28: Polar diagram of the Mach number at the injectors exit superimposed to numerical schlieren at the chamber base. The curves describe the inward radial component in the air gap ($r = 45.1$, $y = 0.6$ mm) and the axial component within a fuel injector ($y = -0.1$ mm).

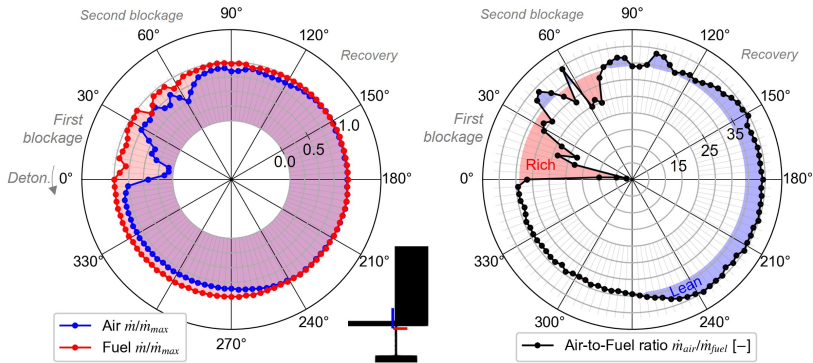


Figure 6.29: Polar diagrams of the local normalized mass flux in the injectors (left) and resulting Air-to-Fuel ratio (AFR, right), where the nominal stoichiometric value is $AFR = 34$. The detonation is located at $\theta = 0$ deg.

the air mass flux is reduced considerably more than the fuel mass flux, determining a local low value of AFR . Therefore, the mixture formed in the first 30 deg behind the detonation front is rich, representing the first mixture which enters the refill region. The air injector recovery brings back the local composition of the mixture around the stoichiometric value ($AFR = 34$) at 40 deg, but then the second blockage of the reflected wave determines again a rich mixture at $60 - 75$ deg.

The polar diagram of AFR in Figure 6.29 clearly shows that the detonation and reflected wave are responsible for the formation of a rich mixture during the first 75 deg behind the front. As observed in Section 6.4, this fuel-rich gas is then convected downstream by the fresh reactants, settling at the top of the refill region as this part is constituted by the first gas entering in the chamber after the wave.

After the second blockage, the fuel mass flow rate rapidly stabilizes to the unperturbed values ($\theta \geq 90$ deg), while the air requires $30 - 40$ deg more. However, while the fuel mass flow rate reaches the choking value, the air mass flow rate exhibits its maximum value between 120

and 270 *deg*, inducing a slightly lean mixture $\phi = 0.85$. Only after 270 *deg* behind the detonation, i.e. 90 *deg* ahead, the air mass flux decreases again, matching the stoichiometric ratio.

This particular phenomenon can be regarded as a consequence of the moving shocks passage inside the air gap and propagating upstream toward the plenum. Since the moving shock induces an increase of total pressure, between 90 and 270 *deg* the local total pressure at the end of the air gap is higher ($\approx +1\text{bar}$), so the fluid is more dense at the throat and the choking mass flow rate is increased (Figure 6.30). This effect

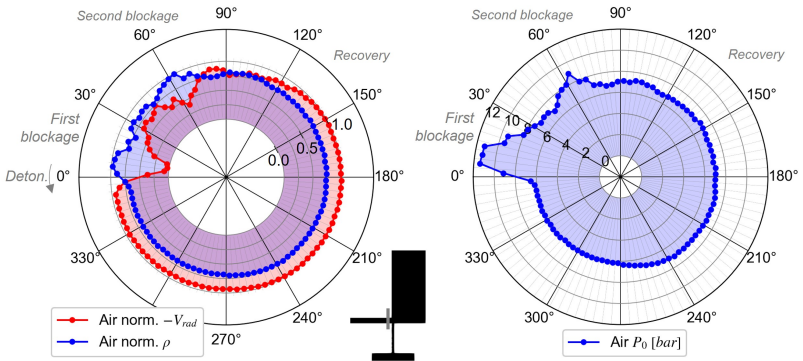


Figure 6.30: Polar diagrams of the local radial velocity and density normalized with their maximum (left) and total pressure (right) in the air injector. The detonation is located at $\theta = 0$ *deg*.

is progressively decreasing with the distance from the shock, until at $\theta = 270$ *deg* the temporary total pressure rise is not relevant, leading to a reduction of mass flow rate.

Secondarily, it is also possible that this mechanism is linked with a local variation of the air throat area. Indeed, the fuel throat area is determined uniquely by the geometry, so that the mass flow rate reaches steadily its choking value. Differently, the air throat area also depends on the shape of the fuel jets, which reduces the geometric area of the air gap. The air mass flow rate is thus influenced by the fuel blockage, and the

air throat area between each fuel jet could to be slightly bigger within 120 and 270 *deg*. However, no evidences of a significant differences in the throat are were observed.

The injectors operation described above determines an axial stratification of the mixture, constituted from the top of the refill height to the chamber base by (1) a rich mixture with $\phi = 1.13 - 1.36$, (2) a lean mixture $\phi \approx 0.85$ and (3) stoichiometric reactants, which have a small time for mixing. Depending on the axial velocity inside the refill region, these three regions will represent different axial portions of the refill height. Their distribution will be presented in Section 7.2.

In conclusion, the analysis carried out in this Section confirms that the detonation and reflected wave have a significant impact on the injectors, determining significant inhomogeneities in the fresh mixture (Figure 6.21), as a consequence of the uncontrolled alteration of fuel and air mass flow rates. Indeed, these are undesired features for the RDC, so the effects of the reflected shock should be taken into account carefully for optimizing the combustor operation. More specifically, The axial stratification of the fresh mixture could be reduced by a re-design of the injectors considering the following points:

- The differential effects of the detonation blockage on the air and fuel injectors determine a rich region at the top of the refill region, so an optimized geometry should try to minimize or equalize the transient response of fuel and air to maintain the equivalence ratio;
- The moving shock propagating upstream in the air injector locally increases the total pressure, increasing the local mass flow rate, thus the injectors geometry should contrast the propagation of the shock;
- The throat area of the air gap is determined by the shape of the fuel jets, so a geometric throat could be preferable as its constant value contributes to reduce mass flow rate imbalances between air and fuel.

6.5.3 Reactants jets flow field in unperturbed and blocked conditions

As observed for the non-reactive condition in Section 5.2, the injectors determine the formation of a jet in cross-flow configuration. Due to the periodic blockage of the detonation, the jets of the reactants which flow from the air gap and the fuel injectors are subject to a continuous variation of their structure. The full capacity of the injectors is reached at the end of the refill region right before the detonation passage, while the minimum capacity is achieved right after the detonation. In between, the injectors are at first hit by the reflected shock but then their flow rate progressively increases (Figure 6.27). Although the pressure conditions in the refill region are influenced by the presence of the detonation, the pressure levels are typically close to the ones at the chamber discharge if no outlet restriction is adopted, as in the present case. This implies that the counter-pressure for the unperturbed nozzles is lower than the critical pressures of both the air (3.9 bar) and the fuel (6.9 bar), so that the reactants enter the chamber as highly under-expanded jets (Figure 5.1). On the other hand, the high pressure behind the detonation distorts completely the jets configuration and the consequent reactants mixing.

For investigating these aspects, the flow field in the proximity of the injectors is reported both before and after the detonation passage. More specifically, the fields of Mach number and hydrogen mass fraction are considered in the x, y cross-section about 4 fuel injectors ahead of the detonation (Figure 6.31) and 4 fuel injectors behind in (Figure 6.34). Additionally, at the same time instants, the axial planes near the base of the chamber are also reported in Figures 6.32 before the passage and 6.35 after.

Full-capacity injectors: due to the lower mass flow rate and the reactive field which is influenced by the gas expanding behind the detonation, the jets configuration is similar to the cold condition but presents different shock structures. The shocks appear to be coherent with a lower degree of under-expansion, with the formation of a barrel shock for the air anchored

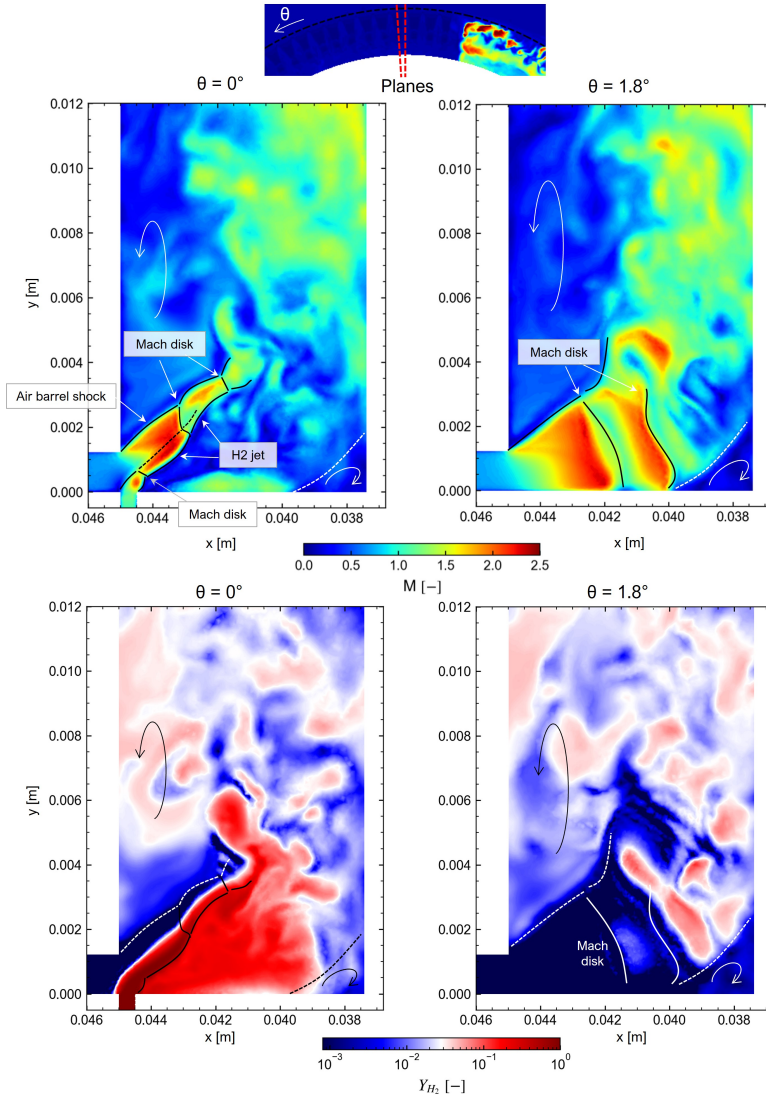


Figure 6.31: Distributions of Mach (top) and H_2 mass fraction (bottom) in the cross-sections through (left) and between (right) the injectors ≈ 14 deg before the detonation passage.

at the air gap edge but significantly nearer the hydrogen jet than in the non-reactive case. The air throat is located in the proximity of the geometric throat, however, it is determined also by the presence of the fuel jets, so that the sonic point is within $44.5 < r < 45$ depending on the plane position. The fuel jet exhibits the typical barrel shock at the exit with a first Mach disc approximately at ($y = 0.5$ mm) and is deflected by approximately 45 deg by the air jet. The fuel jet determines the formation of a subsonic recirculation region aligned with the injectors which is clearly visible from both the Mach and the radial velocity in Figure 6.32. The latter shows that a radial-outward flow settles right behind the hydrogen jets, which promotes consistently the mixing of the jet and results in the formation of a rich region. This zone is confined radially by the periodic supersonic flow of air (Figure 6.32) present between the fuel injectors, so the hydrogen do not reach the $\theta = 91.8$ deg plane (Figure 6.31) at the base of the chamber. Nevertheless, the recirculation region behind the jets progressively expands radially for higher axial location, with the formation of counter-rotating vortices which promotes the hydrogen-air mixing, as shown by the tangential velocity in Figure 6.32.

The air and hydrogen jets form a coherent structure in the plane passing through the injectors, which is featuring two additional Mach disks and a gradual deceleration of the flow. Above $y = 4$ mm, the no defined shock is present but the flow exhibits turbulent fluctuations with slightly supersonic pockets of gas. At this point, the strong fluctuations of the flow disrupt the hydrogen jets and increase the mixing with the air.

Similarly to the non-reactive case, two other recirculation zones are present around the inner corner of the chamber and above the air gap on the outer wall, as displayed in the Mach fields between the injectors (Figure 6.31). In this plane, the flow is dominated by the Mach disks of the air which feature a semi-cylindrical shape (Figure 6.9) and allows the curvature of the flow in the axial direction. As a consequence, a high pressure is present in the inner wall recirculation region to deviate the transonic flow.

The flow which settles in the axial direction is characterised by strong

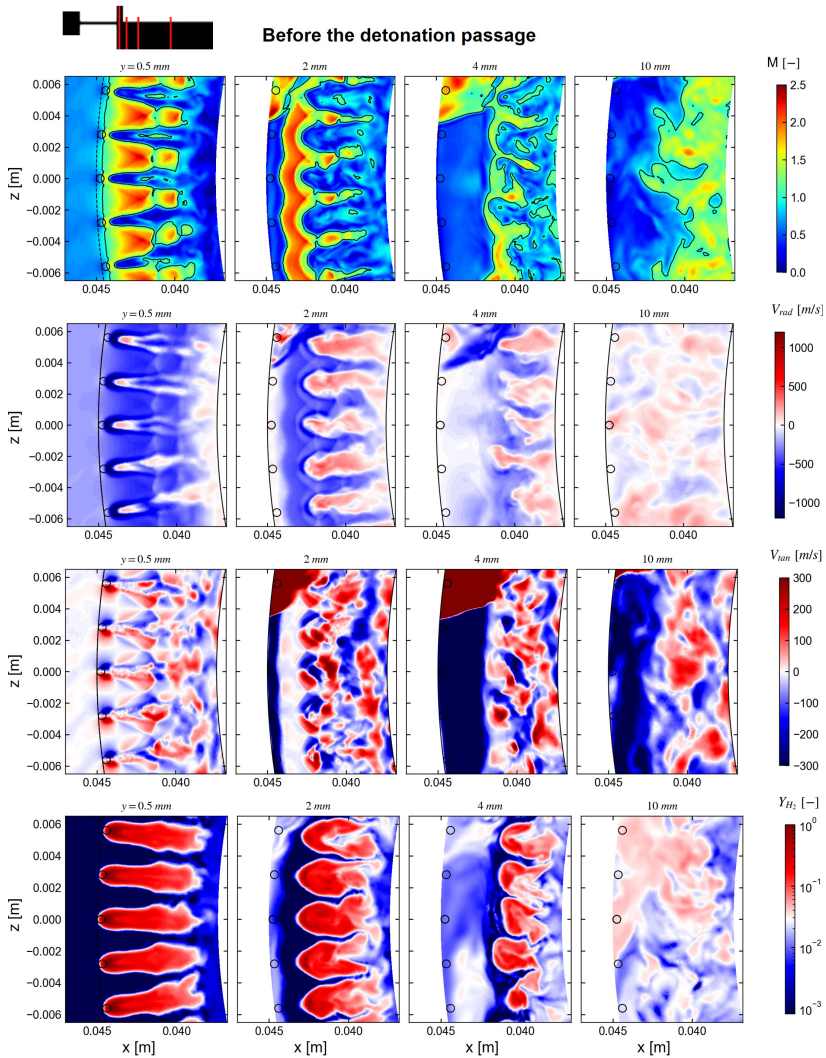


Figure 6.32: Mach number, radial and tangential velocity and Y_{H_2} in the axial planes near the injection before the detonation passage. The white color for the Y_{H_2} corresponds to $\phi = 1$ while positive V_{tan} is counter-clockwise.

fluctuations of the velocity and rapidly accelerates in the axial direction reaching speeds of about 400 m/s (Figure 6.33). The fluctuations of the flow promote the jets mixing way upstream than in the non-reactive case, and the recirculation zone along the outer wall is filled with a nearly stoichiometric mixture at only $y = 4$ mm. This is possible not only for the faster decay of the jets shocks but also because the products expansion induces a negative tangential flow which is particularly fast in along the outer wall, not perturbed by the presence of the jets (Figure 6.32). As a consequence, the recirculation region along the outer wall is mixed with hot gases (Figure 6.33) and, generally, the whole outer wall in the refill region presents high temperature fluctuations. Since the high span region of the refill zone shows a consistent tangential velocity component (see Figure 6.18), it is not clear whether the high temperature represents residual pockets of detonated products or the burnt gases of local deflagrations. Indeed, non-negligible heat release rate reported in Figures 6.33 shows that a flame front is present at the contact between fresh gas and products, even if the heat released there is significantly lower than at the top of the refill region. Therefore, it is likely that both mechanisms contribute to the high temperature near the outer wall, with the detonation products continuously providing local conditions for the development of concentrated deflagrations. However, as explained at the end of Section 6.4, the chemical scheme adopted here is optimized for the detonation regime and underestimates the laminar flame speed (see Figure 2.27), so the deflagration resulting from the model has to be considered carefully.

It is very important highlighting that the detonation front periodically runs into the two mixture states represented in Figures 6.33 (a) and (b), so it faces a periodic oscillation of the fresh mixture properties. This variation needs to be quantified since consistent fluctuations of the gas detonating could potentially alter the front propagation, either locally or globally. The instantaneous maps shown in this section do not allow assessing this aspect, because they do not offer a statistical representation of the average mixture which is ahead of the wave during its rotation in the combustor.

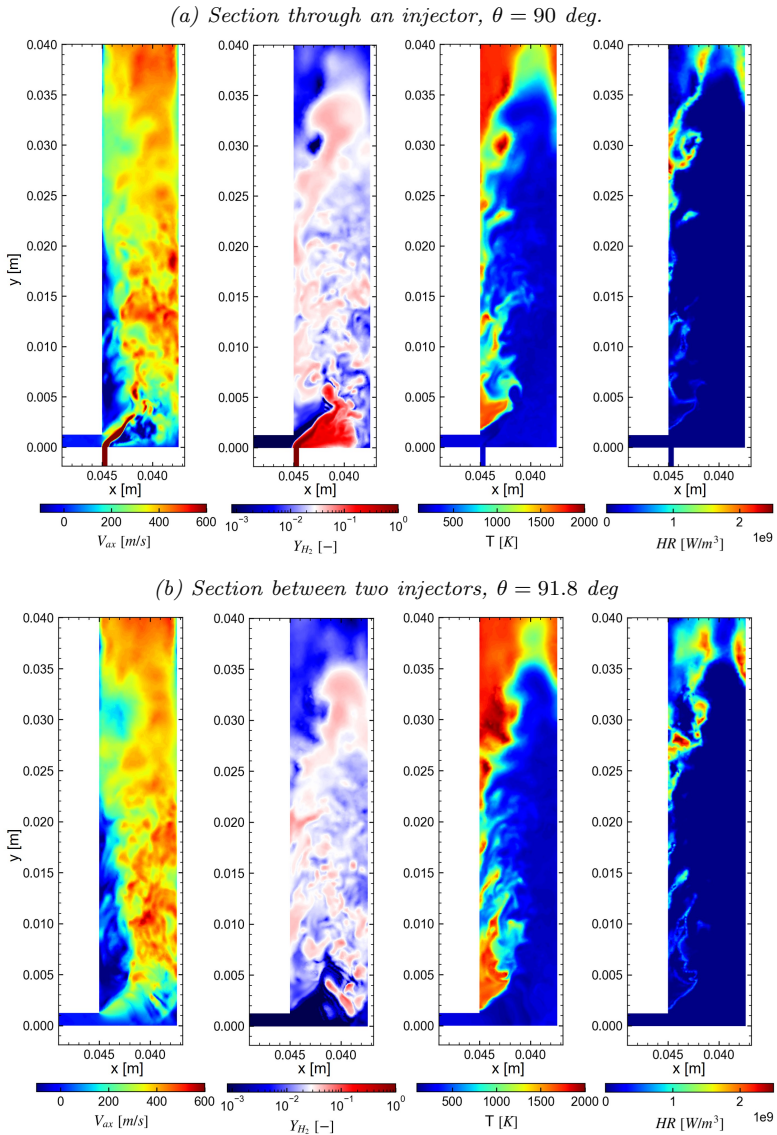


Figure 6.33: Cross-sections ≈ 14 deg before the detonation passage.

More specifically, neglecting rotation-to-rotation variations, three components are contributing to the quantities distributions ahead of the front during a rotation, i.e. a time-average component $\bar{\varphi}$, a periodic variation $\tilde{\varphi}(\theta)$ for the presence of the $N = 100$ injectors ($\Delta\theta_{inj} = 3.6$ deg) and a stochastic fluctuation $\varphi'(\theta)$ due to the flow turbulence [175]:

$$\varphi(\theta) = \bar{\varphi} + \tilde{\varphi}(\theta) + \varphi'(\theta) \quad (6.14)$$

The deterministic periodic component which is encountered by the detonation front can be obtained by removing the stochastic fluctuation but accounting for the periodic variation in phase with the injectors:

$$\varphi_{\text{per}}(\theta) = \bar{\varphi} + \tilde{\varphi}(\theta) \quad (6.15)$$

Introducing the angle $\alpha \in [0, \Delta\theta_{inj})$ to describe the angular position between two generic injectors and expressing $\theta = \alpha + k\Delta\theta_{inj}$ with $k \in \mathbb{N}[0, 99]$, Eq. 6.14 can be recast in:

$$\varphi(\theta) = \varphi_{\text{per}}(\alpha) + \varphi'(\theta) \quad (6.16)$$

where the deterministic periodic component can be evaluated through the Phase-Locked Ensemble Average (PLEA) according to:

$$\varphi_{\text{per}}(\alpha) = \frac{1}{N} \sum_{k=0}^{N-1} \varphi(\alpha + k\Delta\theta_{inj}) \quad (6.17)$$

since the stochastic part vanishes:

$$\frac{1}{N} \sum_{k=0}^{N-1} \varphi'(\alpha + k\Delta\theta_{inj}) = 0 \quad (6.18)$$

The evaluation of Eq. 6.17 requires the extraction of the gas state $\varphi(\theta)$ in each point continuously preceding the detonation front, at a minimum distance. Although this procedure is particularly complex since it requires tracking the detonation front, it guarantees a detailed statistical description of the mixture which detonates, including also the periodic

variation due to the injectors. This specific problem will be addressed in Section 7.1.

Blocked injectors: Although the pressure waves induced by the detonation passage reduces consistently the speed both in the air gap and in the fuel channels (Figure 6.27), the perturbation is instantaneous and the flow speed rapidly recovers. However, the different sound speed in the reactants induces a longer alteration of the operation for the air injector rather than the fuel. This is clear from Figure 6.27 but also from Figure 6.34, where the air Mach number is still very low with respect to the full-capacity value (Figure 6.31). As a consequence, the air flow is subsonic 14 *deg* after the detonation passage and does not accelerate to supersonic values entering the chamber, preventing the formation of the choked or under-expanded jet shocks. On the other hand, at the same instant the fuel nozzles are already choked, showing that after the pressure wave passage in the channel the flow recovers very rapidly. The fuel jet is however very weak and dissipates as soon as enters the chamber, forming rich pockets of hydrogen concentrated around the nozzle exit (Figure 6.35), without reaching the inner wall.

The overall flow in the chamber is thus mostly subsonic, with some supersonic regions determined by gases moving tangentially along the outer wall of the chamber, since the region is dominated by the expansion of the hot products.

The first shock wave reflection behind the detonation is also clearly visible on the Mach fields in Figure 6.34. As this shock wave primarily (see Section 6.3.1) deviates the flow in radial direction, the gas below this shock is expanding toward the outer wall, while above the flow is redirected toward the inner wall (Figure 6.35). At the same time the gas expands toward the chamber outlet, since the hot products cannot expand at the base of the chamber other than to higher axial positions. The combination of these two fluid motions could be probably the cause of the shock inclination. The radial-outward flow around the inner corner contributes also to confining the hydrogen far from the inner wall of

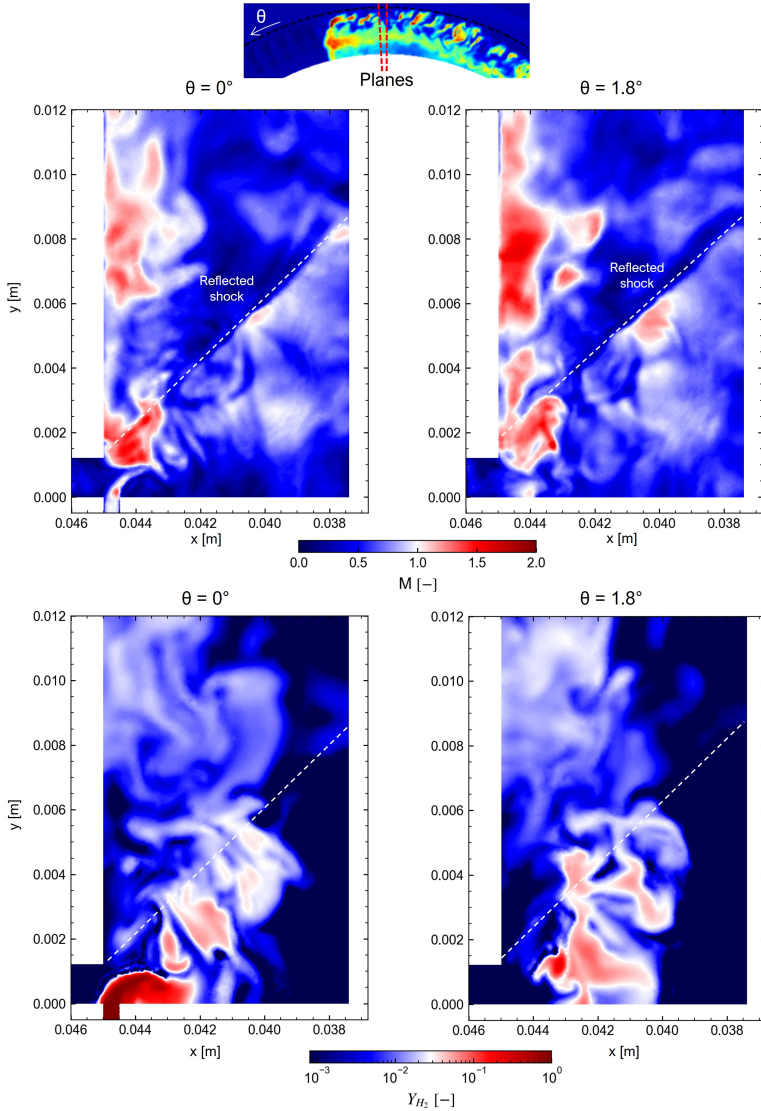


Figure 6.34: Distributions of Mach (top) and H_2 mass fraction (bottom) in the cross-sections through (left) and between (right) the injectors ≈ 14 deg after the detonation passage.

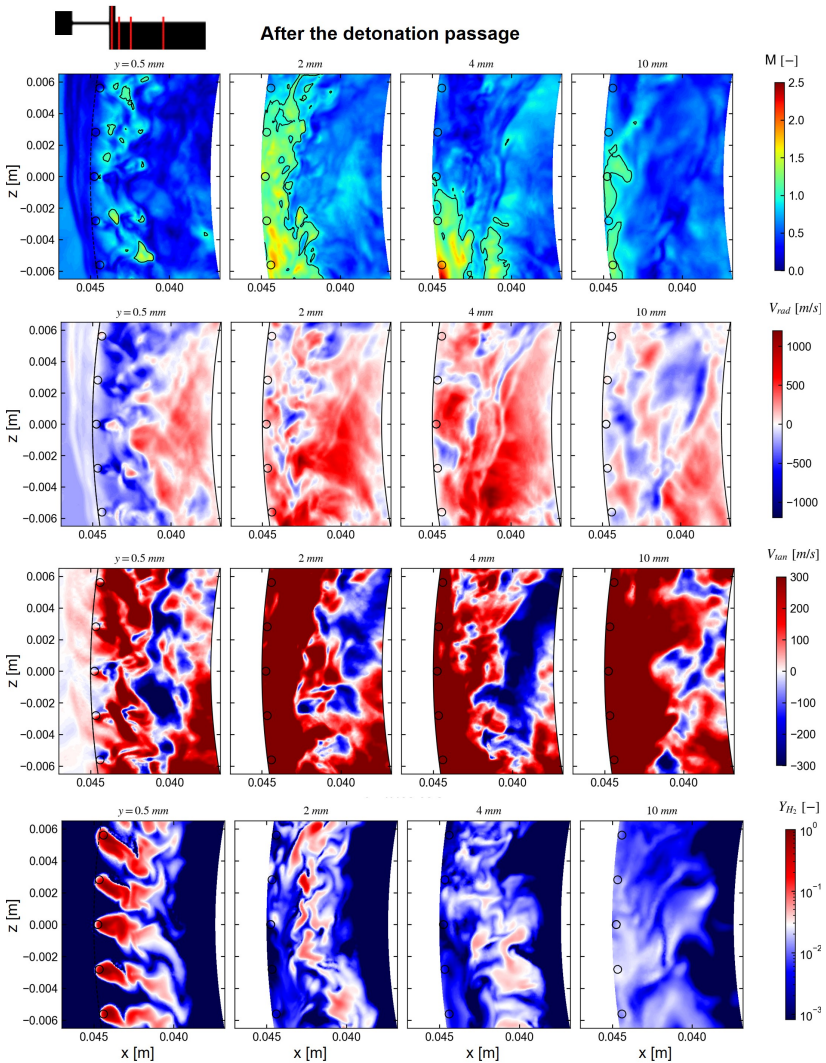


Figure 6.35: Mach number, radial and tangential velocity and Y_{H_2} in the axial planes near the injection after the detonation passage. The white color for the Y_{H_2} corresponds to $\phi = 1$ while positive V_{tan} is counter-clockwise.

the chamber. Despite the presence of the reflected wave in the fields, the effects of its second reflection are still not apparent in the planes of Figure 6.34, and appear only later on the fuel and air injectors (see Section 6.5.2).

6.6 Mesh quality assessment

In this section, an assessment of the simulation resolution in the reactive conditions is carried out to determine the adequacy of the mesh element size to describe the turbulent flow field.

It is worth to remark that the preliminary study of the detonation in a 2D channel presented in Chapter 3 demonstrated that the detonation speed is marginally affected by the element size, as it depends primarily on the thermodynamic properties jump. Although the single-step chemistry relaxes the post-shock gradients, the mesh size adopted in the simulations does not allow a complete resolution of the detonation front and to distinguish between the leading shock compression and the following heat release, as the half-reaction thickness for these conditions (Table 2.3) is of the same order of magnitude as the characteristic cell size. This inaccuracy is expected to potentially influence the detonation in extreme cases such as near the detonability limits, but further studies are necessary to clarify the sensibility of the whole device to these effects. A further refinement of the spatial discretization would consistently increase the computational cost of the analysis, but indeed it should be considered if more detailed chemical scheme involving radicals is used. In other words, the use of a detailed chemistry and the reaction thickness resolution are inevitably coupled and an valuable improvement with respect to the present model is expected only considering both the aspects at the same time.

As far as the turbulent flow field is concerned, due to the complexities connected to the calculation of a time-averaged flow field in the combustor to characterize the turbulent kinetic energy, the Celik's parameter [168] is adopted for the quality assessment. The same procedure applied to the non-reactive case is repeated for the reactive conditions, so that the

indexes can be compared to each other.

The Celik's quality index based on the viscosity QI_v is defined as [168]:

$$QI_v = \frac{1}{1 + \alpha_v \left(\frac{\mu_{sgs} + \mu_{num}}{\mu} \right)^n} \quad (6.19)$$

with $\alpha_v = 0.05$ and $n = 0.53$. The parameter depends on the ratio between the simulation effective viscosity $\mu_{eff} = \mu_{sgs} + \mu_{num}$ where μ_{num} represents the apparent viscosity induced by the numerical discretization. This viscosity is very complex to determine and is here neglected with respect to the sub-grid value calculated according to the WALE model [170]. The resulting quality index is reported in Figures 6.36 and 6.37.

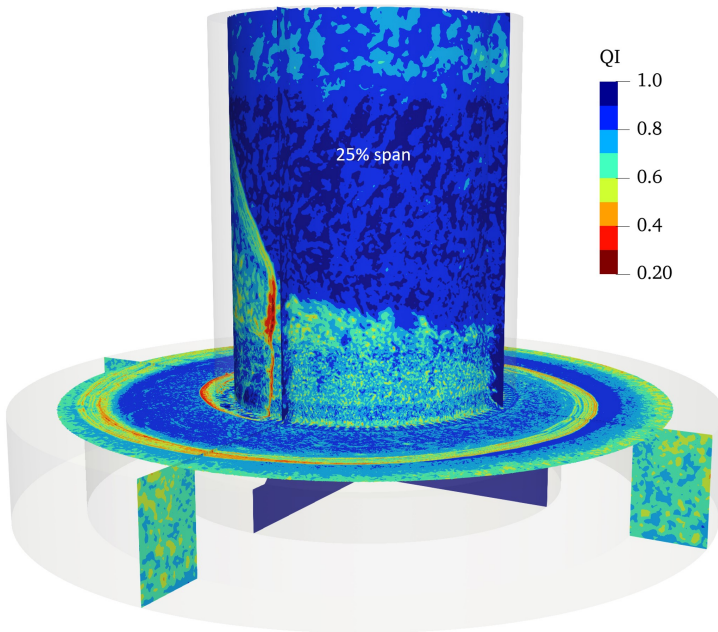


Figure 6.36: Celik's quality index for the reactive LES.

The flow field which settles in the domain is radically different from

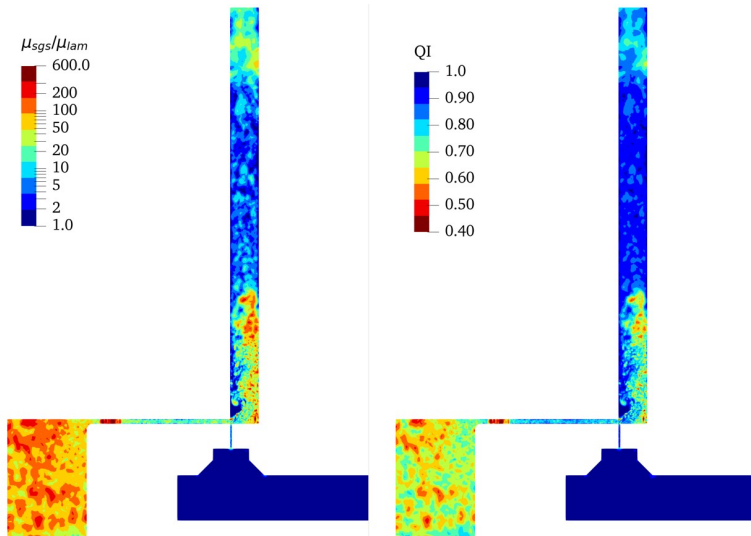


Figure 6.37: Viscosity ratio (left) and Celik's quality index (right) on the x, y cross-section before the detonation passage.

the one of the non-reactive condition and leads to a different index distribution with respect to Figure 5.9. Here, the turbulence in the refill region develops rapidly and leads to values between 0.7 – 0.9, with a lower quality outside the refinement region at the base of the chamber. Nevertheless, the acceleration of the burnt gases in the central region of the chamber is associated to high index quality (0.8 – 1), despite the relatively coarse mesh size in such zone. Across the detonation, the mesh index slightly increases. Considering that low quality values are inherent to the flow discontinuities, the mesh discretization appears adequate for the resolution of the flow field. The main region which could be further improved is the turbulent part of the refill region near the inner wall of the chamber, where a smaller mesh size could help capture the fluctuations and the mixing. Furthermore, the refinement at the base of the chamber could be extended downstream up to $y = 40$ mm, i.e. including the totality of the refill region. In fact, the mesh index highlights how the

most demanding region in terms of spatial discretization is the refilled gas rather than the products in the combustion chamber. Of course the refill height is not known a priori and depends on the wave propagation mode but the present work can provide a baseline value which can be scaled with mass flow rate for the test points with a single dominant wave (SW).

In conclusion, the following recommendations for the future investigations of the TU Berlin RDC can be provided:

- The air gap, the fuel channels and the under-expanded reactants jets require the use of specific mesh refinements;
- The flow field in the refill region is the most important region to be described and should be discretized with a uniform mesh sizing in the axial direction, eventually with coarser elements along the outer wall;
- The detonated products flow can be captured without specific discretization efforts.

6.7 Concluding remarks

In this chapter, the non-premixed RDC installed at TU Berlin is studied numerically by solving the spatially-filtered, fully-compressible, multispecies, reactive Navier-Stokes equations with the AVBP code. For describing the detonation process the 4S1R global scheme, developed and presented in Section 2.3.2.1, is adopted. A stoichiometric, single wave test point is considered for the analysis and investigated in reactive conditions.

The main outcomes of the numerical investigation can be summarised as follows:

- After the detonation initiation, a single wave establishes in the combustor and propagates steadily according to the experimental observations. However, the simulation overpredicts the wave rotation frequency by 19%. On the other hand, the pressure gain of the device is captured with excellent accuracy, with the exit total pressure matching the value measured experimentally.

- The shocks structure in the reactive case shows the presence of a reflected wave following the detonation front, which determines a secondary shock in propagating upstream within the air injector, but delayed with respect to the wave induced by the detonation. This second blockage of the air flow retards the recovery of the injectors, lasting about 30% of the wave rotation period.
- The different blockage of fuel and air injectors induces an axial stratification of the fresh gas composition, constituted by a rich mixture at top of the refill height, a lean mixture in the centre and stoichiometric, partially-mixed reactants at the base. These gas regions are formed at the base of the chamber and then convected downstream as soon as the mass flow recovers.
- The axial stratification of the fresh mixture could be reduced by a re-design of the injectors which (1) minimizes or equalizes the transient blockage of fuel and air to maintain the equivalence ratio, (2) obstructs the propagation of the shocks in the injectors and (3) fixes the throat area of the air gap geometrically, reducing impact of the area blockage due to the fuel jets.
- At full capacity, both the air and fuel injectors are choked and the reactants enters the chamber as under-expanded jets, which quickly decay to a subsonic flow with supersonic pockets concentrated along the inner wall. Above the air gap, a recirculation region is present, with the flow featuring a non-negligible tangential component which moves the hot products away from the detonation. As a consequence, the outer wall is surrounded by burnt gases that also lead to the formation of localized deflagration fronts. Therefore, the refill gas is characterized by a three-dimensional heterogeneity of the gas properties, with vitiated reactants in the outer half of the chamber, a faster flow of fresh gas along the inner wall and a rich region at the top of the refill height produced by the second perturbation of the injectors during the early recovery.

Chapter 7

Analysis of the detonation front topology and propagation

Contents

7.1	Data extraction procedure	226
7.1.1	Detonation speed calculation	228
7.2	Fresh mixture characterization	231
7.2.1	Periodic variation due to the discrete injectors	234
7.2.2	Local Chapman-Jouguet speed	238
7.3	Detonation front topology	242
7.4	Detonation front speed	246
7.4.1	Assessment of the tangential variation . . .	251
7.5	Concluding remarks	255

The characterization of the refill region discussed in Chapter 6.4 showed a three-dimensional dependence of the mixture state with important variations along the radial and axial directions. Moreover, the presence of the discrete fuel injectors induces a periodic variation of the gas properties which could potentially affect the propagation of the detonation front as well as its local orientation.

The high-fidelity simulation allows the detailed investigation of these aspects, so in this chapter the analysis of the front topology and propa-

gation is discussed. In parallel, the fresh mixture ahead of the front is characterised systematically by considering a moving plane preceding the front. A dedicated processing algorithm is developed for tracking the detonation front and sampling the fresh mixture state right before the wave passage. The combined analysis enables the comparison between the front topology and speed to the local gas properties, and thus the investigation of their eventual correlation.

7.1 Data extraction procedure

Since the scope of this section is the study of the detonation front propagation, both the front and the mixture state ahead are determined using a high sampling rate during an additional complete revolution of the wave. A specific extraction algorithm is developed and executed with a constant interval of $\Delta t = 3.25 \times 10^{-8}$ s (31 MHz), corresponding to roughly 4100 samples per revolution (41 per each gap between two injectors). Basically, the procedure is constituted by two steps, which are summarised as follows:

1. **Detonation front identification:** a constant static pressure ($p = 9$ bar) isosurface is exported and processed to discriminate the nodes laying on frontal surface from all the others, i.e. to obtain a surface $\theta(r, y, t)$. This operation is carried out by selecting the points on the isosurface with the maximum angular position within a radial-axial, half overlapping moving window of 0.5×0.5 mm. Also, the mean angular position of the front $\theta_m(t) = \sum_{r,y}^M \theta(r, y, t)/M$ is calculated.
2. **Frontal plane extraction:** the solution is interpolated in a r, y regular planar grid of 0.1×0.1 mm immediately ahead of the detonation. To ensure that the plane never intersects the front a constant forward shift of the mean angular position of the front in the direction of propagation is applied, i.e. the plane at $\theta_p(t) = \theta_m(t) + \Delta\theta$ with $\Delta\theta = 10$ deg is considered.

The final output of the whole process is the series of instantaneous

detonation front surfaces $\theta(r, y, t)$ and fluid properties $\varphi(r, y, \theta_p(t))$ on the plane before the detonation passage. The local values of p, T and composition Y_k are also used as inputs for calculating the Chapman-Jouguet speed D_{CJ} through the Shock Detonation Toolbox [113] based on the Cantera 2.4.0 [111] libraries for Python3. For the CJ speed calculation the 4S1R thermodynamic parameters are used.

It is worth noting that the mixture state in the frontal plane does not correspond exactly to the mixture which detonates, i.e. $\theta(r, y, t) \neq \theta_p(t)$, since the detonation front requires a small but finite time interval $\Delta t \approx (\theta_p - \theta)/\omega_{det}$ to occupy the position of the sampling plane. However, the very high speed of the detonation front ($\omega_{det} \approx 47\,000 \text{ rad/s}$) and the small distance $\theta(r, y, t) - \theta_p(t) \approx 10 \text{ deg}$ between the detonation front $\theta(t)$ and the frontal plane $\theta_p(t)$ allows to neglect the temporal variations of the flow within $t \pm \Delta t$ in a fixed point (r, y, ϑ) :

$$\varphi(r, y, \vartheta, t) \approx \varphi\left(r, y, \vartheta, t \pm \frac{\theta_p - \theta}{\omega_{det}}\right) \quad (7.1)$$

With this assumption, the gas properties on the front can be obtained from the gas state recorded on the plane at a previous instant $t - \Delta t$, i.e. when the frontal plane occupied that angular position on the front:

$$\varphi(\theta(r, y, t)) \approx \varphi\left(r, y, \theta_p\left(t - \frac{\theta_p - \theta}{\omega_{det}}\right)\right) \quad (7.2)$$

Note that while it is assumed that $\Delta t \approx (\theta_p - \theta)/\omega_{det} \approx 0$, the correct spatial sampling at $\theta_p(t - \Delta t) = \theta(r, y, t)$ is preserved, respecting the local gas state with respect to the injectors. For these reasons, a single plane for sampling the state of the gas ahead of the front is used, allowing a consistent simplification of the procedure without compromising the validity of the analysis.

Another important aspect to be mentioned is that the detonation speed is calculated with respect to the global coordinate system and could generally differ from the speed with respect to the reactants. However, the speed of the detonation is about 3 – 7 times the gas speed in the refill region, so in the analysis the front speed in the global system represents

also the speed in the reactants with a good approximation.

As explained in Section 6.5.3 the quantities on the frontal plane exhibit periodic variations due to the presence of the discrete fuel injectors, but are also affected by turbulent fluctuations. To describe the periodic deterministic component of the quantities (see Eq. 6.15) without the spurious contribution of the instantaneous turbulence, the values are also Phase-Locked Ensemble Averaged (PLEA) according to:

$$\varphi_{\text{per}}(r, y, \alpha_p) = \frac{1}{N} \sum_{k=0}^{N-1} \varphi(r, y, \alpha_p + k\Delta\theta_{inj}) \quad (7.3)$$

where N is the number of injectors covered during the simulation and $0 \leq \alpha_p < \Delta\theta_{inj}$ is the angular position between two generic adjacent injectors, with 0 being the injector axis, so that $\theta = \alpha_p + k\Delta\theta_{inj}$ with $k \in \mathbb{N}[0, 99]$ the injector index. Since the data is extracted for discrete values of θ_p and thus α_p , the angular position of the plane is quantized in 20 bands of $\Delta\alpha_p = \pm 2.5\Delta\theta_{inj}$ centred around α_p . The results are also presented as a function of the relative position between two generic injectors:

$$\Theta_p = \frac{\alpha_p}{\Delta\theta_{inj}} = \frac{\theta_p}{\Delta\theta_{inj}} - k = \frac{\theta_p}{\Delta\theta_{inj}} - \left\lfloor \frac{\theta_p}{\Delta\theta_{inj}} \right\rfloor$$

with $0 \leq \Theta_p < 1$.

7.1.1 Detonation speed calculation

The detonation front speed in the global system can be evaluated from the time series of the surfaces $\theta(r, y, t)$ by supposing that the front propagates along its local normal direction \underline{n} . Thus the unit normal of the front is computed from the surface $\theta(r, y, t)$ expressed in a cartesian coordinate system (d, r, y) rotating with the average angular position of the front $\theta_m(t)$ (Figure 7.1).

In such space the detonation surface is described by the function:

$$d(\theta, \theta_m) = d(r, y, t) = r \sin(\theta(r, y, t) - \theta_m(t)) \quad (7.4)$$

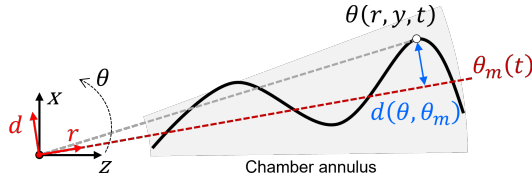


Figure 7.1: Representation of the reference frames adopted to describe the detonation front. (x, y, z) : global cartesian system, (θ, r, y) : global cylindrical system, (d, r, y) : cartesian system rotating with the front.

which can be reformulated in its implicit form $F = f - d(r, y, t) = 0$ and derived spatially to obtain the unit normal vector:

$$\nabla F = \left(1, -\frac{\partial d}{\partial r}, -\frac{\partial d}{\partial y} \right)_t \tag{7.5}$$

$$\underline{n}(r, y, t) = \frac{\nabla F}{|\nabla F|} = (n_d, n_r, n_y) \tag{7.6}$$

The detonation speed at time t_i is then calculated from the displacement of the front along the normal direction as the distance between the points $B(r, y, t_{i+1})$ and $A(r, y, t_{i-1})$, both evaluated with respect to the same angular position $\theta_m(t_i)$ (Figure 7.2):

$$(B - A) = k\underline{n} \tag{7.7}$$

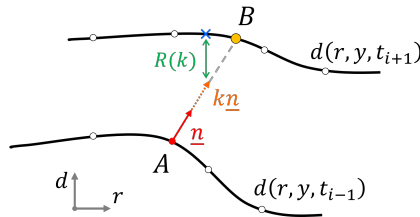


Figure 7.2: Determination of the front normal displacement.

The calculation of the distance requires the position of point B on the detonation front. Since the surface describing the front is discrete,

this point has to be determined iteratively as the intersection between the linear projection of the normal vector and the front at t_{i+1} .

The intersection condition can be mathematically expressed as:

$$d(r_B, y_B, t_{i+1}) = d_B \quad (7.8)$$

and considering that:

$$\begin{pmatrix} d_B \\ r_B \\ y_B \end{pmatrix} - \begin{pmatrix} d_A \\ r_A \\ y_A \end{pmatrix} = k \begin{pmatrix} n_d \\ n_r \\ n_y \end{pmatrix} \quad (7.9)$$

the following parametric function of k is obtained:

$$d(kn_r + r_A, kn_y + y_A, t_{i+1}) = kn_d + d_A \quad (7.10)$$

The distance is then evaluated as the root of the residual $R(k)$:

$$R(k) = d(kn_r + r_A, kn_y + y_A, t_{i+1}) - kn_d - d_A \quad (7.11)$$

using the modified Powell method in Python3. The root k represents the position on the trajectory along \underline{n} , i.e. the scaling factor of the unit normal to intersect the front at t_{i+1} , so its value coincides with the displacement $|B - A| = k$. This procedure is carried out for each point (r, y) of the front and instant t_i , leading to the local instantaneous normal speed of the detonation \vec{D} :

$$\vec{D} = D(r, y, t_i) \underline{n} = \left(\frac{k(r, y, t_i)}{t_{i+1} - t_{i-1}} \right) \underline{n} \quad (7.12)$$

A preliminary application of the procedure using the sampling interval of $\Delta t = 3.25 \times 10^{-8}$ s (31 MHz, 41 samples per fuel injectors pitch) showed a considerable spatial noise affecting the velocity. This was attributed to the excessive sampling rate which is comparable or lower than the time to flow through a mesh element (8.5×10^{-8} s in the refined region and 2.25×10^{-7} s in the chamber). Therefore, only for the velocity calculation, the data is downsampled by 4 times ($\Delta t = 1.3 \times 10^{-7}$, 7.7 MHz), filtering

out the high-frequency fluctuations and improving significantly the quality of the results.

7.2 Fresh mixture characterization

The time-averaged quantities sampled within the refill region ahead of the detonation front are reported in Figure 7.3. The samples constituting the average are collected during one wave rotation according to the instantaneous front position, so they are randomly distributed with respect to the fuel injectors. Although the maps in Figure 7.3 are roughly 7 mm ahead of the majority of the front, the temporal interval required by the detonation for reaching the plane location is fast enough to neglect the variation of the fields in this period, so they are representative of the actual state of the mixture which detonates.

From the maps the refill region is evident and extends up to 38–40 mm from the chamber base. In the whole refill region the static pressure field (not reported) is almost constant ranging between 1 – 1.3 bar. On the other hand, the separate injection of air and hydrogen induces a consistent disuniformity of the mixture properties both in radial and axial directions, confirming the maps in Section 6.4. Three different zones can be identified in the refill region in the axial direction. Within the first 10 mm, the flow field is divided by the presence of the supersonic air flow and its interaction with the axial fuel jet, determining a very rich region at the base of the combustion chamber. This region is characterized by a high unmixedness (see Eq. 6.13), i.e. the H_2 is rapidly stirred but not mixed with fresh air, as shown by the temperature field. On the other hand, the recirculation zone along the outer wall anchored to the air gap edge is not directly reached by the hydrogen and is constantly filled with hot products. This marked division rapidly vanishes as the streams starts mixing near $y = 10$ mm, inducing a quite uniform region of slightly lean mixture up to 23 mm, especially near the inner wall of the chamber below 75% of the span.

The last zone of the refill region is constituted by a rich mixture

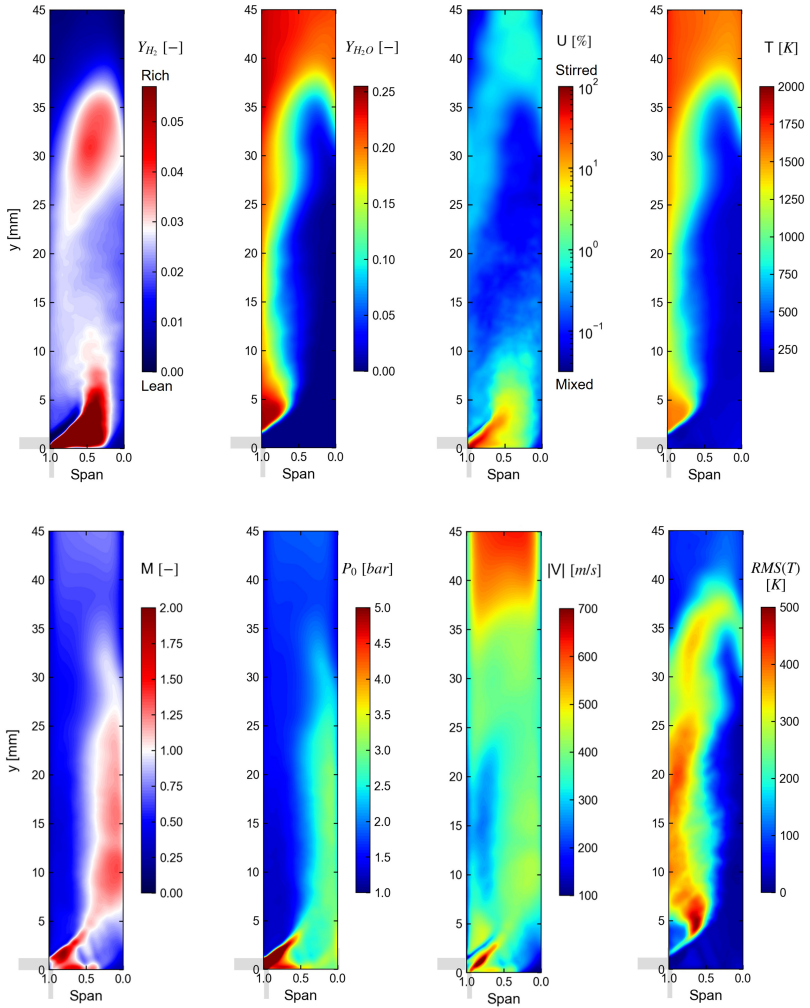


Figure 7.3: Time-averaged quantities on the refill region in the plane ahead of the detonation front ($\Delta\theta = 10$ deg).

and its formation can be explained by considering the effects due to the passage of the reflected wave following the detonation front. As discussed in Section 6.4, this second blockage affects the air flow and determines a reduction of the local flow rate in the chamber which should convect downstream and mix the hydrogen. In fact, due to the different geometric and feeding pressures of the air and fuel channels, their dynamics is different and the latter are less influenced by the detonation blockage. Since the air flow is stopped consistently, while the fuel flow is marginally affected, then a rich mixture accumulates initially at the base of the chamber and only later is transported downstream up to the position shown in Figure 7.3.

Then, the higher local total pressure in the air injectors leads to a slight mass flow rate increase which induces the formation of a lean region, constituting the central region. Only later, at about 270 *deg* behind the detonation front, the local mass flow rates of air and fuel respect the stoichiometric ratio. However, since the mixture entering in the chamber 90 *deg* ahead of the front has a little mixing time, this stoichiometric mixture presents high unmixedness (Figure 7.3). The axial stratification of the fresh mixture is then a direct consequence of the injectors operation summarised in Figure 6.29, composed by three different phases.

As expected, the average flow which settles in the plane is following the trajectory of the air jet, deviating below $y = 5$ mm from a 45 *deg* angle to the axial direction. This curvature is allowed by the subsonic speed of the mixture and induces the formation of a high pressure region in the inner corner of the chamber which provides the centripetal force. The axial flow along the inner wall is slightly supersonic, but it is determined by averaging subsonic and supersonic gas pockets, as shown in Figure 6.31. On the other hand, the speed is subsonic for the outer half span of the chamber, mainly due to the higher sound speed in this region more than a reduction of the flow velocity. The fast flow along the inner wall is also featuring a total pressure around 2.5 bar, about the double of the value near the outer wall.

For higher span-wise positions the hot products, which fill the recir-

culation zone moving tangentially along the outer wall (see Section 6.4), vitiate the mixture and introduce a significant unsteadiness with large temperature and composition fluctuations. A little region along the outer wall within $0 < y < 5$ mm presents high temperature with low RMS, indicating the stable presence of combustion products. On the other hand, the majority of the refill region above 50%, is affected by temperature fluctuations which can be related to a deflagration front. As explained in the previous sections (see Figures 6.26 and 6.33), a non-negligible heat release is present at the contact between reactants and hot gas pockets, revealing the presence of localized deflagrations. In conclusion, only the refill region below 50% span is efficiently flushed with fresh reactants, as a result of the radial-inward air injection and the high mass flow rate. The previous non-reactive study carried out by Weiss et al. [157] showed how a reduction in mass flow rate avoids the formation of the recirculation region along the outer wall, so the same behaviour could be reasonably expected in reactive conditions, even if it implies different wave propagation modes such as counter-rotating waves.

7.2.1 Periodic variation due to the discrete injectors

The refill region characterised by the average maps in Figure 7.3 does not highlight the variation induced by the periodic presence of the $N = 100$ fuel injectors. As shown in Section 6.5.3, the flow field in proximity of the injectors is very different considering an axial-radial plane through the fuel channels or between, since the hydrogen jet deflects the air flow and alters the shocks structure. It is then interesting to quantify the periodic deterministic component of the gas properties in the frontal plane due to the presence of the injectors. This periodic variation is calculated using the Phase-Locked Ensemble Average (PLEA) operation (see Section 7.1) and the maps are reported in Figures 7.4 and 7.6 as a function of the percent position between the injectors.

The PLEA fields do not show a noticeable variation in phase with respect to the presence of the discrete injectors, except for the region below $y = 10$ mm that directly involves the fuel jets. Another visualization

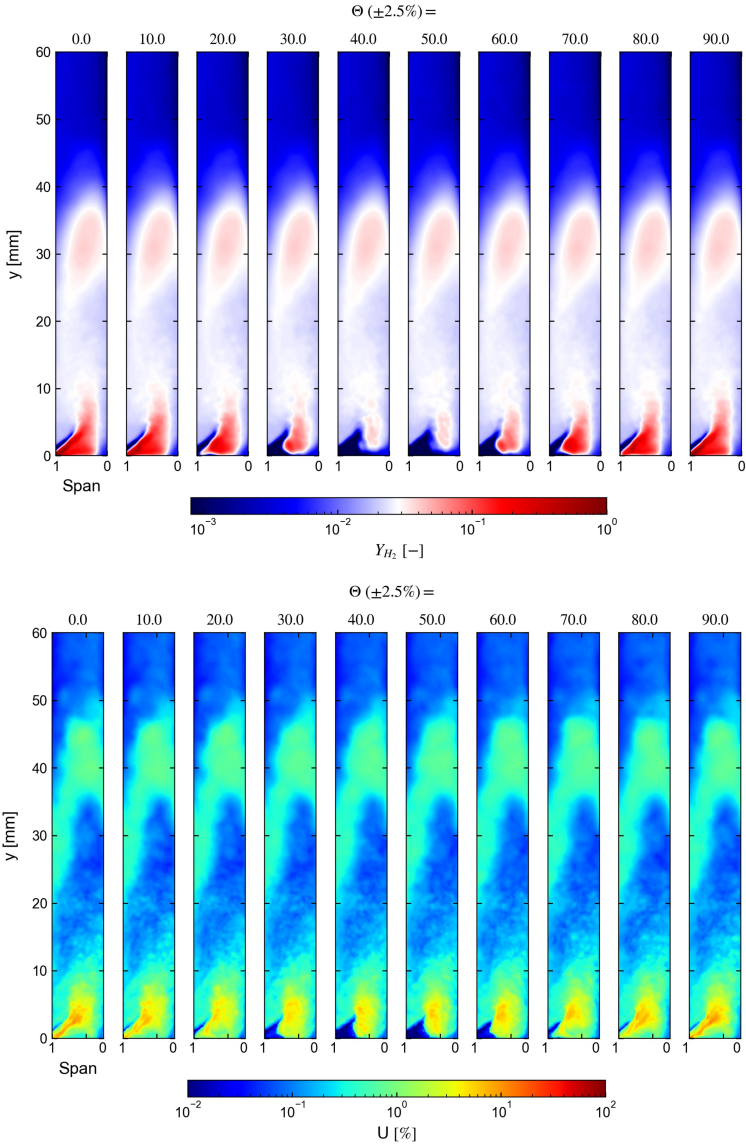


Figure 7.4: Phase-Locked Ensemble Averaged maps of hydrogen mass fraction (top) and unmixedness (bottom) in the frontal plane as a function of the relative position between the injectors Θ_p [%].

of this dependence is also reported through the PLEA distributions of Y_{H_2} for different α_p positions relative to the injectors in Figure 7.5. The

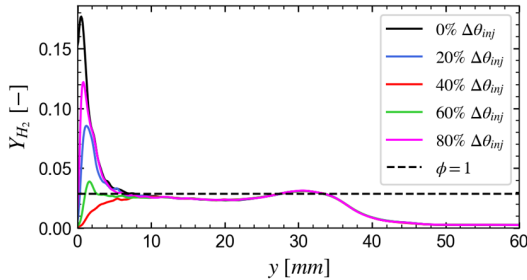


Figure 7.5: Phase-Locked Ensemble Averaged axial distributions of hydrogen mass fraction in the frontal plane.

PLEA axial profiles coincide as soon as the hydrogen jets start mixing with air, showing that in this operating condition the 100 injectors determine a uniform mixture mostly independent of the presence of discrete jets. Moreover, the unmixedness shows that the hydrogen variance is not varying as well as when crossing the injectors, indicating the presence of mixed hydrogen-air in the central region of the refill height. The well-mixed reactants in this zone, combined with the near-stoichiometric composition, constitute excellent mixture properties to stabilize the detonation. At the top of the refill height, again independently from the position relative to the fuel injectors, the unmixedness increases slightly likely due to the fluctuation induced by the deflagration front surrounding the refill region. The hydrogen PLEA fields also confirm that the rich composition present at the top of the refill height is not directly correlated to the injectors flow field, but is due to transient events such as the passage of the reflected wave behind the detonation.

Also the PLEA fields of Mach number and sound speed in Figure 7.6 are characterized by variations circumscribed to $y < 10$ mm. Since the maps are averaged, the Mach number shows clearly that the supersonic jets expansion right in front of the detonation is very stable during

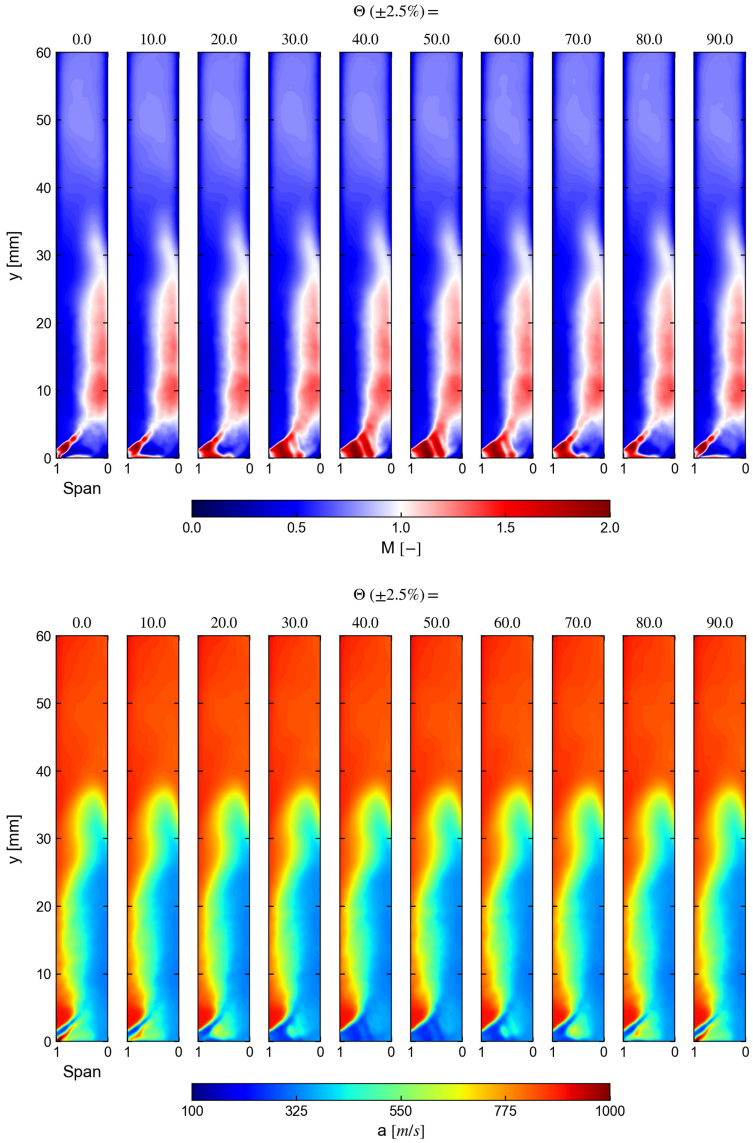


Figure 7.6: Phase-Locked Ensemble Averaged maps of Mach number (top) and sound speed (bottom) in the frontal plane as a function of the relative position between the injectors Θ_p [%].

the rotation, i.e. the injectors recover to the well-defined full-capacity condition reported in Figure 6.31. This is true both in correspondence to the injector ($\Theta_p = 0\%$) and in the middle of two injectors $\Theta_p = 50\%$. The different flow field and shock structure in these positions significantly impact not only the speed below $y = 10$ mm but also the fuel concentration and the sound speed.

An interesting aspect which emerges from the PLEA fields is that the periodic variation near the base of the chamber is not exactly symmetric like the geometry, i.e. is not symmetric around $\Theta_p = 50\%$. For instance, the maps at $\Theta_p = 40, 60\%$ present different hydrogen concentrations in the recirculation region below the fuel jet, with a richer composition at $\Theta_p = 60\%$. The same behaviour can be observed for any corresponding couple of positions between $\Theta_p = 20, 80\%$, where the second half of the space between the injectors is always slightly richer than the first half. This phenomenon can be explained considering that the global flow field induced by the detonation has a tangential component also in the refill region (see Figure 6.18), which is non-zero even at low span. This tangential component moves the gas away from the detonation front and determines a slight propagation of the fuel in the clock-wise direction ($-\theta$).

7.2.2 Local Chapman-Jouguet speed

The knowledge of the local instantaneous gas state (Y_k, T, p) ahead of the detonation front allows to evaluate the Chapman-Jouguet speed in the plane, i.e. the detonation speed which should be achieved at the local mixture properties in 1D steady conditions. The resulting distributions of CJ speed are time-averaged and reported in Figure 7.7.

The CJ Mach number in the fresh mixture $M_{CJ} = D_{CJ}/a$ is also calculated and time-averaged. As the detonation speed depends primarily on the hydrogen content (see Figures 2.19 and 2.24), the D_{CJ} is higher in the rich regions below the fuel jet and in the top part of the refill region, while it decreases along the outer wall both for the lean composition and the high temperature products. The recirculation region immediately above the air gap presents values of D_{CJ} near the local sound speed, high

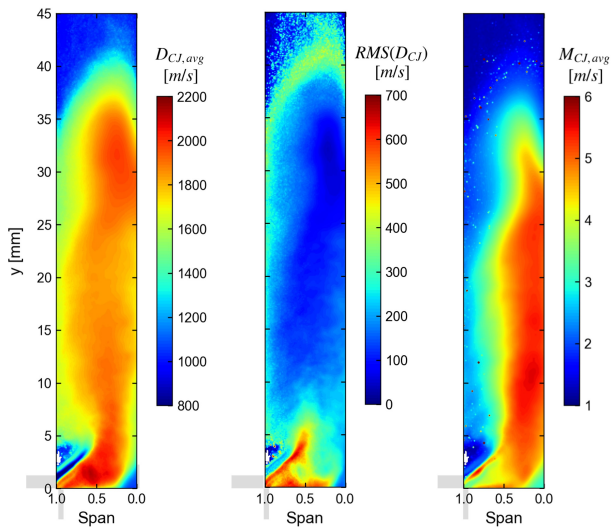


Figure 7.7: Time-averaged CJ speed and Mach number in the fresh gas ahead of the detonation.

for the hot products, as shown by the M_{CJ} distribution which approaches the unity value around $y = 3$ mm on the outer wall. Except for the zone near the injection, the root mean square variation of the CJ speed is limited to values between 50 – 250 m/s. At the top of the refill region, the more intense deflagration vitiates the reactants at the outer wall, reducing the CJ speed up to 75% span. The mixture properties alone would then induce a slower propagation along the outer wall with respect to the inner wall, which is the opposite of what typically observed in curved channels [176] and other RDC studies [79]. The CJ speed map points out that the accurate description of the reactants mixing in the refill region is of great importance for the characterization of the detonation dynamics since the actual gas state differs from the nominal operating conditions. For instance, even when neglecting the radial-axial variation of the CJ speed, its average value between $5 < y < 35$ mm is 1807 m/s, lower than the reference of 1975 m/s for atmospheric, stoichiometric conditions. Moreover, the low value along the outer wall would correspond to a rotation frequency of 5563 Hz, so that both the simulation and the experiment register an over-driven detonation, provided that the propagation is mostly tangential (Table 7.1).

Table 7.1: Time-averaged CJ speed on the chamber outer wall between $10 < y < 35$ mm.

D_{CJ}	$(\omega r_o)_{LES}$	$(\omega r_o)_{exp}$	
1573	2123	1778	[m/s]
100	135	113	[% D_{CJ}]

The values of CJ speed are also Phase-Locked Ensemble Averaged and reported in Figure 7.8 as a function of the relative position between the injectors.

The CJ speed reflects the PLEA distributions of the gas properties on the plane (Figures 7.4 and 7.6), thus exhibiting noticeable variations only near the injection below $y = 10$ mm. In this region, null values of CJ speed are also present, i.e. the local conditions would not allow the development of a steady detonation according to the ZND theory. These

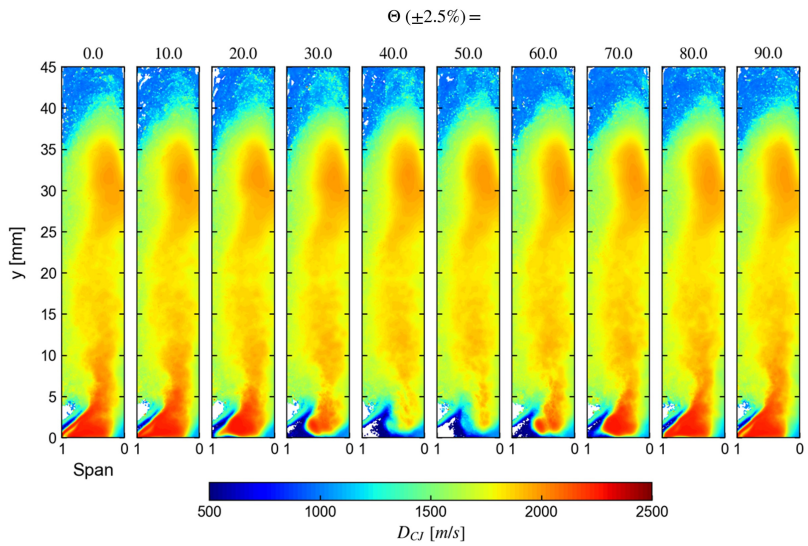


Figure 7.8: Phase-Locked Ensemble Averaged maps of the CJ speed in the frontal plane as a function of the relative position between the injectors Θ_p [%].

”forbidden” regions are located right above the air jet on the outer wall for any position and below the air jet only between $30\% \leq \Theta_p \leq 60\%$, where the fuel jet is not present. Their nature is different since the latter is representing a supersonic region of pure air, while the former is constituted by reactants stirred with products.

Therefore, at the base of the chamber the CJ speed periodically drops from 2300 m/s to zero since the gas is composed by hydrogen below the fuel jets and by cold air between the fuel channels. This variation could either impact the whole stability of the detonation front or constitute an overall negligible effect since the majority of the refill region ($8 \leq y \leq 40$) is essentially independent from the discrete injectors. It is then important to analyse both the topology and the propagation of the detonation front and establish whether a correlation with the mixture properties shown in Figure 7.3 is present.

7.3 Detonation front topology

The detonation front which stabilizes in the chamber annulus presents a defined 3D shape throughout the revolution, reported in Figure 7.9. The peculiar feature of the front is the presence of an almost conical protrusion along the outer wall with the vertex positioned above the air gap edge. This structure presents continuous and wide fluctuations in contrast to the other parts of the front which exhibit weaker variations. To obtain a statistical description, the instantaneous front angular position with respect to the average angular plane, i.e. $\theta(r, y, t) - \theta_m(t)$, is time-averaged and shown in Figure 7.10 beside the average linear distance $d(\theta, \theta_m)$ (Eq. 7.4).

Additionally, also the average inclination of the front normal with respect to each direction \underline{i} and calculated as $\psi_i = \cos^{-1}(\underline{n} \cdot \underline{i})$ is represented. From the maps the protrusion is clearly visible with the vertex positioned around $y = 2$ mm on the outer wall and the semi-circular base between the air gap edge and about $y = 10$ mm, surrounding the recirculation region shown in Figure 7.3. The surface of the protrusion is

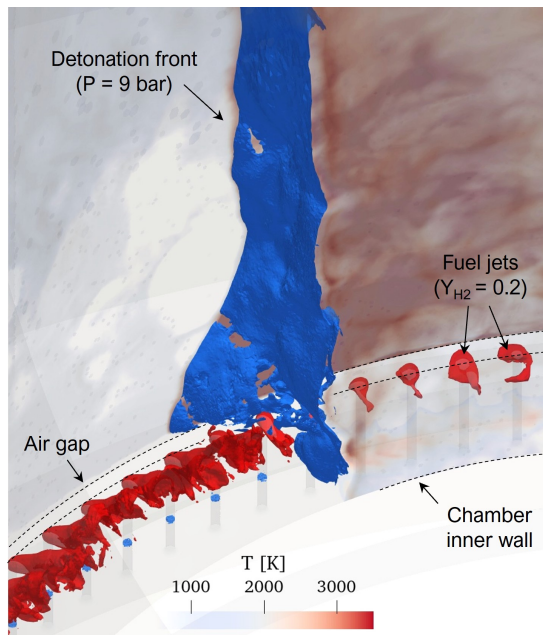


Figure 7.9: Visualization of the instantaneous detonation front with respect to the hydrogen jets.

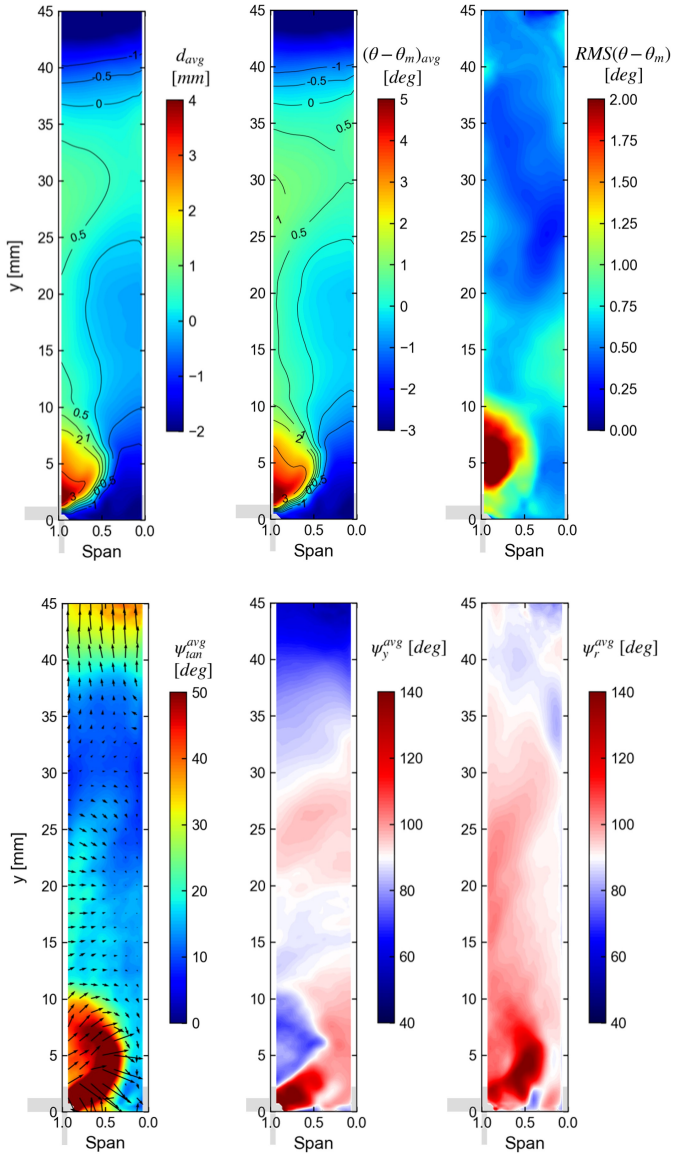


Figure 7.10: Time-averaged front shape (top) and front normal average inclination with respect to the tangential, axial and radial directions (bottom). The vector field represents the front average normal.

also subjected to a more frequent local fragmentation with respect to any other part of the front, and specifically they show in the surface with the highest deviations ψ_{tan} from the tangential direction.

On the contrary, the regions around the inner corner of the chamber exhibit a good stability and are almost flat and recessed with respect to the majority of the front. The remaining part of the front shows a slight inclination towards the radial direction increasing near the outer wall of the chamber. This feature is evident for $10 < y < 25$ mm but decays at the top of the front around $y = 30$ mm (Figure 7.11). Since the curvature

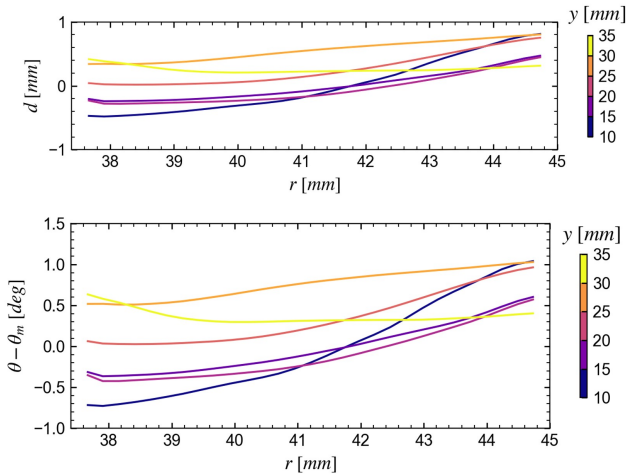


Figure 7.11: Time-averaged detonation front cuts at different axial positions in terms of linear (top) and angular (bottom) distance from the average front plane.

of the chamber annulus is constant in the axial direction, these alterations of the average front shape must be linked to the local mixture properties. However, the fresh mixture fields reveal that above 25 mm the gas is characterised by a higher radial variation than below, which appears to be in contrast to a more flat front. Although a clear correlation between the surface shape and the gas state in the frontal plane is not observed,

the most protruding regions appear to be positioned in correspondence of a high temperature and sound speed.

It is worth to highlight that the slight centripetal inclination of the detonation front is not usually observed in curved channels filled with uniform mixtures [173, 176]. Nevertheless, the refill region of the present case features consistent non-uniformities in each direction which could be the cause of the front topology. For instance, the higher sound speed near the outer wall and the flow speed along the inner wall could be additional effects absent in the simplified experiments. Further studies are required to fully understand the peculiar shape of the detonation front and the possible correlation with the refill gas properties. Finally, the development of defined detonation cells is not observed or at least is not clearly emerging from the small-scale front fluctuations related to the local pre-shock gas turbulent conditions.

7.4 Detonation front speed

The time-averaged normal velocity of the front D is reported in Figure 7.12 beside its components, the Mach number in the fresh gases $M_0 = D/a$ and the angular velocity $\omega = \partial\theta/\partial t$. Since the speed is evaluated by supposing a normal propagation of the front, the average orientation of the velocity vector corresponds to the vector field in Figure 7.10 (bottom-left). Considering the stable part of the front, far from the injection ($y > 10$ mm), the detonation speed presents a clear dependence on the radial position, linearly increasing from the inner to the outer wall. The relatively small variation does not appear to be correlated to the mixture properties in the refill region, as shown by the Mach number of the detonation in the fresh gas, that is around 5.5 near the inner wall and 2.5 – 3 in the outer wall. Due to the high Mach variation in the radial direction the leading shock strength is thus very different between the outer and inner half of the combustion chamber. Additionally, the rich region at the top of the refill height is not affecting noticeably the detonation speed of the front, which slightly accelerates where the

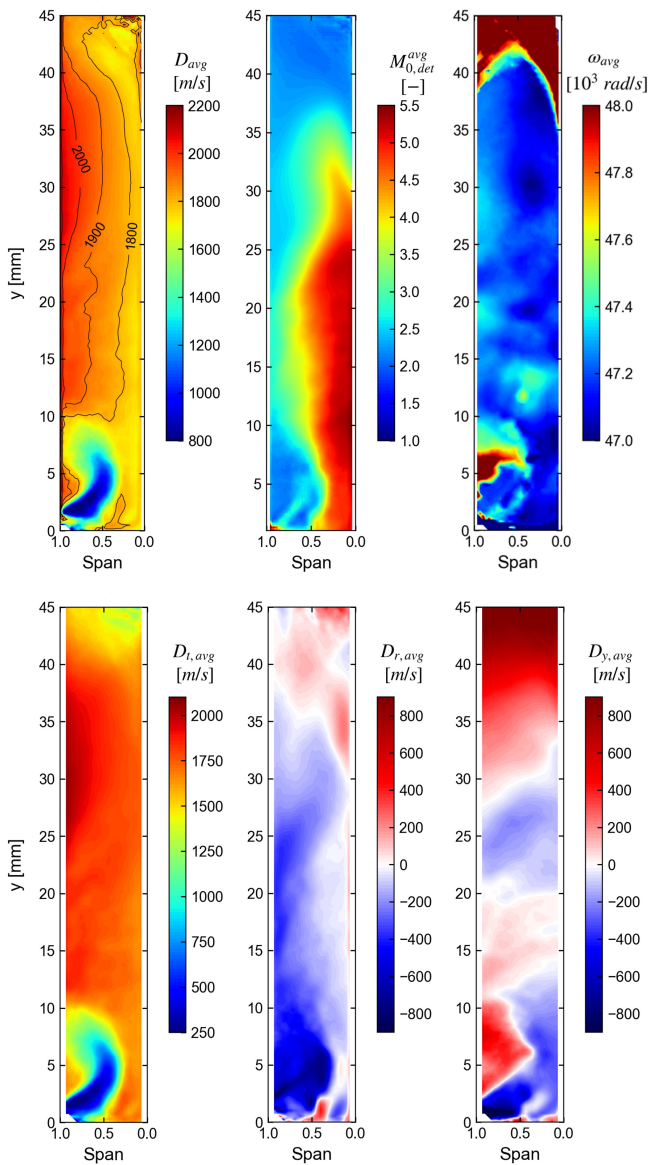


Figure 7.12: Time-averaged normal propagation speed of the detonation front D and angular speed ω .

temperature is higher and the gas more vitiated by the products.

The angular speed of the detonation front is around 47200 rad/s (7512 Hz), aligned with the values obtained from the punctual pressure signals (see Section 6.2), and is quite constant throughout the whole front, except the region immediately above the air gap. This field shows how the front propagates coherently in the revolution, apart from the part in the recirculation region above the air gap which exhibits important fluctuations.

Since the front is assumed to propagate along its normal direction, the speed is mostly tangential, with a radial-inward component of around -200 m/s and a variable axial component. The upper part of the protrusion induces the highest axial component of about 300 m/s, while the stable part of the front ($10 < y < 35$ mm) propagates with a relatively low axial speed.

The hypothesis that the front propagates in the normal direction appears to be violated by the coherent shape of the protrusion along the rotation, since the positive axial speed of this region would expand the conical bulge. However, this is not observed by the front tracking and its topology, with the protrusion fluctuating but never extending above $y = 10$ mm. This behaviour could be explained either (1) considering that the oblique part of the protrusion is not locally a detonation but rather a trailing shock of the surrounding detonation or (2) that the flow speed in the refill region is directed normally to the protrusion, i.e. inclined toward the chamber base below $y = 10$ mm at high span. The former explanation appears not to be confirmed since a high heat release rate is registered at high span in Figure 6.26 and there are no other evidences that the protrusion is non-reactive shock. Unfortunately, since the velocity direction in the frontal plane is not extracted during the analysis, the latter explanation cannot be verified rigorously but can be only supported by the streamlines in Figure 6.18, which show a negative axial velocity at high span, potentially able to balance the front.

The normal detonation speed is also compared to the local D_{CJ} to highlight the over-driven and under-driven regions through the maps

of the ratio D/D_{CJ} in Figure 7.13. The normal velocity is distributed

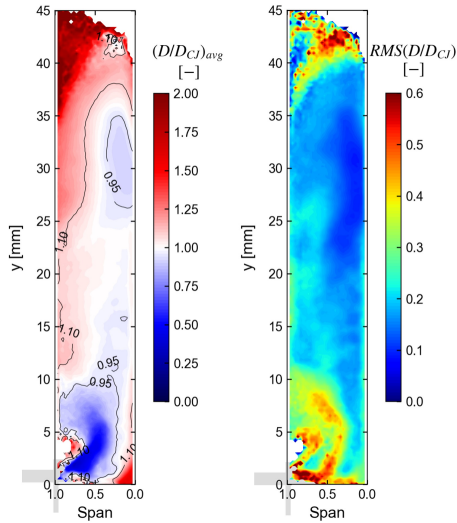


Figure 7.13: Time-average (left) and RMS (right) of the ratio between the normal detonation speed and the local CJ speed on the front.

around the CJ speed so that the regions adjacent to the inner wall are slightly below D_{CJ} while for the spans above 50% the front presents an increasing over-drive level up to $+30\%D_{CJ}$. This is partially due to the lower CJ speed near the outer wall (Figure 7.7), so the absolute speed of the front raises to only $+20\%$ of the 1750 m/s along the inner wall. The ratio D/D_{CJ} is also characterised by a low variation above $y = 10$ mm, with a slight increase near the outer wall for the variability of the CJ speed.

To analyse the radial trends of the front and the CJ speed, the respective fields are averaged in the axial direction considering only the part of the detonation front far from the injection, i.e. $10 < y < 35$ mm. The profiles are reported in Figure 7.14. The linear increase of the normal speed in the main part of the detonation front is evident from the axially-averaged profiles and does not appear correlated to the

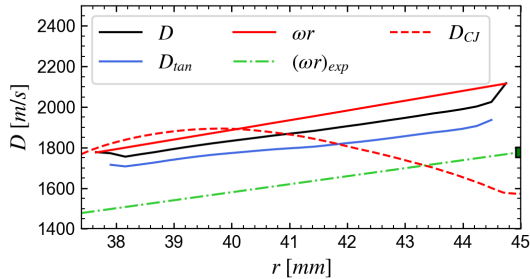


Figure 7.14: Time-averaged radial distribution of the detonation speed between $10 < y < 35$ mm.

local CJ speed, which decreases near the outer wall. Nevertheless, the normal speed is not very different from the CJ speed in the inner half of the chamber, where the front is also more flat. The diagram represents also the tangential component D_{tan} of the normal velocity D and the tangential velocities ωr derived from the frequency measurements at a constant (r, y) position $\omega r = r\partial\theta/\partial t$, which correspond to the values reported in Table 6.3 for the outer wall. In the case of a pure tangential propagation the velocities are equivalent, i.e. $D = D_{tan} = \omega r$. The speed of the front is primarily tangential with a minor radial-inward component and a negligible speed in axial direction (Table 7.2).

Table 7.2: Detonation speed components and CJ speed averaged over one revolution between $10 < y < 35$ mm.

D	D_{tan}	D_{rad}	D_{ax}	D_{CJ}	
1884	1806	-144	-9	1812	[m/s]

The normal velocity increase with the radial position can be attributed to the the annulus curvature which determines the compression along the outer surface and the formation of expansion waves in the inner side which alter the detonation speed with respect to the CJ value. The linear trend of the speed could also indicate that the propagation is only

partially driven by local mixture state, while a more important effect is due to the curvature and geometry of the chamber. A uniform reactant mixture might be necessary for the stabilization of the wave, but also it may have only a secondary influence on the local propagation of the front. Indeed, the over-driven speed at the outer wall as well as the reduction at lower radii is consistent with what was observed in other studies in other studies [79, 176], where the mixture properties were uniform.

The region near the injection below $y = 10$ mm deserves a specific discussion since here the front shows a peculiar shape and the speed is influenced by the continuous fragmentation of the front, especially in correspondence to the high speed jet (Figure 7.12). The part of the protrusion which exhibits the higher stability is the peak at $y = 2$ mm along the outer wall and constitutes always the leading point of the front. The propagation of this portion occurs at speeds of 1900 – 2000 m/s, consistent with the other parts of the front, but not with the CJ speed, resulting in a highly over-driven region. There the CJ speed (Figure 7.7) is low and near the sound speed, while the front presents a Mach number in the fresh gas of approximately 2. The discrepancy with the CJ speed at the leading edge of the protrusion is also exacerbated by the presence of a tangential velocity component of the gas directed toward the front, leading to an even higher propagation speed with respect to the reactants. The nature of the detonation in the recirculation above the air gap is thus not clear and seems not to be explained by the CJ theory. Instead, the local features of the flow with the proximity of the wall and the barrel shock of the air jet and the hot products could play an important role for the development of this peculiar region of the front.

7.4.1 Assessment of the tangential variation

Finally, at each point of the front the instantaneous normal speed is related to the point position with respect to the injectors to highlight any periodic variation in phase with the discrete fuel injectors. The detonation front is divided in four quadrants in the radial-axial plane to characterize the behaviour of the front in different regions, specifically

near and far from the injection (below and above $y = 10$ mm) and in the inner and outer half of the chamber (below and above 50% span). As discussed in the previous Section 7.2.1, the refilled gas ahead of the front exhibits a clear dependence on the injectors relative position Θ only in the near-injection zone below $y = 10$ mm, especially above 50% span but with non-negligible variations even at low spans. As a consequence, the CJ speed in such region fluctuates consistently (Figure 7.8), so an impact at least on the base of the front could be expected. To highlight the local fluctuations of the detonation speed as a function of the relative injectors position ($\Theta = \alpha/\Delta\theta_{inj}$), the two-dimensional Probability Density Functions (PDF) of the detonation speed for each point in the front and instant are reported in Figure 7.15, distinguishing four regions. The color in the maps represents the probability density of the samples around an angular position relative to the injectors Θ , where $\Theta = 0, 1$ correspond to the adjacent injectors axes and $\Theta = 0.5$ describes the plane in between.

As expected from the spatial average distribution in Figure 7.12, the maps register different speed occurrences depending on the radial-axial quadrant considered. The normal velocity far from the injection ($y > 10$ mm) does not show any specific dependence on the injector position, even at the middle of the gap between the fuel channels $\Theta = 0.5$. The velocity at each position is distributed with a Gaussian function and the average value is constant in a single quadrant, while it reflects the radial variation already described in Figure 7.14.

On the other hand, the quadrants near the injection ($y < 10$ mm) feature a deviation from the average speed of the corresponding regions at higher axial positions, as shown by the spot highlighted by the arrow in Figure 7.15. Indeed, the detonation front in the outer-low quadrant is aligned to the protrusion of the front which is also associated with considerable fluctuations of the detonation front. This unstable behaviour is clearly observable from the probability distribution of the speed, as the Gaussian variation is replaced by a large, flat variation between about 500 and 2200 m/s with a peak around 1950 m/s, comparable to the value at $y > 10$ mm. In addition to this distribution independent from the

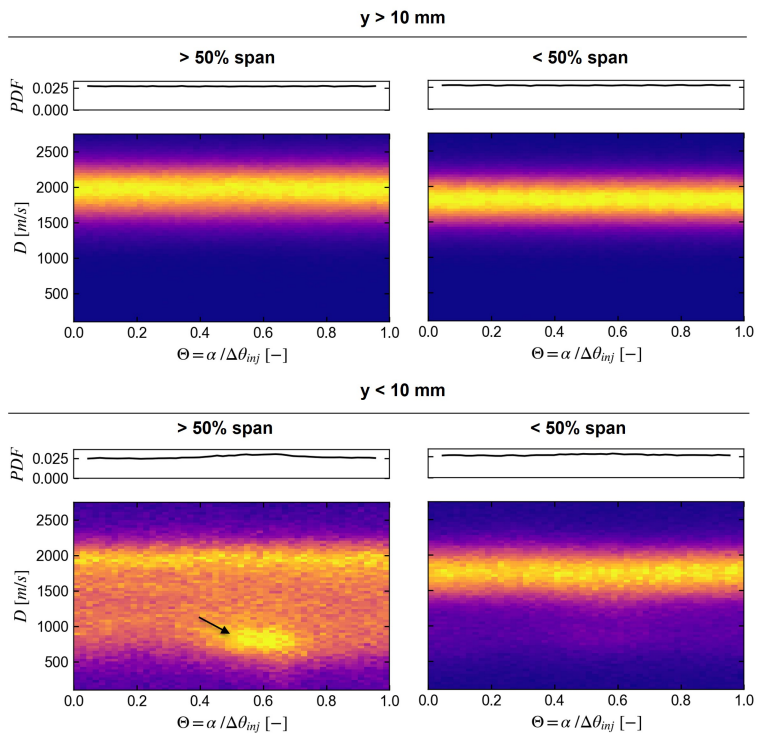


Figure 7.15: Probability density functions of the local detonation normal speed with respect to the relative position between the injectors. The maps are relative to four quadrants in the radial-axial plane and are normalized with the local maximum value.

relative injectors position Θ , a distinct peak is also present between the injectors around $\Theta = 0.6$ and $D = 750$ m/s, showing low speed values with a higher probability between the fuel jets. This observation appears aligned with the low CJ speed in Figure 7.8 around $\Theta = 0.5$, indicating a slight delay between the lowest local values of CJ speed in the pure air and the response of the detonation speed. In other words, the probability of a local drop in the detonation speed is higher about 0.36 deg after the passage of the front in a region with low values of CJ speed. Indeed, the CJ theory and the ZND models are steady descriptions which are not completely representing the local behaviour of the front in the proximity of the injectors, where the relative flow unsteadiness is significant. However, a temporary, local variation of the detonation speed is occurring in a region where the CJ speed in the fresh gas is low. This speed drop is observed once per injectors gap, thus it is ideally associated to a frequency of about 750 kHz, even if the stochastic maps in Figure 7.15 do not ensure that each gap presents a velocity drop, but only that the velocity is likely to assume low values between the injectors in the outer-low region.

Although this observation is very evident, the other quadrant around the inner corner of the chamber does not highlight a similar drop in the detonation speed, but only a slight increase of the variance around the average value around $\Theta = 0.6$. This region presents indeed a variation of CJ speed (Figure 7.8) more limited than in the outer quadrant, but also a flow field which is less influenced by the presence of the supersonic reactants jets. These two aspects are likely the main causes of difference with the outer region and demonstrate how the speed drop is localized near the injection only above 50% span. This behaviour evidences that the detonation front at the base of the chamber is likely to have a secondary importance for the stability of the whole front and that the high-frequency fluctuations are not harming the global stability of the detonation.

In conclusion, except for the region directly affected by the presence of the reactants jets, the detonation front in the combustor does not present an appreciable variation when crossing the discrete fuel injectors, as the fresh mixture above $y = 10$ mm is uniform in tangential direction and

loses the discrete features associated to the injection. The central region of the refill region is likely the most important region for the stabilization of the detonation, so it is expected to drive also the global speed of the front.

7.5 Concluding remarks

The detonation front topology and propagation speed is analysed in the non-premixed RDC installed at TU Berlin. The study builds upon the simulation reported in Chapter 6 and is carried out by solving the fully-compressible, multispecies, reactive Navier-Stokes equations with the AVBP code. To describe the detonation process the 4S1R global scheme, developed and presented in Section 2.3.2.1, is adopted. For the investigated operating conditions, the detonation stabilizes as a single dominant wave.

Here, an advanced data analysis is developed and applied for tracking the 3D evolution of the detonation front as well as the properties in the plane ahead of the wave, allowing a stochastic characterization of both the front speed and the refill region and highlighting their potential correlation.

The results of the analysis can be summarised in the following points:

- The average gas which precedes the detonation front presents consistent variations in radial and axial directions, with a rich region at the top of the refill height, a well-mixed central region and a rich concentration near the base of the chamber. The outer half of the refill region is mostly composed by hot products, so only the refill region below 50% span is efficiently flushed with fresh reactants, as a result of the radial-inward air injection and the high mass flow rate.
- The detonation front tracking reveals that the front maintains a defined shape with a protrusion in the recirculation zone above the air jet and a slight radial-inward inclination which increases near the outer wall. The fluctuations of the front do not highlight the

presence of evident detonation cells, and could be only related to the turbulent flow field of the refilled gas.

- The average normal front velocity features a slight linear increase with the radial position and is quite uniform far from the injection, without showing a distinct local dependence on the mixture state in front of the wave. The speed distribution is well described by the CJ speed near the inner wall of the chamber, while it does not decrease at high span, determining an over-driven detonation above 50% span. These observations indicate that the propagation of the front may be more sensible to the annulus curvature rather than to the local gas state.
- Except in the region directly influenced by the presence of the reactants jets, the detonation front does not show an appreciable variation when crossing the discrete fuel injectors, as the fresh mixture above $y = 10$ mm is uniform in tangential direction and loses the discrete features associated to the injection.
- Although the mixture ahead of the detonation presents a periodic variation due to the discrete fuel injectors near the base of the chamber, the global detonation speed does not show any dependence on the position relative to the injectors. Instead, the wave front in correspondence to the reactants jets has a higher probability to move at lower speed values between the injectors, where the local CJ speed is lower for the presence of the supersonic air flow.

Conclusions

In the present research the non-premixed Rotating Detonation Combustor (RDC) installed at TU Berlin is investigated numerically in reactive conditions by means of fully-compressible, multispecies, reactive Large Eddy Simulations. Due to the extremely fast transients and peculiar phenomena characterising these devices, the key steps enabling the numerical investigation have been carefully explored, proposing numerical methods, simulation strategies and post-processing techniques to study the test rig. The simulation requires a description of the detonation process which is at the same time accurate and cost-efficient, so that the overall cost of the CFD calculation is not compromised.

For this purpose, the work starts with the numerical modelling of the hydrogen-air detonation, testing different detailed reaction mechanisms available in the literature. The generally accurate prediction of the schemes in the conditions relevant for a detonation allows the detonation analysis according to the ZND theory and the determination of the post-shock and CJ states as well as the detonation speed. Building upon these descriptions, two single-step mechanisms are developed and optimised for the H_2 -air detonation near the atmospheric condition, allowing a cost-efficient description of the detonative combustion for the next CFD simulations. The chemical schemes are verified in simplified detonation cases of increasing complexity, demonstrating the ability in matching their design targets. Then, the unsteady propagation of a 2D detonation in a H_2 -air mixture is studied with LES in order to investigate the resulting detonation speed, half-reaction thickness and cellular structure. The anal-

ysis confirms that the numerical model and the reduced kinetic schemes are suitable for the simulation of multi-dimensional H_2 -air detonation, with a limited degeneration of the performances when the element size does not allow to resolve completely the reaction zone. This finding is of great interest since the element size adopted in real configurations is usually larger or similar to the half-reaction thickness, so the study ensures that no unexpected behaviour is exhibited by the numerical model with coarse meshes.

The second part of the work is focused on the numerical investigation of the TU Berlin non-premixed Rotating Detonation Combustor (RDC). A stoichiometric, single wave test point is considered for the analysis and investigated both in cold and reactive conditions through fully-compressible Large Eddy Simulations with the AVBP code. To describe the detonation process, the global single-step scheme with real species developed in the first part of the work is adopted. The results of the non-reactive simulation highlight the presence of a complex shocks structures within the combustion chamber, arising from the under-expanded reactants jets and their interaction with the chamber walls. The high flow-rate of the cold condition induces a supersonic speed for the lower half of the chamber, leading to a scarce overall mixing efficiency of the reactants, which cannot take advantage of the turbulent fluctuations.

After the detonation initiation, a single wave establishes in the combustor and propagates steadily according to the experimental observations. However, the simulation overpredicts the wave rotation frequency by 19%. On the other hand, the pressure gain of the device is captured with excellent accuracy, with the exit total pressure matching the value measured experimentally. The reactive case shows the presence of a reflected wave following the detonation front, which determines an additional, delayed shock interfering with the flow in the injectors. The different blockage of fuel and air injectors induces an axial stratification of the fresh gas composition, constituted by a rich mixture at the top of the refill height, a lean mixture in the centre and stoichiometric, partially-mixed reactants at the base. These gas regions are formed at the base of the chamber and

then convected downstream as soon as the mass flow recovers. Above the air gap, a recirculation region is present, with the flow featuring a non-negligible tangential component which moves the hot products away from the detonation. As a consequence, the outer wall is constantly surrounded by burnt gases that also determine the formation of localized deflagration fronts. Therefore, the refill region is characterized by a three-dimensional non-uniformity of the gas properties, with vitiated reactants in the outer half of the chamber, a faster flow of fresh gas along the inner wall and a rich region at the top.

The presence of the discrete fuel injectors induces a periodic variation of the gas state at the chamber base, which could potentially affect the propagation of the detonation front as well as its local orientation and stability. To investigate these aspects, an advanced analysis is developed and implemented to track the three-dimensional evolution of the detonation front as well as the gas properties in the plane ahead of the wave, allowing a stochastic characterization of both the front speed and the refill region and highlighting their correlation. The detonation front tracking reveals that the front maintains a defined shape with a protrusion in the recirculation zone above the air jet and a slight radial-inward inclination which increases near the outer wall. The average normal front velocity features a linear increase with the radial position and does not show a distinct local dependence on the disuniform mixture state in front of the wave. The speed distribution is well described by the CJ speed near the inner wall of the chamber, while it does not decrease at high span, determining an over-driven detonation above 50% span. These observations indicate that the propagation of the front may be more sensible to the annulus curvature rather than to the local gas state. Although the mixture ahead of the detonation presents a periodic variation due to the presence of the discrete fuel injectors near the base of the chamber, the global detonation speed does not show a dependence on the position relative to the injectors. Instead, the front speed in correspondence to the reactants jets has a higher probability to feature low values between the injectors, where the local CJ speed is lower because of the supersonic air flow.

Finally, the present study shows also how the complete resolution of the injection system is fundamental to capture the interaction between the waves and the reactants, and it should be included not only for non-premixed but also any premixed RDC. The deep understanding of the injectors is indeed an essential aspect for the optimization of the RDC performances, since it not only drives the mixture preparation, but also the overall pressure gain which can be effectively achieved by the device. In this context, the present study represents a first step for characterizing the main aspects related to the RDC operation and provides valuable insights for the future development of design improvements.

Further studies of the test rig will complement this investigation for studying also different operating conditions and wave propagation modes. The future numerical analyses could extend the numerical model by including additional important effects on the detonation process such as the heat losses through the walls and a more accurate description of the deflagration. The introduction of these real effects on the detonation will increase the accuracy of the model, thus providing an essential and reliable tool for the analysis of the RDC operation.

List of Figures

1.1	Global temperature increase relative to the average during 1850-1900°C. Adapted from [8].	2
1.2	Ideal thermodynamic cycles in temperature-entropy diagram (a) and ideal efficiency (b). The ZND and Humphrey cycles are relative to a normalized heat addition of $q/c_p T_0 = 5$. Adapted from [14, 18].	5
1.3	Representation of the detonation in the pressure-volume diagram. Adapted from [21].	6
1.4	Schematic illustrating the Rotating Detonation Combustion and the typical flow field.	9
1.5	Schematic of the spinning detonation apparatus. Adapted from [30].	13
1.6	Cross-section of the RDE rig developed by Nicholls and Cullen [30].	14
2.1	Explosion limits for hydrogen-oxygen system in a spherical vessel, showing the neutral competition between R2 and R3 as a red dashed line. Picture (a) adapted from (a) [92] and (b) [93].	26
2.2	Representation of the measurements in Table 2.2 with respect to the post-shock states in an atmospheric, stoichiometric H_2 -air detonation.	30

2.3	Time evolution of temperature and major species in a 0D constant volume reactor initially filled with a stoichiometric H_2 -air mixture at $T_0 = 1500\text{ K}$, $p_0 = 28\text{ bar}$ (vN point), obtained with the ELTE mechanism [103].	32
2.4	Predicted ignition delay times in comparison to the measurements by Kéromnès et al. [102] (98%v Ar dilution). . .	34
2.5	Predicted ignition delay times in comparison to the measurements by Kéromnès et al. [102] (98%v Ar dilution). . .	35
2.6	Ignition delay times predicted by different mechanisms in comparison to the measurements by Petersen et al. [109] ($\phi = 1$).	36
2.7	Ignition delay times predicted by different mechanisms in comparison to the measurements by Herzler and Naumann [110] ($\phi = 1, p_0 = 16\text{ bar}, 91\%v N_2$ dilution).	37
2.8	Ignition delay times of a H_2 -air stoichiometric mixture at the vN state ($T_0 = 1538\text{ K}$, $p_0 = 28\text{ bar}$) of a CJ detonation.	38
2.9	Ignition delay time maps as a function of initial pressure and temperature obtained with different reaction schemes. The white points indicates the post-shock conditions for different fractions of CJ speed.	39
2.10	Reduced effective activation energy maps as a function of initial pressure and temperature obtained with different reaction schemes. The white points indicate the post-shock conditions for different fractions of CJ speed.	41
2.11	1D CJ detonation profiles predicted through the ZND model in the wave frame of reference.	43
2.12	Post-shock (vN) and Chapman-Jouguet (CJ) states predicted by the Boivin et al. [100] mechanism in a CJ detonation for different combinations of initial pressure and temperature (H_2 -air, $\phi = 1$).	47

2.13	Chapman-Jouguet detonation speed (left) and Mach number (right) with respect to fresh gas predicted by the Boivin et al. [100] mechanism in a CJ detonation for different combinations of initial pressure and temperature (H_2 -air, $\phi = 1$).	47
2.14	H_2O mass fraction (left) and heat capacity ratio (right) at the Chapman-Jouguet state predicted by the Boivin et al. [100] mechanism for different combinations of initial pressure and temperature.	48
2.15	Activation energy evaluated with the explosion theory for different equivalence ratios and unity reaction order. E_a/RT_0 refers to the pre-shock temperature $T_0 = 298 K$.	60
2.16	Post-shock (vN) and Chapman-Jouguet (CJ) states predicted by the 2S1R mechanism in a CJ detonation for different combinations of initial pressure and temperature.	63
2.17	Chapman-Jouguet detonation speed (left) and Mach number (right) with respect to fresh gas predicted by the 2S1R mechanism in a CJ detonation for different combinations of initial pressure and temperature.	63
2.18	Half-reaction thickness as a function of CJ speed obtained through a 1D steady detonation (ZND) model with the 2S1R scheme.	65
2.19	Post-shock (vN) and Chapman-Jouguet states predicted by the 4S1R mechanism for different equivalent ratios and compared with the Boivin et al. [100] mechanism.	70
2.20	Reaction order and activation energy evaluated with the explosion theory for different equivalence ratios. E_a/RT_0 refers to the pre-shock temperature $T_0 = 298 K$	72
2.21	Reaction order and activation energy evaluated with the explosion theory for different H_2 -air equivalence ratios at atmospheric conditions.	74

2.22	Laminar viscosity dependence on temperature of the 4S1R mechanism with either a Sutherland or Power law fit of the full multi-component description calculated with Cantera (points).	77
2.23	Post-shock (vN) and Chapman-Jouguet (CJ) states predicted by the 4S1R mechanism for different combinations of initial pressure and temperature.	80
2.24	Chapman-Jouguet detonation speed (left) and Mach number (right) with respect to fresh gas predicted by the 4S1R mechanism for different combinations of initial pressure and temperature.	80
2.25	Half-reaction thickness as a function of CJ speed obtained through a 1D steady detonation (ZND) model with the 4S1R scheme.	81
2.26	1D detonation profiles (ZND model) for an atmospheric, stoichiometric H_2 -air mixture moving at CJ speed (1975 m/s).	83
2.27	Laminar flame speed in an atmospheric H_2 -air mixture for different mechanisms. The white squares are values measured by Krejci et al. [141].	85
3.1	Computational grid with the different refinement criteria. A: region of interest, B: buffer region, C: far field.	93
3.2	1D detonation profile (CJ speed) used for the initialization (2S1R mechanism).	97
3.3	Detail of the initial solution showing the staggered 1D detonation profiles (2S1R mechanism).	98
3.4	Temperature fields showing the formation of transverse instabilities. The white arrows and letters indicate the triple points which originates in the top half part of the domain.	101
3.5	Numerical smoked foil during the development of cellular instabilities showing the pressure peaks traces.	102

3.6	Instantaneous detonation front for three mesh sizings (2S1R mechanism).	104
3.7	Numerical smoked foils varying the mesh element size. . .	106
3.8	Scatter plots of the unburnt mixture state. The red dashed line describes the post-shock points varying the shock speed. The magenta dashed lines are additional post-shock states starting from the post-shock state at 75% and 110% of the CJ speed.	107
3.9	Instantaneous detonation profiles along the $y = 4$ mm line. The detonation speeds are 2060 m/s for (a) and 1995 m/s for (b) respectively.	109
3.10	Time trends of the leading shock speed at $y = 4$ mm for the different element sizings.	110
3.11	Time trends of the half reaction thickness at $y = 4$ mm for the different element sizings.	111
3.12	Half-reaction thickness as a function of the detonation wave speed for the 2D detonations (points) compared to the results from the 1D steady ZND model (lines) with both the Boivin [100] and the single-step reaction mechanisms.	113
3.13	Scatter plots of the unburnt mixture state ($\Delta_e = 30 \mu m$). The red line describes the post-shock points varying the shock speed. The magenta lines are additional post-shock states starting from the post-shock state at 75% and 110% of the CJ speed.	115
3.14	Time trends of the detonation speed (top) and half reaction thickness (bottom) at $y = 4$ mm for the different reaction mechanisms.	117
3.15	Numerical smoked foils (a,b) obtained with two different kinetic mechanisms ($\Delta_e = 30 \mu m$) and experimental smoked foil (c) for a stoichiometric H_2 -air mixture at $p=0.961$ atm [23] (the image has been cropped and resized to match the scale of the numerical results).	119

3.16	Instantaneous detonation front for the two mechanisms 4S1R (top row) and 2S1R (bottom row).	121
4.1	Schematics of the TU Berlin RDC test rig.	127
4.2	Picture of the test rig with the instrumentation [55].	128
4.3	Representation of the different wave modes observed ex- perimentally [49].	131
4.4	Schematic of the coordinate systems and sections of interest within the domain.	135
4.5	Cross-section of the mesh used for the simulations with the characteristic element size.	137
4.6	Initial solution adopted for the reactive simulation.	141
5.1	Schematic of a highly under-expanded jet [164].	147
5.2	Schematic of a transverse jet in a supersonic cross flow [165].	148
5.3	3D visualization of the shocks in the combustor.	149
5.4	Distributions of Mach (top) and H_2 mass fraction (bottom) in the cross-sections passing through (left) and between (right) the injectors. The white color corresponds to $\phi = 1$.	151
5.5	Mach number, tangential velocity and Y_{H_2} in the axial planes near the injection. The white color for the Y_{H_2} corresponds to $\phi = 1$ while positive V_{tan} is counter-clockwise.	152
5.6	Fields in the cross-sections passing through (top) and be- tween (bottom) the injectors. The black line represents $M = 1$	154
5.7	Velocity components in the cross-sections passing through (top) and between (bottom) the injectors.	155
5.8	Unwrapped cylindrical sections at different spans of the combustion chamber. The white color indicates $\phi = 1$	157
5.9	Celik's quality index for the non-reactive case LES.	159
6.1	Temporal history of the inlet mass flow rates and the resulting equivalence ratio.	163

6.2	Temporal history of the maximum temperature, pressure and heat release rate in the domain (7.7 MHz sampling).	164
6.3	Static pressure and temperature signals sampled at 50% span and $y = 25$ mm (7.7 MHz sampling).	164
6.4	Static pressure signals sampled at 7.7 MHz in four consecutive locations within the chamber at $y = 25$ mm and 50% span (top) and the resulting rotation frequency (bottom).	167
6.5	Instantaneous total pressure calculated at the outlet section. The dotted line indicates the measurements by Bach et al. [156].	170
6.6	Time-averaged axial distributions of total pressure at different spans of the combustion chamber. The dashed line indicates the refill height. The experimental value is reported from Bach et al. [156].	171
6.7	Instantaneous, punctual quantities predicted at the half span of the outlet section (e), i.e. $(\theta, r, y) = (340^\circ, 41.2 \text{ mm}, 109 \text{ mm})$.	175
6.8	Instantaneous EAP_i and total pressure calculated at the outlet section. The dotted line indicates the total pressure measurements by Bach et al. [156].	176
6.9	Shock structures visualised through the $\nabla P/P = 2000 \text{ m}^{-1}$ isosurface and coloured by static pressure.	178
6.10	Static pressure in different axial sections near the detonation.	179
6.11	Radial velocity in different axial sections near the detonation.	180
6.12	Numerical schlieren ($\nabla P/P$) the base of the chamber ($y = 0$ mm).	181
6.13	Position of the cylindrical sections at constant span in the combustion chamber. (a) xy plane cross section, (b) three-dimensional view.	183

6.14	Instantaneous temperature on unwrapped cylindrical sections at different spans of the combustion chamber. The dashed line indicates the slip line. (1) detonation; (2) oblique shock; (3) slip line in products; (4) refill region; (5) detonation products.	183
6.15	Instantaneous static pressure on unwrapped cylindrical sections at different spans of the combustion chamber. . .	184
6.16	Instantaneous species mass fractions on unwrapped cylindrical sections at different spans of the combustion chamber.	185
6.17	Instantaneous temperature on different axial planes of the combustion chamber.	187
6.18	Averaged Mach number on unwrapped cylindrical sections at different spans of the combustion chamber and velocity streamlines. The dashed lines denote the refill region. . .	189
6.19	Averaged temperature on unwrapped cylindrical sections at different spans of the combustion chamber.	190
6.20	Time-averaged axial distributions of temperature at different spans of the combustion chamber. The dashed line indicates the refill height.	191
6.21	Averaged Y_{H_2} on unwrapped cylindrical sections at different spans of the combustion chamber. The white color indicates $\phi = 1$ when Y_{H_2O} is negligible.	192
6.22	Averaged Y_{H_2O} on unwrapped cylindrical sections at different spans of the combustion chamber.	192
6.23	Hydrogen unmixedness on unwrapped cylindrical sections at different spans of the combustion chamber.	193
6.24	Instantaneous Y_{H_2} on different axial planes of the combustion chamber.	195
6.25	Refill region visualised by the nodes with $Y_{H_2O} \leq 0.125$ and coloured by Y_{H_2} . (a) isometric view, (b) top view. . .	196
6.26	Instantaneous heat release rate on unwrapped cylindrical sections at different spans of the combustion chamber. . .	199

6.27	From top to bottom: static pressure at the inner (I7) and mid (M7) radius of the chamber ($y = 25$ mm); radial and axial speed and static temperature in the air gap (G1) and in a fuel injector (N1) respectively 1 and 3 mm before the exit in the chamber. The signals are sampled at 7.7 MHz.	202
6.28	Polar diagram of the Mach number at the injectors exit superimposed to numerical schlieren at the chamber base. The curves describe the inward radial component in the air gap ($r = 45.1$, $y = 0.6$ mm) and the axial component within a fuel injector ($y = -0.1$ mm).	205
6.29	Polar diagrams of the local normalized mass flux in the injectors (left) and resulting Air-to-Fuel ratio (AFR, right), where the nominal stoichiometric value is $AFR = 34$. The detonation is located at $\theta = 0$ deg.	206
6.30	Polar diagrams of the local radial velocity and density normalized with their maximum (left) and total pressure (right) in the air injector. The detonation is located at $\theta = 0$ deg.	207
6.31	Distributions of Mach (top) and H_2 mass fraction (bottom) in the cross-sections through (left) and between (right) the injectors ≈ 14 deg before the detonation passage.	210
6.32	Mach number, radial and tangential velocity and Y_{H_2} in the axial planes near the injection before the detonation passage. The white color for the Y_{H_2} corresponds to $\phi = 1$ while positive V_{tan} is counter-clockwise.	212
6.33	Cross-sections ≈ 14 deg before the detonation passage.	214
6.34	Distributions of Mach (top) and H_2 mass fraction (bottom) in the cross-sections through (left) and between (right) the injectors ≈ 14 deg after the detonation passage.	217
6.35	Mach number, radial and tangential velocity and Y_{H_2} in the axial planes near the injection after the detonation passage. The white color for the Y_{H_2} corresponds to $\phi = 1$ while positive V_{tan} is counter-clockwise.	218

6.36	Celik's quality index for the reactive LES.	220
6.37	Viscosity ratio (left) and Celik's quality index (right) on the x, y cross-section before the detonation passage.	221
7.1	Representation of the reference frames adopted to describe the detonation front. (x, y, z) : global cartesian system, (θ, r, y) : global cylindrical system, (d, r, y) : cartesian system rotating with the front.	229
7.2	Determination of the front normal displacement.	229
7.3	Time-averaged quantities on the refill region in the plane ahead of the detonation front ($\Delta\theta = 10$ deg).	232
7.4	Phase-Locked Ensemble Averaged maps of hydrogen mass fraction (top) and unmixedness (bottom) in the frontal plane as a function of the relative position between the injectors Θ_p [%].	235
7.5	Phase-Locked Ensemble Averaged axial distributions of hydrogen mass fraction in the frontal plane.	236
7.6	Phase-Locked Ensemble Averaged maps of Mach number (top) and sound speed (bottom) in the frontal plane as a function of the relative position between the injectors Θ_p [%].	237
7.7	Time-averaged CJ speed and Mach number in the fresh gas ahead of the detonation.	239
7.8	Phase-Locked Ensemble Averaged maps of the CJ speed in the frontal plane as a function of the relative position between the injectors Θ_p [%].	241
7.9	Visualization of the instantaneous detonation front with respect to the hydrogen jets.	243
7.10	Time-averaged front shape (top) and front normal average inclination with respect to the tangential, axial and radial directions (bottom). The vector field represents the front average normal.	244

7.11	Time-averaged detonation front cuts at different axial positions in terms of linear (top) and angular (bottom) distance from the average front plane.	245
7.12	Time-averaged normal propagation speed of the detonation front D and angular speed ω	247
7.13	Time-average (left) and RMS (right) of the ratio between the normal detonation speed and the local CJ speed on the front.	249
7.14	Time-averaged radial distribution of the detonation speed between $10 < y < 35$ mm.	250
7.15	Probability density functions of the local detonation normal speed with respect to the relative position between the injectors. The maps are relative to four quadrants in the radial-axial plane and are normalized with the local maximum value.	253

List of Tables

1.1	Summary of recent published 3D annular RDC simulations. Legend: LIH=Lavrentyev Institute of Hydrodynamics (RU), WUT=Warsaw University of Technology (PL), AFRL=Air Force Research Laboratory (US), ONERA=Office National d'Etudes et de Recherches Aérospatiales (FR); P=premixed, NP=non-premixed; S=species, R=reactions.	19
2.1	Summary of reaction mechanisms for $H_2 - O_2$ combustion.	27
2.2	Available shock-tube measurements near the conditions of interest for a H_2 -air detonation.	29
2.3	Characteristic reaction zone widths and estimated cell size (λ) according to Ng et al. [117] correlation.	45
2.4	Thermodynamic and detonation properties predicted with different mechanisms thermodynamic data. The quantities are expressed in $[g/mol]$, $[kg/m^3]$, $[m/s]$, $[K]$, $[bar]$, respectively. The bold numbers highlight the values within a relative difference of $\pm 8\%$ with respect to the Boivin [100] mechanism.	57
2.5	Summary of the main parameters for the 2S1R mechanism for a detonation in a stoichiometric, atmospheric H_2 -air mixture.	61
2.6	Correction of the H_2O formation enthalpy for the 4S1R scheme.	69

2.7	Summary of the main parameters for the 4S1R mechanism for a detonation in a H_2 -air mixture ($T_0 = 298\text{ K}$).	75
2.8	Transport properties at the adiabatic equilibrium of an H_2 -air stoichiometric mixture initially at atmospheric conditions.	78
3.1	Details of the tested grids.	95
3.2	Summary of the simulations.	100
3.3	Average detonation characteristics calculated from the simulations.	111
3.4	Average detonation characteristics calculated from the simulations ($\Delta_e = 30\ \mu m$) and experiments.	116
4.1	Geometric dimensions of the configuration analysed.	129
4.2	Main operating conditions of the analysed test point.	132
4.3	Computational requirements of the simulations.	143
5.1	Operating conditions resulting from the LES with respect to the nominal isentropic values (non-reactive case).	146
6.1	Operating conditions resulting from the LES with respect to the nominal test point (reactive case).	165
6.2	Predicted and measured blockage of the detonation with respect to the non-reactive condition.	165
6.3	Predicted and measured wave features.	168
6.4	Predicted and measured exit total pressure and gain.	170
6.5	Predicted total pressure and EAPi at the combustor exit and corresponding pressure gain.	176
6.6	Timeline of the injectors operation.	205
7.1	Time-averaged CJ speed on the chamber outer wall between $10 < y < 35\text{ mm}$	240
7.2	Detonation speed components and CJ speed averaged over one revolution between $10 < y < 35\text{ mm}$	250

Bibliography

- [1] IEA. “International energy outlook 2021.” 2021.
- [2] IEA. “Global energy review 2021.” 2021.
- [3] Stathopoulos, Panagiotis. “Comprehensive Thermodynamic Analysis of the Humphrey Cycle for Gas Turbines with Pressure Gain Combustion.” *Energies*, 11(12):3521, 2018. doi: 10.3390/en11123521.
- [4] Sousa, Jorge, Paniagua, Guillermo, and Collado Morata, Elena. “Thermodynamic analysis of a gas turbine engine with a rotating detonation combustor.” *Applied Energy*, 195:247–256, 2017. ISSN 03062619. doi: 10.1016/j.apenergy.2017.03.045. URL <http://dx.doi.org/10.1016/j.apenergy.2017.03.045>.
- [5] Gicquel, Laurent Y M, Staffelbach, Gabriel, and Poinso, Thierry. “Large Eddy Simulations of gaseous flames in gas turbine combustion chambers.” *Progress in Energy and Combustion Science*, 38(6):782–817, 2013. doi: 10.1016/j.pecs.2012.04.004.
- [6] Manabe, Syukuro. Role of greenhouse gas in climate change. In *Dynamic Meteorology and Oceanography*, volume 71, pages 1–13. Taylor and Francis, 2019. doi: 10.1080/16000870.2019.1620078. URL <https://doi.org/10.1080/16000870.2019.1620078>.
- [7] Lenssen, N., Schmidt, G., Hansen, J., Menne, M., Persin, A., Ruedy, R., and Zyss, D. “Improvements in the gistemp uncer-

- tainty model.” *J. Geophys. Res. Atmos.*, 124(12):6307–6326, 2019. doi: 10.1029/2018JD029522.
- [8] IPCC. “The intergovernmental panel on climate change.” 2021.
- [9] United nations framework convention on climate change, paris agreement: Un climate conference.
- [10] Posdziech, Oliver, Schwarze, Konstantin, and Brabandt, Jörg. “Efficient hydrogen production for industry and electricity storage via high-temperature electrolysis.” *International Journal of Hydrogen Energy*, 4:19089–19101, 2019. ISSN 03603199. doi: 10.1016/j.ijhydene.2018.05.169.
- [11] European turbine network, hydrogen gas turbines, 2020.
- [12] Perkins, H Douglas and Paxson, Daniel E. “Summary of Pressure Gain Combustion Research at NASA.” (April), 2018. URL <http://www.sti.nasa.gov>.
- [13] Bellenoue, M, Boust, B, Vidal, P, Zitoun, R, Gaillard, T, Davidenko, D, Leyko, M, and Le Naour, B. “New Combustion Concepts to Enhance the Thermodynamic Efficiency of Propulsion Engines.” *Challenge in Combustion for Aerospace Propulsion*, (11):1–13, 2016. doi: 10.12762/2016.AL11-12.
- [14] Heiser, William H. and Pratt, David T. “Thermodynamic Cycle Analysis of Pulse Detonation Engines.” *Journal of Propulsion and Power*, 18(1):68–76, 2002. ISSN 0748-4658. doi: 10.2514/2.5899.
- [15] Akbari, P. and Nalim, M. R. “Review of recent developments in wave rotor combustion technology.” *Journal of Propulsion and Power*, 25(4):833–844, 2009. doi: 10.2514/1.34081. URL <https://doi.org/10.2514/1.34081>.
- [16] Kailasanath, K. “The rotating-detonation-wave engine concept: A brief status report.” *49th AIAA Aerospace Sciences Meeting*

- Including the New Horizons Forum and Aerospace Exposition*, (January), 2011. doi: 10.2514/6.2011-580.
- [17] Anand, Vijay and Gutmark, Ephraim. “A review of pollutants emissions in various pressure gain combustors.” *International Journal of Spray and Combustion Dynamics*, 11:1–18, 2019. ISSN 17568285. doi: 10.1177/1756827719870724.
- [18] Bluemner, Richard. “Bluemner-Operating Mode Dynamics in Rotating Detonation Combustors.” 2020. URL <https://depositonce.tu-berlin.de/handle/11303/11517>.
- [19] Lutoschkin, E. “Pressure-gain combustion for gas turbines based on shock-flame interaction.” 2014. URL <http://d-nb.info/105202100X/34>.
- [20] Lee, John H.S. *The Detonation Phenomenon*. Cambridge University Press, 2008. ISBN 9780521897235.
- [21] Law, Chung K. *Combustion Physics*. Cambridge University Press, 2006. ISBN 9780521870528.
- [22] Browne, S., Ziegler, J., and Shepherd, J. E. “Numerical Solution Methods for Shock and Detonation Jump Conditions.” *GALCIT Report FM2006.006*, (July 2004), 2008.
- [23] Bull, D. C., Elsworth, J. E., Shuff, P. J., and Metcalfe, E. “Detonation cell structures in fuel/air mixtures.” *Combustion and Flame*, 45 (C):7–22, 1982. ISSN 00102180. doi: 10.1016/0010-2180(82)90028-1.
- [24] Peraldi, O, Knystautas, R, and Lee, J H. “Criteria for Transition To Detonation.” *Twenty first symposium on Combustion*, pages 1629–1637, 1986.
- [25] Guirao, C M, Knystautas, R, and Lee, J H. “A Summary of Hydrogen-Air Detonation Experiments.” *Nureg/Cr-4961 Sand87-7128 R3*, pages 1–88, 1989.

- [26] Tang, Xin Meng, Wang, Jian Ping, and Shao, Ye Tao. “Three-dimensional numerical investigations of the rotating detonation engine with a hollow combustor.” *Combustion and Flame*, 162(4): 997–1008, 2015. ISSN 15562921. doi: 10.1016/j.combustflame.2014.09.023. URL <http://dx.doi.org/10.1016/j.combustflame.2014.09.023>.
- [27] Nakagami, Soma, Matsuoka, Ken, Kasahara, Jiro, Kumazawa, Yoshiki, Fujii, Jumpei, Matsuo, Akiko, and Funaki, Ikkoh. “Experimental visualization of the structure of rotating detonation waves in a disk-shaped combustor.” *Journal of Propulsion and Power*, 33(1):80–88, 2017. ISSN 15333876. doi: 10.2514/1.B36084.
- [28] Lu, Frank K., Braun, Eric M., Massa, Luca, and Wilson, Donald R. “Rotating detonation wave propulsion: Experimental challenges, modeling, and engine concepts (Invited).” *47th AIAA/ASME/SAE/ASEE Joint Propulsion Conference and Exhibit 2011*, (August):464–470, 2011. doi: 10.2514/6.2011-6043.
- [29] Voitsekhovskii, B.V. “Spinning maintained detonations.” *Zhurnal Prikladnaya Mekhanika i Tekhnicheskaya Fizika 1 (3)*, 1(3): 157–164.
- [30] Nicholls, J. A. and Cullen, R. E. The Feasibility of a Rotating Detonation Wave Rocket Motor. Technical report, US Air Force Flight Test Center, 1964.
- [31] Adamson, T. and Olsson, G. “Performance analysis of a rotating detonation wave rocket engine.” *Acta Astronautica*, 13(4):405–415, 1967.
- [32] Eidelman, S., Grossmann, I., and Lottati, I. “Review of propulsion applications and numerical simulations of the pulsed detonation engine concept.” *Journal of Propulsion and Power*, 7(6):857–865, 1991.

- [33] Zhdan, S., Mitrofanov, V., and Sychev, A. "Impulse produced by gas detonation in open chamber." *Combustion, detonation, shock waves. Zeldovich Memorial Proceedings*, page 422–25, 1994.
- [34] Zitoun, R., Gamezo, V., Guerroud, V., and Desbordes, D. "Experimental study of propulsive efficiency of pulsed detonation." *Proceedings of the 21st International Symposium on Shock Waves*, page 421–425, 1997.
- [35] Norris, G. "Pulse power: pulse detonation engine-powered flight demonstration marks milestone in mojave." *Aviation Week and Space Technology*, 168(7), 2008.
- [36] Rasheed, A., Furman, H., and Dean, J. "Experimental investigations of the performance of a multitube pulse detonation turbine system." *Journal of Propulsion and Power*, 27(3):586–596, 2011.
- [37] Wolański, Piotr. "Detonative propulsion." *Proceedings of the Combustion Institute*, 34(1):125–158, 2013. ISSN 15407489. doi: 10.1016/j.proci.2012.10.005.
- [38] Bykovskii, Fedor A., Zhdan, Sergey A., and Vedernikov, Evgenii F. "Continuous spin detonations." *Journal of Propulsion and Power*, 22(6):1204–1216, 2006. ISSN 15333876. doi: 10.2514/1.17656.
- [39] Frolov, S. M., Aksenov, V. S., Ivanov, V. S., and Shamshin, I. O. "Large-scale hydrogen-air continuous detonation combustor." *International Journal of Hydrogen Energy*, 40(3):1616–1623, 2015. ISSN 03603199. doi: 10.1016/j.ijhydene.2014.11.112. URL <http://dx.doi.org/10.1016/j.ijhydene.2014.11.112>.
- [40] Lentsch, A., Bec, R., Serre, L., Falempin, F., Daniau, D., Piton, D., Prigent, A., Canteins, G., Zitoun, R., Desbordes, D., Jouot, F., and Gokalp, I. *Overview of Current French Activities on PDRE and Continuous Detonation Wave Rocket Engines*. doi: 10.2514/6.2005-3232. URL <https://arc.aiaa.org/doi/abs/10.2514/6.2005-3232>.

- [41] Thomas, L., Schauer, F., Hoke, J., and Naples, A. *Buildup and Operation of a Rotating Detonation Engine*. doi: 10.2514/6.2011-602. URL <https://arc.aiaa.org/doi/abs/10.2514/6.2011-602>.
- [42] St. George, Andrew, Driscoll, Robert, Anand, Vijay, Randall, Steve, Munday, David, and Gutmark, Ephraim J. "Development of a rotating detonation engine facility at the university of Cincinnati." *53rd AIAA Aerospace Sciences Meeting*, (November), 2015. doi: 10.2514/6.2015-0635.
- [43] Naples, Andrew, Hoke, John, Battelle, Ryan, Wagner, Matt, and Schauer, Fred. "Rotating detonation engine implementation into an open-loop T63 gas turbine engine." *AIAA SciTech Forum - 55th AIAA Aerospace Sciences Meeting*, (January):1-9, 2017. doi: 10.2514/6.2017-1747.
- [44] Rankin, Brent A., Richardson, Daniel R., Caswell, Andrew W., Naples, Andrew G., Hoke, John L., and Schauer, Frederick R. "Chemiluminescence imaging of an optically accessible non-premixed rotating detonation engine." *Combustion and Flame*, 176:12-22, 2017. ISSN 15562921. doi: 10.1016/j.combustflame.2016.09.020. URL <http://dx.doi.org/10.1016/j.combustflame.2016.09.020>.
- [45] Ishihara, Kazuki, Kato, Yuichi, Matsuoka, Ken, Kasahara, Jiro, Matsuo, Akiko, and Funaki, Ikkoh. "Thrust Performance Evaluation of a Rotating Detonation Engine with a Conical Plug." *25th ICDEERS*, (January):1-12, 2015.
- [46] Shao, Ye-Tao, Liu, Meng, and Wang, Jian-Ping. "Numerical investigation of rotating detonation engine propulsive performance." *Combustion Science and Technology*, 182(11-12):1586-1597, 2010. doi: 10.1080/00102202.2010.497316. URL <https://doi.org/10.1080/00102202.2010.497316>.

- [47] Bohon, M. D., Bluemner, R., Paschereit, C. O., and Gutmark, E. J. “High-speed imaging of wave modes in an RDC.” *Experimental Thermal and Fluid Science*, 102(October 2018):28–37, 2019. ISSN 08941777. doi: 10.1016/j.exptthermflusci.2018.10.031. URL <https://doi.org/10.1016/j.exptthermflusci.2018.10.031>.
- [48] Bluemner, Richard, Bohon, Myles D., Paschereit, Christian Oliver, and Gutmark, Ephraim J. “Effect of inlet and outlet boundary conditions on rotating detonation combustion.” *Combustion and Flame*, 216:300–315, 2020. ISSN 15562921. doi: 10.1016/j.combustflame.2020.03.011.
- [49] Bach, Eric, Stathopoulos, Panagiotis, Paschereit, Christian Oliver, and Bohon, Myles D. “Performance analysis of a rotating detonation combustor based on stagnation pressure measurements.” *Combustion and Flame*, 217:21–36, 2020. ISSN 15562921. doi: 10.1016/j.combustflame.2020.03.017. URL <https://doi.org/10.1016/j.combustflame.2020.03.017>.
- [50] Wolański, Piotr. Application of the continuous rotating detonation to gas turbine. In *Experimental Mechanics and Effects of Intensive Loading*, volume 782 of *Applied Mechanics and Materials*, pages 3–12. Trans Tech Publications Ltd, 9 2015. doi: 10.4028/www.scientific.net/AMM.782.3.
- [51] Frolov, S.M., Aksenov, V.S., and Ivanov, V.S. “Experimental proof of zel’dovich cycle efficiency gain over cycle with constant pressure combustion for hydrogen–oxygen fuel mixture.” *International Journal of Hydrogen Energy*, 40(21):6970–6975, 2015. ISSN 0360-3199. doi: <https://doi.org/10.1016/j.ijhydene.2015.03.128>. URL <https://www.sciencedirect.com/science/article/pii/S0360319915007740>.
- [52] Fotia, Matthew, Kaemming, Thomas A., Hoke, John, and Schauer, Frederick. *Study of the Experimental Performance of a Rotating Detonation Engine with Nozzled Exhaust Flow*. doi:

- 10.2514/6.2015-0631. URL <https://arc.aiaa.org/doi/abs/10.2514/6.2015-0631>.
- [53] Paxson, Daniel E. and Naples, Andrew. *Numerical and Analytical Assessment of a Coupled Rotating Detonation Engine and Turbine Experiment*. doi: 10.2514/6.2017-1746. URL <https://arc.aiaa.org/doi/abs/10.2514/6.2017-1746>.
- [54] Kaemming, Thomas A. and Paxson, Daniel E. “Determining the pressure gain of pressure gain combustion.” *2018 Joint Propulsion Conference*, pages 1–15, 2018. doi: 10.2514/6.2018-4567.
- [55] Bach, Eric, Bohon, Myles D, Paschereit, Christian Oliver, and Stathopoulos, Panagiotis. Impact of outlet restriction on RDC performance and stagnation pressure rise. In *AIAA Scitech 2019 Forum*, number January, 2019. ISBN 9781624105784. doi: 10.2514/6.2019-0476.
- [56] Prakash, Supraj, Raman, Venkat, Lietz, Christopher F., Hargus, William A., and Schumaker, Stephen A. “Numerical simulation of a methane-oxygen rotating detonation rocket engine.” *Proceedings of the Combustion Institute*, 38(3):3777–3786, 2021. ISSN 15407489. doi: 10.1016/j.proci.2020.06.288. URL <https://doi.org/10.1016/j.proci.2020.06.288>.
- [57] Liu, Z., Braun, J., and Paniagua, G. “Characterization of a Supersonic Turbine Downstream of a Rotating Detonation Combustor.” *Journal of Engineering for Gas Turbines and Power*, 141(3):1–13, 2019. ISSN 15288919. doi: 10.1115/1.4040815.
- [58] Asli, Majid, Stathopoulos, Panagiotis, and Paschereit, Christian Oliver. “Aerodynamic Investigation of Guide Vane Configurations Downstream a Rotating Detonation Combustor.” *Journal of Engineering for Gas Turbines and Power*, 143(6):1–7, 2021. ISSN 0742-4795. doi: 10.1115/1.4049188.

- [59] Kailasanath, K. and Schwer, D. A. “High-fidelity simulations of pressure-gain combustion devices based on detonations.” *Journal of Propulsion and Power*, 33(1):153–162, 2017. ISSN 15333876. doi: 10.2514/1.B36169.
- [60] Davidenko, Dmitry M., Gökalp, Iskender, and Kudryavtsev, Alexey N. “Numerical Simulation of the Continuous Rotating Hydrogen-Oxygen Detonation with a Detailed Chemical Mechanism.” *West-East High Speed Flow Field Conference*, (November), 2007.
- [61] Schwer, Douglas A. and Kailasanath, Kailas. “Feedback into mixture plenums in rotating detonation engines.” *50th AIAA Aerospace Sciences Meeting Including the New Horizons Forum and Aerospace Exposition*, (January):1–17, 2012. doi: 10.2514/6.2012-617.
- [62] Paxson, Daniel E. “Impact of an exhaust throat on semi-idealized rotating detonation engine performance.” *54th AIAA Aerospace Sciences Meeting*, (January):1–10, 2016.
- [63] Yi, Tae Hyeong, Turangan, Cary, Lou, Jing, Wolanski, Piotr, and Kindracki, Jan. “A three-dimensional numerical study of rotational detonation in an annular chamber.” *47th AIAA Aerospace Sciences Meeting including the New Horizons Forum and Aerospace Exposition*, (January), 2009. doi: 10.2514/6.2009-634.
- [64] Ma, Fuhua, Choi, Jeong Yeol, and Yang, Vigor. “Thrust chamber dynamics and propulsive performance of multitude pulse detonation engines.” *Journal of Propulsion and Power*, 21(4):681–691, 2005. ISSN 07484658. doi: 10.2514/1.8182.
- [65] Schwer, Douglas A. and Kailasanath, K. “Effect of inlet on fill region and performance of rotating detonation engines.” *47th AIAA/ASME/SAE/ASEE Joint Propulsion Conference and Exhibit 2011*, (August):1–17, 2011.

- [66] Kindracki, J., Kobiera, A., Wolański, P., Gut, Z., Folusiak, M., and Swiderski, K. “Experimental and numerical study of the rotating detonation engine in hydrogen-air mixtures.” 2:555–582, 2011. doi: 10.1051/eucass/201102555.
- [67] Eude, Yohann, Davidenko, Dmitry M., Gökalp, Iskender, and Falempin, François. “Use of the adaptive mesh refinement for 3D simulations of a CDWRE (Continuous Detonation Wave Rocket Engine).” *17th AIAA International Space Planes and Hypersonic Systems and Technologies Conference 2011*, (April):1–12, 2011. doi: 10.2514/6.2011-2236.
- [68] Davidenko, Dmitry, Gökalp, Iskender, Dufour, Emmanuel, and Magre, Philippe. “Numerical simulation of hydrogen supersonic combustion and validation of computational approach.” *12th AIAA International Space Planes and Hypersonic Systems and Technologies*, (December):1–11, 2003. doi: 10.2514/6.2003-7033.
- [69] Frolov, S. M., Dubrovskii, A. V., and Ivanov, V. S. “Three-dimensional numerical simulation of the operation of a rotating-detonation chamber with separate supply of fuel and oxidizer.” *Russian Journal of Physical Chemistry B*, 7(1):35–43, 2013. ISSN 19907931. doi: 10.1134/S1990793113010119.
- [70] Zhou, R. and Wang, J. P. “Numerical investigation of shock wave reflections near the head ends of rotating detonation engines.” *Shock Waves*, 23(5):461–472, 2013. ISSN 09381287. doi: 10.1007/s00193-013-0440-0.
- [71] Schwer, Douglas A., Corrigan, Andrew, and Kailasanath, K. “Towards efficient, unsteady, three-dimensional rotating detonation engine simulations.” *52nd Aerospace Sciences Meeting*, (January): 1–17, 2014. doi: 10.2514/6.2014-1014.
- [72] Schwer, Douglas A. and Kailasanath, K. “Effect of low pressure ratio on exhaust plumes of rotating detonation engines.” *50th*

- AIAA/ASME/SAE/ASEE Joint Propulsion Conference 2014*, pages 1–16, 2014. doi: 10.2514/6.2014-3901.
- [73] Escobar, Sergio. “Rotating detonation combustion: A computational study for stationary power generation.” 2014.
- [74] Wu, Dan, Liu, Yan, Liu, Yusi, and Wang, Jianping. “Numerical investigations of the restabilization of hydrogen-air rotating detonation engines.” *International Journal of Hydrogen Energy*, 39(28):15803–15809, 2014. ISSN 03603199. doi: 10.1016/j.ijhydene.2014.07.159. URL <http://dx.doi.org/10.1016/j.ijhydene.2014.07.159>.
- [75] Tsuboi, Nobuyuki, Watanabe, Yusuke, Kojima, Takayuki, and Hayashi, A. Koichi. “Numerical estimation of the thrust performance on a rotating detonation engine for a hydrogen-oxygen mixture.” *Proceedings of the Combustion Institute*, 35(2):2005–2013, 2015. ISSN 15407489. doi: 10.1016/j.proci.2014.09.010. URL <http://dx.doi.org/10.1016/j.proci.2014.09.010>.
- [76] Dubrovskii, A. V., Ivanov, V. S., and Frolov, S. M. “Three-dimensional numerical simulation of the operation process in a continuous detonation combustor with separate feeding of hydrogen and air.” *Russian Journal of Physical Chemistry B*, 9(1):104–119, 2015. ISSN 19907923. doi: 10.1134/S1990793115010157.
- [77] Cocks, Peter A.T., Holley, Adam T., and Rankin, Brent A. “High fidelity simulations of a non-premixed rotating detonation engine.” *54th AIAA Aerospace Sciences Meeting*, 0(January):1–18, 2016. doi: 10.2514/6.2016-0125.
- [78] Eklund, Dean and Stouffer, Scott. “A numerical and experimental study of a supersonic combustor employing sweep ramp fuel injectors.” 1994. doi: 10.2514/6.1994-2819.
- [79] Tsuboi, Nobuyuki, Eto, Seiichiro, Hayashi, A. Koichi, and Kojima, Takayuki. “Front cellular structure and thrust performance

- on hydrogen-oxygen rotating detonation engine.” *Journal of Propulsion and Power*, 33(1):100–111, 2017. ISSN 15333876. doi: 10.2514/1.B36095.
- [80] Sun, Jian, Zhou, Jin, Liu, Shijie, Lin, Zhiyong, and Cai, Jianhua. “Effects of injection nozzle exit width on rotating detonation engine.” *Acta Astronautica*, 140(September):388–401, 2017. ISSN 00945765. doi: 10.1016/j.actaastro.2017.09.008. URL <https://doi.org/10.1016/j.actaastro.2017.09.008>.
- [81] Gaillard, Thomas, Davidenko, Dmitry M, Kudryavtsev, Alexey N, and Gökalp, Iskender. “Numerical Simulation of a Rotating Detonation under Conditions of Premixed and Separate Injection of H₂-O₂.” *Eucass*, pages 1–14, 2017. doi: 10.13009/EUCASS2017-171.
- [82] Sato, Takuma and Raman, Venkat. “Detonation structure in ethylene/air based non-premixed rotating detonation engine.” *AIAA Scitech 2019 Forum*, (January 2019), 2019. doi: 10.2514/6.2019-2023.
- [83] Varatharajan, B. and Williams, F. “Ethylene ignition and detonation chemistry, part 2: Ignition histories and reduced mechanisms.” *Journal of Propulsion and Power*, 18(2):352–362, 2002.
- [84] Foundational fuel chemistry model version 1.0 (ffcm-1). URL <http://nanoenergy.stanford.edu/ffcm1>.
- [85] Sato, Takuma, Chacon, Fabian, White, Logan, Raman, Venkat, and Gamba, Mirko. “Mixing and detonation structure in a rotating detonation engine with an axial air inlet.” *Proceedings of the Combustion Institute*, 38(3):3769–3776, 2021. ISSN 15407489. doi: 10.1016/j.proci.2020.06.283. URL <https://doi.org/10.1016/j.proci.2020.06.283>.
- [86] Mueller, M. A., Kim, T. J., Yetter, R. A., and Dryer, F. L. “Flow reactor studies and kinetic modeling of the H₂/O₂ reaction.” *International Journal of Chemical Kinetics*, 31(2):113–125,

1999. ISSN 05388066. doi: 10.1002/(SICI)1097-4601(1999)31:2<113::AID-KIN5>3.0.CO;2-0.
- [87] Sánchez, Antonio L and Williams, Forman A. “Recent advances in understanding of flammability characteristics of hydrogen.” *Progress in Energy and Combustion Science*, 41:1–55, 2014. ISSN 0360-1285. doi: 10.1016/j.pecs.2013.10.002. URL <http://dx.doi.org/10.1016/j.pecs.2013.10.002>.
- [88] Taylor, B. D., Kessler, D. A., Gamezo, V. N., and Oran, E. S. “Numerical simulations of hydrogen detonations with detailed chemical kinetics.” *Proceedings of the Combustion Institute*, 34(2):2009–2016, 2013. ISSN 15407489. doi: 10.1016/j.proci.2012.05.045. URL <http://dx.doi.org/10.1016/j.proci.2012.05.045>.
- [89] Shepherd, J. E. “Detonation in gases.” *Proceedings of the Combustion Institute*, 32 I(1):83–98, 2009. ISSN 15407489. doi: 10.1016/j.proci.2008.08.006. URL <http://dx.doi.org/10.1016/j.proci.2008.08.006>.
- [90] Radulescu, Matei I., Sharpe, Gary J., Law, Chung K., and Lee, John H.S. “The hydrodynamic structure of unstable cellular detonations.” *Journal of Fluid Mechanics*, 580:31–81, 2007. ISSN 00221120. doi: 10.1017/S0022112007005046.
- [91] Curran, Henry J. “Developing detailed chemical kinetic mechanisms for fuel combustion.” *Proceedings of the Combustion Institute*, 37 (1):57–81, 2019. ISSN 15407489. doi: 10.1016/j.proci.2018.06.054.
- [92] Kee, Robert J., Coltrin, Michael E., and Glarborg, Peter. *Chemically Reacting Flow*. 2005. ISBN 9780471461296. doi: 10.1002/0471461296. URL <http://doi.wiley.com/10.1002/0471461296>.
- [93] Wang, Xianming and Law, Chung K. “An analysis of the explosion limits of hydrogen-oxygen mixtures.” *Journal of Chemical Physics*, 138(13), 2013. ISSN 00219606. doi: 10.1063/1.4798459.

- [94] Browne, S., Liang, Z., and Shepherd, J. E. "Detailed and simplified chemical reaction mechanisms for detonation simulation." *Fall Technical Meeting of the Western States Section of the Combustion Institute 2005, WSS/CI 2005 Fall Meeting*, 1:274–291, 2005.
- [95] Smith, Gregory P., Golden, David M., Frenklach, Michael, Moriarty, Nigel W., Eiteneer, Boris, Goldenberg, Mikhail, Bowman, C. Thomas, Hanson, Ronald K., Song, Soonho, William C. Gardiner, Jr., Lissianski, Vitali V., and Qin, Zhiwei. GRI30 mechanism, 1999.
- [96] Li, Juan, Zhao, Zhenwei, Kazakov, Andrei, and Dryer, Frederick L. "An Updated Comprehensive Kinetic Model of Hydrogen Combustion." 2004. doi: 10.1002/kin.20026.
- [97] Ó Conaire, Marcus, Curran, Henry J., Simmie, John M., Pitz, William J., and Westbrook, Charles K. "A comprehensive modeling study of hydrogen oxidation." *International Journal of Chemical Kinetics*, 36(11):603–622, 2004. ISSN 05388066. doi: 10.1002/kin.20036.
- [98] ANSYS. Fluent 2019R3 Theory Guide, 2019.
- [99] Hong, Zekai, Davidson, David F., and Hanson, Ronald K. "An improved H₂/O₂ mechanism based on recent shock tube/laser absorption measurements." *Combustion and Flame*, 158(4):633–644, 2011. ISSN 00102180. doi: 10.1016/j.combustflame.2010.10.002. URL <http://dx.doi.org/10.1016/j.combustflame.2010.10.002>.
- [100] Boivin, Pierre, Jiménez, C., Sánchez, A. L., and Williams, F. A. "An explicit reduced mechanism for H₂-air combustion." *Proceedings of the Combustion Institute*, 33(1):517–523, 2011. ISSN 15407489. doi: 10.1016/j.proci.2010.05.002.
- [101] Burke, Michael P., Chaos, Marcos, Ju, Yiguang, Dryer, Frederick L., and Klippenstein, Stephen J. "Comprehensive H₂/O₂ kinetic

- model for high-pressure combustion.” *International Journal of Chemical Kinetics*, 44(7):444–474, 2012. ISSN 05388066. doi: 10.1002/kin.20603.
- [102] Kéromnès, Alan, Metcalfe, Wayne K., Heufer, Karl A., Donohoe, Nicola, Das, Apurba K., Sung, Chih Jen, Herzler, Jürgen, Naumann, Clemens, Griebel, Peter, Mathieu, Olivier, Krejci, Michael C., Petersen, Eric L., Pitz, William J., and Curran, Henry J. “An experimental and detailed chemical kinetic modeling study of hydrogen and syngas mixture oxidation at elevated pressures.” *Combustion and Flame*, 160(6):995–1011, 2013. ISSN 00102180. doi: 10.1016/j.combustflame.2013.01.001.
- [103] Varga, T., Nagy, T., Olm, C., Zsély, I. Gy, Pálvölgyi, R., Valkó, Vincze, G., Cserhádi, M., Curran, H. J., and Turányi, T. “Optimization of a hydrogen combustion mechanism using both direct and indirect measurements.” *Proceedings of the Combustion Institute*, 35(1):589–596, 2015. ISSN 15407489. doi: 10.1016/j.proci.2014.06.071.
- [104] Hashemi, Hamid, Christensen, Jakob M., Gersen, Sander, and Glarborg, Peter. “Hydrogen oxidation at high pressure and intermediate temperatures: Experiments and kinetic modeling.” *Proceedings of the Combustion Institute*, 35(1):553–560, 2015. ISSN 15407489. doi: 10.1016/j.proci.2014.05.101. URL <http://dx.doi.org/10.1016/j.proci.2014.05.101>.
- [105] Mével, R., Davidenko, D., Austin, J. M., Pintgen, F., and Shepherd, J. E. “Application of a laser induced fluorescence model to the numerical simulation of detonation waves in hydrogen-oxygen-diluent mixtures.” *International Journal of Hydrogen Energy*, 39(11):6044–6060, 2014. ISSN 03603199. doi: 10.1016/j.ijhydene.2014.01.182.
- [106] Konnov, Alexander A. “Yet another kinetic mechanism for hydrogen combustion.” *Combustion and Flame*, 203:14–22, 2019.

- ISSN 15562921. doi: 10.1016/j.combustflame.2019.01.032. URL <https://doi.org/10.1016/j.combustflame.2019.01.032>.
- [107] Schultz, E and Shepherd, J. Validation of Detailed Reaction Mechanisms for Detonation Simulation. Technical report, 2000.
- [108] Schultz, E and Shepherd, J. “Detonation analysis using detailed reaction mechanisms.” *Proceedings of 22nd International Symposium on Shock Waves*, pages 273–278, 2000.
- [109] Petersen, E. L., Davidson, D. F., Röhrig, M., and Hanson, R. K. High-Pressure Shock-Tube Measurements of Ignition Times in Stoichiometric H₂/O₂/Ar Mixtures. In Sturtevant, B., Shephard, J. E., and Hornung, H. G, editors, *Proceedings of the 20th International Symposium on Shock Waves*, pages 941–946, New Jersey, 1996. World Scientific.
- [110] Herzler, J. and Naumann, C. “Shock-tube study of the ignition of methane/ethane/hydrogen mixtures with hydrogen contents from 0different pressures.” *Proceedings of the Combustion Institute*, 32 I (1):213–220, 2009. ISSN 15407489. doi: 10.1016/j.proci.2008.07.034. URL <http://dx.doi.org/10.1016/j.proci.2008.07.034>.
- [111] Goodwin, David G., Speth, Raymond L., Moffat, Harry K., and Weber, Bryan W. Cantera: An object-oriented software toolkit for chemical kinetics, thermodynamics, and transport processes. <https://www.cantera.org>, 2021. Version 2.4.0.
- [112] Kao, S. and Shepherd, J. E. “Numerical Solution Methods for Control Volume Explosions and ZND Detonation Structure.” *GALCIT Report FM2006.007*, (July 2004):1–46, 2008.
- [113] Shepherd, Joseph E. Shock and Detonation Toolbox, 2019.
- [114] Liang, Z., Browne, S., Deiterding, R., and Shepherd, J. E. “Detonation front structure and the competition for radicals.” *Proceedings of*

- the Combustion Institute*, 31 II(2):2445–2453, 2007. ISSN 15407489. doi: 10.1016/j.proci.2006.07.244.
- [115] Ng, H. D., Radulescu, M. I., Higgins, A. J., Nikiforakis, N., and Lee, J. H.S. “Numerical investigation of the instability for one-dimensional Chapman-Jouguet detonations with chain-branching kinetics.” *Combustion Theory and Modelling*, 9(3):385–401, 2005. ISSN 13647830. doi: 10.1080/13647830500307758.
- [116] Ng, Hoi Dick. *The effect of chemical reaction kinetics on the structure of gaseous detonations*, volume 68. 2005. ISBN 9780494216828.
- [117] Ng, Hoi Dick, Ju, Yiguang, and Lee, John H.S. “Assessment of detonation hazards in high-pressure hydrogen storage from chemical sensitivity analysis.” *International Journal of Hydrogen Energy*, 32(1):93–99, 2007. ISSN 03603199. doi: 10.1016/j.ijhydene.2006.03.012.
- [118] Ciccarelli, G., Ginsburg, T., Boccio, J., Economos, C., Finfrook, C., Gerlach, L., Sato, K., and Kinoshita, M. “High-Temperature Hydrogen-Air- Steam Detonation Experiments in the BNL Small-Scale Development Apparatus.” *NUREG/Cr-6213 BNL-NUREG-42414*, 1994. URL <http://pbadupws.nrc.gov/docs/ML0717/ML071700089.pdf>.
- [119] Lewis, Bernard and Friauf, James B. “Explosions in detonating gas mixtures. I. Calculation of rates of explosions in mixtures of hydrogen and oxygen and the influence of rare gases.” *Journal of the American Chemical Society*, 52(10):3905–3920, 1930. ISSN 15205126. doi: 10.1021/ja01373a022.
- [120] Ng, Hoi Dick and Lee, John H.S. “Direct initiation of detonation with a multi-step reaction scheme.” *Journal of Fluid Mechanics*, 476(476): 179–211, 2003. ISSN 00221120. doi: 10.1017/S0022112002002872.

- [121] Franzelli, Benedetta Giulia. *Impact of the chemical description on direct numerical simulations and large eddy simulations of turbulent combustion in industrial aero-engines*. PhD thesis, 2011.
- [122] Kessler, D. A., Gamezo, V. N., and Oran, E. S. “Simulations of flame acceleration and deflagration-to-detonation transitions in methane-air systems.” *Combustion and Flame*, 157(11):2063–2077, 2010. ISSN 00102180. doi: 10.1016/j.combustflame.2010.04.011. URL <http://dx.doi.org/10.1016/j.combustflame.2010.04.011>.
- [123] Wang, Chang Jian, Wen, Jennifer, Lu, Shou Xiang, and Guo, Jin. “Single-step chemistry model and transport coefficient model for hydrogen combustion.” *Science China Technological Sciences*, 55(8): 2163–2168, 2012. ISSN 16747321. doi: 10.1007/s11431-012-4932-4.
- [124] Dounia, O., Vermorel, O., Misdariis, A., and Poinso, T. “Influence of kinetics on DDT simulations.” *Combustion and Flame*, 200:1–14, 2019. ISSN 15562921. doi: 10.1016/j.combustflame.2018.11.009. URL <https://doi.org/10.1016/j.combustflame.2018.11.009>.
- [125] Tsuboi, N., Eto, K., and Hayashi, A. K. “Detailed structure of spinning detonation in a circular tube.” *Combustion and Flame*, 149 (1-2):144–161, 2007. ISSN 00102180. doi: 10.1016/j.combustflame.2006.12.004.
- [126] Zhao, Majie and Zhang, Huangwei. “Origin and chaotic propagation of multiple rotating detonation waves in hydrogen/air mixtures.” *Fuel*, 275(December 2019):117986, 2020. ISSN 00162361. doi: 10.1016/j.fuel.2020.117986. URL <https://doi.org/10.1016/j.fuel.2020.117986>.
- [127] Davidenko, Dmitry M., Eude, Yohann, Gökalp, Iskender, and Falempin, François. “Theoretical and numerical studies on continuous detonation wave engines.” *17th AIAA International Space Planes and Hypersonic Systems and Technologies Conference 2011*, (April):1–17, 2011. doi: 10.2514/6.2011-2334.

- [128] Paxson, Daniel E. “Numerical Analysis of a Rotating Detonation Engine in the Relative Reference Frame.” *52nd Aerospace Sciences Meeting*, (March 2014), 2014. doi: 10.2514/6.2014-0284. URL <http://arc.aiaa.org/doi/10.2514/6.2014-0284>.
- [129] Schwer, Douglas and Kailasanath, Kailas. “Numerical investigation of the physics of rotating-detonation-engines.” *Proceedings of the Combustion Institute*, 33(2):2195–2202, 2010. ISSN 15407489. doi: 10.1016/j.proci.2010.07.050. URL <http://dx.doi.org/10.1016/j.proci.2010.07.050>.
- [130] Schwer, Douglas and Kailasanath, Kailas. “Numerical Study of the Effects of Engine Size in Rotating Detonation Engines.” *49th AIAA Aerospace Sciences Meeting including the New Horizons Forum and Aerospace Exposition*, (January):1–13, 2011. doi: 10.2514/6.2011-581.
- [131] Williams, Forman A. *Combustion Theory*, (1985). 1985. ISBN 978-0201407778.
- [132] Konnov, Alexander A., Mohammad, Akram, Kishore, Velamati Ratna, Kim, Nam Il, Prathap, Chockalingam, and Kumar, Sudarshan. “A comprehensive review of measurements and data analysis of laminar burning velocities for various fuel+air mixtures.” *Progress in Energy and Combustion Science*, 68:197–267, 2018. ISSN 03601285. doi: 10.1016/j.pecs.2018.05.003.
- [133] Mével, R., Javoy, S., Lafosse, F., Chaumeix, N., Dupré, G., and Paillard, C. E. “Hydrogen-nitrous oxide delay times: Shock tube experimental study and kinetic modelling.” *Proceedings of the Combustion Institute*, 32 I(1):359–366, 2009. ISSN 15407489. doi: 10.1016/j.proci.2008.06.171.
- [134] Bane, Spm, Ziegler, JI, and Shepherd, Je. “Development of one-step chemistry models for flame and ignition simulation.” *GALCIT Report GALTCITFM*, page 53, 2010.

- URL http://www2.galcit.caltech.edu/EDL/publications/reprints/galcit_fm2010-002.pdf.
- [135] Lee, H. I. and Stewart, D. S. “Calculation of linear detonation instability: one-dimensional instability of plane detonation.” *Journal of Fluid Mechanics*, 216:103–132, 1990. doi: 10.1017/S0022112090000362.
- [136] Austin, Joanna M. *The Role of Instability in Gaseous Detonation-Thesis*. PhD thesis, 2003.
- [137] B. J. McBride, M. J. Zehe, and S. Gordon. NASA Glenn coefficients for calculating thermodynamic properties of individual species: National Aeronautics and Space Administration. Technical Report NASA/TP—2002-211556, 2002. URL <http://gltrs.grc.nasa.gov/GLTRS>.
- [138] Chase, Jr. M.W. Nist-janaf thermochemical tables, fourth edition. Technical report, J. Phys. Chem. Ref. Data, Monograph 9, 1998.
- [139] Franzelli, Benedetta Giulia. *Impact of the chemical description on direct numerical simulations and large eddy simulations of turbulent combustion in industrial aero-engines*. PhD thesis, 2011.
- [140] Poinso, Thierry and Veynante, Denis. *Theoretical and Numerical Combustion*. 2005.
- [141] Krejci, Michael C., Mathieu, Olivier, Vissotski, Andrew J., Ravi, Sankaranarayanan, Sikes, Travis G., Petersen, Eric L., Kérmonès, Alan, Metcalfe, Wayne, and Curran, Henry J. “Laminar flame speed and ignition delay time data for the kinetic modeling of hydrogen and syngas fuel blends.” *Journal of Engineering for Gas Turbines and Power*, 135(2):1–9, 2013. ISSN 07424795. doi: 10.1115/1.4007737.
- [142] Gamezo, Vadim N., Desbordes, Daniel, and Oran, Elaine S. “Formation and evolution of two-dimensional cellular detonations.” *Com-*

- bustion and Flame*, 116(1-2):154–165, 1999. ISSN 00102180. doi: 10.1016/S0010-2180(98)00031-5.
- [143] Tsuboi, Nobuyuki, Katoh, Seiji, and Hayashi, A. Koichi. “Three-dimensional numerical simulation for hydrogen/air detonation: Rectangular and diagonal structures.” *Proceedings of the Combustion Institute*, 29(2):2783–2788, 2002. ISSN 15407489. doi: 10.1016/S1540-7489(02)80339-X.
- [144] Reynaud, Maxime, Virot, Florent, and Chinnayya, Ashwin. “A computational study of the interaction of gaseous detonations with a compressible layer.” *Physics of Fluids*, 29(5), 2017. ISSN 10897666. doi: 10.1063/1.4982659. URL <http://dx.doi.org/10.1063/1.4982659>.
- [145] Ciccarelli, G., Ginsberg, T., Boccio, J., Economos, C., Sato, K., and Kinoshita, M. “Detonation cell size measurements and predictions in hydrogen-air-steam mixtures at elevated temperatures.” *Combustion and Flame*, 99(2):212–220, 1994. ISSN 00102180. doi: 10.1016/0010-2180(94)90124-4.
- [146] Pintgen, F., Eckett, C. A., Austin, J. M., and Shepherd, J. E. “Direct observations of reaction zone structure in propagating detonations.” *Combustion and Flame*, 133(3):211–229, 2003. ISSN 00102180. doi: 10.1016/S0010-2180(02)00458-3.
- [147] Viguier, C., Gueraud, C., and Debordes, D. “H₂-air and CH₄-air detonations and combustions behind oblique shock waves.” *Symposium (International) on Combustion*, 25(1):53–59, 1994. ISSN 00820784. doi: 10.1016/S0082-0784(06)80627-2.
- [148] Schönfeld, Thilo and Rudgyard, Michael. “Steady and unsteady flow simulations using the hybrid flow solver AVBP.” *AIAA journal*, 37(11):1378–1385, 1999. ISSN 00011452. doi: 10.2514/2.636.
- [149] <https://www.cerfacs.fr/avbp7x/>, 2021.

- [150] Colin, Olivier and Rudgyard, Michael. “Development of High-Order Taylor-Galerkin Schemes for LES.” *Journal of Computational Physics*, 162(2):338–371, 2000. ISSN 00219991. doi: 10.1006/jcph.2000.6538.
- [151] Lilly, D. K. “A proposed modification of the Germano subgrid-scale closure method.” *Physics of Fluids A*, 4(3):633–635, 1992. ISSN 08998213. doi: 10.1063/1.858280.
- [152] Cook, Andrew W. and Cabot, William H. “A high-wavenumber viscosity for high-resolution numerical methods.” *Journal of Computational Physics*, 195(2):594–601, 2004. ISSN 00219991. doi: 10.1016/j.jcp.2003.10.012.
- [153] Takai, R., Yoneda, K., and Hikita, T. “Study of detonation wave structure.” *Symposium (International) on Combustion*, 15(1):69–78, 1975. ISSN 00820784. doi: 10.1016/S0082-0784(75)80285-2.
- [154] Shank, Jason C. “Development and Testing of a Rotating Detonation Engine Run on Hydrogen and Air.” 2012.
- [155] St. George, A., Driscoll, R., Anand, V., and Gutmark, E. “On the existence and multiplicity of rotating detonations.” *Proceedings of the Combustion Institute*, 36(2):2691–2698, 2017. ISSN 15407489. doi: 10.1016/j.proci.2016.06.132. URL <http://dx.doi.org/10.1016/j.proci.2016.06.132>.
- [156] Bach, Eric, Paschereit, C. O., Stathopoulos, Panagiotis, and Bohon, Myles D. “An empirical model for stagnation pressure gain in rotating detonation combustors.” *Proceedings of the Combustion Institute*, 38(3):3807–3814, 2021. ISSN 15407489. doi: 10.1016/j.proci.2020.07.071. URL <https://doi.org/10.1016/j.proci.2020.07.071>.
- [157] Weiss, Sebastian, Bohon, Myles D., Paschereit, C. Oliver, and Gutmark, Ephraim J. “Computational Study of Reactants Mixing

- in a Rotating Detonation Combustor Using Compressible RANS.” *Flow, Turbulence and Combustion*, 2019. ISSN 15731987. doi: 10.1007/s10494-019-00097-x.
- [158] Schwer, Douglas A. and Kailasanath, K. “Modeling exhaust effects in rotating detonation engines.” *48th AIAA/ASME/SAE/ASEE Joint Propulsion Conference and Exhibit 2012*, (August):1–15, 2012. doi: 10.2514/6.2012-3943.
- [159] Van Driest, E. “Turbulent Boundary Layer in Compressible Fluids.” *Journal Of The Aeronautical Sciences*, 18(3), 1951.
- [160] Lax, Peter D. and Wendroff, Burton. “Difference schemes for hyperbolic equations with high order of accuracy.” *Communications on Pure and Applied Mathematics*, 17(3):381–398, 1964. ISSN 10970312. doi: 10.1002/cpa.3160170311.
- [161] Ducros, F., Nicoud, F., and Poinso, T. “Wall-adapting local eddy-viscosity models for simulations in complex geometries.” *Conference on Numerical Methods in Fluid Dynamics*, pages 1–7, 1998.
- [162] Kawai, S. and Lele, S. K. “Localized artificial diffusivity scheme for discontinuity capturing on curvilinear meshes.” *Journal of Computational Physics*, 227(22):9498–9526, 2008. ISSN 10902716. doi: 10.1016/j.jcp.2008.06.034.
- [163] Bohon, Myles D., Bluemner, Richard, Paschereit, Christian Oliver, and Gutmark, Ephraim J. “Experimental study of reactants mixing in model rotating detonation combustor geometries.” *53rd AIAA/SAE/ASEE Joint Propulsion Conference, 2017*, (July):1–13, 2017. doi: 10.2514/6.2017-4739.
- [164] Crist, S, Sherman, P M, and Glass, D. R. “Study of the Highly Underexpanded Sonic Jet.” *AIAA journal*, 4(1), 1966. doi: 10.2514/3.3386.

- [165] Dickmann, Dean A. and Lu, Frank K. “Shock/boundary-layer interaction effects on transverse jets in crossflow over a flat plate.” *Journal of Spacecraft and Rockets*, 46(6):1132–1141, 2009. ISSN 15336794. doi: 10.2514/1.39297.
- [166] Driscoll, Robert, St. George, Andrew, and Gutmark, Ephraim J. “Numerical investigation of injection within an axisymmetric rotating detonation engine.” *International Journal of Hydrogen Energy*, 41(3):2052–2063, 2016. ISSN 03603199. doi: 10.1016/j.ijhydene.2015.10.055. URL <http://dx.doi.org/10.1016/j.ijhydene.2015.10.055>.
- [167] Driscoll, Robert, Aghasi, Paul, St George, Andrew, and Gutmark, Ephraim J. “Three-dimensional, numerical investigation of reactant injection variation in a H₂/air rotating detonation engine.” *International Journal of Hydrogen Energy*, 41(9):5162–5175, 2016. ISSN 03603199. doi: 10.1016/j.ijhydene.2016.01.116. URL <http://dx.doi.org/10.1016/j.ijhydene.2016.01.116>.
- [168] Celik, I. B., Cehreli, Z. N., and Yavuz, I. “Index of resolution quality for large eddy simulations.” *Journal of Fluids Engineering, Transactions of the ASME*, 127(5):949–958, 2005. ISSN 00982202. doi: 10.1115/1.1990201.
- [169] Pope, Stephen B. “Turbulent Flows.” 2000.
- [170] Nicoud, Franck, Toda, Hubert Baya, Cabrit, Olivier, Bose, Sanjeeb, and Lee, Jungil. “Using singular values to build a subgrid-scale model for large eddy simulations.” *Physics of Fluids*, 23(8), 2011. ISSN 10706631. doi: 10.1063/1.3623274.
- [171] Brophy, Christopher M., Codoni, Joshua R., Teneyck, Joshua A., and Ewing, Spencer. “Experimental performance characterization of an RDE using equivalent available pressure.” *AIAA Propulsion and Energy Forum and Exposition, 2019*, (August), 2019. doi: 10.2514/6.2019-4212.

- [172] Bach, Eric, Paschereit, Christian O., Stathopoulos, Panagiotis, and Bohon, Myles. “RDC Operation and Performance with Varying Air Injector Pressure Loss.” 2020. doi: 10.2514/6.2020-0199.
- [173] Nakayama, Hisahiro, Moriya, Takahiro, Kasahara, Jiro, Matsuo, Akiko, Sasamoto, Yuya, and Funaki, Ikkoh. “Stable detonation wave propagation in rectangular-cross-section curved channels.” *Combustion and Flame*, 159(2):859–869, 2012. ISSN 00102180. doi: 10.1016/j.combustflame.2011.07.022. URL <http://dx.doi.org/10.1016/j.combustflame.2011.07.022>.
- [174] Fric, T. F. “Effects of fuel-air unmixedness on NO_x emissions.” *AIAA/ASME/SAE/ASEE 28th Joint Propulsion Conference and Exhibit*, 1992, 9(5), 1992. doi: 10.2514/6.1992-3345.
- [175] Kluge, T., Henke, M., and Seume, J. R. “Comparison of Different Methods for the Analysis of Time-Resolved Flow Field Measurements in an Axial Turbine.” *11th European Conference on Turbomachinery Fluid Dynamics and Thermodynamics, ETC 2015*, pages 1–12, 2015.
- [176] Rodriguez, V., Jourdain, C., Vidal, P., and Zitoun, R. “An experimental evidence of steadily-rotating overdriven detonation.” *Combustion and Flame*, 202:132–142, 2019. ISSN 15562921. doi: 10.1016/j.combustflame.2019.01.016. URL <https://doi.org/10.1016/j.combustflame.2019.01.016>.